DESIGN AND OPTIMUM OPERATION OF A RE-CONFIGURABLE PLANAR GOUGH-STEWART MACHINING PLATFORM

by

Lukas Johannes du Plessis

A dissertation submitted in partial fulfillment of the
requirements for the degree of

Philosophiae Doctor (Mechanical Engineering)

in the

Faculty of Engineering, Built Environment and Information
Technology, University of Pretoria

December 2001

Dedicated to my family

and in memory of

"Oom Nap & Tannie Lalie Esterhuizen"

ABSTRACT

DESIGN AND OPTIMUM OPERATION OF A RE-CONFIGURABLE PLANAR GOUGH-STEWART MACHINING PLATFORM

by

Lukas Johannes du Plessis

Promoter: **Professor J.A. Snyman**

Department of Mechanical and Aeronautical Engineering

Degree: <u>Philosophiae Doctor (Mechanical Engineering)</u>

<u>Keywords</u>: Gough-Stewart platform, re-configurable machine tool, adjustable geometry, inverse kinematics, inverse dynamic analysis, trajectory-planning, cubic spline interpolation, mathematical optimization, constrained optimization problem.

This study presents a computer operating system for a novel *re-configurable planar Gough-Stewart machining platform*. The operating system is tested on a physically constructed *test-model* of the proposed re-configurable platform. In doing so, the proposed concept of a re-configurable planar machine tool, consisting of a moving platform connected to a fixed base via three linear actuators is validated, both from a theoretical and practical point of view.

The computer operating system consists of four sections:

1. **Simulation**: A computer program for simulating the motion of a planar Gough-Stewart platform was developed. This was done by applying the basic principles of Newton-Euler dynamics to a mechanical model of the platform. In particular, this special purpose simulation program allows for the *inverse dynamic analysis* of a planar Gough-Stewart platform so as to give closed-form expressions for the required actuator forces necessary for the execution of a *specified trajectory*. As a prerequisite for the inverse dynamic analysis, the special purpose program that was developed, also performs the *inverse kinematic analysis* of the mechanism by solving closed-form expressions for the positions, velocities and accelerations of the individual bodies comprising the machine.

2. **Trajectory-planning**: A new *path-planning* interpolation algorithm has been developed with which a user may specify the desired path to be followed by any *planar* industrial robot, and therefore in particular also the planar Gough-Stewart platform. Given prescribed kinematical requirements and

specified points along the path, a *cubic spline interpolation curve* is fitted in the time-domain, and further user-specified information is used to determine how the end-effector orientation angle should vary along the specified curve. This trajectory-planning algorithm is combined with the above-mentioned inverse dynamic simulation program to determine and monitor the required actuator forces as the planar Gough-Stewart platform traces the prescribed trajectory.

3. **Optimization**: With the ability to determine the required actuator forces at any instant along any prescribed path, an *adjustable geometry* planar Gough-Stewart machining platform becomes a viable option. The rationale is that the simulation of the mechanism allows for the off-line *optimization* of the operational geometry of the mechanism for the prescribed path. The single criterion objective function used is the minimization of the "maximum magnitude actuator force" identified via the above-mentioned dynamic simulation. The minimization of this objective function with respect to the variable geometry, ensures that singular configurations are avoided as the specified path is traced. The minimization of the objective function is further subjected to compliance with formulated inequality constraints that ensures mechanical feasibility as the *constrained optimization problem* is solved.

Once the optimum operational geometry is determined, the physical re-configurable planar Gough-Stewart platform can be adjusted accordingly to ensure the successful execution of the desired trajectory. If it is not possible to trace the prescribed path, then user intervention is required. This may be done in a rational manner since the specific numerical optimization algorithm used here (LFOPC), gives a best compromised solution if no feasible design exists for the specified trajectory. The importance of this compromised solution is that it points out which constraints are violated and to what extent. This provides information for determining a piece-wise execution strategy by means of which the complete task may be performed, both feasibly and optimally.

4. **Control**: Apart from optimizing the Gough-Stewart platform configuration for a given task, the computer operating system also generates the necessary commands for controlling the required variation of the actuator leg lengths. This allowed for the physical execution of a number of representative prescribed machining paths.

SAMEVATTING

ONTWERP EN OPTIMALE WERKING VAN 'n
HERKONFIGUREERBARE VLAK GOUGH-STEWART-
MASJINERINGSPLATFORM

deur

Lukas Johannes du Plessis

Promotor: **Professor J.A. Snyman**
Department Meganiese and Lugvaartkundige Ingenieurswese

Graadbenaming: <u>Philosophiae Doctor (Meganiese Ingenieurswese)</u>

<u>Sleutelwoorde</u>: Gough-Stewart platform, herkonfigureerbare masjienwerktuig, verstelbare geometrie, terugwaartse kinematika, terugwaartse dinamiese analise, kubiese lat-interpolasie, wiskundige optimering, begrensde optimeringsprobleem.

Hierdie studie handel oor 'n rekenaarbedryfstelsel vir die inwerkingstelling van 'n unieke *herkonfigureerbare vlak Gough-Stewart-masjineringsplatform*. Die bedryfstelsel is getoets met behulp van 'n toetsmodel van die voorgestelde herkonfigureerbare platform, wat spesiaal vir die doel ontwerp en gebou is. Sodoende is die uitvoerbaarheid van die voorgestelde konsep van 'n herkonfigureerbare vlak masjienwerktuig bevestig, beide vanuit 'n teoretiese en praktiese oogpunt. Die herkonfigureerbare vlak Gough-Stewart-masjineringsplatform waarna verwys word, bestaan uit 'n bewegende platform wat deur middel van drie lineêre aktueerders aan 'n vaste basis gekoppel is.

Die rekenaarbedryfstelsel bestaan uit vier dele:
1. **Simulasie**: 'n Rekenaarprogram is geskryf om die beweging van 'n vlak, Gough-Stewart-platform na te boots. Dit is gedoen deur die basiese beginsels van Newton-Euler-dinamika toe te pas op 'n meganiese model van die platform. Hierdie doelgerigte en toegewyde simulasieprogram stel 'n mens in staat om die *terugwaartse dinamiese analise* van 'n vlak Goug-Stewart-platform ekonomies te doen. Dit behels die gebruik van geslote-vorm wiskundige uitdrukkings waardeur die onbekende aktueerderkragte tydens die uitvoering van die *voorgeskrewe baan* bereken kan word. As deel van die terugwaarste dinamiese analise voer hierdie spesiale rekenaarprogram ook die terugwaartse kinematiese analise uit deur gebruik te maak van geslote-vorm uitdrukkings vir die posisies, snelhede en versnellings van die individuele liggame waaruit die masjien bestaan.

2. **Trajekbeplanning**: 'n Nuwe intepolerende *trajekbeplannings*-algoritme is ontwikkel waarmee die gebruiker die verlangde baan, wat deur enige *vlak* industrieële robot en gevolglik ook die vlak Gough-Stewart-platform gevolg moet word, analities kan spesifiseer. Met sekere voorgeskrewe kinematiese vereistes bekend, asook die gespesifiseerde node-punte langs die baan, pas die trajekbeplannings-algoritme interpolerende kubiese latfunksies in die tyddomein. Verdere insette van die gebruiker is egter nodig om te bepaal hoe die orientasie-hoek van die meganisme se beheerde eindwerktuig moet varieer langs die voorgeskrewe baan. Ten einde die aktueerderkragte langs verskillende voorgeskrewe bane te bereken, is die trajekbeplannings-algoritme gekombineer met bogenoemde terugwaartse dinamiese analise van die vlak Gough-Stewart-masjineringsplatform.

3. **Optimering**: Die lewensvatbaarheid van 'n vlak Gough-Stewart-platform met 'n *verstelbare geometrie*, lê daarin opgesluit dat dit moontlik is om die onbekende aktueerderkragte langs enige voorgeskrewe baan en op enige gegewe tydstip te bereken. Die rekenaarsimulasie van die meganisme stel 'n mens in staat stel om die werkingsgeometrie van die meganisme te *optimeer* na gelang van die voorgeskrewe baan. Die enkelmaatstafdoelfunksie wat hiervoor gebruik word, is die mimimering van die "maksimum-grootte-aktueerderkrag" wat via bogenoemde dinamiese rekenaarsimulasie geïdentifiseer word. Die minimering van hierdie doelfunksie, met betrekking tot die verstelbare geometrie, waarborg dat singuliere konfigurasies geassosieer met oneindige groot aktueerderkragte tydens die uitvoering van die voorgeskrewe baan, vermy word. Verder moet die minimering van hierdie doelfunksie uitgevoer word met inagneming van geformuleerde ongelykheidsbegrensings. Sodoende word die meganiese uitvoerbaarheid van die berekende oplossing tot die *begrensde optimeringsprobleem*, verseker.

Sodra die optimale werkingsgeometrie bepaal is, word die fisiese herkonfigureerbare vlak Gough-Stewart-platform dienooreenkomstig verstel, ten einde die voorgeskrewe baan suksesvol uit te voer. Indien dit onmoontlik is om die voorgeskrewe baan te volg, moet die gebruiker 'n beredeneerde besluit maak. Die spesifieke numeriese optimerings-algoritme wat in hierdie studie gebruik word (LFOPC), bereken die beste moontlike kompromie-oplossing indien daar geen lewensvatbare ontwerp vir 'n voorgeskrewe baan bestaan nie. Die beste kompromie-oplossing dui aan watter ongelykheidsbegrensings oorskry is, en tot watter mate. Hierdie kompromie-oplossing is noodsaaklik om 'n beredeneerde besluit te maak aangaande die stuksgewyse uitvoering van die voorgeskrewe baan op 'n lewensvatbare en optimale wyse.

4. **Beheer**: Afgesien van die konfigurasie-optimering van die Gough-Stewart-platform na gelang van 'n gegewe taak, genereer die rekenaarbedryfstelsel ook die beheerkode wat nodig is vir die verlangde variasie in aktueerderbeenlengtes. Gevolglik is 'n paar verteenwoordigende masjineringsbane fisies uitgevoer met behulp van die toetsmodel.

ACKNOWLEDGEMENTS

TABLE OF CONTENTS

TABLE OF CONTENTS

1 INTRODUCTION: OVERVIEW OF GOUGH-STEWART PLATFORMS USED AS MACHINING CENTERS

1.1 Introduction

The main objective of this study is to verify the feasibility, both from a theoretical and practical point of view, of a novel proposed concept of a re-configurable planar Gough-Stewart machining platform.

The selective literature presented in this chapter gives a brief overview of the history of Gough-Stewart platforms, and then focuses on the limited industrial application of this technology to machine tools. The potential of re-configuration is put into perspective, and the existing methods for optimizing the designs of Gough-Stewart platform machine tools are presented. In the concluding Section 1.6, the novel concept proposed in this study is motivated based on the literature survey presented in this chapter.

1.2 History of Gough-Stewart platforms

A robotic manipulator is a mechanical device for the remote handling of objects or materials. Broadly speaking, industrial robotic manipulators may be categorized as either *serial manipulators* or *parallel manipulators*.

A *serial manipulator* consists of a number of links connected one after the other in series. The most well known serial manipulator is in fact the human arm since it fulfills this requirement. Most industrial robotic manipulators in use today are serial manipulators [1, 2]. An explanation for this phenomenon is given in [2]: "As the science and technology of robotics originated with the spirit of developing mechanical systems which would *carry out tasks normally ascribed to human beings*, it is quite natural that the main thrust was towards using *open-loop serial chains* as robot manipulators. Such robot manipulators have the advantage of sweeping workspaces and dextrous maneuverability like the *human arm, ...*".

In spite of the many applications where serial manipulators are used with great success, researchers agree that these manipulators are not ideally suited to deliver high load carrying capacity, good dynamic performance or precise positioning [1, 2]. Many serial manipulators have a *cantilever structure*, which tends to bend under heavy load and therefore inhibits the manipulator's load carrying capacity [2]. To address this problem, bulky links are used for certain applications, but this has a negative influence on the ratio of load capacity to manipulator mass [1].

The intuitive alternative for greater rigidity and superior positional capability is to have the end-effector linked to the base via *several parallel-actuated chains* as illustrated by two very practical examples in [2]:

- human beings use both arms in cooperation to handle heavy loads, and
- for precise work such as writing, three fingers actuated in parallel are used.

More formally, Merlet [1] defines a *generalized parallel manipulator* as a *closed-loop* kinematic chain whose end-effector is linked to the base by several independent chains.

Dasgupta and Mruthyunjaya [2] distinguish between two classifications of robot manipulators (*serial* vs. *parallel*) and (*open-loop* vs. *closed-loop*) and explain that although open-loop manipulators are always serial and parallel ones are always with closed loop(s), it is possible to have closed-loop manipulators which are serial in nature. As an example, they mention that a robot manipulator having single degree-of-freedom (DOF) closed-loop linkages in series is essentially a serial manipulator. They further point out that some robot manipulators have both open and closed kinematic loops and /or complicated series-parallel combinations of actuators, concluding that such manipulators are called *hybrid manipulators*, since they can be *hybrid* in the sense of both classifications.

A particularly important and famous subclass [2, 3] of generalized parallel manipulators is the so-called *Gough-Stewart platforms*. For the purposes of this study, a Gough-Stewart platform is defined as a parallel manipulator consisting of two platforms: a fixed platform (the base) and a moving platform. The moving platform is connected to the base by *six prismatic joints* acting in parallel to control the 6-DOF of the moving platform. Furthermore, all the fixed base joints and the moving platform support joints, respectively, *lie in the same base and platform planes*.

The first working prototype of such a parallel manipulator is the tire test machine of Gough and Whitehall [4] shown in Figure 1.1, and which was operational in 1954-1955 [5].
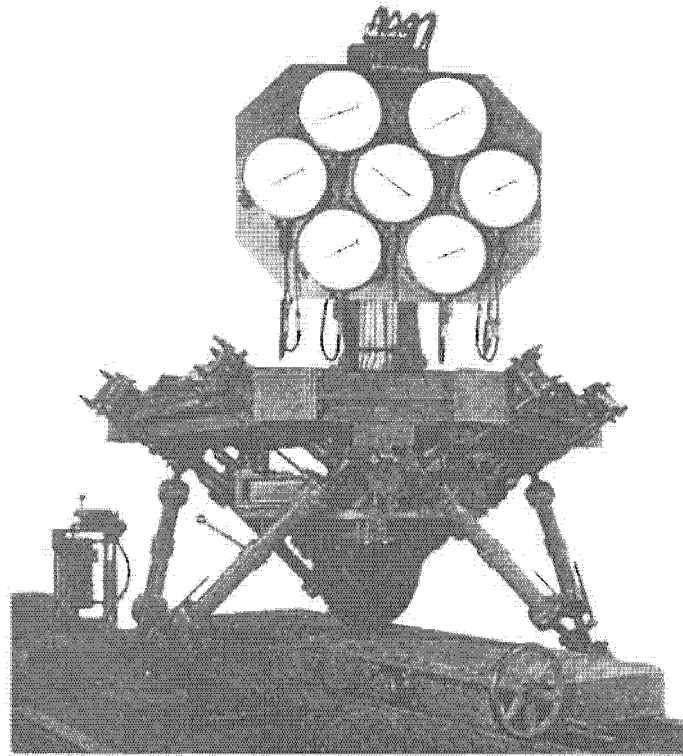
Figure 1.1: The tire test machine of Gough and Whitehall (after [5]).

It is however the classic 1965 paper of Stewart [5] that attracted research attention to the field of parallel manipulators [2]. The mechanism that Stewart proposed as a flight simulator is shown in Figure 1.2. It consists of a triangular platform supported by ball joints over three legs of adjustable lengths and adjustable angular altitudes. The three legs are connected to the ground through two-axis joints (see [2]).
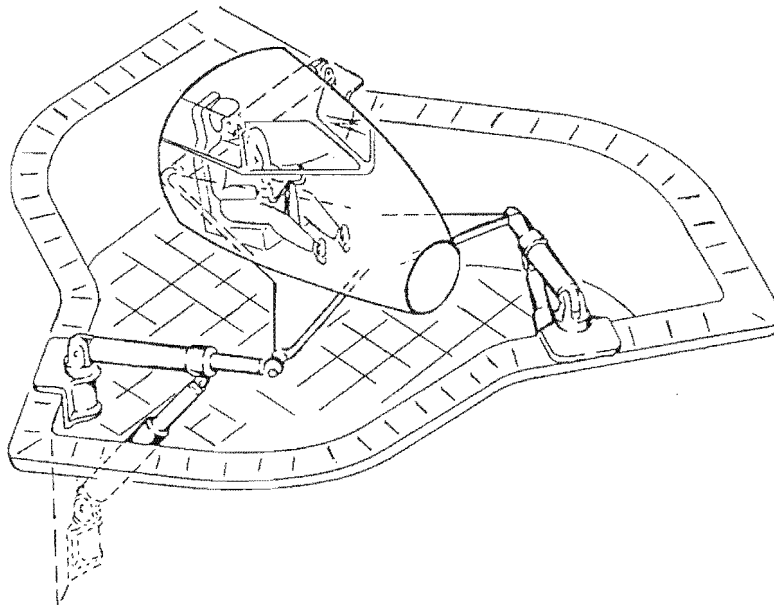
Figure 1.2: Stewart's proposed flight simulator (after [5]).

Note that this particular mechanism cannot be strictly categorized as a Gough-Stewart platform in the sense of the definition given above, because of its leg arrangement ("polar coordinate control leg

system") depicted in Figure 1.3. However, in his paper Stewart [5] points out that the moving platform may be controlled in any combination by six "motors" each having a "ground abutment". As a result of this, he describes the use of a "linear coordinate control leg system", (see Figures 15 and 20 in [5]), resulting in a Gough-Stewart platform consistent with the definition used here.
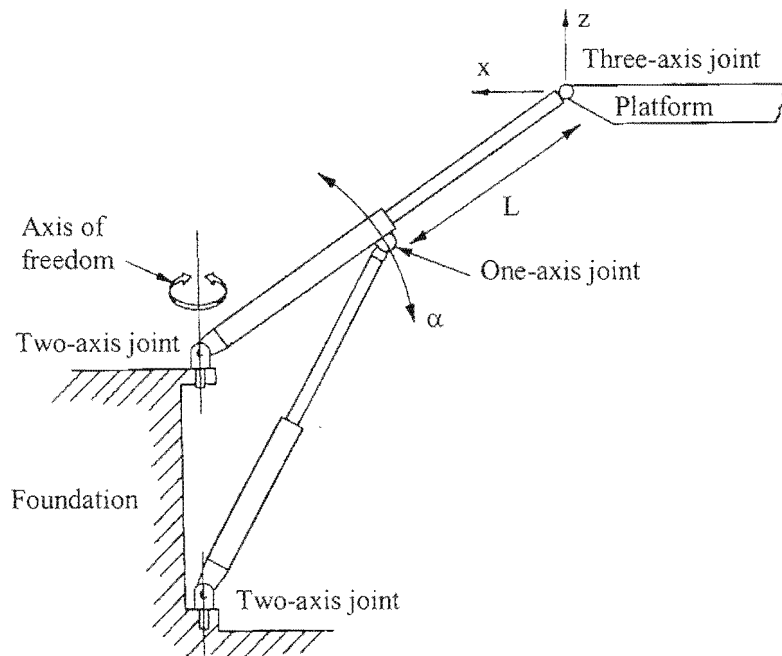
Figure 1.3: Stewart's original platform: "polar coordinate control leg system" (after [5]).

Stewart [5] comments that although his platform fitted with linear control leg systems is very similar to Gough's mechanism, it was independently conceived, and therefore the current usage of the name Gough-Stewart platform to denote such a parallel manipulator.

Researchers agree that parallel manipulators in general evolved into a popular research topic only in the 1980's [2, 6]. This happened after Hunt [7] realized that the stiffness and precise positioning capabilities of parallel manipulators are distinct advantages over serial manipulators, and as such, potential applications of parallel manipulators should be studied in more detail [2].

The systematic study of parallel manipulators in general, and Gough-Stewart platforms in particular, revealed that many theoretical problems that are easily solved for serial manipulators are much more difficult to solve for parallel manipulators, and vice versa. According to Dasgupta and Mruthyunjaya [2], the *generalized 6-DOF Gough-Stewart platform* is the parallel manipulator in which the contrast with respect to serial manipulators is manifested in the most prominent manner, making it the most celebrated manipulator in the entire class.

One specific contrast is the *limited workspace* of a 6-DOF Gough-Stewart platform compared to the *sweeping workspace* and *dextrous maneuverability* of a 6-DOF serial manipulator. The Gough-Stewart platform designs of the 1980's made use of pair wise meeting of the legs on either or both the moving platform and the fixed base. However, researchers of this era soon realized that the coalescence of spherical joints *severely restricts* the mobility of the manipulator [2].

Based on the definition of Gough-Stewart platforms, the most general 6-DOF Gough-Stewart platform would have six distinct leg support joints on *both* the moving platform and fixed base planes (see Figure 1.4).
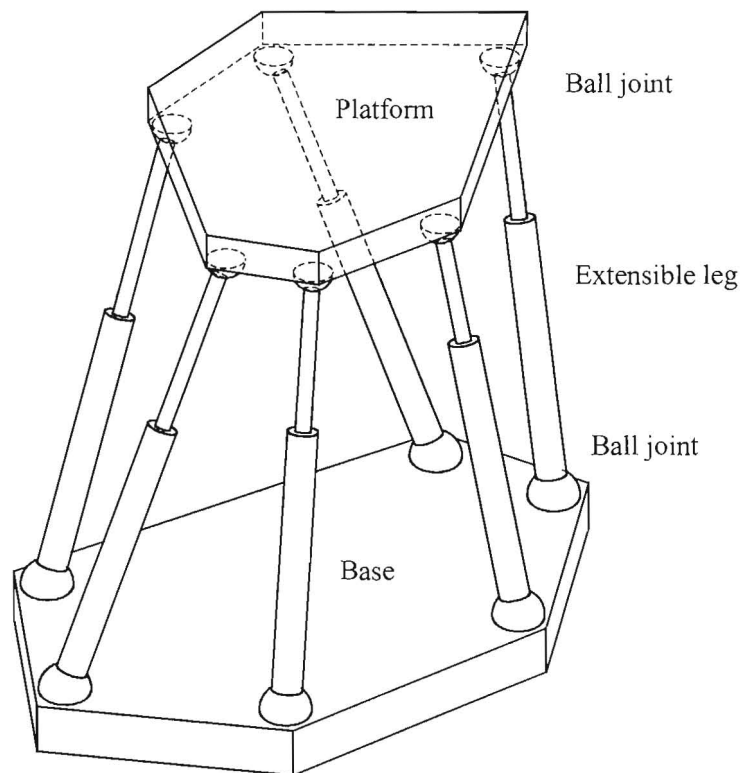
Figure 1.4: Schematic representations of a general 6-DOF Gough-Stewart platform (after [2]).

Over the past two decades, there has been an ever-increasing research interest in the field of parallel manipulators [1, 2]. In their recent review article, with an extensive list of more than 200 references, Dasgupta and Mruthyunjaya [2] present a state-of-the-art review of the literature on Gough-Stewart platforms with critical examination of solved and unsolved problems in various aspects of kinematics, dynamics and design. According to them, and with regard to Gough-Stewart platforms in particular, three of the main areas in which open problems exists are:

- dynamics and control,
- workspace and singularity analysis, and
- design.

More specifically, Dasgupta and Mruthyunjaya [2] state that there are very few works on the *systematic design* of Gough-Stewart platforms and emphasize the importance of further research in this direction for the enhancement and realization of the mechanism's potential.

With reference to parallel manipulators in general, one of the concluding remarks in the Gough-Stewart platform review [2] is that the different nature of parallel manipulators, compared to their conventional serial counterparts, calls for *unconventional strategies* and *novel concepts* for *analysis* and *design*. This is in agreement with one of the main conclusions reached by Merlet [1] in his recent comprehensive book on parallel robots and in which more than 600 literature references are cited. He states that: "Among the open research fields are *synthesis*, *design* and *optimal design*".

1.3 Gough-Stewart platforms as machining centers

1.3.1 6-DOF Gough-Stewart machining platforms

In reaction to Stewart's paper [5], researchers immediately realized the potential application of Gough-Stewart platforms as machine tools. For instance, in the communications on Stewart's article [5], Tindale presents an artistic impression of a "universal mill" based on the platform Stewart proposed as a flight simulator. In his accompanying description, Tindale explains that such a milling machine could be used to machine complicated shapes (such as propellers) with simple cutters. He adds that the economically viability of such a machine tool would require a period of expensive study and development.

In 1966 Lewis [8] also gave a very detailed description of how such a machine tool could be applied in practice. In spite of this, it was only 28 years later that "...two American machine tool companies, Giddings & Lewis and Ingersoll, *surprised* the world with the presentation of a *new type of machine tool* at the 1994 International Manufacturing Technology Show (IMTS) in Chicago". This quotation is taken from Pritschow's [9] presentation on "Research and development in the field of parallel kinematic systems in Europe" at the first "European-American Forum on Parallel Kinematic Machines: Theoretical Aspects and Industrial Requirements" that was held in Milan, Italy in 1998 [10].

The machine tools that were presented in Chicago in 1994 were the "Variax Hexacenter" by Giddings and Lewis [11] shown in Figure 1.5, and the "Octahedral Hexapod" machine tool from the Ingersoll Milling Machine Company [12] shown in Figure 1.6.
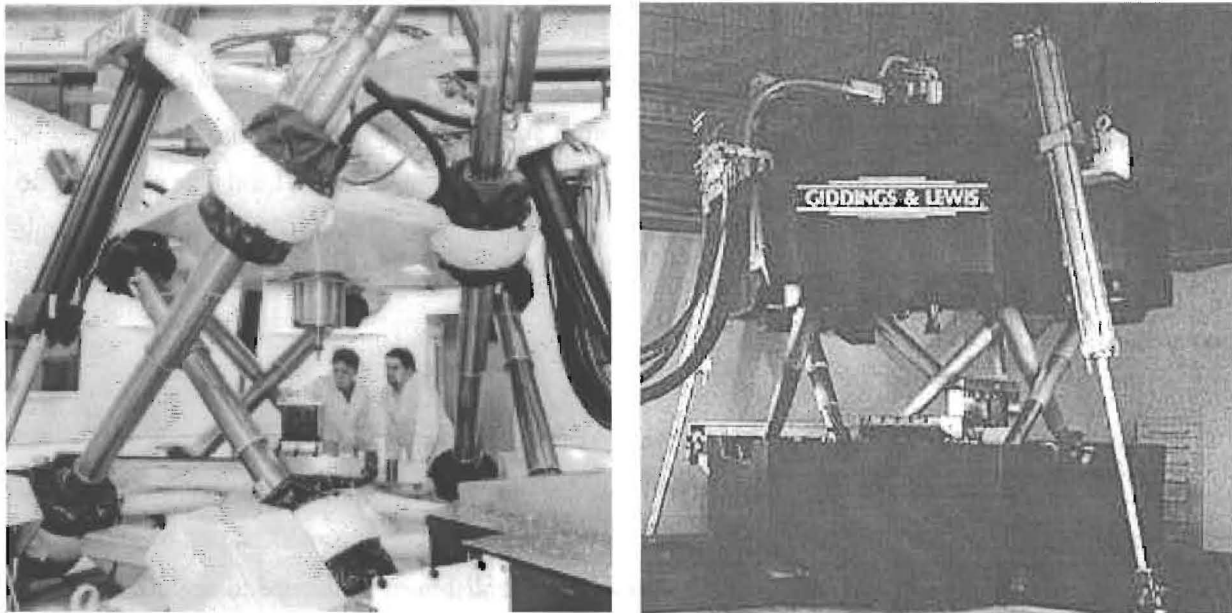
Figure 1.5: The "Variax Hexacenter".

Gindy et al. [13] explain that the "Variax" structure consists of a triangulated arrangement of three pairs of crossed legs. The prismatic legs of the "Variax" are all based on a "simple ball screw design, each powered by a separate servomotor". By inspection of the left hand photograph in Figure 1.5, the fixed base joints and the moving platform support joints all lie in the same base and moving platform planes. The additional cylinders that can be seen in the right hand photograph in Figure 1.5, are the three "counterbalance cylinders" that "support the weight of the upper platform so that the ball screws can perform the singular task of moving the machine" [13]. In spite of these additional cylinders, the "Variax Hexacenter" is categorized as a general Gough-Stewart platform.
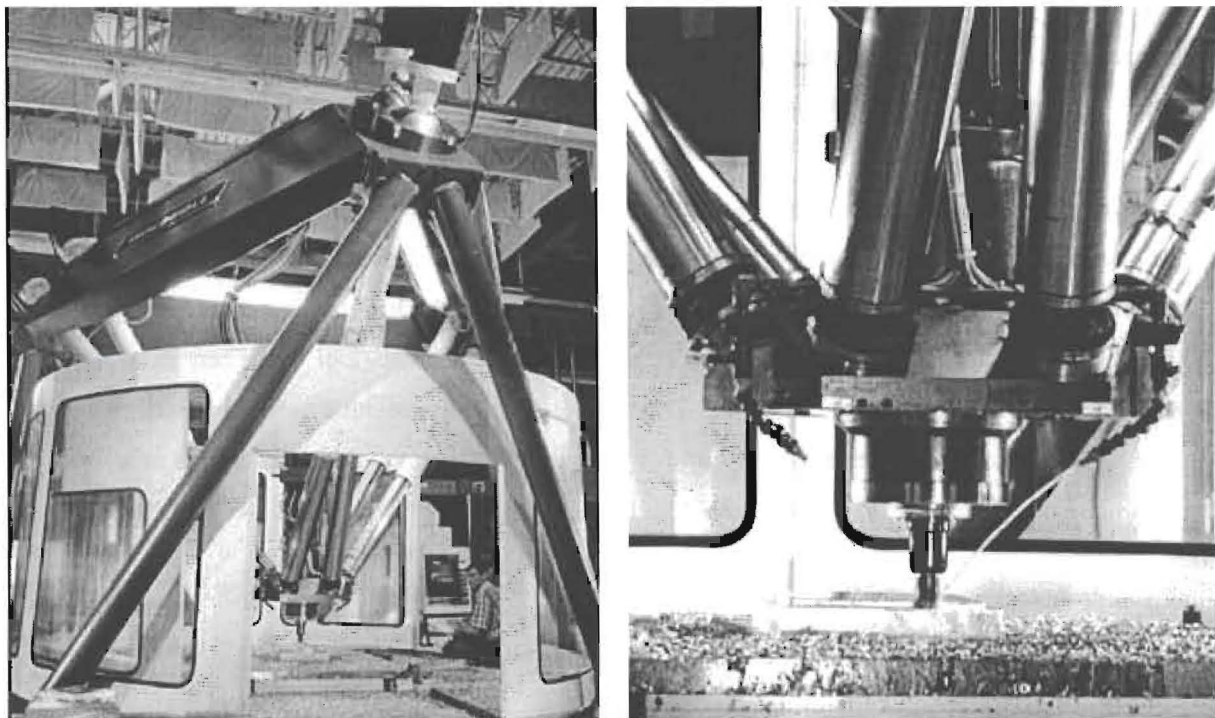
Figure 1.6: The "Octahedral Hexapod" (after [12]).

From Figure 1.6 it is evident that the pairs of base joints (each pair consisting of three joints), of the "Octahedral Hexapod" lie in two separate parallel planes. The offset between the two parallel base planes appears to be very small compared to the overall size of the machine, which is reported to be approximately 5 m tall [12]. Visual inspection of the enlarged view on the right hand side of Figure 1.6 shows that the moving platform support joints all lie in the same plane. Hence, for the purposes of this overview, the "Octahedral Hexapod" may also be considered a general Gough-Stewart platform according to the definition given in Section 1.2.

Interestingly, both these Gough-Stewart platform machine tools were installed at research institutions shortly after their introduction. The Department of Mechanical Engineering and Operations Management at The University of Nottingham purchased the "Variax Hexacenter" as part of a four-year research initiative, and in doing so, was the first research establishment in Europe to acquire a parallel manipulator type machine tool [11]. The Ingersoll Milling Machine Company installed its "Octahedral Hexapod" at the American Department of Commerce, National Institute for Standards and Technology (NIST) in May 1995 [12].

By 1998 the respective research institutions concluded that:
- "The research into these machines (parallel manipulator machine tools) is in its early stages and much work is still required in their design, optimization and control" [11], and
- "Parallel kinematic machine tools continue to look promising, and yet some very interesting and difficult challenges remain" [12].

Apart from the above less than promising conclusions, the unveiling of these Gough-Stewart platform machine tools in 1994 triggered the search for *new improved kinematic structures for machine tools* [9].

Conventional machine tools are largely constructed as serial kinematic chains connecting the workpiece to the tool. By far the largest majority of machine tools are of the Cartesian type, with two or three linear slides arranged in a mutually perpendicular fashion [14] such that the lower axis carries the one above it [15]. Ziegert et al. [14] comment that this basic type of machine tool has been in widespread development and use for nearly 200 years. During that time, this machine configuration has become well understood and now represents a very mature technology. Continuous improvements in technology and manufacturing methods have led to the high levels of performance expected of "modern" machine tools.

In spite of the success of this technology, increasingly challenging requirements with regard to productivity, economy and flexibility in manufacturing increasingly revealed the limitations of conventional machine tools:

- the machine structure is subject to bending loads, causing deformations,

- the structure of the machine requires large masses to be moved, and

- there is an accumulation of errors due to the in series arrangement of the axes [15].

Consequently, after the "surprise" unveiling in 1994, many joint research efforts and consortiums were formed by industry and universities worldwide, which were aimed specifically at applying parallel manipulators as machine tools [1, 9, 11, 12, 16]. In order to further stimulate the exchange of ideas and findings in this regard, a biannual international conference is organized for this research community. The first gathering was at the 1998 "European-American Forum on Parallel Kinematic Machines" mentioned earlier, and the second was the "Year 2000 Parallel Kinematic Machines International Conference", held in Ann Arbor, Michigan USA [17].

With reference to 6-DOF Gough-Stewart platforms, the conclusive outcome of this intensified research effort is that there are limitations prohibiting their application as production machine tools [16]:

- the unfavorable ratio of manipulator size to manipulator workspace,

- limited dexterity and tilting angles ($15° - 30°$),

- inherent danger of strut collision, and

- singularities inside the workspace.

It is therefore no surprise that one of the more successful parallel manipulator type machine tools used by industry is *not* a Gough-Stewart platform. Instead it is a 3-DOF parallel manipulator with fixed leg lengths, and actuated base joints. The patented "Z^3-head", developed by DS Technologie Gmbh (DST), is shown in Figure 1.7. It has two rotational DOF with *tilting angles* of $\pm 40°$ *within* a 370 mm stroke length of the translational DOF. The *maximum stroke length* of the translational DOF is 670 mm [18].
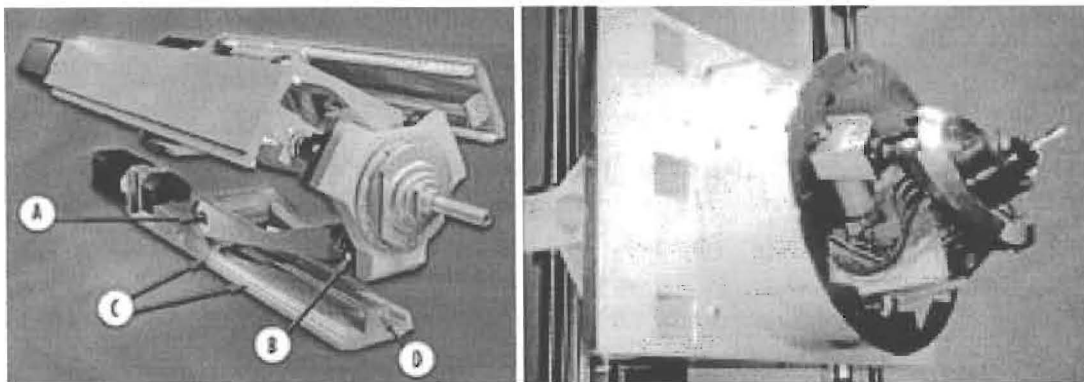
Figure 1.7: The "Z^3-head" (after [18]).

The "Z^3-head" accommodates a motorized spindle that holds the cutting tool. It forms part of a five-axis *hybrid* machine tool [19], with the parallel manipulator head mounted on a two-axis Cartesian base.

This machine tool is marketed in the aerospace industry through the alliance formed by Cincinnati Machine and DS Technologie [18].

1.3.2 Planar Gough-Stewart machining platforms

1.3.2.1 The "Smartcuts" planar Gough-Stewart platform

Dasgupta and Mruthyunjaya [2] also review the so-called "lower dimensional parallel manipulating structures" that are similar to the 6-DOF Gough-Stewart platform, in that they are also equipped with linear actuators. One such sub-class is the "planar 3-DOF parallel manipulator" schematically shown in Figure 1.8.
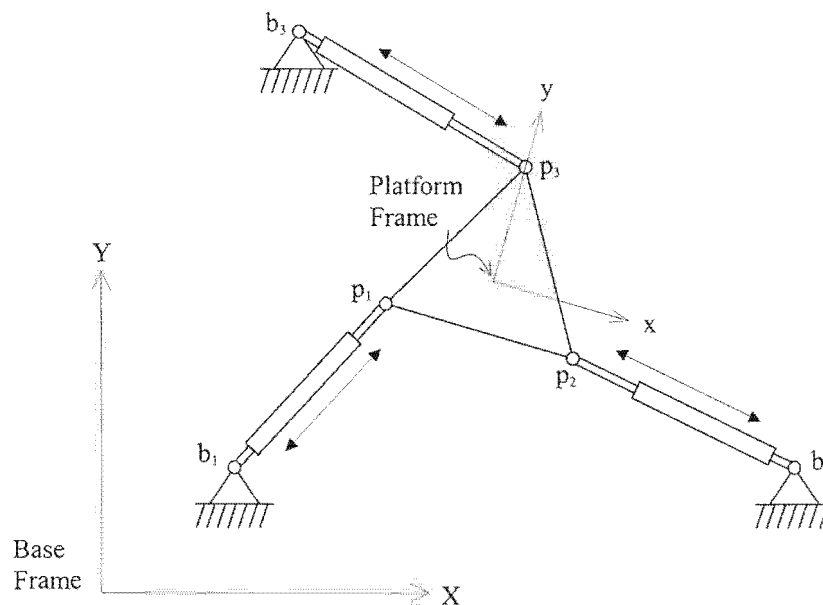
Figure 1.8: Planar 3-DOF parallel manipulator (after [2]).

The research relevance of this mechanism is evident from the respective overviews given in [1] and [2]. More specifically, the book by Duffy [20] presents the kinematic analysis of several planar parallel mechanisms. Many other authors have studied planar parallel mechanisms in a context of robotics. For instants, the inverse and direct kinematic problems have been solved [21, 22, 23, 24, 25], dynamic models have been developed [26], the singularities have been studied [27] and the kinematic design has been addressed [28, 29, 30].

For the purposes of this study a *planar 3-DOF Gough-Stewart platform* is considered a subclass of the (general) planar 3-DOF parallel manipulator shown in Figure 1.8.   More specifically (and in correspondence with the Gough-Stewart platform definition given in Section 1.2), the revolute joints connecting the three linear actuator legs of the *planar 3-DOF Gough-Stewart platform* to the moving platform and base, respectively lie in the in the same base and moving platform *lines*.

Of particular importance with reference to this study, is that Satya et al. [31] have proposed a planar 3-DOF Gough-Stewart platform as an alternative to the "6-DOF Gough-Stewart platform" type machine tool in 1995. They also constructed a prototype 3-DOF platform as part of the "Smartcuts" research project of the University of Illinois at Urbana-Champaign [32]. A schematic representation of the "Smartcuts" planar manipulator, showing its three DOF, is given in Figure 1.9.
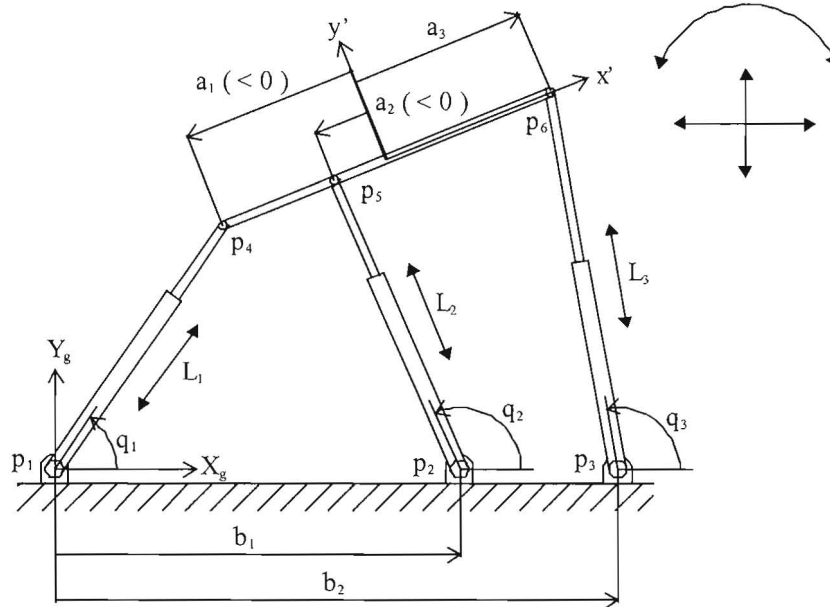
Figure 1.9: Schematic of the "Smartcuts" planar Gough-Stewart platform (after [31]).

Satya et al. [31] acknowledge that in order for a machine tool to perform any task, it should have five DOF (three orthogonal translations with rotations about two of these axes), and hence propose a hybrid serial-parallel scheme with two of the "Smartcuts" planar platforms (see Figure 1.10). The simultaneous control of both mechanisms shown in Figure 1.10 is required for five axis machining. In particular, if the spindle carrying the cutting tool is attached to one of the planar platforms, and the workpiece to the other, the two rotational DOF of the hybrid machine are about two orthogonal translational axes, both of which are also orthogonal to the third translational axis.
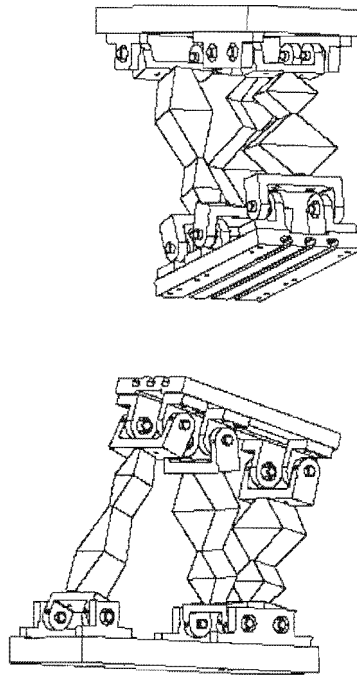
Figure 1.10: Schematic of two "Smartcuts" mechanisms in a series-parallel hybrid 5-axis machine tool (after [31, 33]).

Besides the fact that a simplified Gough-Stewart platform is easier to analyze than the 6-DOF version, another noteworthy advantage of the suggested series-parallel hybrid approach over purely parallel schemes [33] is that the use of 3-DOF systems obviously results in *simplified mechanical construction.*

In spite of its promising features, the use of the "Smartcuts" planar Gough-Stewart platform is inhibited by two potential drawbacks: *small workspace* and *insufficient lateral stiffness* as discussed below.

- In another related paper, El-Khasawneh and Ferreira [34] determine the reachable workspace of a *modified* "Smartcuts" planar Gough-Stewart platform. This specific mechanism has the three "moving platform leg joints" in line, but not the "base leg joints". Although it is not explicitly stated, from the results presented it is clear that the associated *workspace* of this planar parallel manipulator is very small compared to the physical size of the manipulator. In correspondence with the disadvantages of the 6-DOF Gough-Stewart platform (Section 1.3.1), an unfavorable ratio of manipulator size to manipulator workspace is considered a severe limitation for the practical application of the mechanism as a machine tool.

- Although a planar Gough-Stewart platform has as an inherent characteristic a good stiffness in the plane of motion, the *lateral stiffness* (perpendicular to the plane of motion of the moving platform) is in general dependent on the bending stiffness of the "beam-like" actuator legs. The problem is that a cantilever beam in general shows large deflections under a bending moment load [35], and hence insufficient lateral stiffness of the moving platform can be expected.

1.3.2.2 The "Dyna-M" and "Honda HVS-5000" machine tools

Both the above drawbacks associated with the "Smartcuts" platform have been addressed in the similarly designed "Dyna-M" [36] and "Honda HVS-5000" [37] planar parallel manipulator type machine tools. Both machines are *hybrid* 3-axis machine tools with the three orthogonal translations of a Cartesian coordinate system as the three axes of motion. More specifically, the "ram" [36] or "head" [37] of the machine tool is positioned in the xy-plane by a planar 2-DOF parallel manipulator consisting of two linear actuators, the respective *stationary ends* of which are connected to the base via two revolute joints, and the respective *extendable ends* of which are connected to each other and to the ram / head via fork-type revolute joint. The ram / head is a *serial mechanism* which moves in the z-direction, and carries the tool.

The xyz-translational workspace of the "Dyna-M" is reported to be $630\,\text{mm} \times 630\,\text{mm} \times 500\,\text{mm}$ with the projected area of the machine $3\,\text{m} \times 6\,\text{m}$ [36]. A three-dimensional schematic representation of the "Dyna-M", and its associated workspace is shown on the left-hand side of Figure 1.11. The right-hand side of Figure 1.11 is a photograph of the "Dyna-M" prototype machine tool.
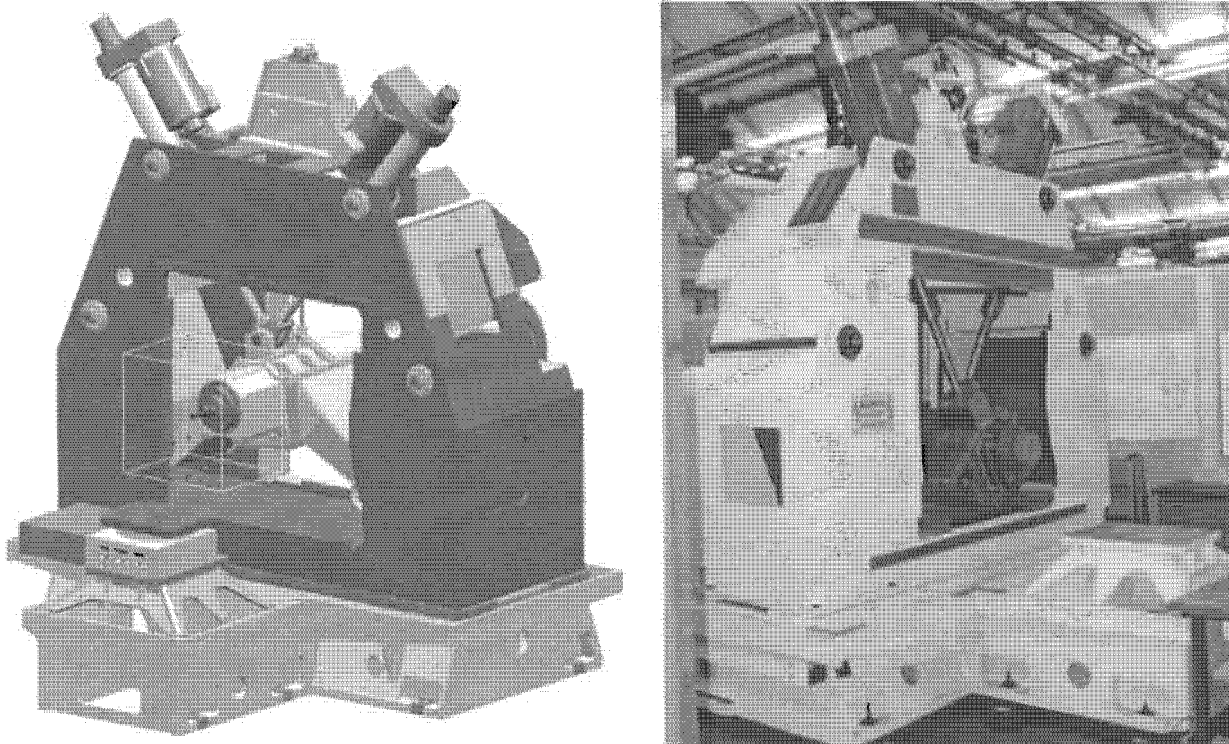
Figure 1.11: The "Dyna-M" (after [36]).

The "Dyna-M" shows a slight improvement in terms of the workspace to "projected machine area" relation over the 6-DOF Gough-Stewart platform type machine tools. For example, according to Tönshoff and Grendel [16], the 6-DOF "Ingersoll HOH-600" has a workspace cube in the xyz-Cartesian space of $600\,\text{mm} \times 600\,\text{mm} \times 800\,\text{mm}$, with a projected machine area of $6.7\,\text{m} \times 5.6\,\text{m}$.

Furthermore, once an angular tilt is specified for the moving platform, the associated workspace volume of the spatial Gough-Stewart platform decreases significantly. Researchers at the University of Nottingham specify the angular capabilities of the "Variax Hexacenter" in terms of *cone angles*, where the perpendicular axis to the moving platform is tilted from the vertical by a fixed angle but in any direction [38]. The "Variax Hexacenter" reportedly has a 5° angular capability within a 630 mm work cube [39]. However, the maximum angular tilt *changes* depending on the position within the workspace, and hence Whittingham et al. [39] express the need for additional analysis tools to define exactly what these angular limits of the machine are throughout the workspace. In this regard, Du Plessis and Snyman [40] have recently proposed a new numerical method for determining workspaces and their results, for both planar and spatial Gough-Stewart platforms, confirm the earlier statement about the decreasing workspace size associated with larger angular orientation specifications.

Evidently, the "Dyna-M" and the "Honda HVS-5000" machine tools are not affected by this orientation limitation, since they only have three translational DOF. Furthermore, Moriwaki [37] reports that the "Honda HVS-5000" has a more compact structure compared to the "Dyna-M", which would further improve the workspace to "projected machine area" ratio.

In terms of the lateral stiffness of these machine tools, the ram / head is connected to the frame with two additional chain links. Each of these additional chain links consist of two pivoting bodies connected to both the base and ram / head via separate revolute joints. Figure 1.12 (a) shows an assembled view of the "Dyna-M" machine tool. Two isolated views of the "Dyna-M" ram as positioned by the two linear actuators, and supported laterally by the stabilizing chain links are shown for illustrative purposes in Figure 1.12 (b) and (c). The middle cylinder attached to the ram and shown in Figure 1.12 (b) and (c), is presumably a measuring device.
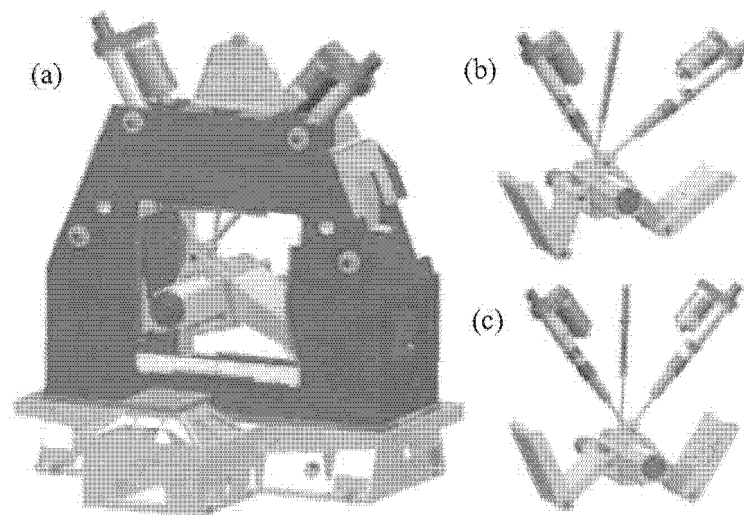
Figure 1.12: (a) The "Dyna-M". (b) and (c) The "Dyna-M" ram as positioned by the two linear actuators and supported laterally by two stabilizing chain links (after [36]).

The minimum lateral stiffness of the "Dyna-M" prototype is $60 \, \text{N}/\mu\text{m}$, which compares well with the minimum stiffness of $39.4 \, \text{N}/\mu\text{m}$ ($2.25 \times 10^5 \, \text{lb/in}$) reported by El-Khasawneh and Ferreira [35] for the specific spatial Gough-Stewart platform they studied. Note that for a single leg of the latter mechanism, the stiffness in average is about $175 \, \text{N}/\mu\text{m}$ ($1.0 \times 10^6 \, \text{lb/in}$). The minimum stiffness in the x- and y-directions of the "Dyna-M" is $30 \, \text{N}/\mu\text{m}$, which is of course dependent on the linear stiffness of the two linear actuators.

It is of interest that the "Dyna-M" is a *prototype* 3-axis machine tool intended for application in the automotive industry. It is reported to have a maximum velocity of $90 \, \text{m/min}$ and a maximum acceleration of $15 \, \text{m/s}^2$ in all three axes [36].

The "Honda HVS-5000" is presumably also a prototype, since it is *intended* to replace existing transfer machines in the automotive industry for the machining of automobile cylinder heads and cylinder blocks. The stabilizing links are made of aluminum, and it is also equipped with an automatic tool changer that requires only $0.5 \, \text{s}$ for a tool change. The positional accuracy of the HVS-5000 is $0.01 \, \text{mm}$ ($10 \, \mu\text{m}$), and the "accuracy of drilling is $\pm 0.05 \, \text{mm}$ ($\pm 50 \, \mu\text{m}$)" [37].

1.4 The re-configurable concept

Looking at machine tools from a different angle, the recent trend in manufacturing systems is *re-configurability*. Gopalakrishnan et al. [19] explain that "*re-configurable machine tools* assembled from machine modules such as spindles, slides and worktables (see also [41]) are designed to be *easily re-configured to accommodate new machining requirements*". They elaborate, stating that these systems are required in order to quickly respond to changes in market demand and the resulting product design changes. Furthermore, the essential characteristics of re-configurable machine tools are listed in [19] as modularity, flexibility, convertibility and cost effectiveness. Finally, Gopalakrishnan et al. state that "the goal of *re-configurable machining systems*, composed of *re-configurable machine tools* and other types of machines, is to provide *exactly* the capacity and functionality, *exactly* when needed". According to Koren [42] a recent report of the US National Research Council (Visionary 2020) mentioned that *adaptive re-configurable manufacturing* is considered as *first priority* for future (manufacturing) systems. As a result 2001 saw the "CIRP 1st International Conference on Agile, Re-configurable Manufacturing" [42] as a communication forum for this important issue.

Researchers have come to realize that Gough-Stewart platforms in particular, have unique features allowing for re-configurability, thus making these manipulators applicable for consideration as re-

configurable machine tools. The two main approaches that have been proposed for the re-configuration of Gough-Stewart platforms are *modular design* and a *variable geometry*.

1.4.1 Modular Gough-Stewart platforms

The prototype re-configurable 6-DOF Gough-Stewart platform, of the Department of Mechanical Engineering at the New Jersey Institute of Technology [43, 44], is discussed here as an illustrative example. Its re-configuration is achieved through *modular design* such that any of the leg modules can be replaced with a different range of motion, and can be placed on the mobile platform and the base at any desired location and orientation.

A previous study by Ji [45] has shown that the *moving range* of the legs and the *placement* of the legs have a great effect on the *shape* and *size* of the *workspace*. Ji and Song [44] further comment that since the workspace of a Gough-Stewart platform is difficult to visualize, and usually *limited*, such a mechanism should be *re-configurable to allow for the specification of different task requirements*, especially the workspace requirement.

Given a set of legs, the Ji [43, 44] approach to re-configuration involves the determination of the position and orientation of joints on the mobile platform and the base for a specified task. When legs of different ranges are available, the re-configuration must also consider what combination of legs to use.

Ji and Leu [43] explain that they use a discretization procedure to determine the so-called foot-placement space for a given desired workspace of the mobile platform. The foot-placement space is a set of all base locations where the foot of the leg can be placed to ensure the required workspace. Here, having *chosen* the position of the leg joint on the moving platform, the motion limits of the upper spherical joint and the minimum and maximum leg length limits are also taken into consideration. If the resultant foot-placement space is the null space, then the desired workspace cannot be obtained no matter where the foot is placed. One then has to *choose* a different location for the leg joint on the moving platform, or use another leg of different range. The same process has to be applied to all six legs to obtain six foot placement spaces, one for each leg.

In essence, this is a trial-and-error methodology to re-configuration. Ji and Song [44] conclude by saying that the idea is to develop an inventory of standardized leg modules and customized mobile and base platforms, so that their modular Gough-Stewart platform can be custom-configured, portable and easy to repair.

1.4.2 Variable geometry Gough-Stewart platforms

In their 1993 layman evaluation of (Gough)-Stewart platforms for manufacturing, Fitzgerald and Lewis [46] recognized that a *variable geometry base* would *improve the practical working volume* of the manipulator "so *singularities can be moved relative to the workpiece*". They explain that one of the problems with a Gough-Stewart platform is that it can collapse and may not be able to recover under its own power when it loses control near singularities. Correspondingly, a "straight forward" solution is proposed: "*Stay away from singularities*, which effectively are regions of non-performance in the robot's space. *Predict where they will be and plan paths around them*; many applications do not require operating near singularities, and *more flexible applications will depend on routine generation of large path sequences that will require new, more intelligent path-planning methods.*"

At the time, Fitzgerald was the Program Coordinator, and Lewis the Technical Leader of the Advanced Controls and Sensors Group, Automation and Robotics Research Institute (ARRI). This research institute, which is affiliated with the University of Texas at Arlington, built a prototype Gough-Stewart platform with a variable base geometry. Figure 1.13 shows a photograph of this manipulator, from which it is clear that each of the three pairs of base joints are individually adjustable.
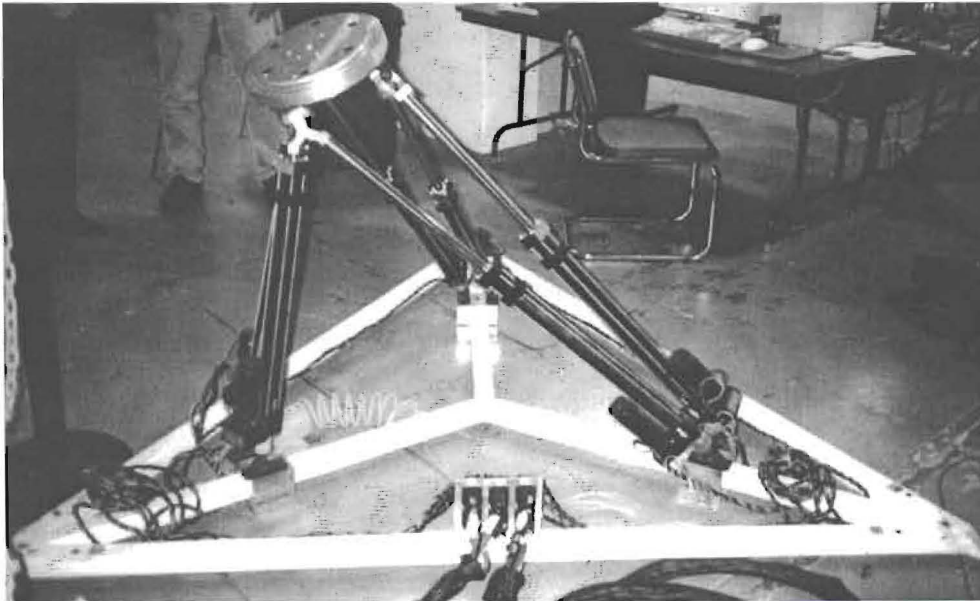
Figure 1.13: Photograph of the ARRI-(variable geometry base) Gough-Stewart platform.

The specially designed moving platform joints (gimbals) of the ARRI-Gough-Stewart platform are however not adjustable (see Figure 1.14).
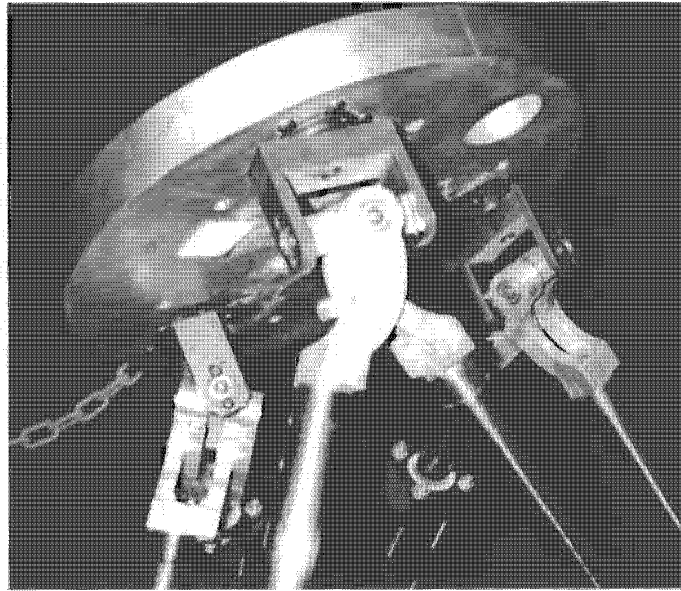
Figure 1.14: Photograph of the moving platform gimbals of the ARRI- Gough-Stewart platform.

Machine tools are continually being reprogrammed to move along different prescribed paths, implying that the corresponding workspace requirements of the machine tool is also continually changing. Therefore, a re-configurable Gough-Stewart platform type machine tool, where re-configuration is achieved via a variable geometry, may potentially overcome the workspace limitations that has been hindering its application as a machine tool. Experience with such adjustable tools will also contribute to the important research field of re-configurable manufacturing systems.

The potential improvement that the variable geometry capability could have on the practical working volume of Gough-Stewart platform type machine tools can, however, only be realized if its adjustable capability is combined with an *efficient methodology* for determining the *optimum geometry* for the machining task at hand. This observation follows simply from the fact that, if each leg joint can be adjusted separately and in a continuous manner, then infinitely many possible combinations exist. Thus if such a capability could be found it would be far superior to the trail-and-error selection method in situations where the task requirement varies.

1.5   The optimum design of Gough-Stewart platforms

Although to date re-configurable geometry Gough-Stewart platforms have not received much attention in literature, the related and extremely important subject of the *optimum design* of (fixed configuration) parallel manipulators has indeed been a very important issue.

Merlet [1] explains that the (optimal) *design* of a general parallel manipulator essentially is *"the determination of the dimensions of the manipulator so that it complies as closely as possible with the performance needed for the task at hand"*.

Speaking in very broad terms, parallel manipulator research is conducted via two fundamentally different (but complementary) approaches, namely the *analytical approach*, and the *numerical approach*.

1.5.1 *The analytical approach*

In his review paper of the optimization of multi-DOF mechanisms, Chedmail [47], distinguishes between the *analysis phase* ("given a set of design variables of a mechanism, which is its mechanical behavior?"), and the *synthesis phase* of a mechanism ("given an expected mechanical behavior of a mechanism, define its design variables").

By far the most popular choice when it comes to the *analysis* of parallel manipulators, the *analytical approach* would be to find an analytical relationship between any given set of design parameters, and the mechanical behavior of the manipulator. The two very recent reviews by Merlet [1] and Dasgupta and Mruthyunjaya [2] respectively, give comprehensive and detailed accounts of the work done to date in this regard.

Some of the very successful analytical results that were obtained are based on the "monumental theory of screws of Ball" [2] that was developed over a *century* ago. Dasgupta and Mruthyunjaya [2], explain that Ball's theory of screws provides an elegant framework for the analytical representation and *analysis* of mechanical systems.

Merlet [1] should be credited, not only for presenting an extensive overview of the research done on parallel manipulators, but also for contributing towards the *analytical approach* for the analysis of these mechanisms.

The inverse of the analysis process is the synthesis (design) process, and indeed, if an analytical relationship – between any required *performance criterion / criteria* and the chosen *design parameter(s)* – exists, such that *analytical closed-form mathematical equations* may be formulated, then the *optimum* values of the design parameter(s) may be *determined exactly* and *very efficiently*, using *algebraic* methods. Unfortunately, it is a very challenging task in general to formulate such closed-form mathematical solutions. This may explain why the leading authority, Merlet [1], states that in spite of all the research that has been published in this field, there is still no answer to the question of determining the best parallel manipulator for realizing a given task.

1.5.2 The numerical approach

The use of (numerical) optimization techniques in mechanical engineering is becoming increasingly more popular, due to the sustained increase of computer power [47].

As far as the *optimum design* of *structures* is concerned, *numerical techniques* are currently in widespread use [48]. Chedmail [47] mentions, for example, that it is now possible to (numerically) optimize subsets of complex products such as the wings of an airplane, and hence conclude that (numerical) optimization is one of the possible approaches to mechanism synthesis.

Following the explanation given in [1], the typical layout of the *numerical approach* to the design and optimum design of parallel manipulators involves

- the *selection* of a specific *mechanical architecture* for the parallel manipulator (Gough-Stewart platform or any other type of *general* parallel manipulator), and

- the *computer simulation* of the specific architecture for *determining* the *physical and geometrical characteristics* (values of the design variables or parameters) of the mechanism that are best suited for the prescribed task. Two general techniques are listed for *utilizing* the *simulation output*:

  - the simulation output may be used directly by the user to *select* values of the design parameters via *trial-and-error*, or

  - the simulation output can be used to construct a *cost-function*, and one of several available *numerical optimization techniques* may be applied to *determine* the *optimum* values of the design variables through the *minimization of the cost-function*.

1.5.2.1 Genetic Algorithms

Due to the inherent characteristics (such as non-linearity, discontinuity and the presence of local minima) of typical cost-functions formulated for parallel manipulators, it is no surprise that numerical optimization using *genetic algorithms* is preferred by most researchers attempting to optimize a parallel manipulator design through the minimizing of a cost-function. Genetic algorithms are easy to program, and are able to take into account any type of variable (discrete or continuous) [47].

Typical of work done using a genetic algorithm in the optimal design of parallel manipulator machine tools is that of Zhang and Gosselin [49]. They optimized the "Tricept" machine tool with respect to its global stiffness, using a genetic algorithm, and explain that genetic algorithms are *powerful* and *broadly applicable stochastic* search and optimization techniques based on the evolutionary principle of natural chromosomes. The evolution of chromosomes due to the operation of crossover, mutation and natural

selection, is based on Darwin's survival-of-the-fittest principles, and is artificially simulated to constitute a *robust search* and optimization procedure.

The "Tricept" machine tool is a special type of parallel manipulator, although it has similarities to the Gough-Stewart platform, with prismatic actuators connecting the moving platform to the base. It is also equipped with a *passive constraining leg* between the moving platform and the base. The specific degrees of freedom of this type of parallel manipulator are determined by the specific degrees of freedom of the passive leg. In particular, the "Tricept" machine tool has three DOF (one translational and two rotational). The respective leg joints on the moving platform and the base coincide with the vertices of two respective equilateral triangles, one on the moving platform and one on the base. The radii of the respective circles circumscribing the respective equilateral triangles are referred to as the *radius of the base platform* (R_b), and the *radius of the moving platform* (R_p).

In order to obtain the maximum global stiffness of the "Tricept" machine tool, three *architectural parameters* are considered as optimization variables. They are R_b, R_p and the height of the moving platform relative to the base (z). Zhang and Gosselin [49] comment that using these three parameters, it is *very difficult* obtain the *analytical expressions* for each of the six stiffness elements of the moving platform (also see Section 1.5.1). The six stiffness elements are related to the 6-DOF of a rigid body in three-dimensional space. They further comment that *traditional* numerical optimization methods can be expected to experience convergence problems when faced with these types of cost-functions they consider.

In searching for an optimal design, the feasible ranges of the three architectural parameters of the "Tricept" machine tool may be expressed as inequality constraints: $200 \leq R_p \leq 300$, $400 \leq R_b \leq 600$ and $900 \leq z \leq 1500$, where all extreme values are given in mm.

Fixing the two rotational DOF of the moving platform, Zhang and Gosselin [49] maximize the sum of the six stiffness elements, starting with an *initial design* given by: $R_p = 225$ mm, $R_b = 500$ mm and $z = 1300$ mm. The sum of the six stiffness elements for the initial design is 0.0078189. The *optimal design* found after 100 generations of the genetic algorithm, is given by $R_p = 300$ mm (maximum allowable), $R_b = 600$ mm (maximum allowable) and $z = 900$ mm (minimum allowable). The sum of the six stiffness elements of the *optimal design* is 0.0153369.

Zhang and Gosselin [49] thus *improved* the sum of the stiffness elements by a factor of 1.96 using a genetic algorithm. In practical terms their approach may be used not only for the optimal design of a

machine tool, but also for the optimum placement of the workpiece relative to the base. This placement is an important issue as explained by Chrisp and Gindy [38], who studied the component (workpiece) positioning for the "Variax Hexacenter", mentioned in Section 1.3. Another recent paper on this subject is the one by Wang et al. [50].

Although the solution of the problem posed by Zhang and Gosselin [49] is an important achievement, the particular design optimization problem they considered is incomplete. In their problem the stiffness of the moving platform is optimized for a single position inside the workspace of the manipulator, and with the moving platform fixed at a specific orientation. Machine tools are, however, normally required to have good stiffness characteristics over the complete workspace.

Kirchner and Neugebauer [51] emphasize that a parallel manipulator machine tool cannot be optimized by considering a single performance criterion. Also using a genetic algorithm, they consider multiple design criteria, such as the "velocity relationship" between the moving platform and the actuator legs, the influence of actuator leg errors on the accuracy of the moving platform, actuator forces, stiffness as well as a singularity-free workspace. These specified design criteria are summarized into three discrete objectives (cost-functions) related to the Jacobian matrix of the manipulator:

- *maximize* the minimum singular value of the Jacobian matrix over the workspace,
- *minimize* the maximum singular value of the Jacobian matrix over the workspace, and
- *maximize* the inverse condition number over the workspace.

The size of the workspace, and the rotational capability of the moving platform inside the workspace are additional design criteria, i.e. the rectangular shaped workspace should be as large as possible, with a maximum rotational capability of the moving platform inside the workspace [51].

Kirchner and Neugebauer [51] use 13 architectural design parameters in the simulation of their six-DOF Gough-Stewart platform machine tool.

As an alternative to solving the optimization problem by formulating a weighted multi-criteria objective function, the so-called "Pareto optimal-region" is determined. The number of criteria in the multi-criteria objective function determines the dimension of the Pareto optimal region. If only two criteria are optimized for, the associated Pareto-optimal region should be a curve representing all the optimum designs, and showing how the respective criteria weigh up with one another [52]. Once the Pareto optimal region is determined, the user evaluates the individual criteria against each other, and selects a design based on the compromise reached between the different criteria [51].

Some specific disadvantages associated with the use of genetic algorithms are [47]:

- the *stochastic exploration* of the space of design variables is very expensive in terms of CPU time,

- it is necessary to *experimentally predetermine* the mutation and cross over parameters,

- there is *no proof of convergence*, and

- compared with a pure random approach, the gain is rarely greater than a factor of 5.

1.5.2.2 The "Democrat" design methodology

Merlet [1, 53] lists some disadvantages of the classical approach to optimizing a parallel manipulator design through the minimization of a *cost-function*:

- the weights given to the various criteria of a multi-criteria cost-function strongly influences the results that are obtained by numerical optimization procedure,

- a single criterion objective function, such as for example maximizing the workspace, does not always account for "hidden criteria" such as singularity considerations throughout the workspace,

- non-continuous cost-functions are difficult to handle for most numerical optimization techniques. In addition to this difficulty, the cost-function may have numerous local minima and consequently the minimization procedure may have difficulty to locate the global minima, and

- the computational time may be excessive if the evaluation of the cost-function requires computer simulations of the performance of the manipulator over the whole workspace. This is considered a serious drawback for most numerical optimization methods requiring frequent evaluations of the cost-function.

As an *alternative* to the cost-function approach, Merlet [1, 53] proposes the so-called "Democrat" design methodology for the optimum design of parallel manipulators, where a *specified set of performance requirements are considered* to determine the optimum design.

This design methodology is based on the concept of the *parameter space*, where each dimension of this space represents a design parameter of the parallel manipulator. It works in two phases: during the *cutting phase* different *analytical design criteria* are mapped as *criterion regions* in the parameter space. The subset of all the criterion regions in the parameter space where all specified criteria are satisfied, is isolated and referred to as the *search region*. Finally, during the *refining phase*, the search space is *sampled* at regular intervals for evaluation against the specified set of *performance requirements*, to obtain the optimum parallel manipulator design(s).

1.5.2.2.1 Democrat: the cutting phase

For a general parallel manipulator with six in-parallel links, and under the assumptions made in [1] and [53], six architectural parameters represent the positions of the respective six leg joints on the base, relative to the base coordinate frame. An additional six architectural parameters represent the respective

positions of the six leg joints on the moving platform, relative to the moving platform coordinate frame. These twelve parameters are in fact radii of twelve circles, six of which are centered at the base coordinate frame, and six of which are centered at the moving platform coordinate frame. The respective *heights*, and respective *orientation angles* of the moving platform and base joints are assumed to be known *relative* to the respective *coordinate frames*. The twelve architectural parameters specified result in a twelve-dimensional *parameter space.*

The following two *criterion regions* are considered in [1]:

- The *prescribed workspace criterion* is associated with known minimum and maximum values of the respective actuator legs. The user defines line segments inside the prescribed workspace for the moving platform to trace with a specified fixed orientation. The "workspace criterion region" in the twelve dimensional parameter space indicates all the allowable designs of the parallel manipulator, i.e. all the designs that would allow the parallel manipulator to follow the prescribed line segments without violating the extreme leg lengths.

  At any time instant, each of the six leg lengths only depend on the position and orientation of the moving platform along the specified line segment, and the respective positions of the two leg joints (moving platform and base) of that specific leg. Hence, the twelve dimensional parameter space is decomposed into six different *parameter planes*. For a "circular" 6-DOF Gough-Stewart platform with the respective moving platform and base joints spaced at known angular intervals on two circles, the twelve dimensional parameter space reduces to a single parameter plane, since the respective radii of the two circles are the only two architectural parameters needed to describe the design of the manipulator.

  The *analytical* workspace criterion that Merlet [1] formulates, allows him to trace the "workspace criterion region" in the parameter plane in approximately $500\,ms$. Furthermore, for the 6-DOF "circular" Gough-Stewart platform described above, Merlet [54] shows that interferences between the actuator links may easily be included in the analytical workspace criterion.

- The second criterion considered by Merlet [1] deals with constraints on *articular velocities* of the in-parallel links of the parallel manipulator. Here, the requirement is that a specified point on the moving platform be able to reach a specified velocity (speed and direction), at all locations in the desired workspace, without the articular velocities violating the allowable extreme values. The desired workspace is again approximated by a set of line segments, and the parameter space is again decomposed into parameter planes.

The *analytical* "articular velocities criterion" is used to trace the "articular velocities criterion region" in the parameter plane in typically $2.5\,s$. Merlet [1] points out that this region is not necessarily closed. Hence mapping the "articular velocities criterion region" requires the specification of the maximum values on both parameters of each parameter plane.

In [53] Merlet reports that the mapping of each criterion region can be as quick as $100\,ms$, or can take a few minutes, depending on the number of line segments analyzed inside the workspace.

In each parameter plane, the two-dimensional *search region* is then isolated as the intersection of the "workspace criterion region" and the "articular velocities criterion region". For the general parallel manipulator considered by Merlet [1, 53], the six two-dimensional search regions constitute the twelve dimensional search region. Six points, one in each two-dimensional search region, are required to define a unique geometry. For the 6-DOF "circular" Gough-Stewart platform, there is only a single two-dimensional search region, and any point in this search region defines a unique geometry that satisfies both the workspace and articular velocities *design criteria*. Some user interaction is required to isolate the search region [53].

1.5.2.2.2 Democrat: the refining phase

Once all the *feasible geometrical designs* are isolated, the fully automated [53] *refining phase* discretizes the search region, and compares each feasible design based on a set of performance criteria deemed necessary for that application, in search for the optimal design.

A *high-level computer language* was developed for the evaluation of specific parallel manipulator performance criteria in a modular fashion. As an example, Merlet [1] shows that the *absence of singularities* inside the prescribed workspace, monitoring of *positioning errors*, as well as *stiffness consideration* may readily be incorporated as performance criteria. The high-level computer language also allows for the evaluation of any cost-function that would normally be defined for a numerical optimization procedure.

Note that the performance criteria are evaluated for *all positions* of the moving platform in the specified volume – the "translation workspace" [53]. The evaluation is done *without discretizing* the translational workspace because of the ability of the *high-level computer language* to treat specific types of "translational workspaces". In particular, the translational workspace can be a normal cube, or it can have a complex shape (see Figure 1.15), in which case it will be defined by a set of two-dimensional cross-sections in three-dimensional Cartesian space.
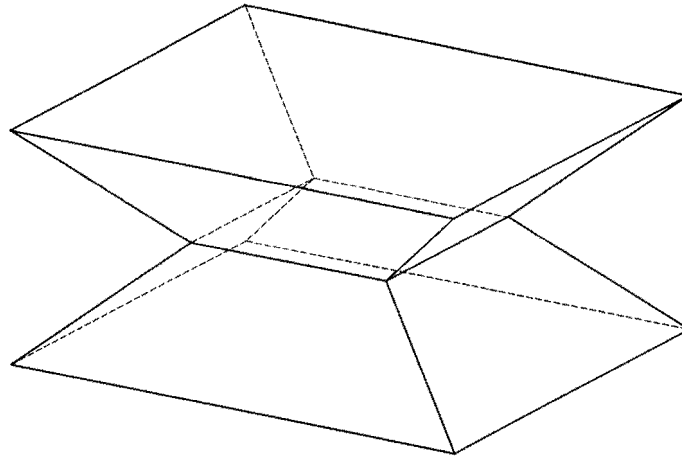
Figure 1.15: An example of a translational workspace volume that can be treated by the algorithms in Democrat (after [53]).

The volume can also be specified in the high-level computer language as a prescribed "hypercube" in the "articular space". The number of articulated in-parallel links of a parallel manipulator determines the number of dimensions of the articular space. For a 6-DOF Gough-Stewart platform with six arbitrary spaced actuator legs, a six dimensional "articular space" is required to define the "hypercube" $\ell_i^{min} \leq \ell_i \leq \ell_i^{max}$, $i = 1,2,...,6$; with ℓ_i^{min} and ℓ_i^{max} respectively the minimum and maximum allowable leg lengths of legs $i = 1,2,...,6$.

Merlet [53] distinguishes between a *translation workspace* as described above, and a *general workspace* which, apart from the specified Cartesian volume, also includes specified *ranges for the three orientation angles* of the moving platform. In the latter case, the high-level computer language "continuously" evaluates the performance criteria for the specified three-dimensional displacement volume, but the "three-dimensional *orientation* volume" is discretized during the evaluation process.

As a specific example of how the high-level computer language works, Merlet [53] explains the instruction:

%VO = minimal stiffness in cube center 0   0   30,   0   10   10   10

This instruction *commands* the computation of the "minimal values of the diagonal of the stiffness matrix of the parallel manipulator" for *all positions* of the moving platform in the specified cubic volume $(10 \times 10 \times 10)$, centered at $(x, y, z) = (0, 0, 30)$. The returned minimal values are stored in the array **VO**.

The user specifies *allowable* minimal values as the "stiffness performance requirement", which is then used in the evaluation of the different *feasible* designs given by the discretized search region. In particular, the high-level computer language returns "0" if the feasible design does not fulfill the user's

requirement, "1" if it fulfills the requirement and "2" if it fulfills the requirement and is better than the previous solution [53].

It is reported that the computational time of this final stage of the proposed design methodology is dependent on the size (and dimension) of the search region, and the efficiency with which the performance criteria is evaluated [1].

1.5.2.2.3 Democrat: Optimizing the "HFM2" 6-DOF Gough-Stewart platform design

The "HFM2" 6-DOF "circular" Gough-Stewart platform "meant to be used for fine motions of heavy loads ($850\,\text{kg}$) in a relatively small workspace", is presented in [1] and [53] as a case study for the "Democrat" design methodology.
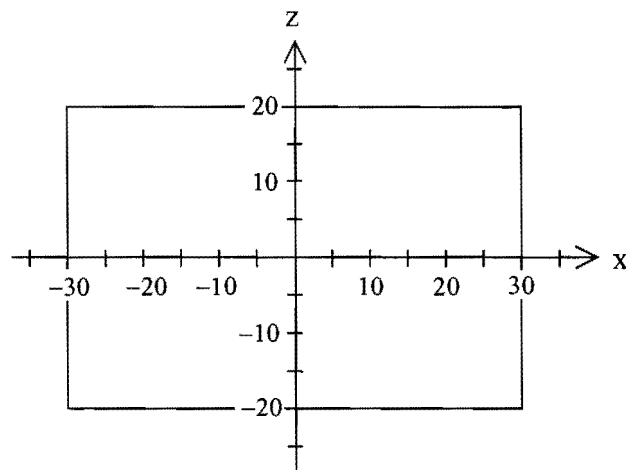
Figure 1.16: Rectangle (scale 1:1) showing the x and z workspace constraints of the "HFM2" [1] 6-DOF "circular" Gough-Stewart platform.

Figure 1.16 shows a rectangle in the $x - z$ plane, where the position of the coordinate system is chosen to represent the x and z workspace "constraints" as given Merlet [1, 53] for the HFM2 manipulator:

x (mm)	y (mm)	z (mm)
± 30	–	± 20

The remaining workspace constraints listed for the HFM2 platform are

θ_x (mrad)	θ_y (mrad)	θ_z (mrad)
± 5	± 5	$0 - 10$

which may be interpreted as follows:

The three respective orientation angles of the moving platform, θ_x, θ_y and θ_z, are required to assume *all* values in the respective ranges $[(-0.2865°) - (0.2865°)]$, $[(-0.2865°) - (0.2865°)]$ and

$[(0°) - (0.573°)]$, at *any* point inside the rectangle shown in Figure 1.16. Such a workspace, where positional and rotational requirements are specified, is formally known as a *dextrous workspace* [40].

Other than the workspace constraints, Merlet [1, 53] specifies positional and accuracy requirements, the most stringent of which are $\pm 0.01\,mm$ positioning accuracy in the x-direction, and $\pm 0.05\,mrad$ ($\pm 0.002865°$) rotation accuracy about the z-axis (θ_z). Optimization of the manipulator should be done firstly with regard to maximizing the "rotational stiffness" about the z-axis, and secondly with regard to maximizing the "positional stiffness" in the x-direction.

One of the issues in determining the optimum design of the manipulator is, of course to determine the position of the prescribed dextrous workspace and manipulator base relative to each other. This *"base / required workspace"-position* introduces *additional parameters* to the two "leg joint position" parameters that are required for describing the design of the 6-DOF "circular" Gough-Stewart platform. They should also be considered during the optimization procedure.

Merlet [1, 53] does not mention this "base / required workspace" position as such, but in requiring the use of linear actuators with known and fixed stroke lengths, he indirectly addresses the positioning problem by *determining* a minimum actuator leg length for all six actuator legs. In essence, for any *specified* "base / *required* workspace"-position, the "base / *actual* workspace"-position may be *adjusted*, until it coincides with the "base / *required* workspace"-position. In practice this adjustment is made possible in one of two ways:

- extensions may be added to the lower ends of all six actuators to lengthen the minimum actuator leg length of all six actuators, and hence *lifting* the "base / actual workspace" (see the illustrative 2-DOF example in Figure 1.17), or
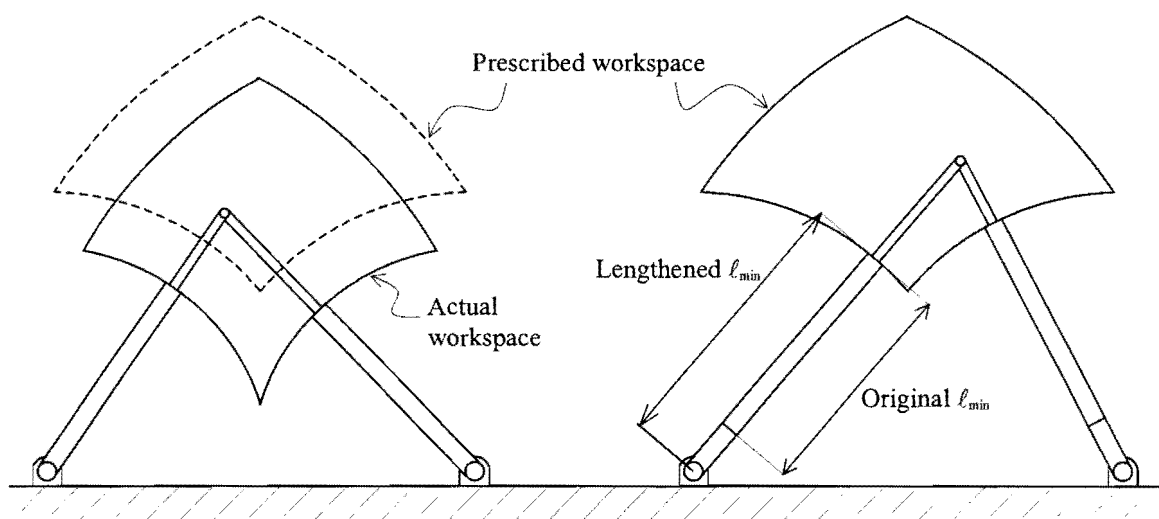
Figure 1.17: The adjustment of the base / *actual* **workspace position by lengthening the minimum actuator lengths.**

- shortening the minimum actuator leg length of all six actuators by mounting the actuator leg base joint at the required location along the casing of, for example, a hydraulic actuator (see the illustrative 2-DOF example in Figure 1.18).
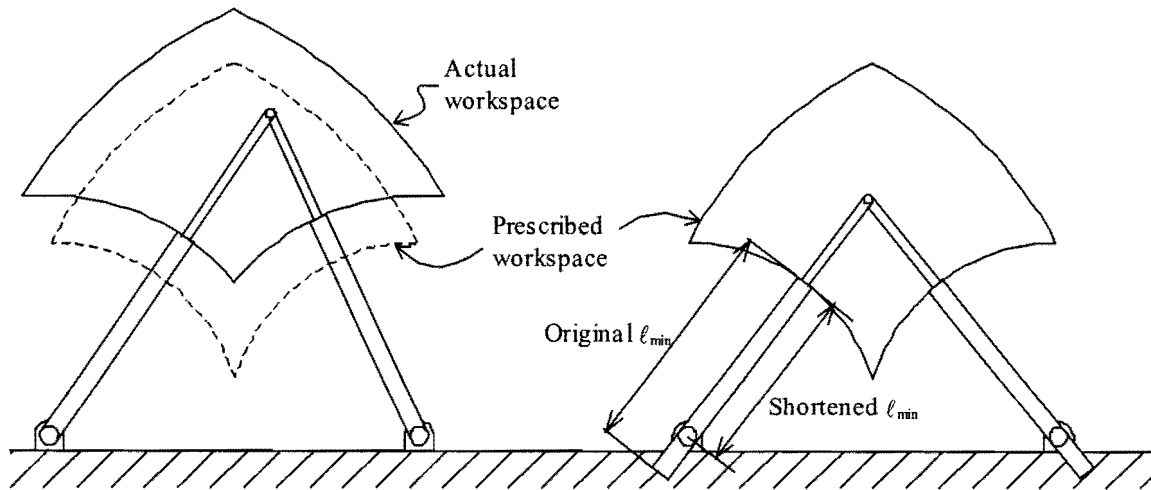
Figure 1.18: The adjustment of the base / *actual* workspace position by shortening the minimum actuator lengths.

For the "HFM2" manipulator, Merlet [1, 53] defines 19 line segments to analytically represent the prescribed dextrous workspace, and then calculates the "area of the search region" as a function of the "minimum actuator leg length". This is presumably done by choosing different "minimum actuator leg length" values, and calculating the corresponding "area of the search region" value. This being the case, the discrete data points could be represented on a graph, either by connecting them using straight-lines, or by fitting an approximation polynomial through them [55].

With the best value of the "minimum actuator leg length" ($750\,\mathrm{mm}$) determined through a "systematic search" involving "various trials" in the domain plotted ($590\,\mathrm{mm} - 835\,\mathrm{mm}$), Merlet [1, 53] finally shows the associated search plane from which the optimum HFM2 "circular" Gough-Stewart platform is to be determined, using the high-level computer language algorithm. Merlet [1, 53] comments that the optimum manipulator geometry in terms of the "rotational stiffness" about the z-axis, is to be fitted with sensors capable of a $\pm 2\,\mu\mathrm{m}$ accuracy in order to comply with the specified manipulator accuracy.

Without *giving specific parameter values or reporting on the computational effort*, a photograph of the prototype "HFM2" manipulator that was built according to the optimum design parameters, is shown in [53]. Merlet [53] reports that the repeatability of the prototype under a load of $230\,\mathrm{kg}$ is estimated to be better than $0.1\,\mu\mathrm{m}$, and that 10 other prototypes have subsequently been built.

1.5.2.2.4 Democrat: Optimizing the "HDM1" 6-DOF Gough-Stewart platform design

In a second example, which has a similarly small dextrous workspace requirement (see Figure 1.19), and exactly the same accuracy requirements as before, Merlet [1] attempts to optimize another "circular" Gough-Stewart platform ("HDM1"), firstly in terms of the "rotational stiffness" about the z-axis, and secondly in terms of the positional stiffness in the x-direction. As additional constraints, the respective radii of the base and moving platforms are also limited.
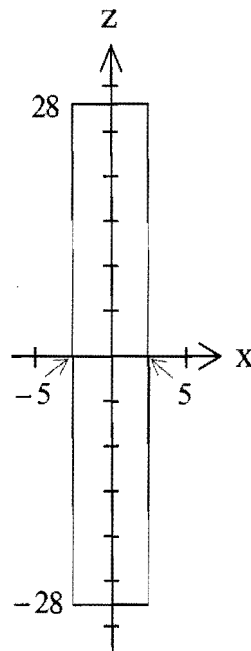
Figure 1.19: Rectangle (scale 1:1) showing the x and z workspace constraints of the "HDM1" [1] 6-DOF "circular" Gough-Stewart platform.

For this case study, Merlet [1, 53] considers the "rotational stiffness" about the z-axis, as a function of two *additional design parameters*: the angle between two adjacent joint centers on the moving platform, and the angle between two adjacent joint centers on the base. Note that for the 6-DOF "circular" Gough-Stewart platform, the three pairs of adjacent joints on the moving platform, as well as the three pairs of adjacent joints on the base, are equally spaced at $120°$ angular intervals. The *minimum limits* imposed on the respective angles are $10°$ for the angle between two adjacent joint centers on the base, and $20°$ for the angle between two adjacent joint centers on the moving platform.

Subject to the above constraints, different values of the two angles are *iteratively* chosen [53]. For each choice of angles, Merlet [1]:

- determines a best value for the minimum actuator leg length, which is associated with a maximal possible "rotational stiffness" in the z-direction for the manipulator in its nominal position (the six linear actuator legs in the middle of their respective ranges),

- calculates the associated search plane, and

- utilizes a special "procedure" in the high-level computer language, to discretize and analyze the search plane, in search of a manipulator design with which the required specified accuracies may be obtained with the least stringent sensor accuracy.

No information is given regarding the number of different choices of angle-pairs evaluated. Furthermore, *without giving any specific parameter values or reporting on the computational effort*, Merlet [1] comments that the two best solutions, in terms of least stringent sensor accuracies, are $2.4 \, \mu m$ and $2.79 \, \mu m$ respectively.

As a conclusion to the discussion of the Democrat design methodology, some of its reported advantages and disadvantages are listed here. Merlet [1, 53] points to the advantageous modularity and versatility with which the high-level computer language can evaluate almost any type of performance requirement. Furthermore, although the reduction of the parameter space into a search region is considered as an advantage in limiting the required computational time, the constraints imposed on the criterion regions (Section 1.5.2.2.1) and consequently also on search region, admittedly, limit the number of feasible designs when searching for an optimum parallel manipulator design.

1.6 Motivation for the present study

In conclusion to, and as part of the literature review presented here, the concept of a novel re-configurable planar Gough-Stewart machining platform will now be motivated. In doing so the scope of the present study will also be outlined.

1.6.1 The concept of a re-configurable planar Gough-Stewart machining platform

1.6.1.1 Mechanical feasibility

Although to date the concept of a *re-configurable* planar Gough-Stewart machine has not been satisfactorily demonstrated, researchers have recently shown an increased interest in such re-configurable platforms. This renewed interest is stimulated by the desire to overcome the workspace and singularity limitations (see Section 1.4), which have been inhibiting the practical application of conventional Gough-Stewart platforms as machine tools. The case studies presented by Merlet [1, 53] reconfirm the fact that the conventional 6-DOF Gough-Stewart platforms have very small usable workspaces (see Figure 1.16 and Figure 1.19).

The *simplified mechanical construction* of the planar 3-DOF Gough-Stewart platform (see Figure 1.9) to be studied here, makes it well suited for the implementation of re-configuration. This is so because its variable geometry allows for the easy adjustment of the relative positions of the base and moving platform revolute joints as shown in **Appendix D**.

Furthermore, the existing "Dyna-M" and "Honda HVS-5000" machine tools (Section 1.3.2) prove that a planar parallel manipulator can be constructed in such a way that sufficient lateral stiffness is provided for hybrid serial-parallel machining operations.

The above indicates that the successful implementation of a planar re-configurable platform as a machine tool is not so much limited by its mechanical design, but rather by the availability of a suitable *operating system*. Here the operating system should ensure that any reasonably specified trajectory is feasible and can accurately be followed. In particular, the operating system should be able to a priori *simulate* the motion of the mechanism along the prescribed trajectory. Based on the simulation the system should be capable of deciding on the *necessary adjustments of the variable geometry* so that the prescribed trajectory can accurately and optimally be followed. The first part of the current study is therefore the development of a reliable and efficient dynamic simulation module for the "overall operating system".

1.6.1.2 Simulation of a planar Gough-Stewart platform

1.6.1.2.1 Inverse Dynamic simulation

Shamblin and Wiens [56] characterize the dynamics of two 6-DOF Gough-Stewart machining platforms for which they derive the equations of motion with inclusion of the strut masses. They state that in order to capture dynamics (i.e. determine the actuator forces), a *motion trajectory must be specified*, along which the mechanism's dynamical behavior is *simulated*. Accordingly **Chapter 2** of this study shows how the *inverse dynamic analysis* of a planar Gough-Stewart platform may be performed so as to give *closed-form expressions* for the *required actuator forces* necessary for the execution of a *specified trajectory*. This inverse dynamic analysis is specifically developed for implementation on a computer in near real time, hence the need for closed-form mathematical solutions to the forces at discrete and *appropriately chosen time instants* along the path.

The advantage of the inverse dynamic analysis is that for different *adjustable parameter values*, which give rise to different *mechanism geometries* and different *relative positions of the prescribed trajectory*, the corresponding motions may be analyzed and compared with each other.

The output of the inverse dynamic analysis is a set of actuator forces at discrete time instants. The usefulness of this information lies in the fact that if the prescribed trajectory is positioned such that the

simulation shows that the Gough-Stewart platform will move through or near a *singular configuration* in tracing the trajectory, then this will be evident from the *near infinitely large actuator forces* in the simulation output at certain time instants. By comparing the discrete computed actuator forces at the discrete time instants for any specific prescribed trajectory, the computer simulation can be utilized to isolate the "maximum magnitude actuator force" for the *specific positioning* of the prescribed trajectory and the given mechanism *geometry*. This information can in turn be utilized to *determine* an appropriate relative *positioning* for the prescribed trajectory, as well as an appropriate mechanism *geometry*, such that a large "maximum magnitude actuator force" resulting from passing through or near a singular configuration, may be avoided.

In their related investigation, Shamblin and Wiens [56] specify a trajectory to "simulate a chamfering and deburring operation along the edge of a workpiece as well as to show the dominant forces under a variety of conditions". It follows that a further function to be performed by the operating system being developed here, is that of *kinematic trajectory-planning*. This subject will be dealt with in the next sub section.

1.6.1.2.2 Trajectory-planning

Many researchers have studied trajectory-planning from the point of view that, given an initial and final pose of the manipulator end-effector, it is required to *determine* how the manipulator should be actuated in between these two poses (see for instance [57]). With specific reference to Gough-Stewart platforms, this approach is popular, since it allows for the *avoidance of singularities inside the workspace* of the manipulator [58]. To avoid singularities, Merlet [59] proposes a trajectory verifier and indicates analytically which part of the specified trajectory is outside the reachable workspace of the parallel manipulator, and whether the specified trajectory will lead to a singular configuration. The application of this trajectory verifier is limited to a 6-DOF Gough-Stewart platform, although it is claimed to be easily extendable to general parallel manipulators.

Trajectory-planning as defined by Wolovich [60] is the specification of desired time-dependent paths in either Cartesian or link space. In terms of performing the *inverse dynamic analysis* of a planar machining platform, the tool trajectory must be specified in Cartesian space. The inertia forces in the dynamic analysis of the motion of a machine are of course dependent on the manner in which the Cartesian path is specified in the *time domain* [56]. If the trajectory is specified in such a way that the resulting accelerations are discontinuous, then the inertia forces will also be discontinuous.

With specific reference to trajectory-planning for existing Computer Numerical Control (CNC) machine tools, Zhang and Greenway [61] state that CNC systems typically only support motion along straight-line and circular paths. However, *free-form* design and machining have become important in a variety of

applications in the automotive-, aerospace-, and ship building industries. Specific examples are the design and machining of dies and molds, as well as propeller and impeller blades [62]. The consensus seems to be that free-form surfaces can easily be modeled in 3-D space, but that the manufacturing of free-form surfaces has been a difficulty up to now.

The difference between various *representation schemes* with which free-form surfaces are modeled in 3-D space, lies in the utilization of different geometrical and polynomial properties required to control and modify the desired geometrical shapes [62]. More specifically, Non-Uniform Rational B-Splines (NURBS) have long been favored in Computer-Aided Design (CAD) systems, since "they offer exact uniform representation of both analytical and free-form parametric curves" [61].

Bahr et al. [62] explain that a typical way to *machine* parts with spline surfaces (including NURBS) on a CNC machine tool is converting or transforming the surfaces to linear or circular segments according to a prescribed error tolerance, so that the CNC machines can reproduce the parts. For many applications, these conversions or transformations will produce a large amount of data. Furthermore, with the path divided into straight-line segments, in current five-axis machining with off-line programming, the *tool orientation is maintained constant during each segment*. This implies that the *orientation of the tool must be changed abruptly between two segments*, which according to Kim et al. [63] can produce an unpredictable reaction at the point of contact with the surface and *prevent a smooth finish*.

Kim et al. [63] acknowledge the value of a real-time NURBS curve interpolator for a 6-axis robot developed by Zhang and Greenway [61]. They state that real-time parametric interpolators reduce the memory requirement and communication load in guaranteeing continuity in the first-order and second-order properties of the tool position. They emphasize however, that *the most significant problem in the generation and control of a five-axis NC trajectory is a continuous and smooth description of the tool orientation that will change smoothly along the contour surface*. Therefore, an important area of research is to generate a control algorithm that will accommodate a continuous and sufficiently smooth description of the orientation of the tool.

Kim et al. [63] focus on the fact that the tool tip and a unit line vector attached to the tool generate a ruled surface. The curvature theory of a ruled surface, which is a study of the differential motion of the ruled surface, is then used to provide the properties of the tool motion in a *strictly mathematical manner*. When the surface to be machined is a free-formed surface and cannot be represented by an analytical closed-form equation, Kim et al. [63] use the Ferguson curve model to *geometrically* represent the ruled surfaces for the tool trajectory.

In **Chapter 3**, an alternative *trajectory-planning interpolation algorithm* is proposed and developed with which a user may specify the desired path to be followed by any *planar* industrial robot, and therefore in particular also by a planar Gough-Stewart platform. Given specified points along the path, an interpolation curve is fitted in such a way that *continuous* displacement, velocity and acceleration curves are generated in the time-domain. The user-specified information is also used to determine how the end-effector orientation angle should vary along the specified curve, and in particular, generates *continuous* orientation angle, orientation angular velocity and orientation angular acceleration time curves.

In terms of the current research, which is focused on a planar Gough-Stewart machining platform, the relevance of the proposed free-form trajectory-planning algorithm lies in the fact this machine tool is ideally suited to machine along non-linear curves. Powell et al. [11] explain that for a conventional machine tool, based on serial kinematic chains, the simplest movements are linear motions along the orthogonal axes (x, y and z). To provide more complex motion requires the synchronized movement of all three of the axes. With the Gough-Stewart platform type machine tools, all motion is derived from the simultaneous motion of all the actuator legs, hence the moving platform orientation can also be varied in a continuous manner.

Of particular importance here, with reference to the machining problems previously experienced and outlined above, is that the algorithm proposed in this study allows for the generation of a kinematically smooth trajectory. The resulting beneficial effect is that the inertia forces in the actuators, as well as the orientation of the tool will vary in a continuous manner. This should ensure smooth finishing during the machining operation.

It should be noted here that for the actual motion of the physical machine tool to correspond with its simulated motion, the proposed trajectory-planning algorithm can not simply be loaded on a conventional CNC controller. In fact, Kim et al. [63] explain that the implementation of any extended algorithm that allows for interpolated motion beyond straight lines and circles, requires an open architecture controller, which is considered a new concept in CNC machining. Although this practical aspect is very important, it falls beyond the scope of this study. However, the ability to accurately simulate the continuous kinematics and associated dynamical behavior of the motion of the planar Gough-Stewart platform along non-trivial prescribed paths, is imperative in determining the optimum mechanism geometry for any prescribed path.

1.6.1.3 Optimal adjustment of the variable geometry

With reference to Sections 1.5.2.1 and 1.5.2.2, Merlet [1, 53] and Kirchner and Neugebauer [51] agree that a single performance objective criterion cannot be used to optimize a Gough-Stewart machining

platform. In particular, Merlet [1, 53] points out that there are "hidden criteria" such as singularity considerations that are not considered when, for example, the workspace is maximized.

In spite of the above reservations, a single criterion cost-function will nevertheless be used in this study to *determine* an appropriate relative *positioning* for the prescribed trajectory, as well as an appropriate planar Gough-Stewart platform *geometry* for different machining tasks. In particular, the cost-function to be minimized here will be the "maximum magnitude actuator force" mentioned in Section 1.6.1.2.1. The rationale is that if the "maximum magnitude actuator force" is *as small as possible*, the corresponding relative *positioning* for the prescribed trajectory and the particular mechanism *geometry* will be such that the prescribed trajectory will successfully be traced. This will be so since the planar manipulator will be *"as far as possible"* from any singular configurations.

Many numerical optimization techniques also allow for non-trivial *inequality* and *equality constraints* to be specified. The careful formulation of such constraints extends the value of the solutions to the corresponding constrained optimization problems, beyond that where only simple limitations are imposed on the minimum and maximum allowable design variable (parameter) values. For example, the minimum and maximum allowable actuator leg lengths of a planar Gough-Stewart platform may be incorporated as inequality constraints, to ensure that the design parameters are adjusted so that the prescribed trajectory lies inside the mechanism's workspace.

In **Chapter 4** it will be shown that, in spite of the non-smooth nature of the "maximum magnitude actuator force" cost-function and "actuator leg length" inequality constraints, the gradient-based mathematical programming LFOPC optimization algorithm [64] used in this study, successfully solves the comprehensively constrained optimization problem. Indeed, LFOPC has in the past been successfully applied to many engineering optimization problems where noise and *discontinuities* were present in the objective and constraint functions [64].

1.6.2 The concept verification: a re-configurable planar Gough-Stewart platform test-model

In **Chapter 5** the ultimate task of designing, constructing and putting into operation a re-configurable planar Gough-Stewart platform test-model is tackled. The chapter shows in particular how the simulation and optimization processes are integrated in an operating system, that allows for the set-up of the machine and the execution of the prescribed tasks.

The constructed test-model may be seen as a technology demonstrator rather than a prototype. The value of this demonstrator lies in the fact that it enables a practical assessment of the feasibility and potential of

the re-configurable device, and associated operating system, as a practical machining center. This evaluation is presented in the concluding **Chapter 6,** in which suggestions for future research are also made.

2 KINEMATIC AND KINETIC MODELING OF A PLANAR MACHINING CENTER

2.1 Introduction

The books by Nikravesh [65] and Haug [66] emphasize the importance of the application of computer-aided analysis techniques to multi-body mechanical systems. This section gives a brief overview of the more important aspects of computer-aided analysis of mechanical systems as highlighted in the introductory chapter of the book by Nikravesh [65].

A mechanical system is defined as a collection of bodies (or links) in which some or all of the bodies can move relative to each other. Furthermore, mechanical systems may range from the very simple to the very complex, and a specific mechanical system may experience either *planar* (two-dimensional) or *spatial* (three-dimensional) motion.

Any mechanical system can be represented *schematically* as a multi-body system where the actual shape or outline of a body may not be of immediate concern in the process of *analysis*. Of primary importance though, are the connectivity of the joints and the physical characteristics of the elements in the system.

The analysis of a mechanical system is an important tool in the *design process*, i.e. the process of determining which physical characteristics are necessary for a mechanical system to perform a prescribed task. Figure 2.1 shows a block diagram of the "analysis branch" called *mechanics*, which is the study of motion, time and forces.
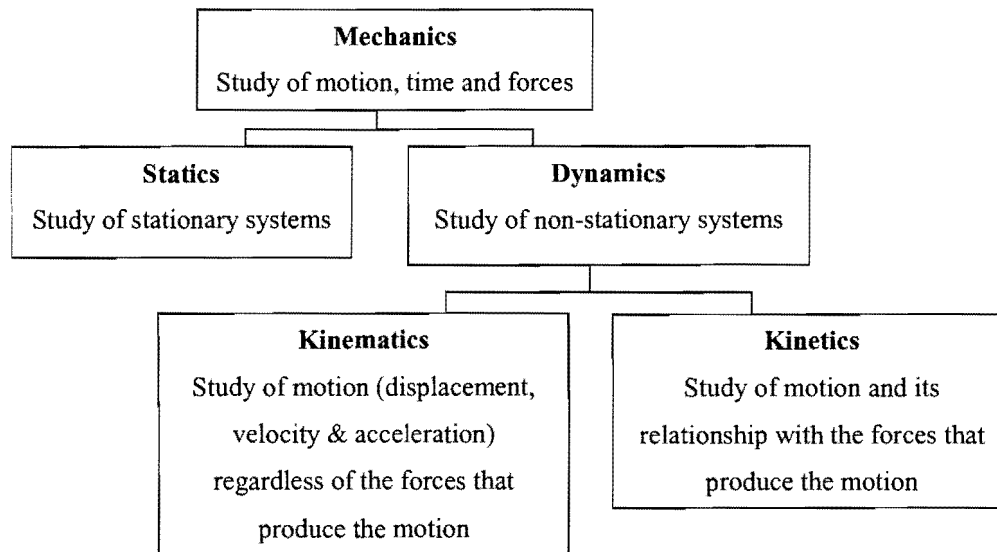
Figure 2.1: Mechanics and its sub-disciplines.

There are two approaches to mechanics: the *graphical approach* and the *analytical approach*. Many classical methods of analysis in mechanics have relied upon graphical and often quite complicated techniques. These techniques are based on geometrical interpretations of the system under consideration. Contrary, the method of solution by vector algebra is an analytical approach, and is more *systematic* when compared to the graphical approach. A problem formulated analytically can be solved repeatedly for different parameter values, a task that is ideally suited to a computer program. The usefulness of writing a computer program becomes even more apparent when the mechanical system under consideration is complex to the extent that, if the system is considered for kinematic analysis, a graphical approach would be very tedious as well as inaccurate.

The purpose of computer-aided analysis of mechanical systems is to develop basic methods for computer formulation and solution of the equations of motion. This requires systematic techniques for formulating the equations and numerical methods for solving them. A computer program for the analysis of mechanical systems can either be a *special-purpose* program or a *general-purpose* program.

A special-purpose program is a rigidly structured computer code that deals with only one type of application. The equations of motion for that particular application are derived a priori and then formulated into the program. As input to the program, the user can provide information such as the dimensions and physical characteristics of each part. Such a program can be made computationally efficient and its storage requirement can be minimized, with the result that it will be suitable for implementation on small personal computers. The major drawback of a special-purpose program is its lack of flexibility for handling other types of applications.

Since the primary interest here is the dynamic analysis of a specific machining center, a special-purpose program is required. The systematic formulation of the relevant equations as applied to the planar machining center, is dealt with in Sections 2.2 – 2.6. The special-purpose computer program that resulted, is tested in Section 2.7.

2.2 Rigid body model

Machining centers are used to control the relative motion between a workpiece and a cutting tool such that the workpiece is shaped into a desired component. The *planar* machining center under consideration consists of a *planar* Gough-Stewart platform with which either the tool or the workpiece can be moved and orientated *in the plane*.

More specifically, the planar Gough-Stewart platform consists of a moving platform connected to a fixed base via three linear actuators as shown in Figure 2.2. Changes in the actuator lengths result in changes in the position and orientation of the moving platform. This planar Gough-Stewart platform corresponds exactly to the simplified planar Stewart platform studied by Haug et al. [67].
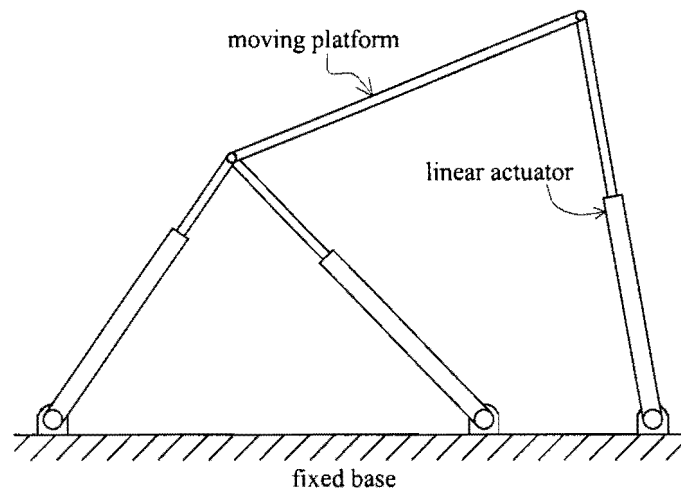
Figure 2.2: Planar Gough-Stewart platform.

A rigid body model is used for analysis purposes of the planar Gough-Stewart platform. Per definition a rigid body is a system of particles for which the distances between particles remain unchanged. Since all solid materials change shape to some extent when forces are applied to them, the concept of rigidity is only acceptable if the movement associated with the changes in shape is small compared with the overall movement of the body. In general this requirement is more than satisfied for most machining centers.

In order to specify the state of the planar Gough-Stewart platform, it is first necessary to define coordinates that specify the location and orientation of each body in the mechanism. Consider the illustrative example shown in Figure 2.3. The 0xy -coordinate system shown in Figure 2.3 is the global

reference frame, and a body-fixed $0_i \xi_i \eta_i$ -coordinate system is embedded in body i. This implies that the position and orientation of body i can be specified in the plane by the position vector $\vec{r}_i$, and the angle of rotation ϕ_i of the body-fixed $0_i \xi_i \eta_i$ -coordinate system relative to the global coordinate system. The angle ϕ_i is considered positive if the rotation from positive x-axis to positive ξ_i -axis is counterclockwise (CCW).
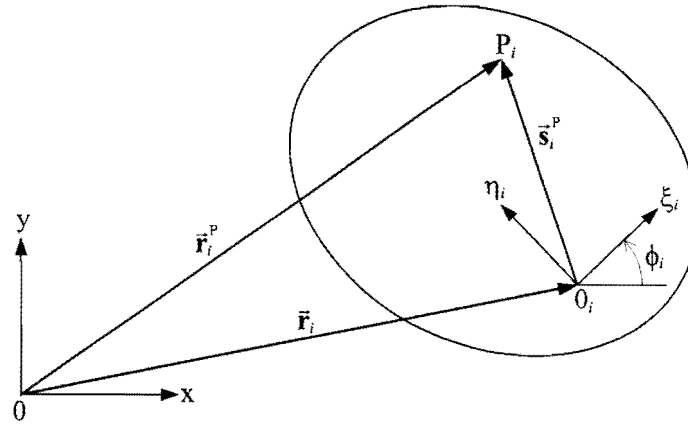
Figure 2.3: Locating point P relative to the body-fixed and global coordinate systems (after [65]).

A fixed point P_i on body i can be located from the origin of the $0_i \xi_i \eta_i$ -axes by the vector $\vec{s}_i^P$. The body-fixed point P_i can also be located from the origin of the global $0xy$ -reference frame by vector $\vec{r}_i^P$.

In general body i is not fixed, and therefore the physical vectors $\vec{r}_i$, $\vec{r}_i^P$ and $\vec{s}_i^P$ are time varying vectors. Hence, the vector representations $\mathbf{r}_i$ and $\mathbf{r}_i^P$ of vectors $\vec{r}_i$ and $\vec{r}_i^P$ have components that vary with time t when represented in the global $0xy$ -reference frame, i.e.

$$\vec{r}_i : \mathbf{r}_i = \begin{bmatrix} x(t) \\ y(t) \end{bmatrix}_i \text{ and } \vec{r}_i^P : \mathbf{r}_i^P = \begin{bmatrix} x^P(t) \\ y^P(t) \end{bmatrix}_i$$

Vector $\vec{s}_i^P$ has *fixed* components when represented in the local $0_i \xi_i \eta_i$ -reference frame, since point P_i is fixed in body i:

$$\vec{s}_i^P : \mathbf{s}_i'^P = \begin{bmatrix} \xi^P \\ \eta^P \end{bmatrix}_i$$

The superscript prime $'$ indicates that the relevant vector is represented in the local coordinate system. It follows that vector $\vec{s}_i^P$ represented in the global $0xy$ -reference frame has time varying components indicated by $\mathbf{s}_i^P$. Figure 2.4 shows the geometrical relationship that exists between the global representation $\mathbf{s}_i^P$, and the local representation $\mathbf{s}_i'^P$ of vector $\vec{s}_i^P$.
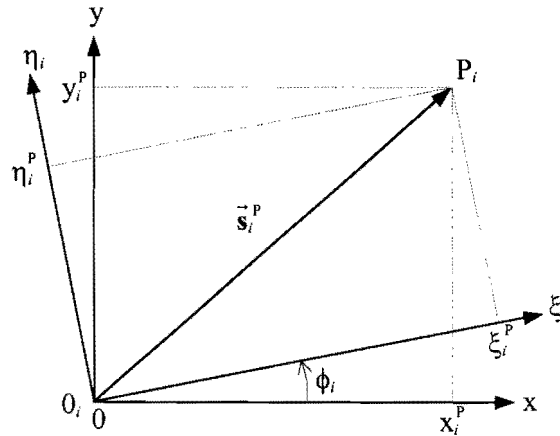
Figure 2.4: Translation between the local and global vector representations.

It follows directly from Figure 2.4 that

$$\mathbf{s}_i^P = \begin{bmatrix} x^P \\ y^P \end{bmatrix}_i = \begin{bmatrix} \xi_i^P \cos\phi_i - \eta_i^P \sin\phi_i \\ \xi_i^P \sin\phi_i + \eta_i^P \cos\phi_i \end{bmatrix} = \begin{bmatrix} \cos\phi_i & -\sin\phi_i \\ \sin\phi_i & \cos\phi_i \end{bmatrix} \begin{bmatrix} \xi^P \\ \eta^P \end{bmatrix}_i \tag{2.1}$$

or more concisely

$$\mathbf{s}_i^P = \mathbf{A}_i \mathbf{s}_i'^P \quad \text{with} \quad \mathbf{A}_i = \begin{bmatrix} \cos\phi_i & -\sin\phi_i \\ \sin\phi_i & \cos\phi_i \end{bmatrix}$$

Furthermore, with reference to Figure 2.3:

$$\mathbf{r}_i^P = \mathbf{r}_i + \mathbf{s}_i^P = \mathbf{r}_i + \mathbf{A}_i \mathbf{s}_i'^P$$

In summary, it is noted that the position and orientation of body i may be represented in the x-y plane by the three-vector representation $\mathbf{q}_i$ consisting of the global components of vector $\mathbf{r}_i$ and the orientation angle ϕ_i, i.e.

$$\mathbf{q}_i = [\mathbf{r}^T, \phi]_i^T = [x, y, \phi]_i^T \tag{2.2}$$

The three components of $\mathbf{q}_i$ are called the *planar coordinates* of body i. It follows that for a system of b bodies situated in the x-y plane, the vector of coordinates for the b bodies is a 3b-vector given by

$$\mathbf{q} = [\mathbf{q}_1^T, \mathbf{q}_2^T, ..., \mathbf{q}_b^T]^T \tag{2.3}$$

Since the planar Gough-Stewart platform consists of eight bodies (see Figure 2.5), the coordinate vector of the entire mechanical system is a 24-vector, i.e.

$$\mathbf{q} = [\mathbf{q}_1^T, \mathbf{q}_2^T, ..., \mathbf{q}_8^T]^T = [x_1, y_1, \phi_1, x_2, y_2, \phi_2, ..., x_8, y_8, \phi_8]^T \tag{2.4}$$

where corresponding to Nikravesh [65], $\mathbf{q}$ without a subscript denotes the vector of coordinates for the entire system.
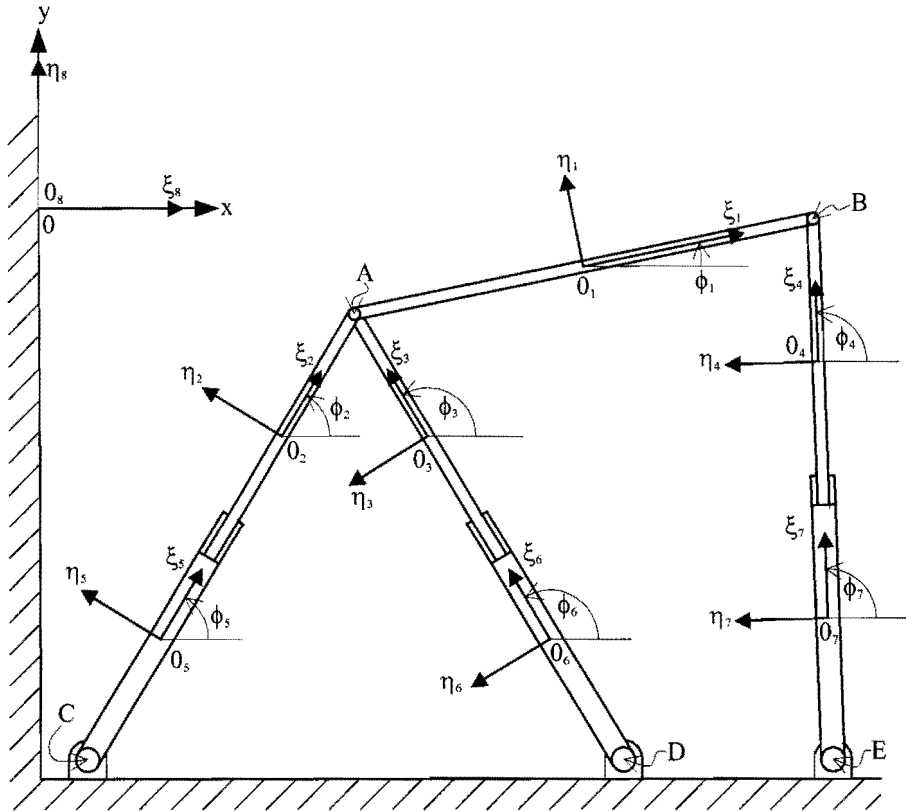
Figure 2.5: Planar Gough-Stewart platform, schematically represented as a mechanical system of eight bodies.

2.3   Kinematic constraint equations

In accordance with the definition of Nikravesh [65], the eight individual bodies that collectively form the planar Gough-Stewart platform shown in Figure 2.5, are called *links*. The combination of two links in contact constitutes a *kinematic pair*, or *joint*. An assemblage of interconnected links is called a *kinematic chain*. A mechanism is formed when at least one of the links of the kinematic chain is held fixed and any of its other links can move. The fixed link of the planar Gough-Stewart platform (link 8 in Figure 2.5) is the *ground* or *frame*. Note that the origin of link 8 is chosen to coincide with the origin of the global $0xy$ -reference frame, and that the local $0_8 \xi_8 \eta_8$ -coordinate system, and the global $0xy$ -reference frame are identically orientated.   Furthermore, the origin of each local $0_i \xi_i \eta_i$ -coordinate system, $i = 1,2,...,7$, is chosen to coincide with the center of mass of respective bodies $1,2,...,7$, and these local coordinate systems are orientated as shown in Figure 2.5.

The primary purpose of the above schematic representation of the planar Gough-Stewart platform is to identify the *connectivity* of the bodies or links, i.e. to identify the *kinematic pairs* or *joints*. A kinematic pair imposes certain conditions on the relative motion between the two bodies it comprises. When these conditions are expressed in analytical form, they are called *equations of constraint*. Constraint equations

are denoted by Φ with a superscript indicating the constraint type and the number of algebraic equations, and a subscript indicating the joined bodies. Thus $\Phi_{i-j}^{(r,2)}$ denotes the revolute (r) joint constraint of joined bodies i and j, which consists of two equations. Similarly $\Phi_{i-j}^{(t,2)}$ denotes the translational joint (t) constraint of joined bodies i and j, which also contains two equations.

2.3.1 Revolute joints

With reference to Figure 2.5, the connections between the moving platform (link 1) and the upper portions of the actuator legs (links 2, 3 and 4) are revolute joints. This is also the case for the connections between ground (link 8) and the lower portions of the actuator legs (links 5, 6 and 7).

In order to find the two algebraic equations of $\Phi_{i-j}^{(r,2)}$, consider the schematic representation of a revolute joint connecting bodies i and j as shown in Figure 2.6. Point P denotes the center of the joint and can be considered to be two coincident points; i.e. point P_i on body i and point P_j on body j.
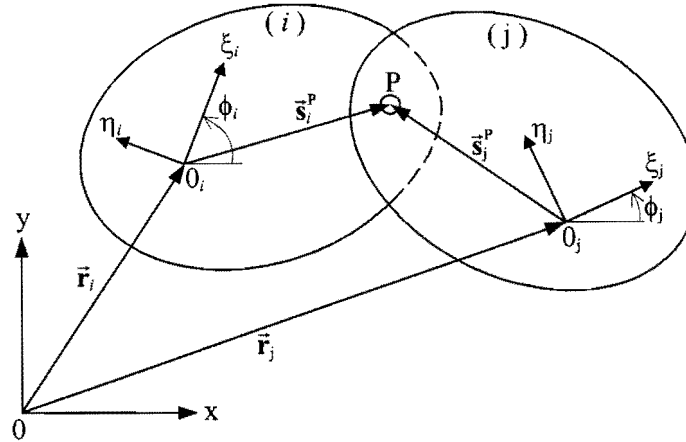
Figure 2.6: Revolute joint P connecting bodies i and j (after [65]).

The vectors $\vec{s}_i^P$ and $\vec{s}_j^P$ respectively describe the location of point P on body i and body j. Taken together with vectors $\vec{r}_i$ and $\vec{r}_j$, the constraint equations for the revolute joint are obtained from the closed vector loop expression:

$$\vec{r}_i + \vec{s}_i^P - \vec{s}_j^P - \vec{r}_j = \vec{0}$$

or in terms of global positional two-vectors:

$$r_i + s_i^P - s_j^P - r_j = 0$$

which is equivalent to

$$\Phi_{i-j}^{(r,2)} \equiv r_i + A_i s_i'^P - r_j - A_j s_j'^P = 0 \tag{2.5}$$

Expression (2.5) consists of two algebraic equations, i.e.

$$\Phi_{i-j}^{(r,2)} \equiv \begin{bmatrix} x_i + \xi_i^P \cos\phi_i - \eta_i^P \sin\phi_i - x_j - \xi_j^P \cos\phi_j + \eta_j^P \sin\phi_j \\ y_i + \xi_i^P \sin\phi_i + \eta_i^P \cos\phi_i - y_j - \xi_j^P \sin\phi_j - \eta_j^P \cos\phi_j \end{bmatrix} = \begin{bmatrix} 0 \\ 0 \end{bmatrix} \qquad (2.6)$$

These two constraint equations reduce the number of degrees of freedom (DOF) of the system of bodies shown in Figure 2.6, by two. Consequently, if the two bodies of Figure 2.6 are not connected to any other bodies, then the system has four DOF.

In particular, the constraint equations of the six revolute joints of the planar Gough-Stewart platform shown in Figure 2.5 are:

$$\Phi_{1-2}^{(r,2)} \equiv \begin{bmatrix} x_1 + \xi_1^A \cos\phi_1 - \eta_1^A \sin\phi_1 - x_2 - \xi_2^A \cos\phi_2 + \eta_2^A \sin\phi_2 \\ y_1 + \xi_1^A \sin\phi_1 + \eta_1^A \cos\phi_1 - y_2 - \xi_2^A \sin\phi_2 - \eta_2^A \cos\phi_2 \end{bmatrix} = \begin{bmatrix} 0 \\ 0 \end{bmatrix} \qquad (2.7)$$

$$\Phi_{1-3}^{(r,2)} \equiv \begin{bmatrix} x_1 + \xi_1^A \cos\phi_1 - \eta_1^A \sin\phi_1 - x_3 - \xi_3^A \cos\phi_3 + \eta_3^A \sin\phi_3 \\ y_1 + \xi_1^A \sin\phi_1 + \eta_1^A \cos\phi_1 - y_3 - \xi_3^A \sin\phi_3 - \eta_3^A \cos\phi_3 \end{bmatrix} = \begin{bmatrix} 0 \\ 0 \end{bmatrix} \qquad (2.8)$$

$$\Phi_{1-4}^{(r,2)} \equiv \begin{bmatrix} x_1 + \xi_1^B \cos\phi_1 - \eta_1^B \sin\phi_1 - x_4 - \xi_4^B \cos\phi_4 + \eta_4^B \sin\phi_4 \\ y_1 + \xi_1^B \sin\phi_1 + \eta_1^B \cos\phi_1 - y_4 - \xi_4^B \sin\phi_4 - \eta_4^B \cos\phi_4 \end{bmatrix} = \begin{bmatrix} 0 \\ 0 \end{bmatrix} \qquad (2.9)$$

$$\Phi_{5-8}^{(r,2)} \equiv \begin{bmatrix} x_5 + \xi_5^C \cos\phi_5 - \eta_5^C \sin\phi_5 - x^C \\ y_5 + \xi_5^C \sin\phi_5 + \eta_5^C \cos\phi_5 - y^C \end{bmatrix} = \begin{bmatrix} 0 \\ 0 \end{bmatrix} \qquad (2.10)$$

$$\Phi_{6-8}^{(r,2)} \equiv \begin{bmatrix} x_6 + \xi_6^D \cos\phi_6 - \eta_6^D \sin\phi_6 - x^D \\ y_6 + \xi_6^D \sin\phi_6 + \eta_6^D \cos\phi_6 - y^D \end{bmatrix} = \begin{bmatrix} 0 \\ 0 \end{bmatrix} \qquad (2.11)$$

$$\Phi_{7-8}^{(r,2)} \equiv \begin{bmatrix} x_7 + \xi_7^E \cos\phi_7 - \eta_7^E \sin\phi_7 - x^E \\ y_7 + \xi_7^E \sin\phi_7 + \eta_7^E \cos\phi_7 - y^E \end{bmatrix} = \begin{bmatrix} 0 \\ 0 \end{bmatrix} \qquad (2.12)$$

The simplification in expressions (2.10), (2.11) and (2.12) follow from the particular choice of position and orientation of the chosen local $0_8\xi_8\eta_8$ -coordinate system.

2.3.2 Translational joints

The three actuator legs shown in Figure 2.2, each consists of two links that translate with respect to each other parallel to an axis known as the *line of translation*. In particular, and with reference to Figure 2.5, the *left* actuator leg is a translational joint between links 2 and 5, the *middle* actuator leg is a translational joint between links 3 and 6 and the *right* actuator leg is a translational joint between links 4 and 7.

Figure 2.7 shows a schematic representation of a translational joint between links i and j, from which the two algebraic equations of $\Phi_{i-j}^{(t,2)}$ may be derived.
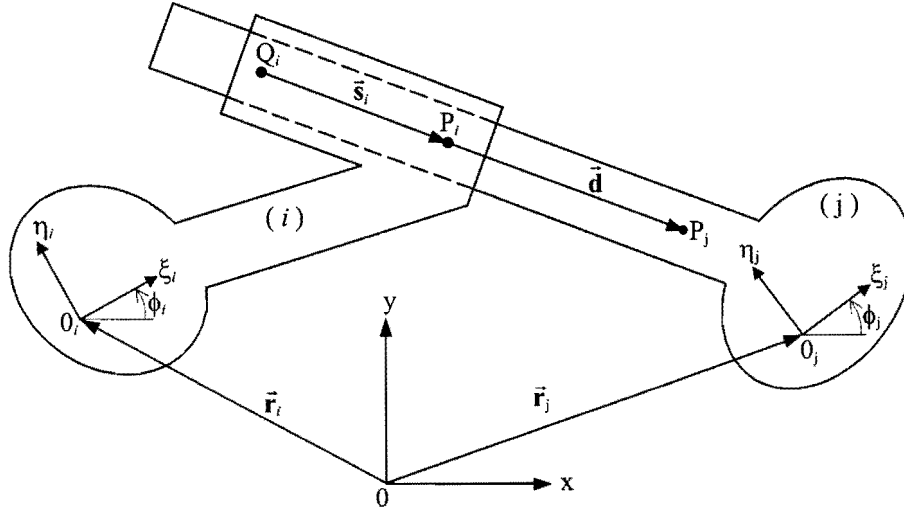
Figure 2.7: A translational joint between bodies *i* and j (after [65]).

A constraint is required to eliminate the relative motion between the two bodies in a direction perpendicular to the line of translation. In order to satisfy this constraint, the two vectors $\vec{s}_i$ and $\vec{d}$ shown in Figure 2.7 must remain parallel. These vectors are defined by locating three points on the line of translation – points Q_i and P_i on body *i*, and point P_j on body j. The first algebraic equation of $\Phi_{i-j}^{(t,2)}$ follows from the fact that the vector product of two parallel vectors is zero, i.e.

$$\vec{s}_i \times \vec{d} = \vec{0}$$

which, for the global components of vector $\vec{s}_i$, i.e. $\vec{s}_i : s_i = \begin{bmatrix} (x_i^P - x_i^Q) \\ (y_i^P - y_i^Q) \end{bmatrix}$ and the global components of

vector $\vec{d}$, i.e. $\vec{d} : d = \begin{bmatrix} (x_j^P - x_i^P) \\ (y_j^P - y_i^P) \end{bmatrix}$, is equivalent to (see [65]):

$$(x_i^P - x_i^Q)(y_j^P - y_i^P) - (x_j^P - x_i^P)(y_i^P - y_i^Q) = 0 \tag{2.13}$$

The second constraint of $\Phi_{i-j}^{(t,2)}$ eliminates the relative rotation between bodies *i* and j, through the condition that

$$\phi_i - \phi_j - (\phi_i^0 - \phi_j^0) = 0 \tag{2.14}$$

where ϕ_i^0 and ϕ_j^0 are the initial orientation angles.

The two constraint equations for a translational joint are therefore given by

$$\Phi_{i-j}^{(t,2)} \equiv \begin{bmatrix} (x_i^P - x_i^Q)(y_j^P - y_i^P) - (x_j^P - x_i^P)(y_i^P - y_i^Q) \\ \phi_i - \phi_j - (\phi_i^0 - \phi_j^0) \end{bmatrix} = \begin{bmatrix} 0 \\ 0 \end{bmatrix} \tag{2.15}$$

As in the case of the revolute joint, the translational joint reduces the number of degrees of freedom of a system by two.

Expression (2.13) may be expanded to give

$$x_i^P y_j^P - x_i^Q y_j^P + x_i^Q y_i^P - x_j^P y_i^P + x_j^P y_i^Q - x_i^P y_i^Q = 0 \tag{2.16}$$

with

$$x_i^P = x_i + \xi_i^P \cos\phi_i - \eta_i^P \sin\phi_i \qquad\qquad y_i^P = y_i + \xi_i^P \sin\phi_i + \eta_i^P \cos\phi_i$$

$$x_i^Q = x_i + \xi_i^Q \cos\phi_i - \eta_i^Q \sin\phi_i \qquad\qquad y_i^Q = y_i + \xi_i^Q \sin\phi_i + \eta_i^Q \cos\phi_i$$

$$x_j^P = x_j + \xi_j^P \cos\phi_j - \eta_j^P \sin\phi_j \qquad\qquad y_j^P = y_j + \xi_j^P \sin\phi_j + \eta_j^P \cos\phi_j$$

Constraint (2.16) may therefore explicitly be stated in terms of the planar coordinates of two bodies.

With reference to Figure 2.5 the relevant vectors of translational joint $2-5$ are defined using points A and 0_2 in link 2, and point 0_5 in link 5. This implies that general constraint (2.16) corresponding to translational joint $2-5$, is:

$$x_2^{0_2} y_5^{0_5} - x_2^A y_5^{0_5} + x_2^A y_2^{0_2} - x_5^{0_5} y_2^{0_2} + x_5^{0_5} y_2^A - x_2^{0_2} y_2^A = 0$$

with

$$x_2^{0_2} = x_2 \qquad\qquad\qquad y_2^{0_2} = y_2$$

$$x_2^A = x_2 + \xi_2^A \cos\phi_2 \qquad\qquad y_2^A = y_2 + \xi_2^A \sin\phi_2$$

$$x_5^{0_5} = x_5 \qquad\qquad\qquad y_5^{0_5} = y_5$$

By substitution and simplification, the two constraint equations of the translational joint $2-5$ of the planar Gough-Stewart platform shown in Figure 2.5 are:

$$\Phi_{2-5}^{(t,2)} \equiv \begin{bmatrix} -x_2\xi_2^A \sin\phi_2 + y_2\xi_2^A \cos\phi_2 + x_5\xi_2^A \sin\phi_2 - y_2\xi_2^A \cos\phi_2 \\ \phi_2 - \phi_5 \end{bmatrix} = \begin{bmatrix} 0 \\ 0 \end{bmatrix} \tag{2.17}$$

Note that since the ξ_2 and ξ_5 axes coincide with the line of translation of translational joint $2-5$, the initial rotational angles ϕ_2^0 and ϕ_5^0 (see expressions (2.14) and (2.15)) fall away from the second constraint equation of $\Phi_{2-5}^{(t,2)}$.

Similarly the constraint equations of translational joints $3-6$ and $4-7$ are respectively found to be

$$\Phi_{3-6}^{(t,2)} \equiv \begin{bmatrix} -x_3\xi_3^A \sin\phi_3 + y_3\xi_3^A \cos\phi_3 + x_6\xi_3^A \sin\phi_3 - y_6\xi_3^A \cos\phi_3 \\ \phi_3 - \phi_6 \end{bmatrix} = \begin{bmatrix} 0 \\ 0 \end{bmatrix} \tag{2.18}$$

$$\Phi_{4-7}^{(t,2)} \equiv \begin{bmatrix} -x_4\xi_4^B \sin\phi_4 + y_4\xi_4^B \cos\phi_4 + x_7\xi_4^B \sin\phi_4 - y_7\xi_4^B \cos\phi_4 \\ \phi_4 - \phi_7 \end{bmatrix} = \begin{bmatrix} 0 \\ 0 \end{bmatrix} \tag{2.19}$$

2.3.3 Simplified constraints

The remaining constraints are related to the fixed ground-link, i.e. link 8 of the planar Gough-Stewart platform (see Figure 2.5). In order to constrain the translation of the origin and angular motion of a fixed rigid body, the following three equations may be used as the necessary simplified constraints [65]:

$$\Phi \equiv x_i - c_1 = 0 \qquad (2.20)$$

$$\Phi \equiv y_i - c_2 = 0 \qquad (2.21)$$

$$\Phi \equiv \phi_i - c_3 = 0 \qquad (2.22)$$

where c_1, c_2 and c_3 are constant quantities.

Since the origin of the local $0_8 \xi_8 \eta_8$-coordinate system coincides with the origin of the global $0xy$-reference frame, and the two coordinate systems are identically orientated (see Figure 2.5), expressions (2.20), (2.21) and (2.22) for link 8 of the planar Gough-Stewart platform, reduces to:

$$\Phi \equiv x_8 = 0 \qquad (2.23)$$

$$\Phi \equiv y_8 = 0 \qquad (2.24)$$

$$\Phi \equiv \phi_8 = 0 \qquad (2.25)$$

For the eight-link kinematic model of the planar Gough-Stewart platform, the 21 *independent* kinematic constraint equations given by expressions (2.7) - (2.12), (2.17) - (2.19) and (2.23) - (2.25) apply. For a system having m *independent kinematic constraint equations* and n *coordinates*, the number of *degrees of freedom* (DOF) is given by:

$$k = n - m \qquad (2.26)$$

Hence, the eight-link model of the planar Gough-Stewart platform has 24 coordinates, and consequently $24 - 21 = 3$ DOF.

2.4   Driving constraints

Any set of k coordinates that are *independent* and are equal in number to the number of DOF of the system, determines the values of the remaining m *dependent* coordinates through the solution of the m independent kinematic constraint equations. Thus for the planar Gough-Stewart platform with three DOF, the values of three *independent* coordinates must be known to completely describe the system.

In particular, the three planar coordinates describing the position and orientation of link 1, i.e. x_1, y_1 and ϕ_1 are the three independent coordinates of the planar Gough-Stewart platform shown in Figure 2.5.

The applicable *driving constraints* are equations expressing each independent coordinate as a function of time, i.e.:

$$\Phi^{(d-1,1)} \equiv x_1 - d_1(t) = 0 \tag{2.27}$$

$$\Phi^{(d-2,1)} \equiv y_1 - d_2(t) = 0 \tag{2.28}$$

$$\Phi^{(d-3,1)} \equiv \phi_1 - d_3(t) = 0 \tag{2.29}$$

Each driving constraint is denoted by Φ with the superscript indicating the driving constraint number, and the number of algebraic equations, e.g. $\Phi^{(d-1,1)}$ is driving constraint number 1, which involves 1 equation.

Expressions (2.27), (2.28) and (2.29) uniquely define the *motion* of link 1. With reference to Figure 2.2, link 1 is the moving platform of the planar Gough-Stewart platform and, with the planar machining center in mind, it is clear that in controlling the relative motion between the workpiece and cutting tool, either one can be attached to the moving platform with the other fixed in the plane.

These two possible scenarios are separately dealt with in the next two sub-sections, with specific reference to obtaining for a given tool path, expressions giving the required *values* of the three independent coordinates x_1, y_1 and ϕ_1 at any given time instant. The details of deriving the analytical functions $d_1(t)$, $d_2(t)$ and $d_3(t)$ that appear in driving constraints (2.27) - (2.29) are explained in **Chapter 3**.

2.4.1 Fixed workpiece

Consider the scenario of the cutting tool mounted on the moving platform with an externally *fixed workpiece* as shown in Figure 2.8. In this case it is required that the cutting tool be moved along a prescribed tool path specified in the global $0xy$-coordinate system.
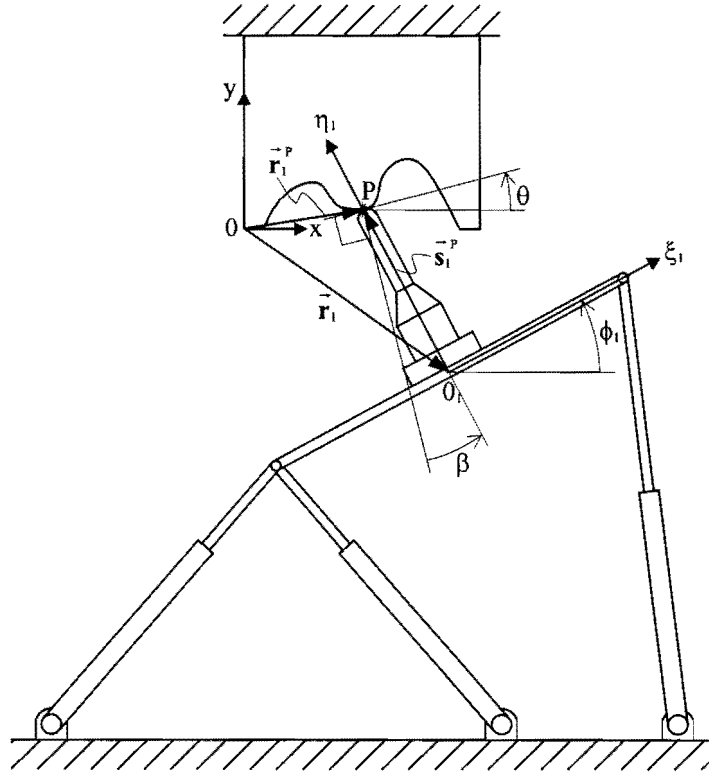
Figure 2.8: Fixed workpiece scenario.

At any given time instant it is assumed that the following are known:

1. the global position of the cutting tool tip (P in Figure 2.8) on the prescribed tool path, and

2. the angle β between the platform-mounted tool and the normal to the tool path at the point of contact (see Figure 2.8) and measured positive in the CCW direction.

Assumption 1 implies that the global representation of the time varying vector $\vec{r}_1^P$, i.e. $\vec{r}_1^P : r_1^P = \begin{bmatrix} x^P \\ y^P \end{bmatrix}_1$ is known at every instant as the prescribed tool path is traced. The tool tip P can also be located relative to the origin of the local $0_1\xi_1\eta_1$ -axes by the time varying vector $\vec{s}_1^P$. The corresponding fixed components of vector $\vec{s}_1^P$, when represented in the local $0_1\xi_1\eta_1$ -reference frame, is $\vec{s}_1^P : s_1'^P = \begin{bmatrix} 0 \\ \eta^P \end{bmatrix}_1$, where for any given tool length, the local η_1^P -component is a known constant.

The following vector loop equation may then be used to find the sought-after global position of link 1:

$$\vec{r}_1 + \vec{s}_1^P = \vec{r}_1^P$$

or in global vector representation:

$$\mathbf{r}_1 + A_1 s_1'^P = r_1^P$$

In terms of components this vector equation may be written as

---

Chapter 2   51

$$\begin{bmatrix} x \\ y \end{bmatrix}_1 + \begin{bmatrix} \cos\phi_1 & -\sin\phi_1 \\ \sin\phi_1 & \cos\phi_1 \end{bmatrix} \begin{bmatrix} 0 \\ \eta^P \end{bmatrix}_1 = \begin{bmatrix} x^P \\ y^P \end{bmatrix}_1 \tag{2.30}$$

Expression (2.30) contains two scalar equations, i.e.

$$x_1 = x_1^P + \eta_1^P \sin\phi_1 \tag{2.31}$$

and

$$y_1 = y_1^P - \eta_1^P \cos\phi_1 \tag{2.32}$$

In order to compute x_1 and y_1, the orientation angle of link 1, ϕ_1, must also be known. At every time instant, as the cutting tool progresses along the prescribed tool path, the orientation angle ϕ_1 is directly related to the known prescribed angle β (see assumption 2 in Section 2.4.1). To find this relationship, consider the simplified fixed workpiece situation depicted in Figure 2.9, where the mounted cutting tool is collinear with the normal to the tool path at the point of contact.
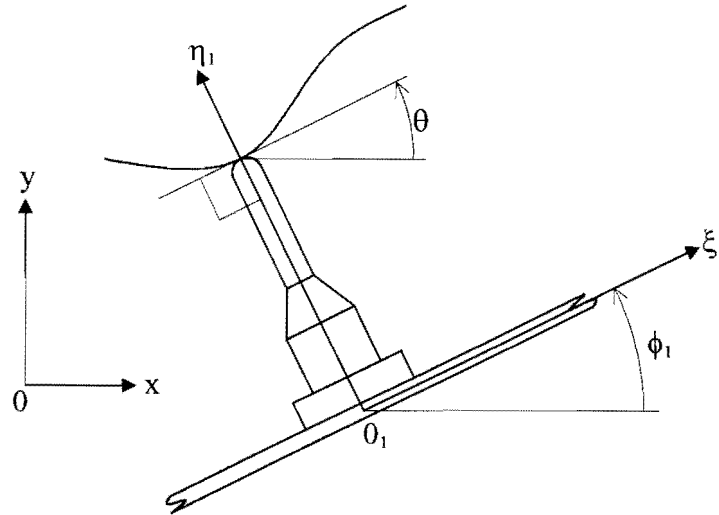
Figure 2.9: Simplified fixed workpiece situation.

For this situation, it is clear that $\beta = 0$ and the orientation angle ϕ_1 is equal to the gradient angle θ of the tool path, where

$$\tan\theta = \frac{dy}{dx} \tag{2.33}$$

and $\frac{dy}{dx}$ represents the (known) gradient of the prescribed tool path $y(x)$ at the point of contact.

With the proposed convention that β be measured positive CCW from the normal to the tool path at the point of contact, the orientation angle for the fixed workpiece situation depicted in Figure 2.8 is (remembering that for CW rotations θ and ϕ_1 take on negative values):

$$\phi_1 = \theta + \beta \qquad\qquad (2.34)$$

with ϕ_1 and θ measured positive CCW from the horizontal, and β measured as defined above.

Substituting expression (2.34) into expressions (2.31) and (2.32) gives:

$$x_1 = x_1^P + \eta_1^P \sin(\theta + \beta) \qquad\qquad (2.35)$$

and

$$y_1 = y_1^P - \eta_1^P \cos(\theta + \beta) \qquad\qquad (2.36)$$

In summary, for the fixed tool scenario it follows that with x^P, y^P and β known at a specific time instant or point along the tool path, the corresponding independent coordinates of the planar Gough-Stewart platform, x_1, y_1 and ϕ_1 are respectively obtained by substituting the tool path gradient angle θ (see expression (2.33)) into expressions (2.35), (2.36) and (2.34).

2.4.2 Fixed cutting tool

The second planar machining center scenario is where the workpiece is mounted to the moving platform, and the cutting tool is externally fixed. This case is depicted in Figure 2.10, and since the tool path is now prescribed in terms of the local $0_1 \xi_1 \eta_1$-coordinate system, it is required that the workpiece be moved such that the fixed cutting tool traces the prescribed tool path.
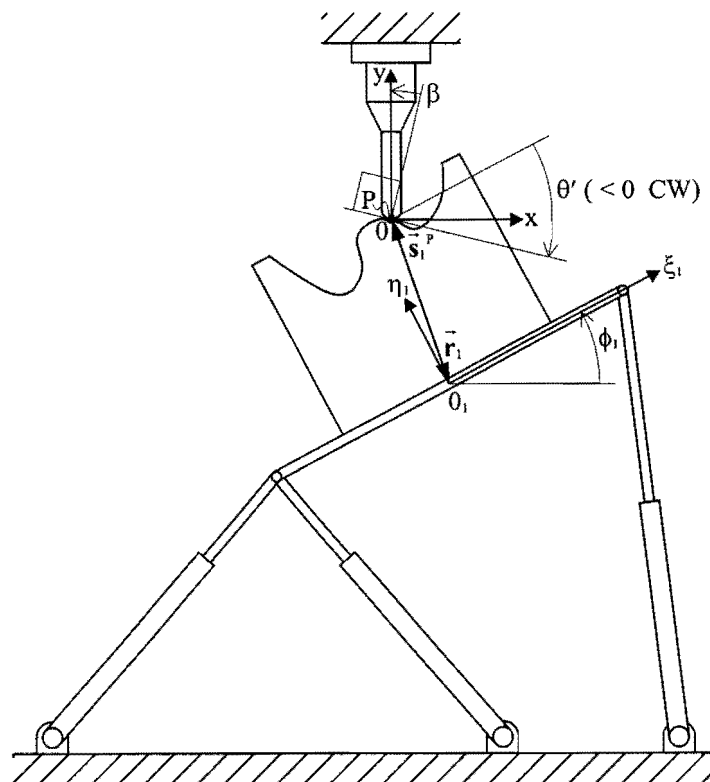
Figure 2.10: Fixed cutting tool scenario.

As in Section 2.4.1, it is also assumed here that at any time instant the following are known:

1. the local position of the cutting tool tip (P in Figure 2.10) on the prescribed tool path, and

2. the angle β (measured positive CCW), from the normal to the tool path at the point of contact, to the vertical axis of the fixed cutting tool (see Figure 2.10).

Assumption 1 implies that the local representation of the time varying vector $\vec{s}_1^P$, i.e. $\vec{s}_1^P : s_1'^P = \begin{bmatrix} \xi^P \\ \eta^P \end{bmatrix}_1$ is

known at every instant as the fixed cutting tool traces the prescribed tool path. The origin of the global reference frame is chosen to coincide with the tool tip P. Hence, vector $\vec{r}_1$ locating the moving platform (link 1 in Figure 2.5) has the same magnitude as vector $\vec{s}_1^P$, but is directed in the exact opposite direction.

To find the global components of vector $\vec{r}_1$, first consider the simplified fixed cutting tool situation shown in Figure 2.11.
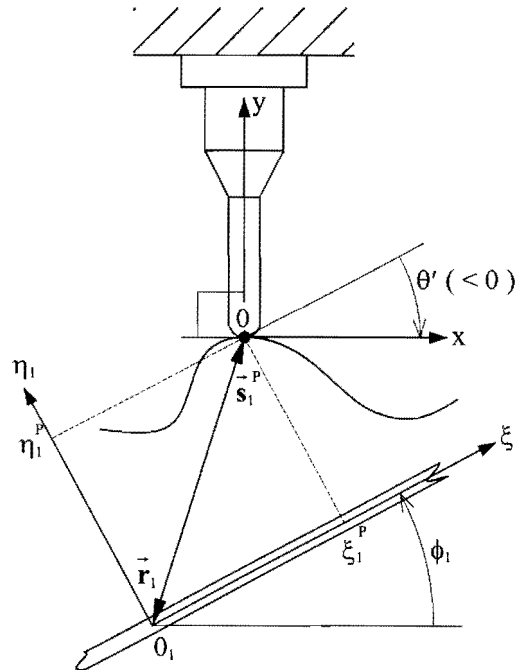
Figure 2.11: Simplified fixed cutting tool situation.

Clearly $\beta = 0$ in this case, which implies that the tangent to the prescribed tool path at the point of contact P is perpendicular to the vertical axis of the fixed cutting tool. The gradient angle of the prescribed tool path in the local coordinate system is θ', where

$$\tan \theta' = \frac{d\eta_1}{d\xi_1} \tag{2.37}$$

and $\dfrac{d\eta_1(\xi_1)}{d\xi_1}$ represents the gradient of the prescribed tool path $\eta_1(\xi_1)$ at the point of contact.

The superscript prime indicates that the gradient angle is determined relative to the local $0_1 \xi_1 \eta_1$- coordinate system.

For the simplified situation shown in Figure 2.11, the orientation angle ϕ_1 is equal in magnitude but oppositely orientated to the gradient angle θ', i.e. $\phi_1 = -\theta'$.

With ϕ_1 known, the global components of vector $\vec{r}_1$ are obtained using a translation that is similar to the one given by expression (2.1). In particular, the global components of vector $\vec{r}_1$ shown in Figure 2.11 are given by the following two scalar equations:

$$x_1 = -\xi_1^P \cos\phi_1 + \eta_1^P \sin\phi_1 \qquad (2.38)$$

and

$$y_1 = -\xi_1^P \sin\phi_1 - \eta_1^P \cos\phi_1 \qquad (2.39)$$

However, for the non-zero angle β shown in Figure 2.10, the orientation angle ϕ_1 of the moving platform is:

$$\phi_1 = -\theta' - \beta \qquad (2.40)$$

using the CCW sign convention previously defined for all three angles.

Substituting expression (2.40) respectively into expressions (2.38) and (2.39) gives:

$$x_1 = -\xi_1^P \cos(\theta' + \beta) - \eta_1^P \sin(\theta' + \beta) \qquad (2.41)$$

and

$$y_1 = \xi_1^P \sin(\theta' + \beta) - \eta_1^P \cos(\theta' + \beta) \qquad (2.42)$$

Consequently, for the fixed cutting tool scenario with ξ_1^P, η_1^P and β known at any specific time instant, the corresponding independent coordinates of the planar Gough-Stewart platform x_1, y_1 and ϕ_1 are respectively obtained by substituting the tool path gradient angle θ' (see expression (2.37)) into expressions (2.41), (2.42) and (2.40).

2.5 Inverse kinematic analysis

In the kinematic analysis of the planar Gough-Stewart platform, the kinematic constraint equations derived in Section 2.3, and the driving constraints derived in Section 2.4 are used. The first and second time derivatives of these constraint equations yield the velocity and acceleration equations.

The method of appended driving constraints [65], is used here for the kinematic analysis of the planar Gough-Stewart platform. This method is presented below in its most general form.

Suppose that the vector of coordinates describing the configuration of a system is given by $\mathbf{q} = [q_1, q_2, \ldots, q_n]^T$ where n is the total number of coordinates. If there are m kinematic constraints expressed in vector form by $\Phi(\mathbf{q}) = \mathbf{0}$, then k driving constraints can be appended to the kinematic constraints to obtain $n = m + k$ equations:

$$\Phi \equiv \Phi(\mathbf{q}) = \mathbf{0} \tag{2.43}$$

$$\Phi^{(d)} \equiv \Phi(\mathbf{q}, t) = \mathbf{0} \tag{2.44}$$

where the superscript (d) denotes the driving constraints. Expressions (2.43) and (2.44) represents n equations in n unknowns $\mathbf{q}$ which can be solved for any specific time t.

The velocity equations are obtained by taking the time derivative of expressions (2.43) and (2.44):

$$\Phi_q \dot{\mathbf{q}} = \mathbf{0} \tag{2.45}$$

$$\Phi_q^{(d)} \dot{\mathbf{q}} + \Phi_t^{(d)} = \mathbf{0} \tag{2.46}$$

where Φ_q represents the Jacobian of the vector function Φ with respect to $\mathbf{q}$ and Φ_t the partial derivative of the function with respect to t.

Expression (2.45) follows from the fact that in general:

$$\Phi(\mathbf{q}) = \begin{bmatrix} \Phi_1(\mathbf{q}) \\ \Phi_2(\mathbf{q}) \\ \vdots \\ \Phi_m(\mathbf{q}) \end{bmatrix} \tag{2.47}$$

and therefore the time derivative of the i-th entry $\Phi_i(\mathbf{q})$ in expression (2.47) is:

$$\frac{d}{dt}\left(\Phi_i(\mathbf{q})\right) = \frac{\partial \Phi_i}{\partial q_1}\dot{q}_1 + \frac{\partial \Phi_i}{\partial q_2}\dot{q}_2 + \cdots + \frac{\partial \Phi_i}{\partial q_n}\dot{q}_n \tag{2.48}$$

Similarly, expression (2.46) follows from the fact that in general the driving constraints are also explicit functions of time:

$$\Phi^{(d)}(\mathbf{q},t) = \begin{bmatrix} \Phi_1^{(d)}(\mathbf{q},t) \\ \Phi_2^{(d)}(\mathbf{q},t) \\ \vdots \\ \Phi_m^{(d)}(\mathbf{q},t) \end{bmatrix} \tag{2.49}$$

and therefore the corresponding time derivative of the i-th entry $\Phi_i^{(d)}(\mathbf{q},t)$ in expression (2.49) is given by

$$\frac{d}{dt}\left(\Phi_i^{(d)}(\mathbf{q},t)\right) = \frac{\partial \Phi_i^{(d)}}{\partial q_1}\dot{q}_1 + \frac{\partial \Phi_i^{(d)}}{\partial q_2}\dot{q}_2 + \cdots + \frac{\partial \Phi_i^{(d)}}{\partial q_n}\dot{q}_n + \frac{\partial \Phi_i^{(d)}}{\partial t} \tag{2.50}$$

The velocity equations (2.45) and (2.46) may also be written as

$$\begin{bmatrix} \Phi_q \\ \Phi_q^{(d)} \end{bmatrix}\dot{\mathbf{q}} = \begin{bmatrix} 0 \\ -\Phi_t^{(d)} \end{bmatrix} \tag{2.51}$$

which represents n algebraic equations, linear in terms of $\dot{\mathbf{q}}$.

The time derivative of expressions (2.45) and (2.46) yields the acceleration equations:

$$\Phi_q\ddot{\mathbf{q}} + (\Phi_q\dot{\mathbf{q}})_q\dot{\mathbf{q}} = 0 \tag{2.52}$$

$$\Phi_q^{(d)}\ddot{\mathbf{q}} + (\Phi_q^{(d)}\dot{\mathbf{q}})_q\dot{\mathbf{q}} + 2\Phi_{qt}^{(d)}\dot{\mathbf{q}} + \Phi_{tt}^{(d)} = 0 \tag{2.53}$$

These expressions are obtained through the following argument. Considering the more general expression (2.46), which also contains t explicitly, it is clear that the left hand side is a vector function **F** of **q**, $\dot{\mathbf{q}}$ and t:

$$\mathbf{F}(\mathbf{q},\dot{\mathbf{q}},t) = \Phi_q(\mathbf{q},t)\dot{\mathbf{q}} + \Phi_t(t,\mathbf{q}) \tag{2.54}$$

where for convenience the superscript has been dropped. The time derivative of (2.54) may therefore be written as

$$\frac{d\mathbf{F}}{dt} = \mathbf{F}_q\dot{\mathbf{q}} + \mathbf{F}_{\dot{q}}\ddot{\mathbf{q}} + \mathbf{F}_t \tag{2.55}$$

where $\mathbf{F}_q = [\Phi_q\dot{\mathbf{q}}]_q + \Phi_{tq}$,

$\mathbf{F}_{\dot{q}} = [\Phi_q\dot{\mathbf{q}}]_{\dot{q}} + \Phi_{t\dot{q}} = \Phi_q$ and

$\mathbf{F}_t = \Phi_{qt}\dot{\mathbf{q}} + \Phi_{tt}$.

Substituting the above into (2.55) and then in (2.46) gives

$$\frac{d\mathbf{F}}{dt} = [\Phi_q\dot{\mathbf{q}}]_q\dot{\mathbf{q}} + \Phi_{tq}\dot{\mathbf{q}} + \Phi_q\ddot{\mathbf{q}} + \Phi_{qt}\dot{\mathbf{q}} + \Phi_{tt} = 0$$

from which (2.53) [and also (2.52)] follows directly.

Accelerations equations (2.52) and (2.53) may also be written as

$$
\begin{bmatrix} \Phi_q \\ \Phi_q^{(d)} \end{bmatrix} \ddot{q} = \begin{bmatrix} -(\Phi_q \dot{q})_q \dot{q} \\ -(\Phi_q^{(d)} \dot{q})_q \dot{q} - 2\Phi_{qt}^{(d)} \dot{q} - \Phi_{tt}^{(d)} \end{bmatrix}
\tag{2.56}
$$

which represents n algebraic equations linear in terms of $\ddot{q}$.

For the planar Gough-Stewart platform under consideration, expression (2.43) represents the 21 equations given by expressions (2.7) - (2.12), (2.17) - (2.19) and (2.23) - (2.25), and expression (2.44) represents the three driving constraints given by expressions (2.27) - (2.29). These 24 nonlinear equations in 24 unknowns $q = [x_1, y_1, \phi_1, x_2, y_2, \phi_2, ..., x_8, y_8, \phi_8]^T$ (see expression (2.4)) may therefore be solved for any specified time t.

More specifically, at any specified time t, expressions (2.27) - (2.29) provide the x_1, y_1 and ϕ_1 values. With reference to Figure 2.5, the global coordinates of points A and B are

$$
\begin{aligned}
x^A &= x_1 + \xi_1^A \cos\phi_1 & y^A &= y_1 + \xi_1^A \sin\phi_1 \\
x^B &= x_1 + \xi_1^B \cos\phi_1 & y^B &= y_1 + \xi_1^B \sin\phi_1
\end{aligned}
\tag{2.57}
$$

Note that for the specific choice of the local coordinate system of body 1 coinciding with the center of mass of body 1 (see Section 2.3), $\xi_1^A < 0$.

The global positions of points C, D and E are also known for any specific design of the planar Gough-Stewart platform.

The orientation angles of links 2 - 7 may be determined using the "two-argument arc tangent function" $a\tan 2\left(\dfrac{y}{x}\right)$. In particular, $a\tan 2\left(\dfrac{y}{x}\right)$ denotes the angle whose tangent is y divided by x. Moreover, both the magnitudes and signs of x and y are used in the definition, so that angles are uniquely defined in all four quadrants. For example: $a\tan 2\left(\dfrac{-1.0}{-1.0}\right) = -135°$, and $a\tan 2\left(\dfrac{1.0}{1.0}\right) = 45°$ (see [60]).

For the specific choice of local axes shown in Figure 2.5, the respective orientation angles of links 2 and 5, links 3 and 6 as well as links 4 and 7 are equal, i.e.

$$\phi_2 = \phi_5 = a\tan 2\left(\frac{y^A - y^C}{x^A - x^C}\right) \tag{2.58}$$

$$\phi_3 = \phi_6 = a\tan 2\left(\frac{y^A - y^D}{x^A - x^D}\right) \tag{2.59}$$

$$\phi_4 = \phi_7 = a\tan 2\left(\frac{y^B - y^E}{x^B - x^E}\right) \tag{2.60}$$

Note that the revolute joint constraints given by expressions (2.7) - (2.12), as well as the translational joint constraints given by expressions (2.17) - (2.19) are implicitly satisfied in expressions (2.58) - (2.60).

The global positions of links 2 – 7 follow directly from the transformation given by expression (2.1), i.e.

$$
\begin{aligned}
x_2 &= x^A - \xi_2^A \cos\phi_2 & \qquad y_2 &= y^A - \xi_2^A \sin\phi_2 \\
x_3 &= x^A - \xi_3^A \cos\phi_3 & \qquad y_3 &= y^A - \xi_3^A \sin\phi_3 \\
x_4 &= x^B - \xi_4^B \cos\phi_4 & \qquad y_4 &= y^B - \xi_4^B \sin\phi_4 \\
x_5 &= x^C - \xi_5^C \cos\phi_5 & \qquad y_5 &= y^C - \xi_5^C \sin\phi_5 \\
x_6 &= x^D - \xi_6^D \cos\phi_6 & \qquad y_6 &= y^D - \xi_6^D \sin\phi_6 \\
x_7 &= x^E - \xi_7^E \cos\phi_7 & \qquad y_7 &= y^E - \xi_7^E \sin\phi_7
\end{aligned}
\tag{2.61}
$$

The global positions and orientation of link 8 (ground) is given by expressions (2.23) - (2.25), i.e. $x_8 = 0$, $y_8 = 0$ and $\phi_8 = 0$. With a known coordinate vector $\mathbf{q} = [x_1, y_1, \phi_1, x_2, y_2, \phi_2, ..., x_8, y_8, \phi_8]^T$, the Jacobian matrix $\mathbf{J} = \begin{bmatrix} \mathbf{\Phi}_q \\ \mathbf{\Phi}_q^{(d)} \end{bmatrix}$ of the planar Gough-Stewart platform is uniquely defined (see following expression (2.62)):

$$\mathbf{J} = \begin{bmatrix} \cdots \end{bmatrix} \tag{2.62}$$

The matrix $\mathbf{J}$ contains, among its non-zero entries, terms of the form:

$-\xi_1^A \sin\phi_1,\ \xi_1^A \cos\phi_1,\ -\xi_1^A \sin\phi_1,\ \xi_1^A \cos\phi_1,\ -\xi_1^B \sin\phi_1,\ \xi_1^B \cos\phi_1$

$\xi_2^A \sin\phi_2,\ -\xi_2^A \cos\phi_2,\ -\xi_2^A \sin\phi_2,\ \xi_2^A \cos\phi_2$

$-x_1\xi_2^A \cos\phi_2 - y_1\xi_2^A \sin\phi_2 + x_3\xi_2^A \cos\phi_2 + y_3\xi_2^A \sin\phi_2 - 1$

$-\xi_3^A \sin\phi_3,\ \xi_3^A \cos\phi_3,\ \xi_3^A \sin\phi_3,\ -\xi_3^A \cos\phi_3$

$-x_3\xi_3^A \cos\phi_3 - y_3\xi_3^A \sin\phi_3 + x_5\xi_3^A \cos\phi_3 + y_5\xi_3^A \sin\phi_3 - 1$

$\xi_4^B \sin\phi_4,\ -\xi_4^B \cos\phi_4$

$-x_5\xi_4^B \cos\phi_4 - y_5\xi_4^B \sin\phi_4 + x_4\xi_4^B \cos\phi_4 + y_4\xi_4^B \sin\phi_4 - 1$

$-\xi_5^C \sin\phi_5,\ \xi_5^C \cos\phi_5$

$\xi_3^A \sin\phi_3,\ -\xi_3^A \cos\phi_3$

$-\xi_6^D \sin\phi_6,\ \xi_6^D \cos\phi_6$

$\xi_{s4}^B \sin\phi_1,\ -\xi_{s4}^B \cos\phi_1$

$-\xi_7^E \sin\phi_7,\ \xi_7^E \cos\phi_7$

The right hand side of expression (2.51) as applied to the planar Gough-Stewart platform is

$$
\begin{bmatrix} \mathbf{0} \\ -\mathbf{\Phi}_t^{(d)} \end{bmatrix} = \begin{bmatrix} 0 \\ 0 \\ \vdots \\ 0 \\ \dfrac{\partial}{\partial t} d_1(t) \\ \dfrac{\partial}{\partial t} d_2(t) \\ \dfrac{\partial}{\partial t} d_3(t) \end{bmatrix}
\tag{2.63}
$$

The partial derivatives of the three driving constraints with respect to time are the velocities of link 1,

i.e.: $\dfrac{\partial}{\partial t} d_1(t) = \dot{x}_1(t)$, $\dfrac{\partial}{\partial t} d_2(t) = \dot{y}_1(t)$ and $\dfrac{\partial}{\partial t} d_3(t) = \dot{\phi}_1(t)$, the calculation of which, for a specific tool

path, is explained in **Chapter 3**.

Substituting expressions (2.62) and (2.63) into expression (2.51) results in 24 algebraic equations, linear in terms of $\dot{\mathbf{q}}$, where $\dot{\mathbf{q}} = [\dot{x}_1, \dot{y}_1, \dot{\phi}_1, \dot{x}_2, \dot{y}_2, \dot{\phi}_2, ..., \dot{x}_8, \dot{y}_8, \dot{\phi}_8]^T$ is the velocity vector of the planar Gough-Stewart platform. This linear system, of the general form $\mathbf{Ax} = \mathbf{c}$, is solved using the L-U factorization method. This method is a compact form of the Gaussian elimination method of operating on matrix $\mathbf{A}$. After the operation is completed, the set of linear equations $\mathbf{Ax} = \mathbf{c}$ is efficiently solved for any given $\mathbf{c}$ vector (see [65] and [55]).

In the linear system (2.56), the Jacobian matrix (expression (2.62)) is also required to solve for the accelerations of the planar Gough-Stewart platform, i.e. for $\ddot{\mathbf{q}} = [\ddot{x}_1, \ddot{y}_1, \ddot{\phi}_1, \ddot{x}_2, \ddot{y}_2, \ddot{\phi}_2, ..., \ddot{x}_8, \ddot{y}_8, \ddot{\phi}_8]^T$. The right hand side of expression (2.56) is a 24 vector given by

$$\begin{bmatrix} -(\Phi_q \dot{q})_q \dot{q} \\ -(\Phi_q^{(d)} \dot{q})_q \dot{q} - 2\Phi_{qt}^{(d)} \dot{q} - \Phi_{tt}^{(d)} \end{bmatrix} = \begin{bmatrix} (\dot{\phi}_1)^2 \xi_1^A \cos\phi_1 - (\dot{\phi}_2)^2 \xi_2^A \cos\phi_2 \\ (\dot{\phi}_1)^2 \xi_1^A \sin\phi_1 - (\dot{\phi}_2)^2 \xi_2^A \sin\phi_2 \\ (\dot{\phi}_1)^2 \xi_1^A \cos\phi_1 - (\dot{\phi}_3)^2 \xi_3^A \cos\phi_3 \\ (\dot{\phi}_1)^2 \xi_1^A \sin\phi_1 - (\dot{\phi}_3)^2 \xi_3^A \sin\phi_3 \\ (\dot{\phi}_1)^2 \xi_1^B \cos\phi_1 - (\dot{\phi}_4)^2 \xi_4^B \cos\phi_4 \\ (\dot{\phi}_1)^2 \xi_1^B \sin\phi_1 - (\dot{\phi}_4)^2 \xi_4^B \sin\phi_4 \\ (\dot{\phi}_5)^2 \xi_5^C \cos\phi_5 \\ (\dot{\phi}_5)^2 \xi_5^C \sin\phi_5 \\ (\dot{\phi}_6)^2 \xi_6^D \cos\phi_6 \\ (\dot{\phi}_6)^2 \xi_6^D \sin\phi_6 \\ (\dot{\phi}_7)^2 \xi_7^E \cos\phi_7 \\ (\dot{\phi}_7)^2 \xi_7^E \sin\phi_7 \\ \left(2\dot{x}_2 - 2\dot{x}_5 + y_5\dot{\phi}_2 - y_5\dot{\phi}_5\right)\dot{\phi}_5\xi_5^A\cos\phi_2 + \left(2\dot{y}_2 - 2\dot{y}_5 - x_5\dot{\phi}_2 + x_5\dot{\phi}_5\right)\dot{\phi}_5\xi_5^A\sin\phi_2 \\ 0 \\ \left(2\dot{x}_3 - 2\dot{x}_6 + y_6\dot{\phi}_3 - y_6\dot{\phi}_6\right)\dot{\phi}_6\xi_6^A\cos\phi_3 + \left(2\dot{y}_3 - 2\dot{y}_6 - x_6\dot{\phi}_3 + x_6\dot{\phi}_6\right)\dot{\phi}_6\xi_6^A\sin\phi_3 \\ 0 \\ \left(2\dot{x}_4 - 2\dot{x}_7 + y_7\dot{\phi}_4 - y_7\dot{\phi}_7\right)\dot{\phi}_7\xi_7^B\cos\phi_4 + \left(2\dot{y}_4 - 2\dot{y}_7 - x_7\dot{\phi}_4 + x_7\dot{\phi}_7\right)\dot{\phi}_7\xi_7^B\sin\phi_4 \\ 0 \\ 0 \\ 0 \\ 0 \\ \frac{\partial^2}{\partial t^2}d_1(t) \\ \frac{\partial^2}{\partial t^2}d_2(t) \\ \frac{\partial^2}{\partial t^2}d_3(t) \end{bmatrix} \quad (2.64)$$

The second partial derivatives of the driving constraints with respect to time are the accelerations of link

1, i.e.: $\dfrac{\partial^2}{\partial t^2}d_1(t) = \ddot{x}_1(t)$, $\dfrac{\partial^2}{\partial t^2}d_2(t) = \ddot{y}_1(t)$ and $\dfrac{\partial^2}{\partial t^2}d_3(t) = \ddot{\phi}_1(t)$. Again the calculation of these accelerations for a prescribed tool path will be explained in **Chapter 3**.

Substituting expressions (2.62) and (2.64) into expression (2.56) results in 24 algebraic equations, linear in terms of $\ddot{q}$, which can again be solved using the L-U factorization method.

2.6 Kinetic analysis

Kinetics is the study of motion and its relationship with the forces that produce the motion (see Figure 2.1). Using Newton's second law, the *equations of motion* of a continuous rigid body are derived in **Appendix A**. This Section deals with the application of the equations of motion to a general system of unconstrained bodies experiencing planar motion. The underlying theory is also applied to a system of constrained bodies experiencing planar motion with specific reference to the planar Gough-Stewart platform.

2.6.1 Planar equations of motion for a system of unconstrained bodies

The equations of motion for a single unconstrained body moving in the plane (see **Appendix A**) may be written in matrix form as

$$\begin{bmatrix} m & & \\ & m & \\ & & \mu \end{bmatrix}_i \begin{bmatrix} \ddot{x} \\ \ddot{y} \\ \ddot{\phi} \end{bmatrix}_i = \begin{bmatrix} f_{(x)} \\ f_{(y)} \\ n \end{bmatrix}_i \qquad (2.65)$$

where for notational simplicity the polar moment of inertia $j_{\zeta\zeta}$ is denoted by μ (see [65]). The subscript i in expression (2.65) indicates that these are the equations of motion of body i.

According to Nikravesh [65], expression (2.65) may also be written as

$$\mathbf{M}_i \ddot{\mathbf{q}}_i = \mathbf{g}_i \qquad (2.66)$$

where $\mathbf{M}_i = \text{diag}[m, m, \mu]_i$,

$\mathbf{q}_i = [x, y, \phi]_i^T$ and

$\mathbf{g}_i = [f_{(x)}, f_{(y)}, n]_i^T$.

Furthermore, for a *system* of b *unconstrained* bodies, expression (2.66) is repeated b times to give

$$\mathbf{M}\ddot{\mathbf{q}} = \mathbf{g} \qquad (2.67)$$

where $\mathbf{M} = \text{diag}[\mathbf{M}_1, \mathbf{M}_2, ..., \mathbf{M}_b]$,

$\mathbf{q} = [\mathbf{q}_1^T, \mathbf{q}_2^T, ..., \mathbf{q}_b^T]^T$ and

$\mathbf{g} = [\mathbf{g}_1^T, \mathbf{g}_2^T, ..., \mathbf{g}_b^T]^T$.

The system mass matrix $\mathbf{M}$ is a $n \times n$ constant diagonal matrix, and vectors $\mathbf{q}$, $\dot{\mathbf{q}}$, $\ddot{\mathbf{q}}$ and $\mathbf{g}$ are n vectors. Note that $n = 3b$, where n is the number of coordinates of the system of b bodies (see expression (2.3)).

2.6.2 Planar equations of motion for a system of constrained bodies.

If the system of bodies is interconnected by kinematic joints, it is referred to as a system of constrained bodies.

In general the system vector of coordinates for b constrained bodies is denoted by $\mathbf{q}$ (see expression (2.3)). Furthermore the kinematic joints in the system can be represented as m independent constraints $\mathbf{\Phi}(\mathbf{q}) = \mathbf{0}$ as given in expression (2.43). These m independent equations are normally nonlinear in terms of $\mathbf{q}$ (see expression (2.47)).

Each kinematic joint introduces reaction forces between connecting bodies. These reaction forces, which are also referred to as constraint forces, are denoted by vector $\mathbf{g}^{(c)}$:

$$\mathbf{g}^{(c)} = \left[\mathbf{g}_1^{(c)^{\mathrm{T}}}, \mathbf{g}_2^{(c)^{\mathrm{T}}}, \ldots, \mathbf{g}_b^{(c)^{\mathrm{T}}}\right]^{\mathrm{T}} \qquad\qquad (2.68)$$

where $\mathbf{g}_i^{(c)}$, $i = 1, 2, \ldots, b$ is the vector of the resultant of the joint reaction forces acting on body i. The sum of the constraint forces $\mathbf{g}^{(c)}$ and the external forces $\mathbf{g}$ provides the total forces acting on the system. Hence, expression (2.67) may be rewritten to read:

$$\mathbf{M\ddot{q}} = \mathbf{g} + \mathbf{g}^{(c)} \qquad\qquad (2.69)$$

For a system of constrained bodies experiencing planar motion, the reaction forces represented by expression (2.68) may be expressed in terms of the same coordinate system as the vector of coordinates $\mathbf{q}$.

Consider the planar example shown in Figure 2.12, where the reaction force $\vec{\mathbf{R}}$ is acting on the body i at the revolute joint P. The three coordinates of the body follow from expression (2.2), i.e., $\mathbf{q}_i = [\mathbf{r}^{\mathrm{T}}, \phi]_i^{\mathrm{T}} = [x, y, \phi]_i^{\mathrm{T}}$ and the local coordinate system is assumed to be centered at C_i the center of mass of body i (see Section 2.3). For convenience the subscript i is dropped in what follows.
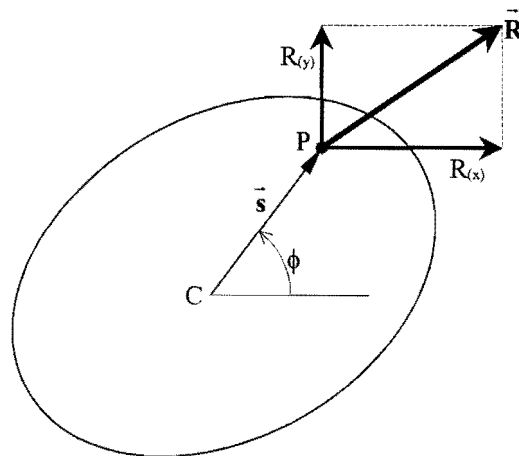
Figure 2.12: Planar body with reaction force applied at the revolute joint.
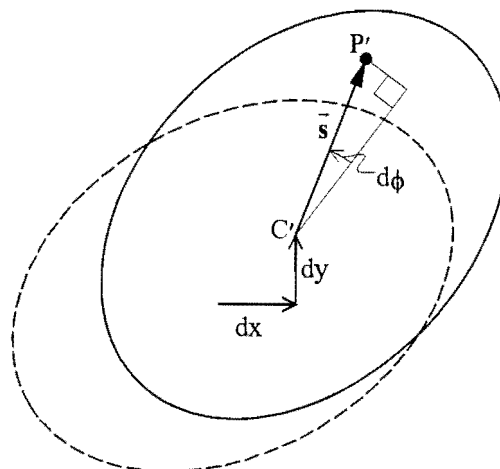
Figure 2.13: Virtual displacement of planar body.

If the body undergoes a virtual displacement such that C' is the new position of the center of mass, and P' is the new position of the revolute joint (see Figure 2.13), the corresponding work done by the reaction force $\vec{\mathbf{R}}$ is

$$
\begin{aligned}
dW &= R_{(x)}(dx - sd\phi\sin\phi) + R_{(y)}(dy + sd\phi\cos\phi) \\
&= R_{(x)}dx + R_{(y)}dy + (-R_{(x)}s\sin\phi + R_{(y)}s\cos\phi)d\phi \\
&= g_{(x)}dx + g_{(y)}dy + g_{(\phi)}d\phi
\end{aligned}
$$

Thus, the reaction force $\vec{\mathbf{R}}$ may be represented by a three-vector $\mathbf{g}$ with each component associated with a planar coordinate, i.e., $\mathbf{g} = [g_{(x)}, g_{(y)}, g_{(\phi)}]^T$. The three components of $\mathbf{g}$ are consistent with the three coordinates x, y and ϕ and are called the *generalized forces* associated with the chosen coordinates $\mathbf{q}$.

The introduction of generalized forces allows for the constraint force vector $\mathbf{g}^{(c)}$ to be expressed in terms of the constraint equations Φ given by expression (2.43). In particular expression (2.43) contains m independent constraint equations $\Phi(\mathbf{q}) = \mathbf{0}$. Furthermore, if the joints are assumed frictionless, the work done by the constraint forces in a virtual (infinitesimal) displacement $d\mathbf{q}$ is zero, i.e.,

$$
\mathbf{g}^{(c)^T}d\mathbf{q} = 0 \tag{2.70}
$$

The Taylor series expansion of expression (2.43) about $\mathbf{q}$ is

$$
\Phi(\mathbf{q} + d\mathbf{q}) = \Phi(\mathbf{q}) + \Phi_q d\mathbf{q} \tag{2.71}
$$

if the higher order terms in $d\mathbf{q}$ are ignored. Since the virtual displacement $d\mathbf{q}$ must be consistent with the constraints (expression (2.43)), it is required that

$$
\Phi(\mathbf{q} + d\mathbf{q}) = \mathbf{0} \tag{2.72}
$$

Substituting expressions (2.43) and (2.72) into expression (2.71), yields

$$
\Phi_q d\mathbf{q} = \mathbf{0} \tag{2.73}
$$

According to Nikravesh [65] the vector of n coordinates $\mathbf{q}$ may be partitioned into a set of m dependent coordinates $\mathbf{u}$ and a set of $n - m$ independent coordinates $\mathbf{v}$, i.e., $\mathbf{q} \equiv [\mathbf{u}^T, \mathbf{v}^T]^T$. This partitioning yields $d\mathbf{q} = [d\mathbf{u}^T, d\mathbf{v}^T]^T$, $\Phi_q = [\Phi_u, \Phi_v]$ and $\mathbf{g}^{(c)} = \left[\mathbf{g}_{(u)}^{(c)^T}, \mathbf{g}_{(v)}^{(c)^T}\right]^T$.

Expression (2.70) may therefore be written as

$$
\mathbf{g}_{(u)}^{(c)^T}d\mathbf{u} = -\mathbf{g}_{(v)}^{(c)^T}d\mathbf{v} \tag{2.74}
$$

and from expression (2.73) it follows that

$$
\Phi_u d\mathbf{u} = -\Phi_v d\mathbf{v} \tag{2.75}
$$

Appending these two expressions to each other gives

$$\begin{bmatrix} \mathbf{g}_{(u)}^{(c)\,T} \\ \mathbf{\Phi}_u \end{bmatrix} d\mathbf{u} = -\begin{bmatrix} \mathbf{g}_{(v)}^{(c)\,T} \\ \mathbf{\Phi}_v \end{bmatrix} d\mathbf{v} \qquad (2.76)$$

Since $\mathbf{\Phi}_u$ is an $m \times m$ matrix with m independent rows, $\mathbf{\Phi}_u$ is a basis in R^m, and $\mathbf{g}_{(u)}^{(c)\,T}$ may therefore be written as a linear combination of the m rows of $\mathbf{\Phi}_u$, i.e.,

$$\mathbf{g}_{(u)}^{(c)} = \mathbf{\Phi}_u^T \boldsymbol{\lambda} \qquad (2.77)$$

where $\boldsymbol{\lambda}$ is a m-vector of multipliers known as *LaGrange multipliers*.

Substitution of expression (2.77) into expression (2.74) yields

$$\boldsymbol{\lambda}^T \mathbf{\Phi}_u d\mathbf{u} = -\mathbf{g}_{(v)}^{(c)\,T} d\mathbf{v} \qquad (2.78)$$

and from expression (2.75) it follows that

$$-\boldsymbol{\lambda}^T \mathbf{\Phi}_v d\mathbf{v} = -\mathbf{g}_{(v)}^{(c)\,T} d\mathbf{v} \qquad (2.79)$$

Since vector $\mathbf{v}$ is independent, expression (2.79) must hold for an arbitrary virtual displacement $d\mathbf{v}$, which implies that

$$\mathbf{g}_{(v)}^{(c)} = \mathbf{\Phi}_v^T \boldsymbol{\lambda} \qquad (2.80)$$

Furthermore, appending expressions (2.77) and (2.80) yields

$$\begin{bmatrix} \mathbf{g}_{(u)}^{(c)} \\ \mathbf{g}_{(v)}^{(c)} \end{bmatrix} = \begin{bmatrix} \mathbf{\Phi}_u^T \\ \mathbf{\Phi}_v^T \end{bmatrix} \boldsymbol{\lambda} \qquad (2.81)$$

or simply

$$\mathbf{g}^{(c)} = \mathbf{\Phi}_q^T \boldsymbol{\lambda} \qquad (2.82)$$

Finally substituting expression (2.82) into expression (2.69) gives the planar equations of motion for a system of constrained bodies, i.e.:

$$\mathbf{M}\ddot{\mathbf{q}} - \mathbf{\Phi}_q^T \boldsymbol{\lambda} = \mathbf{g} \qquad (2.83)$$

Thus for a given vector of external forces $\mathbf{g}$, the *forward dynamic analysis* yields a unique solution for $\mathbf{q}$, $\dot{\mathbf{q}}$, $\ddot{\mathbf{q}}$ and $\boldsymbol{\lambda}$ when the constraint equations (2.43) are considered simultaneously with the differential equations of motion (2.83), and a proper set of initial conditions are specified.

2.6.3 Constraint reaction forces

The joint reaction forces given by expression (2.82) are studied here for the joints (kinematic pairs) of the planar Gough-Stewart platform.

2.6.3.1 Revolute joint

Consider the revolute joint connecting bodies 1 and 2 of the planar Gough-Stewart platform (see Figure 2.5). Figure 2.14 shows a schematic representation of the isolated revolute joint.
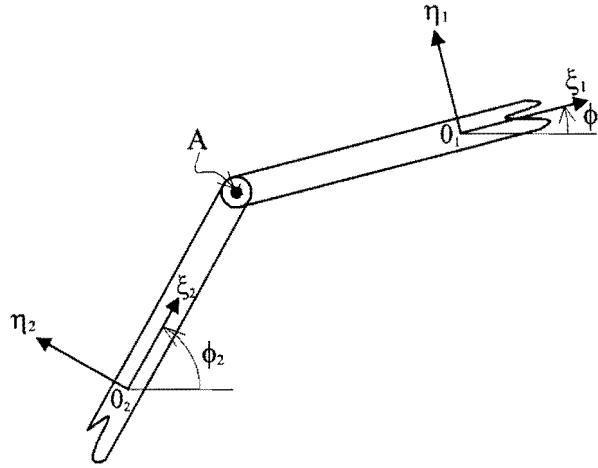
Figure 2.14: Revolute joint connecting bodies 1 and 2 of the planar Gough-Stewart platform.

The equations of motion of bodies 1 and 2 follow from expression (2.83), i.e.,

$$\mathbf{M}_1\ddot{\mathbf{q}}_1 - \mathbf{\Phi}_{q_1}^T\lambda = \mathbf{g}_1 \tag{2.84}$$

and

$$\mathbf{M}_2\ddot{\mathbf{q}}_2 - \mathbf{\Phi}_{q_2}^T\lambda = \mathbf{g}_2 \tag{2.85}$$

Using the applicable entries in the Jacobian matrix of the planar Gough-Stewart platform (see expression (2.62)), expression (2.84) may be written in expanded form:

$$\begin{bmatrix} m & & \\ & m & \\ & & \mu \end{bmatrix}_1 \begin{bmatrix} \ddot{x} \\ \ddot{y} \\ \ddot{\phi} \end{bmatrix}_1 - \begin{bmatrix} 1 & 0 \\ 0 & 1 \\ -\xi_1^A\sin\phi_1 & \xi_1^A\cos\phi_1 \end{bmatrix}\begin{bmatrix} \lambda_1 \\ \lambda_2 \end{bmatrix} = \begin{bmatrix} f_{(x)} \\ f_{(y)} \\ n \end{bmatrix}_1 \tag{2.86}$$

Expression (2.86) may be written as a set of three separate equations:

$$m_1\ddot{x}_1 = f_{(x)_1} + \lambda_1 \tag{2.87}$$

$$m_1\ddot{y}_1 = f_{(y)_1} + \lambda_2 \tag{2.88}$$

$$\mu_1\ddot{\phi}_1 = n_1 - (\xi_1^A\sin\phi_1)\lambda_1 + (\xi_1^A\cos\phi_1)\lambda_2 \tag{2.89}$$

Expression (2.87) indicates that besides the resultant external force $f_{(x)_1}$, another force λ_1 due to the constraints acts in the x-direction on body 1. Similarly, expression (2.88) indicates that besides external force $f_{(y)_1}$, another constraint force λ_2 acts in the y-direction on body 1. Figure 2.15 shows a free-body diagram of body 1, indicating constraint forces λ_1 and λ_2.
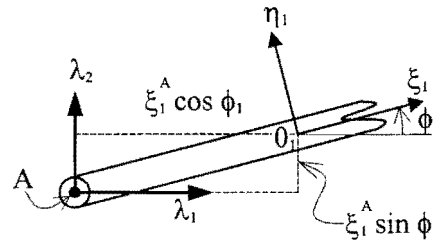
Figure 2.15: Free-body diagram of body 1 as part of the revolute joint with body 2.

The moment arm of λ_1 is $\xi_1^A \sin\phi_1$ with $\xi_1^A < 0$, which results in a positive moment $-(\xi_1^A \sin\phi_1)\lambda_1$ about 0_1 coinciding with the center of mass of body 1. Similarly, the moment arm of λ_2 is $\xi_1^A \cos\phi_1$ with $\xi_1^A < 0$, and therefore moment $(\xi_1^A \cos\phi_1)\lambda_2$ acts in the negative rotational direction.

Expression (2.85) may similarly be written in expanded form using the applicable entries in the Jacobian matrix (expression (2.62)):

$$\begin{bmatrix} m & & \\ & m & \\ & & \mu \end{bmatrix}_2 \begin{bmatrix} \ddot{x} \\ \ddot{y} \\ \ddot{\phi} \end{bmatrix}_2 - \begin{bmatrix} -1 & 0 \\ 0 & -1 \\ \xi_2^A \sin\phi_2 & -\xi_2^A \cos\phi_2 \end{bmatrix} \begin{bmatrix} \lambda_1 \\ \lambda_2 \end{bmatrix} = \begin{bmatrix} f_{(x)} \\ f_{(y)} \\ n \end{bmatrix}_2 \qquad (2.90)$$

or

$$m_2 \ddot{x}_2 = f_{(x)_2} - \lambda_1 \qquad (2.91)$$

$$m_2 \ddot{y}_2 = f_{(y)_2} - \lambda_2 \qquad (2.92)$$

$$\mu_2 \ddot{\phi}_2 = n_2 + (\xi_2^A \sin\phi_2)\lambda_1 - (\xi_2^A \cos\phi_2)\lambda_2 \qquad (2.93)$$

Expressions (2.91) and (2.92) indicate that the constraint forces λ_1 and λ_2 respectively act in the negative x and y-directions on body 2. The corresponding free-body diagram of body 2 is shown in Figure 2.16.
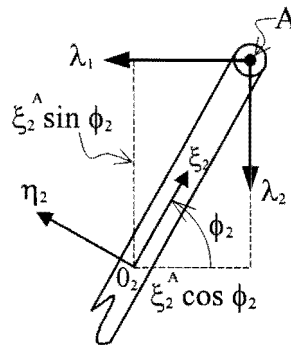
Figure 2.16: Free-body diagram of body 2 as part of the revolute joint with body 1.

From Figure 2.16 it follows that the moment arm of λ_1 is $\xi_2^A \sin\phi_2$ with $\xi_2^A > 0$, which yields a positive moment $(\xi_2^A \sin\phi_2)\lambda_1$ about 0_2 coinciding with the center of mass of body 2. Similarly, the moment arm of λ_2 is $\xi_2^A \cos\phi_2$ with $\xi_2^A > 0$, which gives a negative moment $-(\xi_2^A \cos\phi_2)\lambda_2$ about 0_2.

Note that the multipliers λ_1 and λ_2 can assume both positive and negative values. In any case, the reaction forces acting at the revolute joint on the connecting bodies are always equal in magnitude and mutually opposite in direction.

2.6.3.2 Translational joint

Consider the translational joint between bodies 2 and 5 of the planar Gough-Stewart platform. Figure 2.17 shows a schematic representation of the joint.
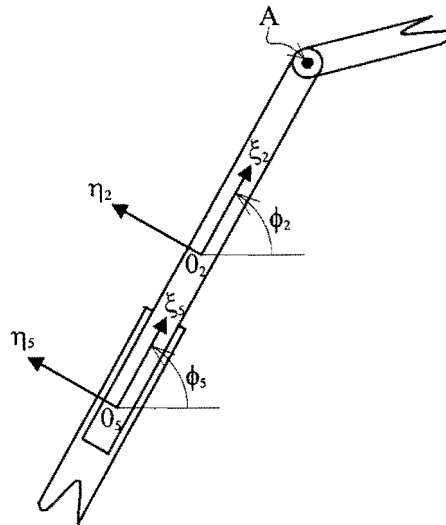
Figure 2.17: Translational joint between bodies 2 and 5 of the planar Gough-Stewart platform.

Following a similar argument as that outlined in Section 2.6.3.1, the equations of motion of body 2 may be written as:

$$\begin{bmatrix} m & & \\ & m & \\ & & \mu \end{bmatrix}_2 \begin{bmatrix} \ddot{x} \\ \ddot{y} \\ \ddot{\phi} \end{bmatrix}_2 - \begin{bmatrix} -\xi_2^A \sin\phi_2 & 0 \\ \xi_2^A \cos\phi_2 & 0 \\ (x_5 - x_2)\xi_2^A \cos\phi_2 + (y_5 - y_2)\xi_2^A \sin\phi_2 & -1 \end{bmatrix} \begin{bmatrix} \lambda_1 \\ \lambda_2 \end{bmatrix} = \begin{bmatrix} f_{(x)} \\ f_{(y)} \\ n \end{bmatrix}_2 \qquad (2.94)$$

or

$$m_2 \ddot{x}_2 = f_{(x)_2} - \xi_2^A \sin\phi_2\lambda_1 \qquad (2.95)$$

$$m_2 \ddot{y}_2 = f_{(y)_2} + \xi_2^A \cos\phi_2\lambda_1 \qquad (2.96)$$

$$\mu_2 \ddot{\phi}_2 = n_2 + (x_5 - x_2)\xi_2^A \cos\phi_2\lambda_1 + (y_5 - y_2)(\xi_2^A \sin\phi_2)\lambda_1 - \lambda_2 \qquad (2.97)$$

The free-body diagram of body 2 is shown in Figure 2.18. Nikravesh [65] explains that the force associated with λ_1 is the reaction force caused by the constraint equation which eliminates relative motion between bodies 2 and 5 in a direction perpendicular to the line of translation. It is therefore expected, as can easily be proved, that this reaction force ($\vec{k}_1$ in Figure 2.18) is perpendicular to the line of translation.

Figure 2.18: Free-body diagram of body 2 as part of the translational joint with body 5.

It follows from (2.97), and as shown in Figure 2.18, that the moment arm of the force $\xi_2^A \cos\phi_2\lambda_1$ about 0_2 is $(x_5 - x_2)$, and the moment arm of the force $-\xi_2^A \sin\phi_2\lambda_1$ is $(y_5 - y_2)$. For the orientation of body 2 shown in Figure 2.18, $(x_5 - x_2) < 0$ and $(y_5 - y_2) < 0$, from which it follows that both moments $(x_5 - x_2)\xi_2^A \cos\phi_2\lambda_1$ and $(y_5 - y_2)\xi_2^A \sin\phi_2\lambda_1$ are negative moments.

The contribution of the second constraint equation, which eliminates relative rotation between bodies 2 and 5, is a couple acting on body 2. Note that λ_2 may be a positive or negative quantity.

The equations of motion of body 5 are similarly given by

$$\begin{bmatrix} m & & \\ & m & \\ & & \mu \end{bmatrix}_5 \begin{bmatrix} \ddot{x} \\ \ddot{y} \\ \ddot{\phi} \end{bmatrix}_5 - \begin{bmatrix} \xi_2^A \sin\phi_2 & 0 \\ -\xi_2^A \cos\phi_2 & 0 \\ 0 & 1 \end{bmatrix} \begin{bmatrix} \lambda_1 \\ \lambda_2 \end{bmatrix} = \begin{bmatrix} f_{(x)} \\ f_{(y)} \\ n \end{bmatrix}_5 \tag{2.98}$$

or

$$m_5\ddot{x}_5 = f_{(x)_5} + \xi_2^A \sin\phi_2\lambda_1 \tag{2.99}$$

$$m_5\ddot{y}_5 = f_{(y)_5} - \xi_2^A \cos\phi_2\lambda_1 \tag{2.100}$$

$$\mu_5\ddot{\phi}_5 = n_5 - \lambda_2 \tag{2.101}$$

The corresponding free-body diagram of body 5 is shown in Figure 2.19. Note that $-\lambda_2$ is the only constraint moment acting on body 5.
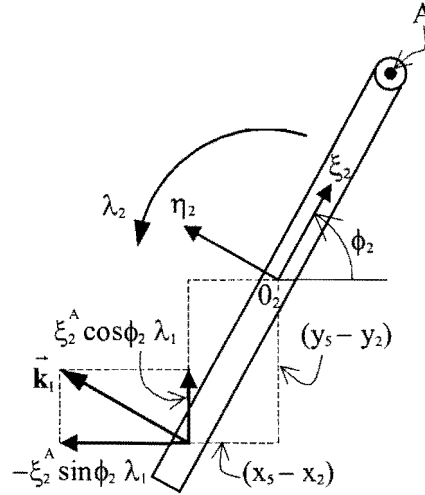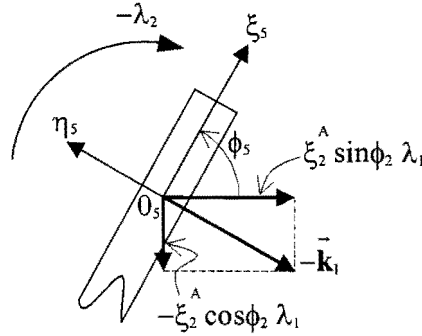

Figure 2.19: Free-body diagram of body 5 as part of the translational joint with body 2.

2.6.4 Vector of forces

The external force vector $\mathbf{g}$ in expression (2.83), contains all the external forces acting on the individual bodies of the system, i.e.,

$$\mathbf{g} = \begin{bmatrix} \mathbf{g}_1^T, \mathbf{g}_2^T, ..., \mathbf{g}_b^T \end{bmatrix}^T \tag{2.102}$$

To construct the vector $\mathbf{g}$, the external force vector for each body must be determined. For a typical body i, the external force vector $\mathbf{g}_i$ is

$$\mathbf{g}_i = [\mathbf{f}_{(x)}, \mathbf{f}_{(y)}, \mathbf{n}]_i^T \tag{2.103}$$

where $\mathbf{f}_{(x)i}$, $\mathbf{f}_{(y)i}$ and $\mathbf{n}_i$ are respectively the sums of all force components in the x and y directions and the sum of all the moments respectively.

In the remainder of this sub-section, the two types of external forces that act on the planar Gough-Stewart platform are discussed, and their contribution to $\mathbf{g}$ determined.

2.6.4.1 Gravity

The first external force acting on the moving bodies that make up the planar Gough-Stewart platform is *gravity*. In accordance with Nikravesh [65], the direction of gravity is chosen to be in the negative y-direction. If $\mathbf{w}_i$ is the weight of the body i, i.e., $\mathbf{w}_i = \mathbf{m}_i g$, then the contribution of this force to the vector of force of body i is:

$$\mathbf{g}_i^{(gravity)} = [0, -w, 0]_i^T \tag{2.104}$$

The first seven bodies of the planar Gough-Stewart platform in Figure 2.5, all have known weights contributing to the vector of external forces of each body, i.e., $\mathbf{g}_i^{(gravity)} = [0,-w,0]_i^T$, for $i = 1,2,...,7$. Since the eighth body is the fixed ground, a zero weight is allocated to it, and a zero contribution is made to the vector of external force of body 8.

2.6.4.2 Single force

The second type of external force that acts on the planar Gough-Stewart platform is what Nikravesh [65] refers to as a *single force*. This is due to the fact that the planar Gough-Stewart platform is to be used as a machining center. For both machining centers with either a fixed workpiece or a fixed cutting tool, there is a contact force between the cutting tool and the workpiece. This contact force may be modeled as a single force.

Consider the general case, where a single force $\vec{\mathbf{f}}_i$ acts with a known direction at point P_i on body i as shown in Figure 2.20.

Figure 2.20: A body acted upon by a constant force (after [65]).

The force $\vec{\mathbf{f}}_i$ in the above figure has components $f_{(x)i}$ and $f_{(y)i}$. If the local coordinates of P_i are known as $\mathbf{s}_i'^P = [\xi^P, \eta^P]_i^T$, then the global coordinates of point P_i are given by $\mathbf{s}_i^P = \mathbf{A}_i \mathbf{s}_i'^P$ (see expression (2.1)). The moment of $\vec{\mathbf{f}}_i$ about 0_i, which coincides with the center of mass of body i is

$$\begin{aligned}
n_i &= (\tilde{\mathbf{s}}_i^P \mathbf{f}_i)_{(z)} \\
&= -s_{(y)i}^P f_{(x)i} + s_{(x)i}^P f_{(y)i} \\
&= -(\xi_i^P \sin\phi_i + \eta_i^P \cos\phi_i)f_{(x)i} + (\xi_i^P \cos\phi_i - \eta_i^P \sin\phi_i)f_{(y)i}
\end{aligned} \qquad (2.105)$$

Note that $\tilde{\mathbf{s}}_i^P$ represents the expansion of $\mathbf{s}_i^P$ into a skew-symmetric matrix (see expression (A.18) and [65]).

The contribution of this force to the vector of forces of body i is

$$\mathbf{g}_i^{(single\ f)} = [f_{(x)}, f_{(y)}, n]_i^T \tag{2.106}$$

In particular, the contact force between the cutting tool and the workpiece may also be referred to as a *cutting force*. For both the fixed workpiece and fixed tool cases of the planar Gough-Stewart platform machining center, this cutting force contributes to the vector of forces of body 1 (the moving platform). The contribution of the cutting force to the vector of forces of body 1 is subsequently labeled as $\mathbf{g}_1^{(cutting\ f)}$.

2.6.4.2.1 Fixed workpiece

The same assumptions as listed under Section 2.4.1, are made here, namely that at any given time instant it is assumed that the following are known:

1. the global position of the cutting tool tip (P in Figure 2.8) on the prescribed tool path, and

2. the angle β between the platform mounted tool and the normal to the tool path at the point of contact (see Figure 2.8) and measured positive in the CCW direction.

The free-body diagram of a typical fixed workpiece scenario is depicted in Figure 2.21. Since the cutting force is applied to body 1 it is designated by $\vec{f}_1^{cut}$.
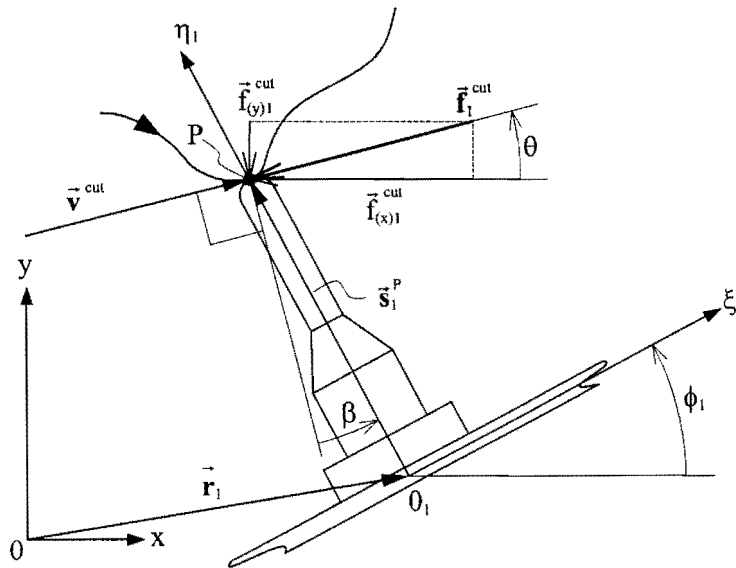
Figure 2.21: Free-body diagram for the fixed workpiece scenario.

The cutting force $\vec{f}_1^{cut}$ is collinear with the tangent to the prescribed tool path at the point of contact, and it is modeled as a "resistance" force. This implies that the cutting force $\vec{f}_1^{cut}$ is *oppositely* directed to the direction of travel, with magnitude assumed to be linearly dependent on the magnitude of tangential speed with which the prescribed tool path is traced $\left| \vec{v}^{cut} \right|$.

It is assumed here that the vector $\vec{v}^{cut}$ has a known magnitude and direction, which are calculated as will be described in **Chapter 3** (see also Section 2.5 expression (2.63)). With the magnitude of the cutting velocity $\left|\vec{v}^{cut}\right|$ known, the magnitude of the cutting force is given by:

$$\left|\vec{f}_1^{cut}\right| = \left|\vec{v}^{cut}\right| C_{cut} \tag{2.107}$$

where C_{cut} is a "cutting force constant" expressed in $\dfrac{Ns}{m}$ as a positive quantity corresponding to the assumption made.

Vector $\vec{f}_1^{cut}$ is represented in the global reference frame by $\mathbf{f}_1^{cut}$, i.e., $\vec{f}_1^{cut} : \mathbf{f}_1^{cut} = [f_{(x)}^{cut}, f_{(y)}^{cut}]_1^T$. Similarly, vector $\vec{v}^{cut}$ is represented in the global reference frame by $\mathbf{v}^{cut}$. Since the gradient angle θ is known at the point of contact, i.e., $\tan\theta = \dfrac{dy}{dx}$ (see expression (2.33)), the components of the cutting force as shown in Figure 2.21 are given by

$$f_{(x)1}^{cut} = -\left|\mathbf{f}_1^{cut}\right|\cos\theta \tag{2.108}$$

and

$$f_{(y)1}^{cut} = -\left|\mathbf{f}_1^{cut}\right|\sin\theta \tag{2.109}$$

The point of contact between the cutting tool and the workpiece is given by $s_1^{\prime P} = \begin{bmatrix} 0 \\ \eta^P \end{bmatrix}_1$ as explained in Section 2.4.1. Hence the moment of $\vec{f}_1^{cut}$ about the center of mass of body 1, n_1^{cut}, may be determined using expression (2.105), i.e.,

$$n_1^{cut} = -(\eta_1^P \cos\phi_1)f_{(x)1}^{cut} - (\eta_1^P \sin\phi_1)f_{(y)1}^{cut} \tag{2.110}$$

The validity of expression (2.110) may be verified by considering the situation depicted in the free-body diagram (Figure 2.21). It is clear that the x-component of the cutting force $f_{(x)1}^{cut}$ in Figure 2.21 is *negative*. The moment arm of $f_{(x)1}^{cut}$ is $\eta_1^P \cos\phi_1$. Thus, the first term in expression (2.110), $-(\eta_1^P \cos\phi_1)f_{(x)1}^{cut}$, yields a *positive* moment.

Similarly, the y-component of the cutting force $f_{(y)1}^{cut}$ in Figure 2.21 is *negative*, and the moment arm of $f_{(y)1}^{cut}$ is $\eta_1^P \sin\phi_1$. The second term of expression (2.110), $-(\eta_1^P \sin\phi_1)f_{(y)1}^{cut}$, therefore also yields a *positive* moment in expression (2.110).

For the fixed workpiece scenario, the contribution of the cutting force to the force vector of body 1, is

$$\mathbf{g}_1^{(\text{cutting f})} = [f_{(x)}^{cut}, f_{(y)}^{cut}, n^{cut}]_1^T \qquad (2.111)$$

where $f_{(x)1}^{cut}$ is given by expressions (2.108), $f_{(y)1}^{cut}$ is given by expressions (2.109), and n_1^{cut} is given by expression (2.110).

2.6.4.2.2 Fixed cutting tool

The same assumptions as listed in Section 2.4.2 apply here, i.e., at any time instant the following are assumed to be known:

1. the local position of the cutting tool tip (P in Figure 2.10) on the prescribed tool path, and

2. the angle β (measured positive CCW), from the normal to the tool path at the point of contact, to the vertical axis of the fixed cutting tool (see Figure 2.10).

The free-body diagram of a typical fixed cutting tool scenario is depicted in Figure 2.22. As in the case of the fixed workpiece, the cutting force is again applied to body 1 and designated by $\vec{f}_1^{cut}$.
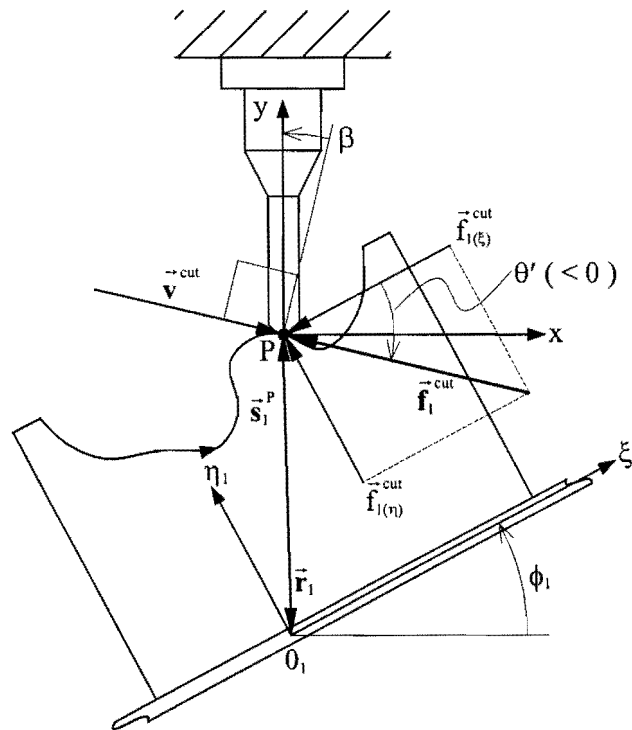
Figure 2.22: Free-body diagram for a fixed cutting tool scenario.

The modeling of the cutting force associated with the fixed cutting tool is done in a similar way to that done for the fixed workpiece.

In particular, the cutting force $\vec{f}_1^{cut}$ shown in Figure 2.22 is collinear with the tangent to the prescribed tool path at the point of contact. The tool path is specified in terms of the local $0_1 \xi_1 \eta_1$ -coordinate

system. Furthermore, the direction of the cutting velocity $\vec{\mathbf{v}}^{cut}$ is also specified in terms of the local $0_1\xi_1\eta_1$-coordinate system ($\vec{\mathbf{v}}^{cut} : \mathbf{v}'^{cut} = [v_{(\xi)}^{cut}, v_{(\eta)}^{cut}]^T$) and the magnitude of the cutting velocity $\left|\mathbf{v}'^{cut}\right|$ is also assumed to be known (see **Chapter 3**).

Since the magnitude of the cutting force is again assumed to be linearly dependent on the magnitude of cutting velocity, expression (2.107) remains valid here, and the magnitude is therefore given by $\left|\vec{\mathbf{f}}_1^{cut}\right| = \left|\vec{\mathbf{v}}^{cut}\right| C_{cut}$.

The gradient angle of the prescribed tool path is known in terms of the local coordinates, $\tan\theta' = \dfrac{d\eta_1}{d\xi_1}$ (see expression (2.37)), hence the cutting force $\vec{\mathbf{f}}_1^{cut}$ may be represented in the local $0_1\xi_1\eta_1$- coordinate system by $\vec{\mathbf{f}}_1^{cut} : \mathbf{f}_1'^{cut} = [f_{(\xi)}^{cut}, f_{(\eta)}^{cut}]_1^T$. The components of $\mathbf{f}_1'^{cut}$ are given by (see Figure 2.22)

$$f_{(\xi)1}^{cut} = -\left|\mathbf{f}_1'^{cut}\right|\cos\theta' \tag{2.112}$$

and

$$f_{(\eta)1}^{cut} = -\left|\mathbf{f}_1'^{cut}\right|\sin\theta' \tag{2.113}$$

The x- and y- components of the global cutting force representation $\vec{\mathbf{f}}_1^{cut} : \mathbf{f}_1^{cut} = [f_{(x)}^{cut}, f_{(y)}^{cut}]_1^T$ may be determined from the transformation given by expression (2.1):

$$f_{(x)1}^{cut} = f_{(\xi)1}^{cut}\cos\phi_1 - f_{(\eta)1}^{cut}\sin\phi_1 \tag{2.114}$$

and

$$f_{(y)1}^{cut} = f_{(\xi)1}^{cut}\sin\phi_1 + f_{(\eta)1}^{cut}\cos\phi_1 \tag{2.115}$$

or equivalently as

$$\mathbf{f}_1^{cut} = \mathbf{A}_1\mathbf{f}_1'^{cut} \text{ with } \mathbf{A}_1 = \begin{bmatrix} \cos\phi_1 & -\sin\phi_1 \\ \sin\phi_1 & \cos\phi_1 \end{bmatrix}$$

With the global components of the cutting force known, the moment of $\vec{\mathbf{f}}_1^{cut}$ about the center of mass of body 1 may be determined using expression (2.105). Note that this moment n_1^{cut} may also be determined using the local components of the cutting force, i.e.

$$\begin{aligned} n_1^{cut} &= (\tilde{\mathbf{s}}_1'^P \mathbf{f}_1'^{cut})_{(z)} \\ &= -\eta_1^P f_{(\xi)1}^{cut} + \xi_1^P f_{(\eta)1}^{cut} \end{aligned} \tag{2.116}$$

The validity of expression (2.116) is borne out by inspection of the free-body diagram depicted in Figure 2.22, from which it follows that the moment arm of $f_{(\xi)1}^{cut}$ is η_1^P. Since the ξ-component of the cutting

force in Figure 2.22 is directed in the negative ξ-direction, the term $-\eta_1^P f_{(\xi)1}^{cut}$ in expression (2.116) results in a positive moment. Similarly, the moment arm of $f_{(\eta)1}^{cut}$ is ξ_1^P, and since the η-component of the cutting force in Figure 2.22 is in the positive η-direction, the term $\xi_1^P f_{(\eta)1}^{cut}$ yields a positive moment.

For the fixed cutting tool scenario, the contribution of the cutting force to the external force vector of body 1 is:

$$\mathbf{g}_1^{(cutting\ f)} = [f_{(x)}^{cut}, f_{(y)}^{cut}, n^{cut}]_1^T \tag{2.117}$$

where $f_{(x)1}^{cut}$ is given by expression (2.114), $f_{(y)1}^{cut}$ is given by expression (2.115) and n_1^{cut} is given by expression (2.116).

2.6.5 Inverse dynamic analysis

If the forces acting on a mechanical system are known, then the *equations of motion* can be solved to obtain the motion of the system [65]. This process is known as the *forward dynamic analysis*. In some problems, a specified motion for a mechanical system is sought and the objective is to determine the forces that must act on the system to produce such a motion. This process is usually referred to as *inverse dynamic* or *kinetostatic analysis*.

Haug [66] explains that inverse dynamic analysis is a hybrid form of kinematic and dynamic analysis in which the time history of positions or relative positions of one or more bodies in the system is prescribed, leading to complete determination of position, velocity, and acceleration of the system from the equations of kinematics. The equations of motion of the system are then solved, with known position, velocity, and acceleration, as algebraic equations to determine the forces that are required to generate the prescribed motion.

In general, for a system of constrained bodies with n coordinates and m independent constraint equations, the inverse dynamic analysis therefore requires k driving constraints of the form $\mathbf{\Phi}^{(d)} \equiv \mathbf{\Phi}(\mathbf{q}, t) = \mathbf{0}$ (see expression (2.44)) to be specified. The number of driving constraints to be specified is equal to the number of degrees of freedom of the system, i.e. $k = n - m$ (see expression (2.26)).

The three driving constraints of the planar Gough-Stewart platform under consideration have already been dealt with in Section 2.4. These constraints uniquely define the motion of body 1 (the moving platform) of the planar Gough-Stewart platform along a prescribed path.

Section 2.5 shows how the inverse kinematic analysis of the planar Gough-Stewart platform is done using the method of appended driving constraints. The inverse kinematic analysis yields the positions $\mathbf{q}$, velocities $\dot{\mathbf{q}}$ and accelerations $\ddot{\mathbf{q}}$ at each time instant as the prescribed path is traced.

The objective of this sub-section is to determine the three actuator forces required to move the moving platform along the prescribed path. For this purpose the equations of motion of a system of constrained bodies (expression (2.83)) are rewritten to include the unknown forces, i.e.,

$$\mathbf{M}\ddot{\mathbf{q}} - \mathbf{\Phi}_q^T \lambda = \mathbf{g}^{(k)} + \mathbf{g}^{(u)} \qquad (2.118)$$

where $\mathbf{g}^{(k)}$ is the vector of *known* forces (see expression (2.102)), and $\mathbf{g}^{(u)}$ is the vector of *unknown* forces. Expression (2.118) may be rewritten as

$$\mathbf{M}\ddot{\mathbf{q}} - \mathbf{\Phi}_q^T \lambda - \mathbf{g}^{(u)} = \mathbf{g}^{(k)} \qquad (2.119)$$

The unknown actuator forces are designated by $\vec{f}_1$, $\vec{f}_2$ and $\vec{f}_3$, and respectively act on bodies 2, 3 and 4 as shown in Figure 2.23. By Newton's third law, for each force there is an equal and opposite reaction force. Hence, reaction forces $-\vec{f}_1$, $-\vec{f}_2$ and $-\vec{f}_3$, respectively act on bodies 5, 6 and 7 and are also shown in the schematic Figure 2.23.

In particular, the lines of action of forces $\vec{f}_1$ and $-\vec{f}_1$ coincide with the line of translation of the translational joint between bodies 2 and 5. Similarly, the lines of action of forces $\vec{f}_2$ and $-\vec{f}_2$ coincide with the common line of translation of the translational joint between bodies 3 and 6, and the lines of action of forces $\vec{f}_3$ and $-\vec{f}_3$ coincide with the common line of translation of bodies 4 and 7.
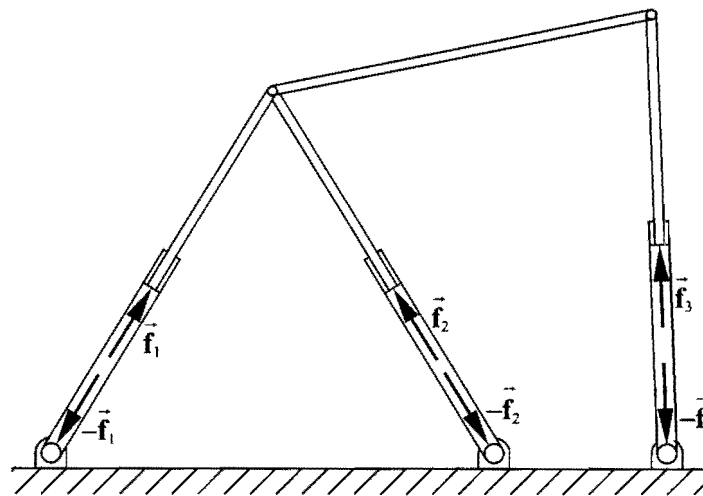
Figure 2.23: Unknown actuator forces of the planar Gough-Stewart platform.

Figure 2.24 shows the free-body diagram of body 2 with the unknown actuator force $\vec{f}_1$ applied to the body, as well as the constraint force $\vec{k}_1$ and constraint moment λ_2 as a result of the translational coupling between bodies 2 and 5.

Figure 2.24: Free-body diagram of body 2 with the applied unknown actuator force $\vec{f}_1$.

From expression (2.119) it follows that the equations of motion of body 2 are given by:

$$\begin{bmatrix} m & & \\ & m & \\ & & \mu \end{bmatrix}_2 \begin{bmatrix} \ddot{x} \\ \ddot{y} \\ \ddot{\phi} \end{bmatrix}_2 - \begin{bmatrix} -\xi_2^A \sin\phi_2 & 0 \\ \xi_2^A \cos\phi_2 & 0 \\ \left\{ \begin{matrix} (x_5-x_2)\xi_2^A \cos\phi_2 \\ +(y_5-y_2)\xi_2^A \sin\phi_2 \end{matrix} \right\} & -1 \end{bmatrix} \begin{bmatrix} \lambda_1 \\ \lambda_2 \end{bmatrix} - \begin{bmatrix} f_1 \cos\phi_2 \\ f_1 \sin\phi_2 \\ 0 \end{bmatrix} = \begin{bmatrix} f_{(x)} \\ f_{(y)} \\ n \end{bmatrix}_2 \qquad (2.120)$$

where $f_1 > 0$ indicates that force $\vec{f}_1$ is a "push-force" as chosen in Figure 2.24. Should the solution of expression (2.120) yield that $f_1 < 0$, then force $\vec{f}_1$ actually is a "pull-force" acting in the opposite direction. Also note that actuator force $\vec{f}_1$ does not cause a couple about the center of mass of body 2.

Expression (2.120) may also be written as

$$\begin{bmatrix} m & & \\ & m & \\ & & \mu \end{bmatrix}_2 \begin{bmatrix} \ddot{x} \\ \ddot{y} \\ \ddot{\phi} \end{bmatrix}_2 - \begin{bmatrix} -\xi_2^A \sin\phi_2 & 0 & \cos\phi_2 \\ \xi_2^A \cos\phi_2 & 0 & \sin\phi_2 \\ \left\{ \begin{matrix} (x_5-x_2)\xi_2^A \cos\phi_2 \\ +(y_5-y_2)\xi_2^A \sin\phi_2 \end{matrix} \right\} & -1 & 0 \end{bmatrix} \begin{bmatrix} \lambda_1 \\ \lambda_2 \\ f_1 \end{bmatrix} = \begin{bmatrix} f_{(x)} \\ f_{(y)} \\ n \end{bmatrix}_2 \qquad (2.121)$$

With regard to the reaction force $-\vec{f}_1$, Figure 2.25 shows the free-body diagram of body 5 with the unknown reaction force $-\vec{f}_1$ applied to the body, as well as the constraint force $-\vec{k}_1$ and constraint moment $-\lambda_2$ as a result of the translational coupling between bodies 2 and 5.
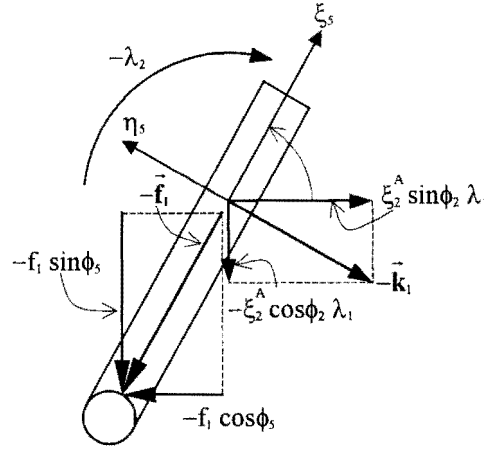
Figure 2.25: Free-body diagram of body 5 with the applied unknown reaction force $-\vec{f}_1$.

From expression (2.119) it follows that the equations of motion of body 5 are given by:

$$\begin{bmatrix} m & & \\ & m & \\ & & \mu \end{bmatrix}_5 \begin{bmatrix} \ddot{x} \\ \ddot{y} \\ \ddot{\phi} \end{bmatrix}_5 - \begin{bmatrix} \xi_2^A \sin\phi_2 & 0 \\ -\xi_2^A \cos\phi_2 & 0 \\ 0 & 1 \end{bmatrix} \begin{bmatrix} \lambda_1 \\ \lambda_2 \end{bmatrix} - \begin{bmatrix} -f_1 \cos\phi_2 \\ -f_1 \sin\phi_2 \\ 0 \end{bmatrix} = \begin{bmatrix} f_{(x)} \\ f_{(y)} \\ n \end{bmatrix}_5 \qquad (2.122)$$

where $f_1 < 0$ indicates that the reaction force $-\vec{f}_1$ is a "push reaction force" as chosen in Figure 2.25. Should the solution of expression (2.122) yield that $f_1 > 0$, the associated reaction force $-\vec{f}_1$ actually is a "pull reaction force" acting in the opposite direction. Note that there is no couple about the center of mass of body 5.

Expression (2.120) may also be written as

$$\begin{bmatrix} m & & \\ & m & \\ & & \mu \end{bmatrix}_5 \begin{bmatrix} \ddot{x} \\ \ddot{y} \\ \ddot{\phi} \end{bmatrix}_5 - \begin{bmatrix} \xi_2^A \sin\phi_2 & 0 & -\cos\phi_2 \\ -\xi_2^A \cos\phi_2 & 0 & -\sin\phi_2 \\ 0 & 1 & 0 \end{bmatrix} \begin{bmatrix} \lambda_1 \\ \lambda_2 \\ f_1 \end{bmatrix} = \begin{bmatrix} f_{(x)} \\ f_{(y)} \\ n \end{bmatrix}_5 \qquad (2.123)$$

Similar expressions are also obtained for bodies 3 and 6, as well as bodies 4 and 7. Hence, the equations of motion of the total planar Gough-Stewart platform system may be written as:

$$\mathbf{M}\ddot{\mathbf{q}} - \begin{bmatrix} \mathbf{\Phi}_q^T & \mathbf{B} \end{bmatrix} \begin{bmatrix} \lambda \\ \mathbf{ff} \end{bmatrix} = \mathbf{g}^{(k)} \qquad (2.124)$$

where $\mathbf{M}$ is a constant diagonal matrix, i.e. $\mathbf{M} = \text{diag}[m_1, m_1, \mu_1, m_2, m_2, \mu_2, ..., m_8, m_8, \mu_8]$,

$\ddot{\mathbf{q}}$ is the acceleration vector $\ddot{\mathbf{q}} = [\ddot{x}_1, \ddot{y}_1, \ddot{\phi}_1, \ddot{x}_2, \ddot{y}_2, \ddot{\phi}_2, ..., \ddot{x}_8, \ddot{y}_8, \ddot{\phi}_8]^T$,

$\mathbf{\Phi}_q$ consist of the first 21 rows of the Jacobian matrix $\mathbf{J}$(see expression (2.62)),

B is the following 24×3 matrix:

$$\mathbf{B} = \begin{bmatrix} 0 & 0 & 0 & \cos\phi_2 & \sin\phi_2 & 0 & 0 & 0 & 0 & 0 & 0 & 0 & -\cos\phi_5 & -\sin\phi_5 & 0 & 0 & 0 & 0 & 0 & 0 & 0 & 0 & 0 \\ 0 & 0 & 0 & 0 & 0 & 0 & \cos\phi_3 & \sin\phi_3 & 0 & 0 & 0 & 0 & 0 & 0 & 0 & -\cos\phi_6 & -\sin\phi_6 & 0 & 0 & 0 & 0 & 0 & 0 \\ 0 & 0 & 0 & 0 & 0 & 0 & 0 & 0 & \cos\phi_4 & \sin\phi_4 & 0 & 0 & 0 & 0 & 0 & 0 & 0 & -\cos\phi_7 & -\sin\phi_7 & 0 & 0 & 0 & 0 \end{bmatrix}^T ,$$

$\boldsymbol{\lambda}$ is a 21-vector containing the LaGrange multipliers, i.e., $\boldsymbol{\lambda} = [\lambda_1, \lambda_2, \lambda_3, ..., \lambda_{21}]^T$,

ff is the vector containing the magnitudes of the unknown actuator forces $\mathbf{ff} = [f_1 \quad f_2 \quad f_3]^T$ using the positive sign convention chosen in Figure 2.24, and

$\mathbf{g}^{(k)}$ is the vector of known external forces given acting on the planar Gough-Stewart platform

$$\mathbf{g}^{(k)} = \left[\left(\mathbf{g}_1^{(gravity)} + \mathbf{g}_1^{(cutting\ f)} \right)^T , \mathbf{g}_2^{(gravity)T} , \mathbf{g}_3^{(gravity)T} , \mathbf{g}_4^{(gravity)T} , \mathbf{g}_5^{(gravity)T} , \mathbf{g}_6^{(gravity)T} , \mathbf{g}_7^{(gravity)T} , 0, 0, 0 \right]^T$$

The cutting force $\mathbf{g}_1^{(cutting\ f)}$ is either given by expression (2.111) or expression (2.117) depending on the particular machining scenario, and finally expression (2.124) may be solved using a linear solver as explained in Section 2.5, to find the 24-vector $\begin{bmatrix} \boldsymbol{\lambda} \\ \mathbf{ff} \end{bmatrix}$.

2.7 Verification of special purpose program

In this section, the special-purpose program for analyzing the planar Gough-Stewart platform machining center is, tested and verified.

2.7.1 Jacobian matrix verification

The Jacobian matrix derived for the planar Gough-Stewart platform (expression (2.62)), is of importance, since it is used in both the inverse kinematic analysis of the mechanism and the inverse dynamic analysis. In order to verify the correctness of the Jacobian matrix constructed here, and to be used in the special purpose program, the general purpose **Kinematic Analysis Program (KAP)** developed by Nikravesh [65] is applied to do the inverse kinematic analysis of a specific planar Gough-Stewart platform following the simple test trajectory shown in Figure 2.26.
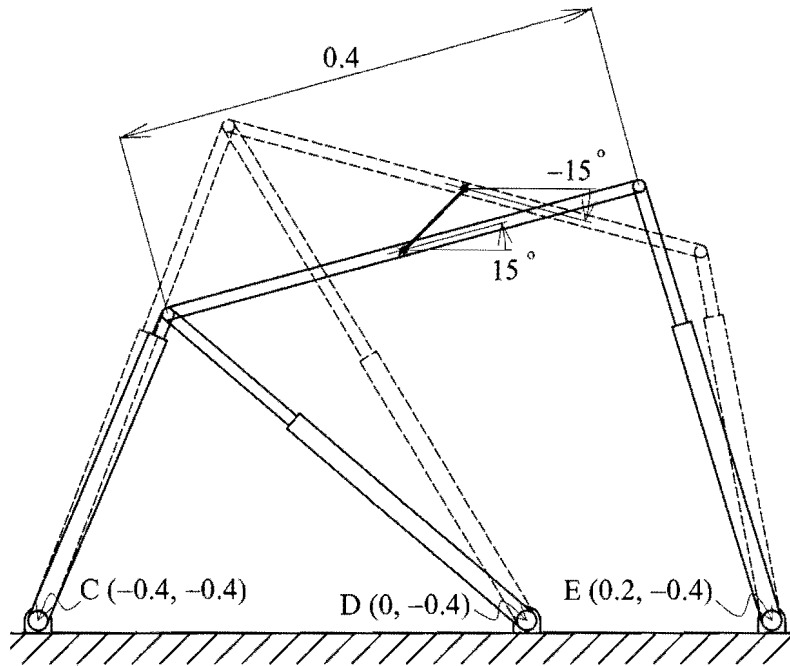
Figure 2.26: Straight line motion.

The length of the moving platform is chosen as 0.4 m, and the coordinates of the lower rotational joints C, D and E are as indicated in Figure 2.26.

Three independent driving constraints of the form given by expressions (2.27) - (2.29) prescribe the motion of the planar Gough-Stewart platform. In particular, for the simple straight line trajectory shown in Figure 2.26, expressions (2.27), (2.28) and (2.29) are respectively:

$$\Phi^{(d-1,1)} \equiv x_1 + 0.1 - 0.05t^2 = 0 \tag{2.125}$$

$$\Phi^{(d-2,1)} \equiv y_1 + 0.1 - 0.05t^2 = 0 \tag{2.126}$$

$$\Phi^{(d-3,1)} \equiv \phi_1 - \frac{\pi}{12} + \frac{\pi}{6}t^2 = 0 \tag{2.127}$$

Driving constraints (2.125) and (2.126) control the displacement of the center of the moving platform (body 1 in Figure 2.5) in the x-y plane along a straight line from $(-0.1, -0.1)$ at $t = 0$, to $(-0.05, -0.05)$ at $t = 1\,\text{s}$. Driving constraint (2.127) controls the rotation of the moving platform from its initial orientation $\phi_1 = 15°$ at $t = 0$, to its final orientation $\phi_1 = -15°$ at $t = 1\,\text{s}$.

The results obtained by KAP [65] for the velocities and accelerations of the seven moving bodies are in exact agreement with the results obtained using expressions (2.51) and (2.56), indicating that the Jacobian matrix of the planar Gough-Stewart platform constructed here (expression (2.62)) is correct.

Furthermore, the analytical solution of the positions and orientations of the 7 bodies obtained from expressions (2.57) - (2.61) is also in exact agreement with the iterative solution obtained using KAP.

2.7.2 Inverse dynamic analysis verification

The objective of this sub-section is to verify the methodology for determining the unknown actuator forces as explained in Section 2.6.5.

The verification of expression (2.124) is done noting that it may also be used to determine the *static* balance forces required to support the planar Gough-Stewart platform in static equilibrium. It follows that with the planar Gough-Stewart platform in static equilibrium, $\ddot{\mathbf{q}} = \mathbf{0}$, and therefore expression (2.124) reduces to:

$$-\begin{bmatrix} \boldsymbol{\Phi}_{\mathbf{q}}^{\mathrm{T}} & \mathbf{B} \end{bmatrix} \begin{bmatrix} \boldsymbol{\lambda} \\ \mathbf{ff} \end{bmatrix} = \mathbf{g}^{(k)} \qquad (2.128)$$

As explained in Sections 2.4 and 2.5, by prescribing the three driving constraints (expressions (2.27) - (2.29)) at any specific time instant, the Jacobian matrix given by expression (2.62) is uniquely defined. Therefore for any given stationary platform configuration, equation (2.128) may be solved for the vector $\begin{bmatrix} \boldsymbol{\lambda} \\ \mathbf{ff} \end{bmatrix}$ using a linear solver.

In expression (2.128):

$\boldsymbol{\Phi}_{\mathbf{q}}$ consist of the first 21 rows of the Jacobian matrix $\mathbf{J}$(see expression (2.62)),

$$\mathbf{B} = \begin{bmatrix} 0 & 0 & 0 & \cos\phi_2 & \sin\phi_2 & 0 & 0 & 0 & 0 & 0 & 0 & 0 & -\cos\phi_5 & -\sin\phi_5 & 0 & 0 & 0 & 0 & 0 & 0 & 0 & 0 & 0 \\ 0 & 0 & 0 & 0 & 0 & 0 & \cos\phi_3 & \sin\phi_3 & 0 & 0 & 0 & 0 & 0 & 0 & 0 & -\cos\phi_6 & -\sin\phi_6 & 0 & 0 & 0 & 0 & 0 & 0 \\ 0 & 0 & 0 & 0 & 0 & 0 & 0 & 0 & 0 & \cos\phi_4 & \sin\phi_4 & 0 & 0 & 0 & 0 & 0 & 0 & -\cos\phi_7 & -\sin\phi_7 & 0 & 0 & 0 & 0 \end{bmatrix}^{\mathrm{T}},$$

$\boldsymbol{\lambda}$ is a 21-vector containing the LaGrange multipliers, i.e., $\boldsymbol{\lambda} = [\lambda_1, \lambda_2, \lambda_3, ..., \lambda_{21}]^{\mathrm{T}}$, and

$$\mathbf{g}^{(k)} = \begin{bmatrix} \mathbf{g}_1^{(k)\mathrm{T}}, \mathbf{g}_2^{(k)\mathrm{T}}, ..., \mathbf{g}_8^{(k)\mathrm{T}} \end{bmatrix}^{\mathrm{T}}.$$

Consider the simple test example shown in Figure 2.27, where the vector of external forces is reduced to

$$\mathbf{g}^{(k)} = [1600, -440, 250, 0, 0, 0, ..., 0]^{\mathrm{T}}.$$
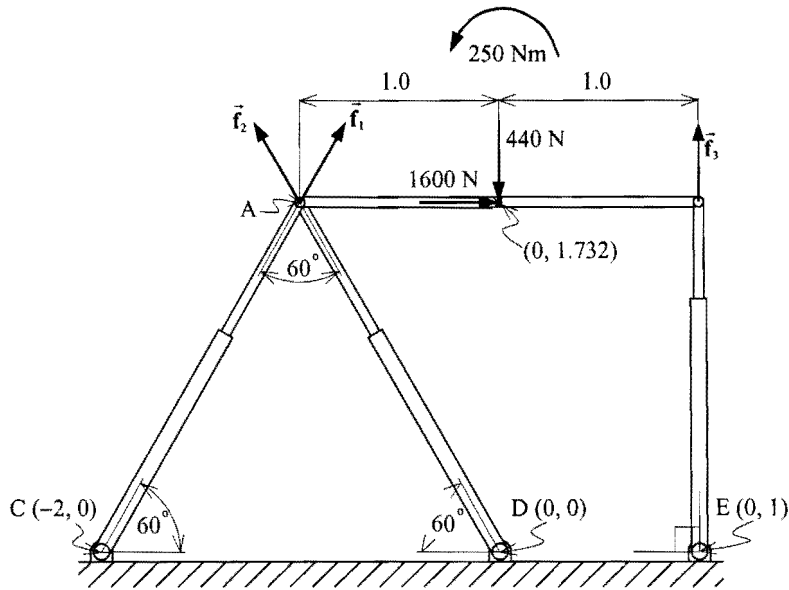
Figure 2.27: Simplified static analysis example.

The results obtained for the unknown actuator forces **ff** by solving expression (2.128) are $f_1 = -1400.8\,\text{N}$, $f_2 = 1799.2\,\text{N}$ and $f_3 = 95\,\text{N}$.

For this simple problem the unknown actuator force f_3 may also be obtained by considering the sum of the moments about A, i.e.: $\sum M_A = 0$: $250 - 440 + 2f_3 = 0$ and thus $f_3 = 95\,\text{N}$.

Also, summing the external forces in the x- and y-directions and substituting the value for f_3 yields the following equations in the unknown actuator forces f_1 and f_2:

$$\sum F_x = 0: \quad f_1 \cos 60° - f_2 \cos 60° + 1600 = 0 \tag{2.129}$$

$$\sum F_y = 0: \quad f_1 \sin 60° + f_2 \sin 60° + f_3 - 440 = 0 \tag{2.130}$$

Solving (2.129) and (2.130) finally gives $f_1 = -1400.8\,\text{N}$ and $f_2 = 1799.2\,\text{N}$. This together with the value of $f_3 = 95\,\text{N}$ confirms the accuracy of the results obtained via (2.128).

2.7.3 Fixed workpiece vs. fixed tool verification

The two modes of operation of the machining center are explained in Sections 2.4.1 and 2.4.2. The objective of this section is to verify the actuator force computations, by reconciling the results for the fixed tool scenario with that of the fixed workpiece scenario. This is done by considering the case where the respective tool path specifications are such that the space path of the platform is identical for both scenarios.

For this illustrative example the fixed workpiece scenario is as depicted in Figure 2.28, and the cutting tool is omitted from the moving platform.
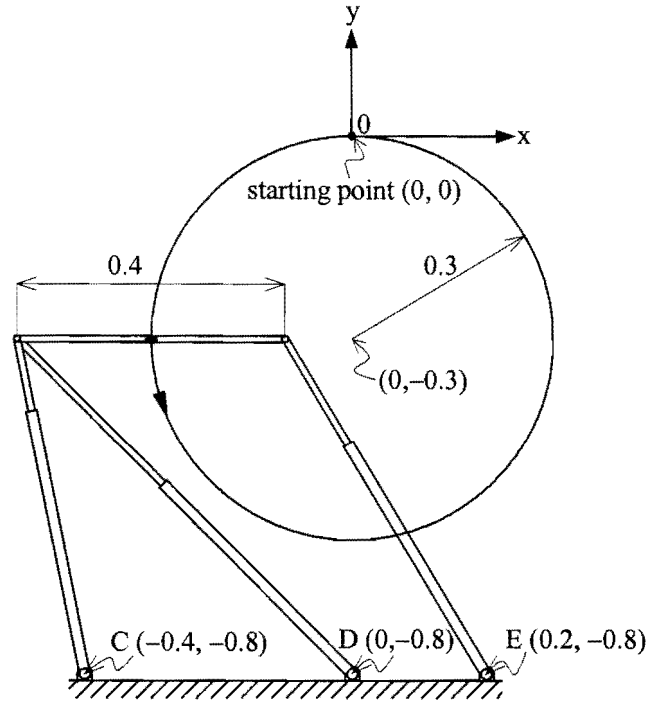
Figure 2.28: Fixed workpiece scenario with prescribed circular path.

The center of mass of the moving platform (body 1 in Figure 2.5) is controlled to trace the circle defined by

$$x^2 + (y + 0.3^2) = 0.3^2 \qquad (2.131)$$

at a constant tangential speed of $0.1\,\mathrm{m/s}$.

This circle is traced in a CCW sense starting at $(x, y) = (0, 0)$. It is furthermore required that the prescribed circular path be traced while a horizontal orientation is maintained by the moving platform, i.e. $\phi_1 \equiv 0$.

With the positional driving constraints and the fixed orientation prescribed, the inverse kinematic analysis may be done to obtain the acceleration vector $\ddot{\mathbf{q}} = [\ddot{\mathbf{q}}_1^{\mathrm{T}}, \ddot{\mathbf{q}}_2^{\mathrm{T}}, ..., \ddot{\mathbf{q}}_8^{\mathrm{T}}]^{\mathrm{T}}$ for any time instant. It is then used in the inverse dynamic analysis, which is done via the equations of motion given by expression (2.124).

The following mass matrix is used for the example planar Gough-Stewart platform shown in Figure 2.28:

$$\mathbf{M} = \mathrm{diag}\,[\mathbf{M}_1^{\mathrm{T}}, \mathbf{M}_2^{\mathrm{T}}, \mathbf{M}_3^{\mathrm{T}}, ..., \mathbf{M}_8^{\mathrm{T}}] \qquad (2.132)$$

with

$$\mathbf{M}_1 = [3, 3, 0.0625]^T$$

$$\mathbf{M}_2 = \mathbf{M}_3 = \mathbf{M}_4 = [0.6, 0.6, 0.02]^T$$

$$\mathbf{M}_5 = \mathbf{M}_6 = \mathbf{M}_7 = [2.5, 2.5, 0.003]^T$$

$$\mathbf{M}_8 = [0, 0, 0]^T$$

and specified in SI units.

Figure 2.29 shows the computed actuator forces required to control the planar Gough-Stewart platform along the prescribed circular path at the specified constant tangential speed of 0.1 m/s. The cutting force, discussed in Section 2.6.4.2.1, is neglected here.
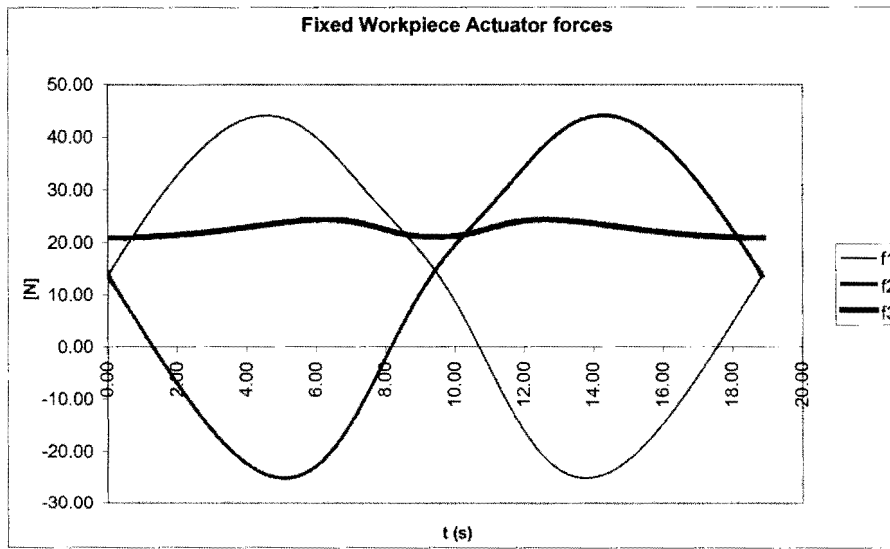
Figure 2.29: Actuator forces for the fixed workpiece circular tool path.

For the fixed tool scenario to be consistent with that of the fixed workpiece scenario, it is required to specify a prescribed path in the moving workpiece such that the motion in space of the moving platform is identical to the motion of the moving platform associated with the fixed workpiece example shown in Figure 2.28. For this to be so, the fixed cutting tool has to trace the prescribed solid circular path shown in Figure 2.30 in a CCW manner starting at $(\xi_1, \eta_1) = (0,0)$.
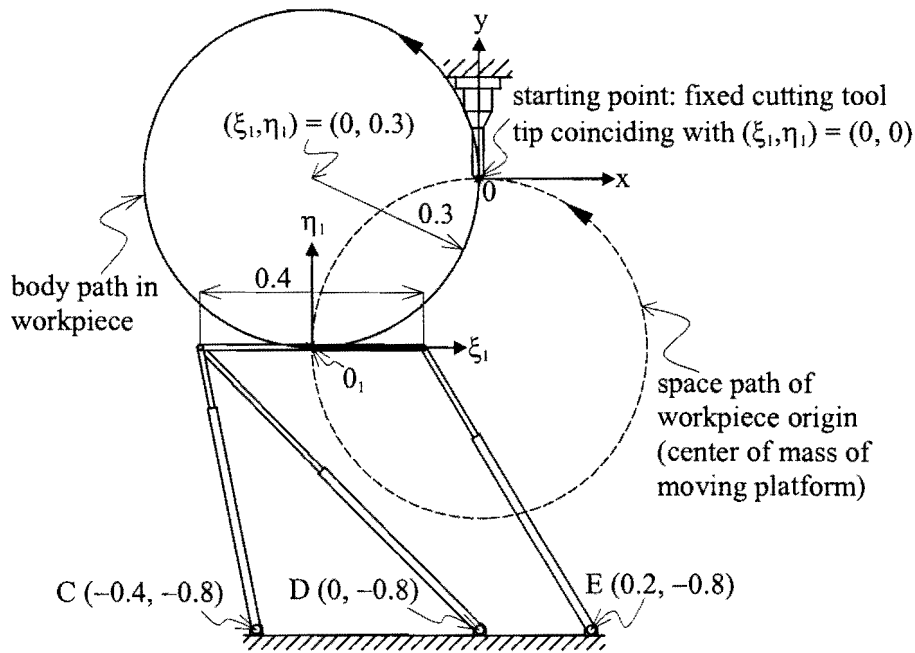
Figure 2.30: Fixed tool scenario with prescribed circular path.

In particular, the circular path in the local platform coordinate frame is defined by

$$\xi_1^2 + (\eta_1 - 0.3^2) = 0.3^2 \tag{2.133}$$

The global coordinate system is shown with its origin coinciding with the cutting tool tip. Using the transformations given by expressions (2.41) and (2.42), the motion of the moving platform in the global reference frame can be computed. This path is shown by the dashed circle in Figure 2.30 and corresponds exactly to the motion of the moving platform associated with the fixed workpiece example shown in Figure 2.28. Figure 2.31 shows the computed actuator forces required to manipulate the moving platform along the prescribed path of Figure 2.30. As is expected they are in exact agreement with the actuator forces shown in Figure 2.29. Note again that the cutting forces, discussed in Section 2.6.4.2.2, are neglected here to ensure that the load conditions are equivalent for both scenarios. This allows for a comparison of results. The fact that the results are identical gives further confidence in the respective methods of analysis.
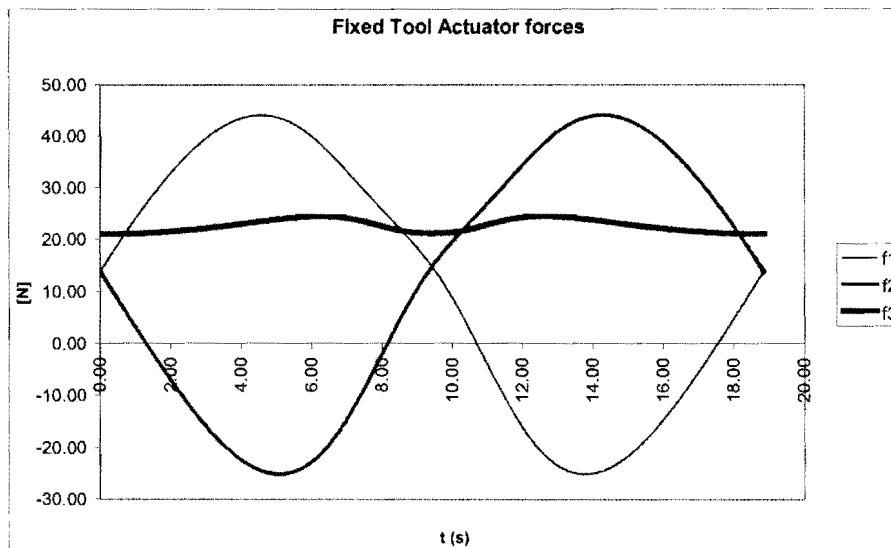
Figure 2.31: Actuator forces for the fixed tool circular tool path.

3 TRAJECTORY-PLANNING THROUGH INTERPOLATION BY OVERLAPPING CUBIC ARCS AND CUBIC SPLINES

3.1 Basic interpolation problem in trajectory planning

Given:

(i)   a set of nodal points $\{P_i = (x_i, y_i), i = 0,1,...,N\}$ along a general curve C to be followed by a working point (wp) from P_0 to P_N as shown in Figure 3.1,

(ii)   prescribed tangential speeds of wp, $\dot{s}_0$ and $\dot{s}_N$ at P_0 and P_N respectively,

(iii)   either prescribed tangential acceleration $\ddot{s}_0$ at P_0 *or* $\ddot{s}_N$ at P_N of wp, and

(iv) $\dfrac{dy}{dx}$ at both P_0 and P_N.

Then it is required to *determine*:

(a)   an acceptable time interval $[0,T]$ during which the curve is executed,

(b)   time parametric curves $X(t)$ and $Y(t)$, $t \in [0,T]$ that interpolate the nodal points (x_i, y_i), and

(c)   continuous time parametric curves for velocities $\dot{X}(t)$ and $\dot{Y}(t)$ as well as for the accelerations $\ddot{X}(t)$ and $\ddot{Y}(t)$, $t \in [0,T]$.
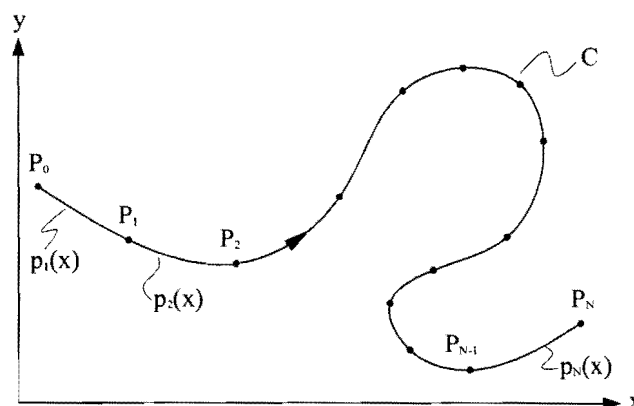
Figure 3.1: Basic interpolation problem.

Without loss in generality consider the case in (iii) where $\ddot{s}_N$ is known at P_N. Objectives (a), (b) and (c) may then be achieved by following the procedure outlined in the following subsections.

3.1.1 *Determination of time parametric intervals*

In order to achieve objective (a) stipulated above, the first task is to determine the total path length S from P_0 to P_N. This is done as follows: for each arc (x_{i-1}, y_{i-1}) to (x_i, y_i), $i = 1, 2, ..., N$, determine the corresponding path length s_i. Firstly determine a cubic interpolating polynomial approximation $p_i(x)$ over each arc interval, i.e. $y(x) \approx p_i(x)$, $x \in [x_{i-1}, x_i]$ (or $x(y) \approx p_i(y)$, $y \in [y_{i-1}, y_i]$ depending on what is the most convenient).

3.1.1.1 Determination of interpolating and overlapping cubic arcs

It is assumed that for any three consecutive nodal points (nodes) P_{i-1}, P_i and P_{i+1}, $i = 1, 2, ..., N-1$ in the given set of nodal points $\{P_i = (x_i, y_i), i = 0, 1, ..., N\}$, at least *one* of the following conditions must hold:

Condition 1(a):	$x_{i+1} > x_i > x_{i-1}$
Condition 1(b):	$x_{i+1} < x_i < x_{i-1}$
Condition 2(a):	$y_{i+1} > y_i > y_{i-1}$
Condition 2(b):	$y_{i+1} < y_i < y_{i-1}$

Table 3.1

In the event of non-compliance with all four the above conditions, the set of nodal points is considered insufficient since it implies that the section of the curve, represented by the three nodes that do not satisfy any of the conditions, cannot be expressed in the form where one of the coordinate variables is a unique valued function of the other. An extreme example of this non-uniqueness is depicted in Figure 3.2 which shows a complete curve C represented by the three nodes P_0, P_1 and P_2.
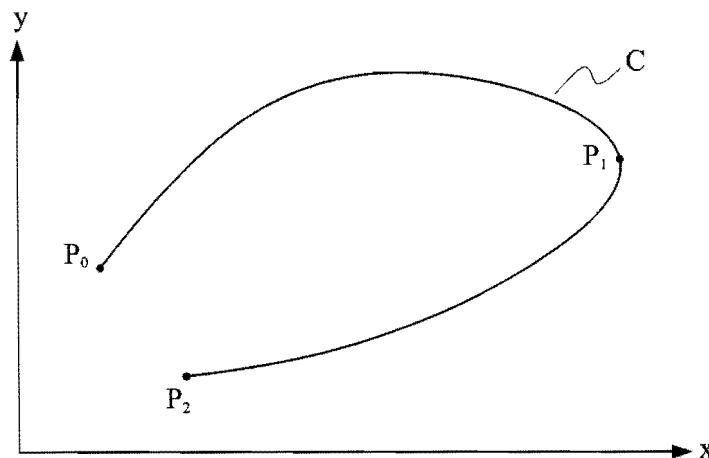
Figure 3.2: Insufficient set of nodal points.

Clearly $x_2 < x_1$ while $x_1 > x_0$, violating both conditions 1(a) and 1(b), and further $y_2 < y_1$ while $y_1 > y_0$, violating both conditions 2(a) and 2(b). This situation can easily be remedied by specifying, for example, two additional nodes, resulting in a set of five nodal points, as shown in Figure 3.3.
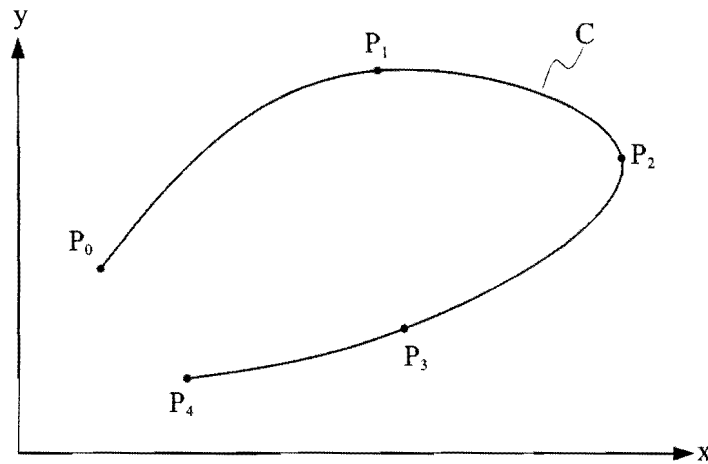
Figure 3.3: Sufficient set of nodal points.

The five nodal points shown in Figure 3.3, $\{P_i = (x_i, y_i), i = 0,1,...,4\}$ may be grouped to form three overlapping triplets of consecutive nodes, i.e.

Triplet 1:	(P_0, P_1, P_2)	$x_2 > x_1 > x_0$ (*satisfying* condition 1(a)) $y_2 < y_1$ and $y_1 > y_0$ (*violating* conditions 2(a) and 2(b))
Triplet 2:	(P_1, P_2, P_3)	$x_3 < x_2$ and $x_2 > x_1$ (*violating* conditions 1(a) and 1(b)) $y_3 < y_2 < y_1$ (*satisfying* condition 2(b))
Triplet 3:	(P_2, P_3, P_4)	$x_4 < x_3 < x_2$ (*satisfying* condition 1(b)) $y_4 < y_3 < y_2$ (*satisfying* condition 2(b))

Table 3.2

Curve C shown in Figure 3.3 may now be approximated by four (in general N) overlapping interpolating arcs shown separately in Figures 3.4, 3.5 and 3.6. Along each arc one variable may be expressed as a *unique* function of the other depending on which condition in Table 3.1 is satisfied. In particular it may be desired to represent each arc by a cubic polynomial interpolating function.
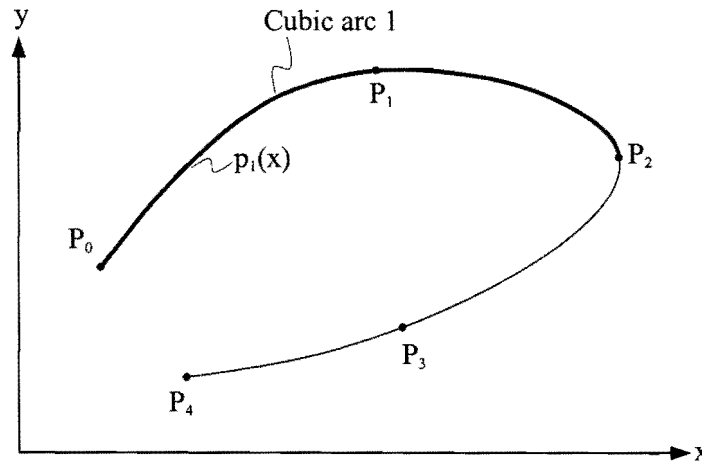
Figure 3.4: Cubic arc 1.

It follows by inspection that arc 1 in Figure 3.4, passing through the three nodes of triplet 1, may be represented by a unique valued function of x (see Tables 3.1 and 3.2). In particular it may be expressed as a cubic polynomial in x of the form:

$$p_1(x) = a_1 + b_1(x - x_0) + c_1(x - x_0)^2 + d_1(x - x_0)^3, \quad x \in [x_0, x_2] \qquad (3.1)$$

The derivative of (3.1) with respect to x is given by

$$\frac{d}{dx}p_1(x) = b_1 + 2c_1(x - x_0) + 3d_1(x - x_0)^2, \quad x \in [x_0, x_2] \qquad (3.2)$$

The four unknown coefficients of the cubic interpolating polynomial (a_1, b_1, c_1 and d_1) may be uniquely determined by utilizing the initial known gradient, i.e. $\frac{dy}{dx}$ at P_0 (see given data (iv), at the start of Section 3.1), as well as the three nodal points of triplet 1. More specifically substituting each of the three nodal points of triplet 1 into equation (3.1), results in three independent equations:

$$y_0 = p_1(x_0) = a_1 \qquad (3.3)$$

$$y_1 = p_1(x_1) = a_1 + b_1(x_1 - x_0) + c_1(x_1 - x_0)^2 + d_1(x_1 - x_0)^3 \qquad (3.4)$$

$$y_2 = p_1(x_2) = a_1 + b_1(x_2 - x_0) + c_1(x_2 - x_0)^2 + d_1(x_2 - x_0)^3 \qquad (3.5)$$

The fourth independent equation follows from substituting the initial gradient $\frac{dy}{dx}$ at P_0 $\left(\left.\frac{dy}{dx}\right|_{P_0} \right)$ into equation (3.2):

$$\left.\frac{dy}{dx}\right|_{P_0} = \frac{dy(x_0)}{dx} \approx \frac{d}{dx}p_1(x_0) = b_1 \qquad (3.6)$$

With a_1 and b_1 known from expressions (3.3) and (3.6) respectively, one may solve for c_1 and d_1 using expressions (3.4) and (3.5):

from (3.4): $c_1 = \dfrac{y_1 - a_1 - b_1(x_1 - x_0)}{(x_1 - x_0)^2} - d_1(x_1 - x_0)$

or $c_1 = e_1 - d_1(x_1 - x_0)$

where $e_1 = \dfrac{y_1 - a_1 - b_1(x_1 - x_0)}{(x_1 - x_0)^2}$, and substituting the expression for c_1

into (3.5): $y_2 = a_1 + b_1(x_2 - x_0) + (e_1 - d_1(x_1 - x_0))(x_2 - x_0)^2 + d_1(x_2 - x_0)^3$

and therefore $d_1 = \dfrac{y_2 - a_1 - b_1(x_2 - x_0) - e_1(x_2 - x_0)^2}{(x_2 - x_0)^3 - (x_1 - x_0)(x_2 - x_0)^2}$

It is proposed here that the cubic interpolating polynomial $p_1(x)$ constructed in this manner be called a clamped three-order interpolating cubic arc, or simply a *C-3 node cubic arc.*

Although cubic arc 1 interpolates through points P_0, P_1 and P_2 and is thus valid over the interval $[x_0, x_2]$, it will only be used to represent the cubic polynomial function over the first interval $[x_0, x_1]$. Cubic arc 1 is forced through the three nodes of triplet 1 (see Table 3.1) with only the initial gradient $\left(\left.\dfrac{dy}{dx}\right|_{P_0}\right)$ being enforced. The approximation $p_1(x)$ is therefore expected to deteriorate in gradient accuracy in the vicinity of node P_2 and this is the reason why it will only be used over $[x_0, x_1]$. To obtain a more reliable approximation between nodes P_1 and P_2 an overlapping strategy is employed to avoid the accumulation of excessive gradient approximation errors, which will result in increasingly inaccurate fitted cubic arcs.
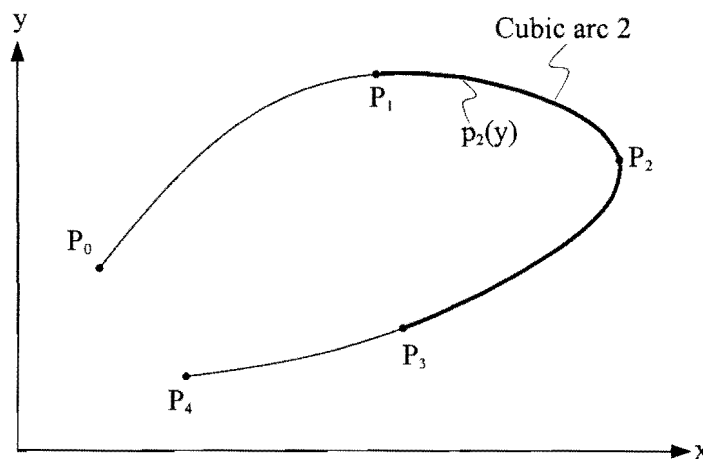
Figure 3.5: Cubic arc 2.

The cubic arc 2 passing through the three nodes of triplet 2, (see Figure 3.5) is also represented by a cubic polynomial function this time of y (see also Table 3.1 and Table 3.2). This function is formally expressed as

$$p_2(y) = a_2 + b_2(y - y_1) + c_2(y - y_1)^2 + d_2(y - y_1)^3, \quad y \in [y_1, y_3] \tag{3.7}$$

The derivative of (3.7) with respect to y is

$$\frac{d}{dy} p_2(y) = b_2 + 2c_2(y - y_1) + 3d_2(y - y_1) \tag{3.8}$$

Again the initial gradient of cubic arc 2 at P_1 $\left(\left. \dfrac{dx}{dy} \right|_{P_1} \right)$ is required together with the three nodes of triplet

2 to calculate the four unknown coefficients (a_2, b_2, c_2 and d_2) of polynomial (3.7). Here, at the start of arc 2 (as for the subsequent arcs) the value of the gradient is not explicitly prescribed and is therefore unknown. However, once the four unknown coefficients of the previous cubic arc 1 have been determined, equation (3.2) provides an approximation to the required gradient at P_1, i.e.

$$\left. \frac{dy}{dx} \right|_{P_1} = \frac{dy(x_1)}{dx} \approx \frac{d}{dx} p_1(x_1) = b_1 + 2c_1(x_1 - x_0) + 3d_1(x_1 - x_0)^2 \tag{3.9}$$

Thus in computing the coefficients of approximating arc 2 the condition $\left. \dfrac{dx}{dy} \right|_{P_1} = \left[\dfrac{dp_1(x_1)}{dx} \right]^{-1}$ is used.

Polynomial $p_2(x)$ will only be used to describe the arc between nodes P_1 and P_2.
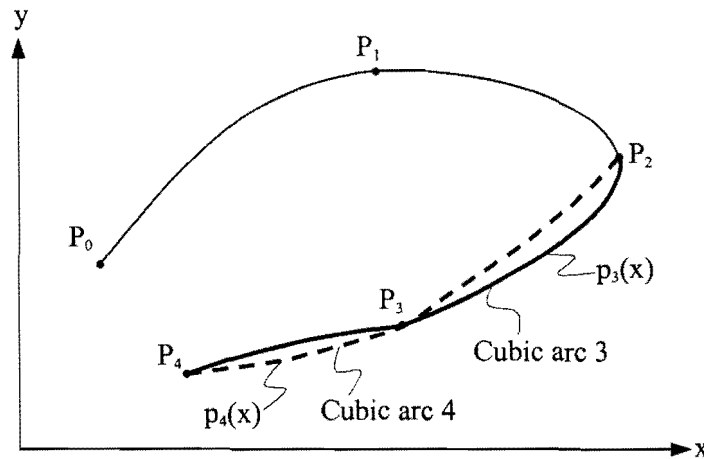
Figure 3.6: Cubic arcs 3 and 4.

Cubic arc 3 passing through the three nodes of triplet 3 (see Figure 3.6) is different to the previous arcs in that both conditions 1(b) and 2(b) are satisfied (see Table 3.1 and Table 3.2). This implies that cubic arc 3 can be expressed as a cubic polynomial function of either x or y and a choice has to be made. If this situation occurs, only one of the following two conditions will be satisfied:

Condition 3(a):	$\left| x_{i+1} - x_{i-1} \right| \geq \left| y_{i+1} - y_{i-1} \right|$
Condition 3(b):	$\left| x_{i+1} - x_{i-1} \right| < \left| y_{i+1} - y_{i-1} \right|$

Table 3.3

Trajectory-planning through interpolation by overlapping cubic arcs and cubic spl...

UNIVERSITEIT VAN PRETORIA
UNIVERSITY OF PRETORIA
YUNIBESITHI YA PRETORIA

For the case depicted in Figure 3.6, cubic arc 3 satisfies condition 3(a) in Table 3.3, and it is therefore clearly preferable to express the arc as a cubic polynomial function of x:

$$p_3(x) = a_3 + b_3(x - x_2) + c_3(x - x_2)^2 + d_3(x - x_2)^3, \; x \in [x_2, x_4] \tag{3.10}$$

The unknown coefficients of cubic polynomial (3.10) are determined in a similar manner to those of cubic arc 2 (equation (3.7)), with the initial gradient at P_2 taken as $\left. \dfrac{dy}{dx} \right|_{P_2} = \left[\dfrac{dp_2(y_2)}{dy} \right]^{-1}$. Again $p_3(x)$ will only be used over the first interpolating interval, i.e., between nodes P_2 and P_3 (Figure 3.6).

Having determined cubic arc 3, it remains to find a suitable cubic interpolating polynomial function $p_4(x)$, $x \in [x_3, x_4]$, which is to represent the final interval P_3 to P_4 of the total curve under consideration.

The overlapping strategy may be continued for the final part of the curve by fitting a cubic arc through nodes P_4, P_3 and P_2, and utilizing the given gradient at P_4 (see given data (iv) at the beginning of Section 3.1). The polynomial has the form

$$p_4(x) = a_4 + b_4(x - x_4) + c_4(x - x_4)^2 + d_4(x - x_4)^3, \; x \in [x_4, x_2] \tag{3.11}$$

The derivative of (3.11) with respect to x is

$$\frac{d}{dx} p_4(x) = b_4 + 2c_4(x - x_4) + 3d_4(x - x_4)^2, \; x \in [x_4, x_2] \tag{3.12}$$

With the given final gradient $\dfrac{dy}{dx}$ at P_4 and interpolating through the three nodes P_4, P_3 and P_2, four independent equations in the unknown coefficients follow from expressions (3.11) and (3.12) as before. These equations may be simultaneously solved to give a_4, b_4, c_4 and d_4. The resultant interpolating polynomial $p_4(x)$, representing arc 4 and to be used over the final interval between nodes P_3 and P_4, is also indicated in Figure 3.6.

The following truth table shows how the different conditions listed in Table 3.1 and Table 3.3 determine the dependent variable for a specific arc. The rows show different combinations of satisfied and violated conditions, where a 1 indicates that a specific condition is satisfied and a 0 that it is violated.

Condition 1(a)	Condition 1(b)	Condition 2(a)	Condition 2(b)	Condition 3(a)	Condition 3(b)	Dependent variable
1	0	0	0			x
0	1	0	0			x
0	0	1	0			y
0	0	0	1			y
1	0	1	0	1	0	x
				0	1	y
1	0	0	1	1	0	x
				0	1	y
0	1	1	0	1	0	x
				0	1	y
0	1	0	1	1	0	x
				0	1	y

Table 3.4

Here, for illustrative purposes, the presentation of the overlapping cubic arc methodology for constructing an approximation to a curve defined by nodal points $P_0, P_1, ..., P_N$, has been restricted to the case $N = 4$. The extension of the method to the more general case where N may be larger than 4 is clear and obvious.

3.1.1.2 Computation of total path length S

With $p_i(x)$ (or $p_i(y)$) representing the approximation to the curve to be used over $[x_{i-1}, x_i]$ known, the corresponding curve length s_i may be obtained by integration. From the differential relationship $ds^2 = dx^2 + dy^2$ it follows that $ds = \sqrt{1 + (\frac{dy}{dx})^2}\,dx$ and therefore the curve length s_i is given by

$$s_i = \int_{x_{i-1}}^{x_i} \sqrt{1 + (\frac{d}{dx}p_i(x))^2}\,dx = \int_a^b f(x)dx$$

with $a = x_{i-1}$, $b = x_i$ and $f(x) = \sqrt{1 + [b_i + 2c_i(x - x_{i-1}) + 3d_i(x - x_{i-1})^2]^2}$

for each $i = 1, 2, ..., N$

It is convenient to do the integration numerically by using the composite Simpson's rule for n subintervals [55]:

$$\int_a^b f(x)dx \approx \frac{h}{3}\left[f(a) + 2\sum_{j=1}^{(n/2)-1} f(x_{2j}) + 4\sum_{j=1}^{(n/2)} f(x_{2j-1}) + f(b) \right] \tag{3.13}$$

where n is even, $h = \frac{(b-a)}{n}$, and $x_k = a + kh$ for $k = 0, 1, ..., n$

The total path length S of curve C is then given by

$$S = \sum_{i=1}^{N} s_i \tag{3.14}$$

3.1.1.3 Dependence of curve length on parameter t

Assume that the distance s of the working point (wp) along the curve is represented by a cubic polynomial in time t of the form:

$$s(t) = a_s + b_s t + c_s t^2 + d_s t^3, \ t \in [0,T] \tag{3.15}$$

Expression (3.15) is associated with a known initial curve length $s(0) = s_0$ (usually $s_0 = 0$), a known initial tangential speed $\dot{s}(0) = v_0$ (usually $v_0 = 0$), as well as a known final curve length $s(T) = S$ (usually found via expression (3.14) above).

For the time being, assume that a gradual increase in tangential speed is required over the time interval $t \in [0,T]$, such that a specified tangential speed v^* is attained at time T, i.e. $\dot{s}(T) = v^*$. The time derivative of (3.15), representing the tangential speed over the total path is

$$\dot{s}(t) = b_s + 2c_s t + 3d_s t^2, \ t \in [0,T] \tag{3.16}$$

The acceleration over the total path may be obtained from the time derivative of (3.16):

$$\ddot{s}(t) = 2c_s + 6d_s t, \ t \in [0,T] \tag{3.17}$$

It is further required that the magnitude of the final tangential acceleration has to be zero, i.e. $\ddot{s}(T) = 0$.

Now, with $s(0) = s_0$, $s(T) = S$, $\dot{s}(0) = v_0$, $\dot{s}(T) = v^*$ and $\ddot{s}(T) = 0$ known, one may solve for a_s, b_s, c_s, d_s and T as follows:

$$s(0) = a_s = s_0$$

$$\dot{s}(0) = b_s = v_0$$

$$s(T) = S = a_s + b_s T + c_s T^2 + d_s T^3 \tag{3.18}$$

$$\dot{s}(T) = v^* = b_s + 2c_s T + 3d_s T^2 \tag{3.19}$$

$$\ddot{s}(T) = 0 = 2c_s + 6d_s T \tag{3.20}$$

$$\text{from (3.20): } c_s = -3d_s T \tag{3.21}$$

and substituting (3.21) into (3.19): $v^* = v_0 - 3d_s T^2$, from which it follows that

$$d_s = \frac{v_0 - v^*}{3T^2} \tag{3.22}$$

Substituting (3.22) into (3.21): $c_s = \dfrac{v^* - v_0}{T}$ \hfill (3.23)

and substituting (3.22) and (3.23) into (3.18): $S = s_0 + T\left(\dfrac{v_0}{3} + \dfrac{2v^*}{3}\right)$ from which it finally follows that

$$T = \frac{3(S - s_0)}{v_0 + 2v^*} \qquad (3.24)$$

Note that if the initial time instant $t_0 \neq 0$, the corresponding polynomial $s(t)$ can readily be obtained by the simple replacement of T by $T - t_0$ in expressions (3.18) - (3.24) and the corresponding replacement of t by $t - t_0$ in expressions (3.17) - (3.19).

For each node $P_i = (x_i, y_i)$, $i = 0,1,...,N$ the total path length up to the specific node may be determined from (3.14):

$$S_i = \sum_{j=1}^{i} s_j \;, \; i = 0,1,...,N \qquad (3.25)$$

Further, with S_i, $i = 1,2,...,N-1$ known, the Newton-Raphson iterative method may be used to solve for the corresponding nodal times t_i, $i = 1,2,...,N-1$ [55]. This well-known and powerful numerical method solves for the root of a non-linear equation of the form $f(x) = 0$ via the iterative scheme:

$$x^{(j)} = \frac{x^{(j-1)} - f(x^{(j-1)})}{\left[\dfrac{df(x^{(j-1)})}{dx}\right]} \;, \; j = 1,2,...$$

where an initial estimate $x^{(0)}$ is given.

To solve for a specific t_i corresponding to distance S_i, requires the solution of the non-linear equation

$$f(t_i) = s(t_i) - S_i = 0$$

where from (3.15): $s(t_i) = a_s + b_s\, t_i + c_s\, t_i^2 + d_s\, t_i^3$, and thus, more explicitly, the equation to be solved becomes

$$f(t_i) = a_s + b_s\, t_i + c_s\, t_i^2 + d_s\, t_i^3 - S_i = 0$$

An equation corresponding to the above, is to be solved for each $i = 1,2,...,N-1$.

Since $t_N = T$ is known from (3.24), good initial approximations for t_i, $i = 1,2,...,N-1$ may be found:

$$t_i^{(0)} = i\left(\frac{T}{N}\right), \; i = 1,2,...,N-1$$

Starting with an initial approximate root given by the above, the Newton-Raphson method generates, for each i, a sequence of approximations $\{t_i^{(j)}, j = 0,1,2,...\}$:

$$t_i^{(j)} = t_i^{(j-1)} - \frac{f(t_i^{(j-1)})}{\left[\dfrac{df(t_i^{(j-1)})}{dt_i}\right]}, \quad j = 1,2,...$$

The iteration continues until convergence is obtained. In practice, with a tolerance $\varepsilon > 0$ specified, the Newton-Raphson iteration continues for each i until one of the following convergence criteria is met:

$$\left| t_i^{(j)} - t_i^{(j-1)} \right| < \varepsilon$$

$$\frac{\left| t_i^{(j)} - t_i^{(j-1)} \right|}{t_i^{(j)}} < \varepsilon, \quad t_i^{(j)} \neq 0$$

$$\text{or } f(t_i^{(j)}) < \varepsilon$$

3.1.2 Cubic spline representations for X(t) and Y(t)

With the time interval $[0, T]$ during which the curve is executed determined (see objective (a) Section 3.1), and the nodal times t_i, $i = 1, 2, ..., N-1$ known, time parametric curves $X(t)$, and $Y(t)$, $t \in [0, T]$ interpolating the nodal points (x_i, y_i) (see objective (b) Section 3.1), can be determined.

Since a unique time instant $t_i \in [0, T]$ is associated with each nodal point (x_i, y_i), $i = 0, 1, ..., N$ and since $0 = t_0 < t_1 < ... < t_N = T$, separate *cubic spline interpolations* $X(t)$ and $Y(t)$ may be fitted to the respective nodal point sets, (x_i, t_i) and (y_i, t_i).

According to Burden and Faires [55] cubic spline interpolation, which fits cubic polynomials between each successive pair of nodes, is the most common piecewise polynomial approximation. Based on their definition, the cubic spline interpolant $X(t)$, is a function that satisfies the following conditions:

$X(t)$ is a cubic polynomial, denoted $X_i(t)$, on subinterval $[t_i, t_{i+1}]$ for each $i = 0, 1, ..., N-1$

$X(t_i) = x_i$ for each $i = 0, 1, ..., N$

$X_{i+1}(t_{i+1}) = X_i(t_{i+1})$ for each $i = 0, 1, ..., N-2$

$\dot{X}_{i+1}(t_{i+1}) = \dot{X}_i(t_{i+1})$ for each $i = 0, 1, ..., N-2$

$\ddot{X}_{i+1}(t_{i+1}) = \ddot{X}_i(t_{i+1})$ for each $i = 0, 1, ..., N-2$

One of the following set of boundary conditions is satisfied:

$\ddot{X}(t_0) = \ddot{X}_i(t_N) = 0$ (free or natural boundary)

or $\dot{X}(t_0) = \dot{x}_0$ and $\dot{X}(t_N) = \dot{x}_N$ (clamped boundary)

When the free boundary conditions are prescribed, the spline is called a natural spline, and its form approximates the shape that a long flexible rod would assume if forced to go through each of the nodal points.

For the interpolants $X(t)$ and $Y(t)$ to be constructed here, however, clamped boundary conditions are used, since they contain more information about the respective functions, and therefore lead to more accurate approximations.

Assume for the moment that the derivatives at the end points ($\dot{x}_0$ and $\dot{x}_N$) are accurately known. To construct the cubic spline interpolant for x as a function of t, the conditions listed above are applied to the cubic polynomials of the following form:

$$X_i(t) = a_{Xi} + b_{Xi}(t - t_i) + c_{Xi}(t - t_i)^2 + d_{Xi}(t - t_i)^3, \quad i = 0,1,...,N-1 \qquad (3.26)$$

The unknown coefficients a_{Xi}, b_{Xi}, c_{Xi} and d_{Xi}, $i = 0,1,...,N-1$, may easily be determined as shown in [55].

If not explicitly known, the initial derivative $\dot{x}_0$ may be accurately approximated using Taylor expansions for x_1, x_2, x_3 and x_4 about t_0:

$$x_1 = x_0 + \Delta t_1 \dot{x}_0 + \frac{(\Delta t_1)^2}{2!}\ddot{x}_0 + \frac{(\Delta t_1)^3}{3!}\dddot{x}_0 + \frac{(\Delta t_1)^4}{4!}\ddddot{x}_0 + O(\Delta t_1)^5$$

$$x_2 = x_0 + \Delta t_2 \dot{x}_0 + \frac{(\Delta t_2)^2}{2!}\ddot{x}_0 + \frac{(\Delta t_2)^3}{3!}\dddot{x}_0 + \frac{(\Delta t_2)^4}{4!}\ddddot{x}_0 + O(\Delta t_2)^5$$

$$x_3 = x_0 + \Delta t_3 \dot{x}_0 + \frac{(\Delta t_3)^2}{2!}\ddot{x}_0 + \frac{(\Delta t_3)^3}{3!}\dddot{x}_0 + \frac{(\Delta t_3)^4}{4!}\ddddot{x}_0 + O(\Delta t_3)^5$$

$$x_4 = x_0 + \Delta t_4 \dot{x}_0 + \frac{(\Delta t_4)^2}{2!}\ddot{x}_0 + \frac{(\Delta t_4)^3}{3!}\dddot{x}_0 + \frac{(\Delta t_4)^4}{4!}\ddddot{x}_0 + O(\Delta t_4)^5$$

where x_i corresponds to $x(t_i)$ and $\Delta t_i = t_i - t_0$, $i = 1, 2, 3, 4$. Ignoring the higher order terms in the above expressions leads to the following set of linear equations:

$$\begin{bmatrix} x_1 - x_0 \\ x_2 - x_0 \\ x_3 - x_0 \\ x_4 - x_0 \end{bmatrix} = \begin{bmatrix} \Delta t_1 & \frac{(\Delta t_1)^2}{2} & \frac{(\Delta t_1)^3}{6} & \frac{(\Delta t_1)^4}{24} \\ \Delta t_2 & \frac{(\Delta t_2)^2}{2} & \frac{(\Delta t_2)^3}{6} & \frac{(\Delta t_2)^4}{24} \\ \Delta t_3 & \frac{(\Delta t_3)^2}{2} & \frac{(\Delta t_3)^3}{6} & \frac{(\Delta t_3)^4}{24} \\ \Delta t_4 & \frac{(\Delta t_4)^2}{2} & \frac{(\Delta t_4)^3}{6} & \frac{(\Delta t_4)^4}{24} \end{bmatrix} \begin{bmatrix} \dot{x}_0 \\ \ddot{x}_0 \\ \dddot{x}_0 \\ \ddddot{x}_0 \end{bmatrix} \qquad (3.27)$$

Expression (3.27) is a linear system of the form $\mathbf{Ax} = \mathbf{b}$, and can be solved directly using a scheme such as LU-factorization [55]. The solution vector $\mathbf{x}$ contains the sought after initial derivative $\dot{x}_0$.

The final derivative $\dot{x}_N$ may be obtained in a similar manner, where the set of linear equations in matrix form is given by:

$$
\begin{bmatrix} x_{N-1} - x_N \\ x_{N-2} - x_N \\ x_{N-3} - x_N \\ x_{N-4} - x_N \end{bmatrix} = \begin{bmatrix} -\Delta t_1 & \dfrac{(\Delta t_1)^2}{2} & -\dfrac{(\Delta t_1)^3}{6} & \dfrac{(\Delta t_1)^4}{24} \\ -\Delta t_2 & \dfrac{(\Delta t_2)^2}{2} & -\dfrac{(\Delta t_2)^3}{6} & \dfrac{(\Delta t_2)^4}{24} \\ -\Delta t_3 & \dfrac{(\Delta t_3)^2}{2} & -\dfrac{(\Delta t_3)^3}{6} & \dfrac{(\Delta t_3)^4}{24} \\ -\Delta t_4 & \dfrac{(\Delta t_4)^2}{2} & -\dfrac{(\Delta t_4)^3}{6} & \dfrac{(\Delta t_4)^4}{24} \end{bmatrix} \begin{bmatrix} \dot{x}_N \\ \ddot{x}_N \\ \dddot{x}_N \\ \ddddot{x}_N \end{bmatrix}
\tag{3.28}
$$

with $\Delta t_i = t_N - t_{N-i}$, $i = 1, 2, 3, 4$.

The advantage of using a cubic spline interpolation for $X(t)$, $t \in [0, T]$ is that each constituent cubic polynomial $X_i(t)$ involves four coefficients, so there is sufficient flexibility in the cubic spline procedure to ensure that the interpolant is not only continuously differentiable, but also has a continuous second derivative over the whole interval $[0, T]$ (see [55]).

Once a_{Xi}, b_{Xi}, c_{Xi}, and d_{Xi}, $i = 0, 1, ..., N-1$ (see (3.26)) are determined, $\dot{X}(t)$ and $\ddot{X}(t)$ are given by:

$$
\dot{X}_i(t) = b_{Xi} + 2c_{Xi}(t - t_i) + 3d_{Xi}(t - t_i)^2, \; i = 0, 1, ..., N-1
\tag{3.29}
$$

$$
\ddot{X}_i(t) = 2c_{Xi} + 6d_{Xi}(t - t_i), \; i = 0, 1, ..., N-1
\tag{3.30}
$$

which are continuous functions over the interval $[0, T]$ (see objective (c) Section 3.1).

It follows that $Y(t)$, $\dot{Y}(t)$ and $\ddot{Y}(t)$ can be found in a similar manner.

3.2 Practical problem of determining $\dfrac{dy}{dx}$ at P_0 and P_N

In general the set of given nodal points $\{P_i = (x_i, y_i), i = 0, 1, ..., N\}$ may represent a curve for which no explicit analytical expression exists, and therefore the exact initial and final gradients ($\dfrac{dy}{dx}$ at P_0 and P_N) will not be known. In this case approximations to these gradients with respect to x may be determined using Taylor expansions in an analogous manner as done for the time derivatives $\dot{x}_0$ and $\dot{x}_N$ in Section 3.1.2 (see expressions (3.27) and (3.28)).

In Section 3.1.1.1 it is apparent that the nodal points representing a curve must be chosen in such a way that certain conditions are satisfied (see Table 3.1 and Table 3.3). These conditions ensure that each consecutive cubic arc can be expressed as a function of either x or y.

Returning to the illustrative example curve of Figure 3.3, it was shown that 5 nodal points along the curve are adequate in terms of the conditions listed in Table 3.1 and Table 3.3, provided that the exact initial and final gradients are known. However, if the exact values of the initial and final gradients are not known, the nodal points should be specified in such a way that sufficiently *accurate approximations* for these gradients may be calculated.
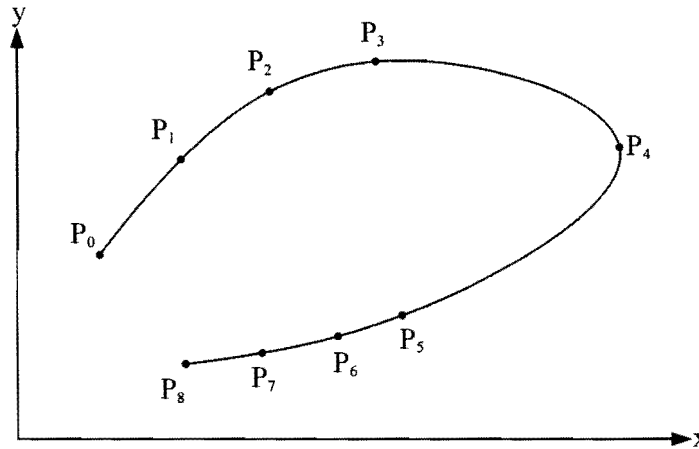
Figure 3.7: Additional nodal points specified.

Figure 3.7 shows the same illustrative example curve, but with four additional nodal points. An approximate value for the initial gradient ($\frac{dy}{dx}$ at P_0, i.e. y_0') may then be determined using the following Taylor expansions:

$$y_1 = y_0 + \Delta x_1 y_0' + \frac{(\Delta x_1)^2}{2!} y_0'' + \frac{(\Delta x_1)^3}{3!} y_0''' + O(\Delta x_1)^4$$

$$y_2 = y_0 + \Delta x_2 y_0' + \frac{(\Delta x_2)^2}{2!} y_0'' + \frac{(\Delta x_2)^3}{3!} y_0''' + O(\Delta x_2)^4$$

$$y_3 = y_0 + \Delta x_3 y_0' + \frac{(\Delta x_3)^2}{2!} y_0'' + \frac{(\Delta x_3)^3}{3!} y_0''' + O(\Delta x_3)^4$$

with $\Delta x_i = x_i - x_0$, $i = 1,2,3$.

The clustered distribution of nodal points P_0, P_1, P_2 and P_3 shown in Figure 3.7 is justified considering the fact that the fourth order error term in the above Taylor expansions becomes smaller using smaller step sizes Δx_1, Δx_2 and Δx_3. Neglecting these error terms an approximate initial gradient y_0' is obtained by solving the following linear system:

$$\begin{bmatrix} y_1 - y_0 \\ y_2 - y_0 \\ y_3 - y_0 \end{bmatrix} = \begin{bmatrix} \Delta x_1 & \dfrac{(\Delta x_1)^2}{4} & \dfrac{(\Delta x_1)^3}{6} \\ \Delta x_2 & \dfrac{(\Delta x_2)^2}{4} & \dfrac{(\Delta x_2)^3}{6} \\ \Delta x_3 & \dfrac{(\Delta x_3)^2}{4} & \dfrac{(\Delta x_3)^3}{6} \end{bmatrix} \begin{bmatrix} y_0' \\ y_0'' \\ y_0''' \end{bmatrix} \tag{3.31}$$

Similarly, an approximate final gradient y_N' may be obtained by solving the linear system:

$$\begin{bmatrix} y_{N-1} - y_N \\ y_{N-2} - y_N \\ y_{N-3} - y_N \end{bmatrix} = \begin{bmatrix} -\Delta x_1 & \dfrac{(\Delta x_1)^2}{4} & -\dfrac{(\Delta x_1)^3}{6} \\ -\Delta x_2 & \dfrac{(\Delta x_2)^2}{4} & -\dfrac{(\Delta x_2)^3}{6} \\ -\Delta x_3 & \dfrac{(\Delta x_3)^2}{4} & -\dfrac{(\Delta x_3)^3}{6} \end{bmatrix} \begin{bmatrix} y_N' \\ y_N'' \\ y_N''' \end{bmatrix} \tag{3.32}$$

with $\Delta x_i = x_N - x_{N-i}$, $i = 1,2,3$.

Depending on the particular circumstances, approximations for $\dfrac{dx}{dy}$ at P_0 and P_N may be determined in a

similar manner using Taylor expansions. The choice between determining $\dfrac{dy}{dx}$ or $\dfrac{dx}{dy}$ at P_0 and P_N

depends on which of the following conditions are satisfied, and which are violated:

Condition 4(a):	$x_3 > x_2 > x_1 > x_0$
Condition 4(b):	$x_0 > x_1 > x_2 > x_3$
Condition 4(c):	$x_{N-3} > x_{N-2} > x_{N-1} > x_N$
Condition 4(d):	$x_N > x_{N-1} > x_{N-2} > x_{N-3}$
Condition 5(a):	$y_3 > y_2 > y_1 > y_0$
Condition 5(b):	$y_0 > y_1 > y_2 > y_3$
Condition 5(c):	$y_{N-3} > y_{N-2} > y_{N-1} > y_N$
Condition 5(d):	$y_N > y_{N-1} > y_{N-2} > y_{N-3}$

Table 3.5

Since four node points are involved in each condition, the clustered distributions of the nodal points P_0,

P_1, P_2 and P_3, as well as P_5, P_6, P_7 and P_8 in Figure 3.7 are further justified considering the

requirement that at least two of the conditions listed in Table 3.5 must be satisfied for any set of nodal

points. In particular, at least *one* of conditions 4(a), 4(b), 5(a) or 5(b), and *one* of conditions 4(c), 4(d),

5(c) or 5(d) must be satisfied for the purposes of determining the sought after initial and final gradients.

For nodal points P_0, P_1, P_2 and P_3 shown in Figure 3.7 it is clear that both conditions 4(a) and 5(a) are satisfied, implying that either $\dfrac{dy}{dx}$ or $\dfrac{dx}{dy}$ can be determined at P_0. Similarly for nodal points P_5, P_6, P_7 and P_8, both conditions 4(c) and 5(c) are satisfied, implying that either $\dfrac{dy}{dx}$ or $\dfrac{dx}{dy}$ can be determined at $P_N = P_8$. In these eventualities, the appropriate choice is made by testing which of the additional conditions listed in Table 3.6 are satisfied.

Condition 6(a):	$\left| x_3 - x_0 \right| \geq \left| y_3 - y_0 \right|$
Condition 6(b):	$\left| x_3 - x_0 \right| < \left| y_3 - y_0 \right|$
Condition 7(a):	$\left| x_N - x_{N-3} \right| \geq \left| y_N - y_{N-3} \right|$
Condition 7(b):	$\left| x_N - x_{N-3} \right| < \left| y_N - y_{N-3} \right|$

Table 3.6

For example, since for nodes P_0 and P_3 shown in Figure 3.7, condition 6(a) is satisfied, the obvious choice is to determine $\dfrac{dy}{dx}$ at node P_0. Similarly, since condition 7(a) is satisfied for nodes P_5 and P_8, $\dfrac{dy}{dx}$ is to be determined at node $P_N = P_8$.

The following truth table shows how the conditions from Table 3.5 and Table 3.6 determine the form of the gradient to be used at node P_0. As before, the rows show different combinations of satisfied and violated conditions, where a 1 indicates that the specific condition is satisfied, and a 0 that it is violated.

Condition 4(a)	Condition 4(b)	Condition 5(a)	Condition 5(b)	Condition 6(a)	Condition 6(b)	Gradient at P_0
1	0	0	0			$\dfrac{dy}{dx}$
0	1	0	0			$\dfrac{dy}{dx}$
0	0	1	0			$\dfrac{dx}{dy}$
0	0	0	1			$\dfrac{dx}{dy}$

1	0	1	0	1	0	$\dfrac{dy}{dx}$
				0	1	$\dfrac{dx}{dy}$
1	0	0	1	1	0	$\dfrac{dy}{dx}$
				0	1	$\dfrac{dx}{dy}$
0	1	1	0	1	0	$\dfrac{dy}{dx}$
				0	1	$\dfrac{dx}{dy}$
0	1	0	1	1	0	$\dfrac{dy}{dx}$
				0	1	$\dfrac{dx}{dy}$

Table 3.7

A similar truth table may be drawn up showing how the different combinations of conditions determine the form of the gradient to be used at P_N.

Of course, with $\dfrac{dy}{dx}$ (or $\dfrac{dx}{dy}$) determined at nodes P_0 and P_N using the above strategy, $\dfrac{dx}{dy}$ (or $\dfrac{dy}{dx}$) at nodes P_0 and P_N is simply given by the reciprocal relationship:

$$\frac{dx(y_i)}{dy} = \left[\frac{dy(x_i)}{dx}\right]^{-1} \quad \text{or} \quad \frac{dy(x_i)}{dy} = \left[\frac{dx(y_i)}{dx}\right]^{-1} \quad \text{for } i = 1, N$$

3.3 Synthesis of more general curves
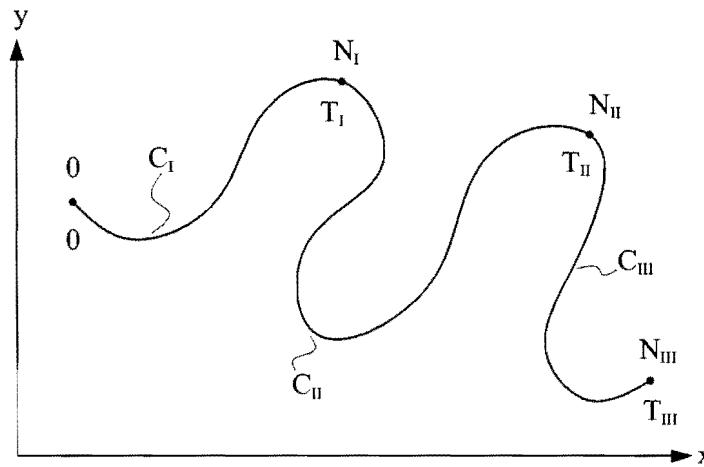
Figure 3.8: General curve where the prescribed speed is achieved.

Section 3.1.1.3 deals with the simplified situation of tangential acceleration along the prescribed curve until a specified tangential speed v^* is achieved at time $t_N = T$. A more realistic example is shown in Figure 3.8 where the motion is executed in three segments: tangential acceleration along curve C_I, constant tangential speed along curve C_{II}, and tangential deceleration along curve C_{III}. The set of nodal points associated with the general curve of Figure 3.8 is $\{P_i = (x_i, y_i), i = 0,1,...,N_I,...,N_{II},...,N_{III}\}$.

This Section proposes a methodology by means of which node numbers N_I and N_{II} may automatically be assigned, given the *prescribed* constant tangential speed v^* along C_{II} and the maximum *allowable* tangential acceleration $\ddot{s}_{ALLOW}$.

In what follows "speed" and "acceleration" refer to *tangential* speed and *tangential* acceleration, unless otherwise specified.

3.3.1 Linear segment with cubic blends

Assume that node numbers N_I and N_{II} are given. Node number N_{III} is automatically known, since it is the final node in the specified data series. Path lengths S_I, S_{II} and S_{III}, corresponding to the respective curves C_I, C_{II} and C_{III}, may then be determined by following the procedure outlined in Sections 3.1.1.1 and 3.1.1.2.

The acceleration curve C_I in Figure 3.8, corresponds to the situation already discussed in Section 3.1.1.3, i.e. a gradual increase in speed is required over the time interval $t \in [0, T_I]$, such that the prescribed speed v^* is attained at time T_I.

For curve C_I the distance along curve s_I at any instant t is represented by the cubic polynomial in time (see expression (3.15)):

$$s_I(t) = a_{sI} + b_{sI} t + c_{sI} t^2 + d_{sI} t^3, \ t \in [0, T_I] \tag{3.33}$$

$$\text{with quadratic expression } \dot{s}_I(t) = b_{sI} + 2c_{sI} t + 3d_{sI} t^2, \text{ for the speed} \tag{3.34}$$

$$\text{and linear form } \ddot{s}_I(t) = 2c_{sI} + 6d_{sI} t, \text{ for the acceleration} \tag{3.35}$$

The motion along the acceleration curve C_I is associated with boundary conditions that are similar to the ones given in Section 3.1.1.3; namely

$$s_I(0) = s_0 \text{ (usually } s_0 = 0 \text{)}$$

$$s_I(T_I) = S_I$$

$$\dot{s}_I(0) = v_0 \text{ (usually } v_0 = 0 \text{)}$$

$$\dot{s}_I(T_I) = v^*$$

$$\ddot{s}_I(T_I) = 0$$

The unknown coefficients a_{sI}, b_{sI}, c_{sI} and d_{sI}, as well as T_I are determined in exactly the same manner as explained in Section 3.1.1.1 (expressions (3.18) - (3.24)). With the coefficients and the time instant T_I known, the nodal times t_i, $i = 1, 2, ..., N_I$ may be obtained using Newton's method (see Section 3.1.1.3).

Along the constant speed segment C_{II} in Figure 3.8 the distance s_{II} along the curve from nodal point P_{N_I} is given by the following linear relationship in time:

$$s_{II}(t) = v^*(t - T_I), \ t \in [T_I, T_{II}] \tag{3.36}$$

For each node $P_i = (x_i, y_i)$, $i = N_I + 1, N_I + 2, ..., N_{II}$, the total path length S_i from P_0 up to the specific node P_i may be determined from (3.25):

$$S_i = \sum_{j=1}^{i} s_j, \ i = N_I + 1, N_I + 2, ..., N_{II} \tag{3.37}$$

The corresponding nodal times t_i, $i = N_I + 1, N_I + 2, ..., N_{II}$ then follow from (3.36):

$$t_i = \frac{S_i - S_I}{v^*} + T_I, \ i = N_I + 1, N_I + 2, ..., N_{II} \tag{3.38}$$

For the final deceleration segment C_{III} in Figure 3.8, the distance along the curve s_{III} from nodal point $P_{N_{II}}$ is also given by a cubic polynomial function of time:

$$s_{III}(t) = a_{s_{III}} + b_{s_{III}}(t - T_{II}) + c_{s_{III}}(t - T_{II})^2 + d_{s_{III}}(t - T_{II})^3, \quad t \in [T_{II}, T_{III}] \tag{3.39}$$

$$\dot{s}_{III}(t) = b_{s_{III}} + 2c_{s_{III}}(t - T_{II}) + 3d_{s_{III}}(t - T_{II})^2 \tag{3.40}$$

$$\ddot{s}_{III}(t) = 2c_{s_{III}} + 6d_{s_{III}}(t - T_{II}) \tag{3.41}$$

Since a decrease in speed is required along the deceleration segment C_{III}, the following boundary conditions are enforced:

$$s_{III}(T_{II}) = S_{II}$$

$$s_{III}(T_{III}) = S_{III}$$

$$\dot{s}_{III}(T_{II}) = v^*$$

$$\dot{s}_{III}(T_{III}) = 0$$

$$\ddot{s}_{III}(T_{II}) = 0$$

from which the coefficients $a_{s_{III}}$, $b_{s_{III}}$, $c_{s_{III}}$, $d_{s_{III}}$ and the final time instant T_{III} can be determined:

$$s_{III}(T_{II}) = a_{s_{III}} = S_{II}$$

$$\dot{s}_{III}(T_{II}) = b_{s_{III}} = v^*$$

$$\ddot{s}_{III}(T_{II}) = 2c_{s_{III}} = 0$$

$$\therefore c_{s_{III}} = 0$$

$$s_{III}(T_{III}) = S_{III} = a_{s_{III}} + b_{s_{III}}(T_{III} - T_{II}) + d_{s_{III}}(T_{III} - T_{II})^3 \tag{3.42}$$

$$\dot{s}_{III}(T_{III}) = 0 = b_{s_{III}} + 3d_{s_{III}}(T_{III} - T_{II})^2 \tag{3.43}$$

and with $b_{s_{III}} = v^*$ it follows from (3.43):

$$d_{s_{III}} = \frac{-v^*}{3(T_{III} - T_{II})^2} \tag{3.44}$$

and substituting (3.44) into (3.42):

$$T_{III} = \frac{3(S_{III} - S_{II})}{2v^*} + T_{II} \tag{3.45}$$

Newton's method is then used to determine the corresponding nodal times t_i, $i = N_{II} + 1, N_{II} + 2, ..., N_{III}$ in the manner already described in Section 3.1.1.3.

It follows that the motion, described in terms of the distance $s(t)$ along the general curve shown in Figure 3.8, is a *linear segment with cubic blends* (LSCB), since the cubic motions along curves C_I and

C_{III} are merged or blended with the constant velocity motion along curve C_{II} at the respective blend times T_I and T_{II} as shown in Figure 3.9 (see [60]).
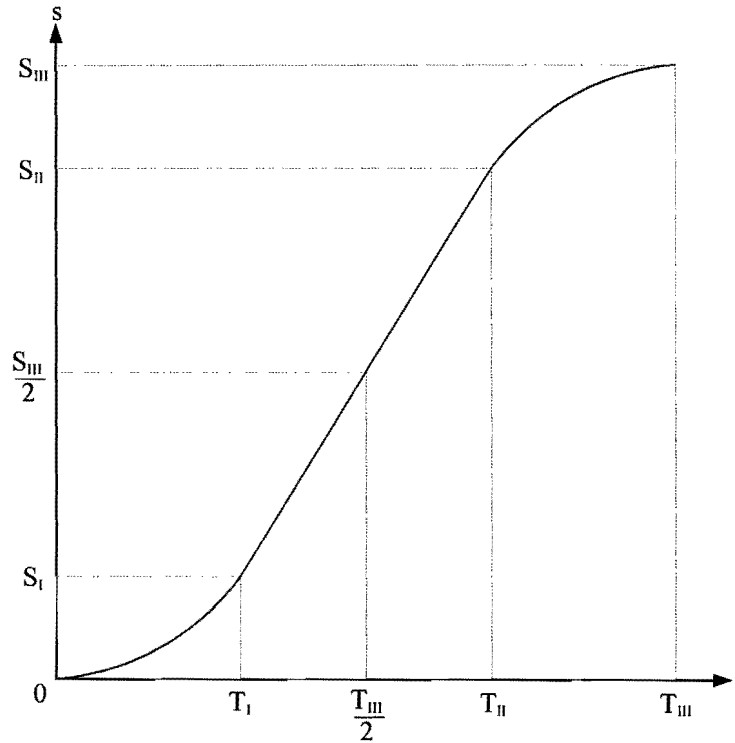
Figure 3.9: Linear segment with cubic blends (LSCB).

Blend time T_I is given by (3.24):

$$T_I = \frac{3(S_I - s_0)}{v_0 + 2v^*} \tag{3.46}$$

which reduces to $T_I = \dfrac{3S_I}{2v^*}$ with $s_0 = 0$ and $v_0 = 0$.

Similarly, blend time T_{II} is given by (3.45):

$$T_{III} - T_{II} = \frac{3(S_{III} - S_{II})}{2v^*} \tag{3.47}$$

The latter two equations indicate that if the nodal points N_I and N_{II} are chosen in such a way that $S_{III} - S_{II} = S_I$, then time spans $(T_I - 0)$ and $(T_{III} - T_{II})$ are equal. In this case the LSCB, as shown in Figure 3.9, is "centro-symmetric" with respect to the midpoint $\left[\dfrac{T_{III}}{2}, \dfrac{S_{III}}{2}\right]$ (see [60]).

Another important and desirable feature of the proposed LSCB motion, is the fact that the corresponding speed and acceleration curves are continuous as depicted in Figure 3.10.
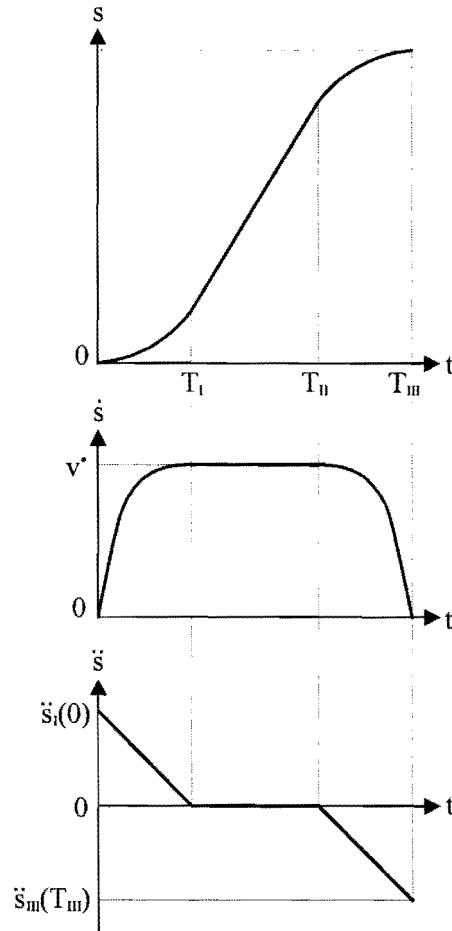
Figure 3.10: LSCB motion with its accompanying speed and acceleration curves.

The initial acceleration $\ddot{s}_I(0)$ is obtained by substituting (3.46) into (3.23) giving

$$c_{sI} = \frac{(v^* - v_0)(v_0 + 2v^*)}{3(S_1 - s_0)}$$

which, after substituting into (3.35) yields

$$\ddot{s}(0)_I = 2c_{sI} = \frac{2(v^* - v_0)(v_0 + 2v^*)}{3(S_1 - s_0)} \qquad (3.48)$$

Expression (3.48) simplifies further if $v_0 = 0$ and $s_0 = 0$, as is usually the case, to give

$$\ddot{s}_I(0) = \frac{4(v^*)^2}{3S_1} \qquad (3.49)$$

Further, by substituting $d_{sIII} = \dfrac{-v^*}{3(T_{III} - T_{II})^2}$ as well as (3.47) into (3.41), the final acceleration is given

by

$$\ddot{s}_{III}(T_{III}) = \frac{-4(v^{\bullet})^2}{3(S_{III} - S_{II})} \qquad (3.50)$$

If $S_{III} - S_{II} = S_I$, the magnitude of the initial acceleration $\ddot{s}_I(0)$ is equal to the magnitude of the final acceleration $\ddot{s}_{III}(T_{III})$ due to the symmetry that exists in this case (compare expressions (3.49) and (3.50)). It is of particular interest to note that for this symmetrical situation, the magnitudes of the accelerations at the initial and final times are not only equal but correspond to the *maximum* acceleration magnitude that occurs along the total curve.

3.3.2 *Treatment of constraint on acceleration*

The practical requirement that the prescribed motion is to be executed as fast as possible, is usually subject to a prescribed maximum *allowable* acceleration magnitude $\ddot{s}_{ALLOW}$. A procedure is now described that may be used to select appropriate node numbers N_I and N_{II} such that the following specific acceleration constraints are not violated:

$$\ddot{s}_I(0) \le \ddot{s}_{ALLOW} \qquad (3.51)$$

$$\left|\ddot{s}_{III}(T_{III})\right| \le \ddot{s}_{ALLOW} \qquad (3.52)$$

Since by (3.35) and (3.41) the acceleration along both C_I and C_{III} vary linearly with time, it follows that if the specific constraints (3.51) and (3.52) are satisfied, that the constraint on the acceleration is also satisfied at each instant along the whole path.

As before, for each node $P_i = (x_i, y_i)$, $i = 0,1,...,N_{III}$, the total path length up to the specific node may be determined using expression (3.25). A special nodal point N_{MID}, corresponding to a point approximately halfway along the total curve (i.e. for which $S_{N_{MID}} \approx \frac{S_{III}}{2}$) can be identified using the following criterion:

$$S_{MID} \le \frac{S_{III}}{2} < S_{MID+1} \qquad (3.53)$$

As a first iteration in finding the appropriate choices for nodes N_I and N_{II}, assume that nodes N_I and N_{II} coincide with node N_{MID} as shown in Figure 3.11.
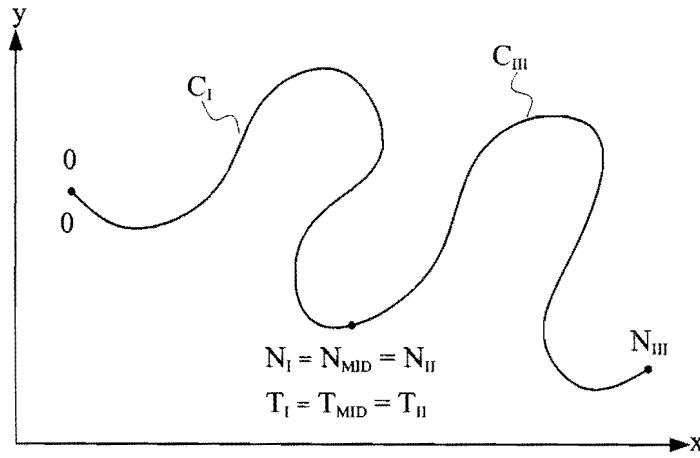
Figure 3.11: General curve showing the midpoint N_{MID}.

From (3.53) it follows that $S_{III} - S_{MID} \geq S_{MID}$, and with nodes N_I and N_{II} coinciding with node N_{MID}, it further follows that $S_{III} - S_{II} \geq S_I$ which, when substituted into (3.49) and (3.50), gives

$$\left| \ddot{s}_{III}(T_{III}) \right| \leq \ddot{s}_I(0) \tag{3.54}$$

Consequently, for the situation depicted in Figure 3.11, if the initial acceleration $\ddot{s}_I(0)$ satisfies constraint (3.51), the final acceleration $\ddot{s}_{III}(T_{III})$ will also satisfy constraint (3.52) and, indeed, the constraint on the magnitude of the acceleration will be satisfied at each instant along the total curve.

3.3.2.1 Attainment of central speed v^*

If the initial acceleration for the situation shown in Figure 3.11 satisfies constraint (3.51), the desired central speed v^* may be reached at node N_{MID}. For practical purposes the ideal objectives are, however:

1. to attain the desired central speed v^* in the *shortest* possible time T_I without exceeding the allowable maximum acceleration magnitude $\ddot{s}_{ALLOW}$, and

2. to maintain the desired speed v^* for the *longest* possible time span $(T_{II} - T_I)$ provided that, over the final time interval $[T_{II}, T_{III}]$, the maximum deceleration magnitude does not exceed the allowable magnitude $\ddot{s}_{ALLOW}$.

With reference to objective 1 above, expressions (3.46) and (3.48) respectively indicate that for a specific speed v^*, a shorter path length S_I will result in a shorter time T_I and a larger initial acceleration $\ddot{s}_I(0)$. By shifting, for example, node N_I to coincide with node $N_{MID} - 1$ the associated path length S_I and corresponding time T_I will be reduced, while the associated initial acceleration $\ddot{s}_I(0)$ will become larger. This increased initial acceleration is then tested against constraint (3.51), and if the constraint is

still satisfied, node N_I is shifted further to coincide with node $N_{MID} - 2$. These integer shifts are continued until, after p integer shifts, the choice of node N_I, coinciding with node $N_{MID} - p$, is such that the initial acceleration satisfies constraint (3.51), while the choice $N_I = N_{MID} - (p+1)$ violates the constraint.

With regard to objective 2, inspection of expressions (3.47) and (3.50), indicates that a decrease in the path length $(S_{III} - S_{II})$ will result in a shorter time span $(T_{III} - T_{II})$, and a larger final acceleration magnitude $|\ddot{s}_{III}(T_{III})|$. For example, if node N_{II} is shifted to coincide with node $N_{MID} + 1$ and thus shortens the path length $(S_{III} - S_{II})$ and the time span $(T_{III} - T_{II})$, it will result in a larger final acceleration magnitude $|\ddot{s}_{III}(T_{III})|$. If the larger $|\ddot{s}_{III}(T_{III})|$ satisfies constraint (3.52), node N_{II} may be shifted further to coincide with node $N_{MID} + 2$, etc. These integer shifts may be continued until, after q shifts, node N_{II}, coinciding with node $N_{MID} + q$ is such that the final acceleration magnitude $|\ddot{s}_{III}(T_{III})|$ satisfies constraint (3.52), while the choice $N_{II} = N_{MID} + (q+1)$ violates the constraint.

3.3.2.2 Violation of maximum allowable acceleration

If the initial acceleration, for the situation depicted in Figure 3.11 with specified central velocity v^*, violates constraint (3.51), a different strategy is proposed which ensures that the maximum allowable acceleration is not exceeded. For this case, the motion along the curve shown in Figure 3.11, consists of two blended cubic polynomials in time. The blend time is T_{MID} as shown in Figure 3.12:
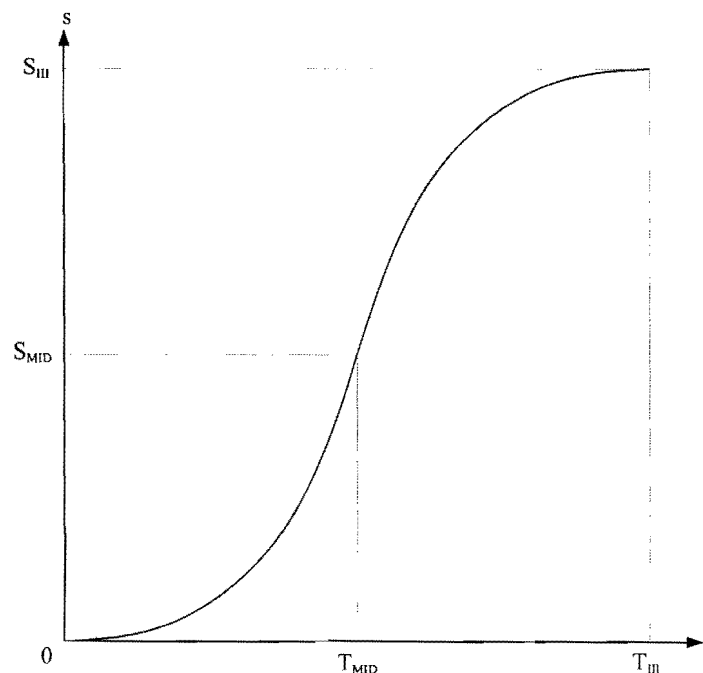
Figure 3.12: Blended cubic polynomials.

More specifically, the two objectives set in this case are:

1. to accelerate as fast as possible along curve C_I without violating constraint (3.51), and

2. to decelerate as fast as possible along curve C_{II} without violating constraint (3.52).

Objective 1 implies a different set of boundary conditions for determining the coefficients of the cubic polynomial function representing the path length along curve C_I (see expression (3.33)). These new boundary conditions are

$$s_I(0) = s_0 \ (\text{usually } s_0 = 0)$$

$$s_I(T_{MID}) = S_{MID}$$

$$\dot{s}_I(0) = v_0 \ (\text{usually } v_0 = 0)$$

$$\ddot{s}_I(0) = \ddot{s}_{ALLOW}$$

$$\ddot{s}_I(T_{MID}) = 0$$

from which a_{sI}, b_{sI}, c_{sI}, d_{sI}, and T_{MID} may be determined as follow:

$$s_I(0) = a_s = s_0$$

$$\dot{s}_I(0) = b_s = v_0$$

$$\ddot{s}_I(0) = \ddot{s}_{ALLOW} = 2c_{sI}$$

$$\text{and therefore } c_{sI} = \frac{\ddot{s}_{ALLOW}}{2},$$

$$s_I(T_{MID}) = S_{MID} = a_{sI} + b_{sI} T_{MID} + c_{sI}(T_{MID})^2 + d_{sI}(T_{MID})^3 \qquad (3.55)$$

$$\ddot{s}_I(T_{MID}) = 0 = 2c_{sI} + 6d_{sI} T_{MID} \qquad (3.56)$$

and thus

$$d_{sI} = \frac{-\ddot{s}_{ALLOW}}{6T_{MID}} \qquad (3.57)$$

Substituting (3.57) into (3.55): $s_I(T_{MID}) = S_{MID} = s_0 + v_0 T_{MID} + \frac{\ddot{s}_{ALLOW}}{3}(T_{MID})^2$

$$\text{which gives } T_{MID} = \frac{-v_0 \pm \sqrt{v_0^2 - 4\left(\frac{\ddot{s}_{ALLOW}}{3}\right)(s_0 - S_{MID})}}{2\left(\frac{\ddot{s}_{ALLOW}}{3}\right)}$$

and which reduces to

$$T_{MID} = \pm\sqrt{\frac{3S_{MID}}{\ddot{s}_{ALLOW}}} \qquad (3.58)$$

if $s_0 = 0$ and $v_0 = 0$

The positive root gives the sought after time instant T_{MID}.

From (3.34) and substituting the values of the coefficients determined above, the speed at node N_{MID} is

$$v_{MID} = \dot{s}_I(T_{MID}) = v_0 + \frac{\ddot{s}_{ALLOW}}{2} T_{MID}$$

which reduces to

$$v_{MID} = \dot{s}_I(T_{MID}) = \frac{\sqrt{3S_{MID}\ddot{s}_{ALLOW}}}{2} \tag{3.59}$$

if $s_0 = 0$ and $v_0 = 0$.

The cubic polynomial function of time representing the deceleration segment C_{III} in Figure 3.11 is given by expression (3.39). The unknown coefficients a_{sIII}, b_{sIII}, c_{sIII} and d_{sIII} as well as T_{III} are solved for by using similar boundary conditions as before:

$$s_{III}(T_{II}) = S_{MID}$$

$$s_{III}(T_{III}) = S_{III}$$

$$\dot{s}_{III}(T_{II}) = v_{MID}$$

$$\dot{s}_{III}(T_{III}) = 0$$

$$\ddot{s}_{III}(T_{II}) = 0$$

Substituting these conditions in the corresponding general expressions (3.39), (3.40) and (3.41) for s, $\dot{s}$ and $\ddot{s}$, and following the identical steps represented by equations (3.42) to (3.45) finally yields:

$$a_{sIII} = S_{MID}$$

$$b_{sIII} = v_{MID}$$

$$c_{sIII} = 0$$

$$d_{sIII} = \frac{-v_{MID}}{3(T_{III} - T_{MID})^2}$$

$$\text{and } T_{III} = \frac{3(S_{III} - S_{MID})}{2v_{MID}} + T_{MID}$$

As with the LSCB motion (see Figure 3.10), the blended cubic polynomials also result in continuous speed and acceleration curves as shown in Figure 3.13.
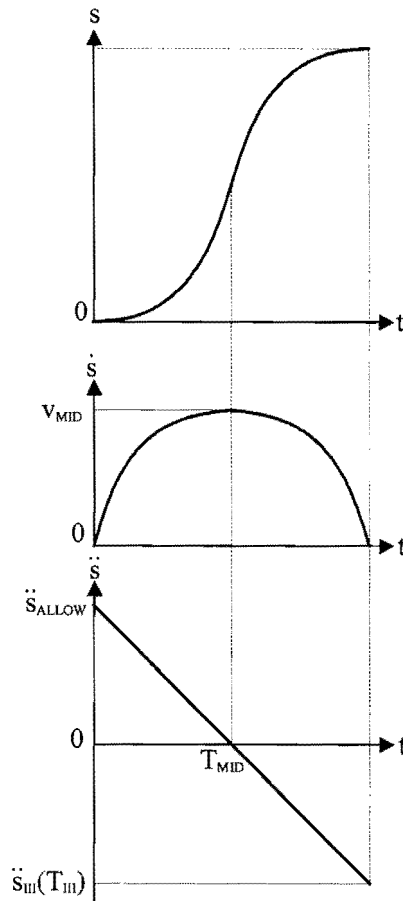
Figure 3.13: Blended cubic polynomials motion with its associated speed and acceleration curves.

From the above acceleration curve, it is clear that the initial acceleration is equal to the allowable maximum acceleration, i.e. $\ddot{s}_I(0) = \ddot{s}_{ALLOW}$. Since the final acceleration magnitude $\left|\ddot{s}_{III}(T_{III})\right|$ is either smaller than or equal to the initial acceleration magnitude $\ddot{s}_I(0)$ (see expression (3.54)), $\left|\ddot{s}_{III}(T_{III})\right|$ automatically satisfies acceleration constraint (3.52).

3.4   Incorporation of an orientation angle ϕ.

For certain applications of planar motion, the time parametric curves $X(t)$ and $Y(t)$ that interpolate the given set of nodal points $\{P_i = (x_i, y_i), i = 0, 1, ..., N\}$, are insufficient for the control of the particular mechanism, e.g. for a planar mechanism where the end-effector is to be orientated in a prescribed manner with respect to the tangent of the given path.

As an example, consider the situation where the orientation of the end-effector is to be exactly tangential to the curve, as the working point on the end-effector progresses along the prescribed curve. The gradient angle θ at any point along the curve is given by

$$\tan\theta = \frac{dy}{dx} \approx \frac{dp_i(x)}{dx} \text{ or } \left[\frac{dp_i(y)}{dy}\right]^{-1} \tag{3.60}$$

Another convenient form of expression (3.60) is

$$\tan\theta = \frac{\left(\dfrac{dy}{dt}\right)}{\left(\dfrac{dx}{dt}\right)} \approx \frac{\dot{Y}(t)}{\dot{X}(t)} \tag{3.61}$$

With the time parametric curves $X(t)$ and $Y(t)$ known, the respective derivatives $\dot{X}(t)$ and $\dot{Y}(t)$ are also known. Expression (3.61) may therefore be evaluated at nodal points P_i, $i = 0,1,...,N$ to find the corresponding values of θ_i, $i = 0,1,...,N$. As will be described below, the actual orientation angle ϕ of the end-effector is related to the angle θ in a non-straightforward manner as the working point executes the path.

In computing θ, care must be taken at nodes P_0 and P_N, since the respective speeds at these nodes are often zero, i.e. $\dot{s}_I(0) = v_0 = 0$ and $\dot{s}_{III}(T_{III}) = 0$. With this being the case, $\dot{X}(0) = \dot{Y}(0) = 0$ and $\dot{X}(T_{III}) = \dot{Y}(T_{III}) = 0$, and consequently expression (3.60) must be used instead of (3.61) to determine θ_0 and θ_N, since $\dfrac{dy}{dx}$ is known at nodes P_0 and P_N (see Section 3.2).

Since the arc tan function, through which θ is determined via (3.60) or (3.61), only assumes values between $-90°$ and $+90°$, a special procedure must be adopted to determine the exact orientation angle ϕ as the working point on the orientated end-effector tangentially follows the prescribed curve.
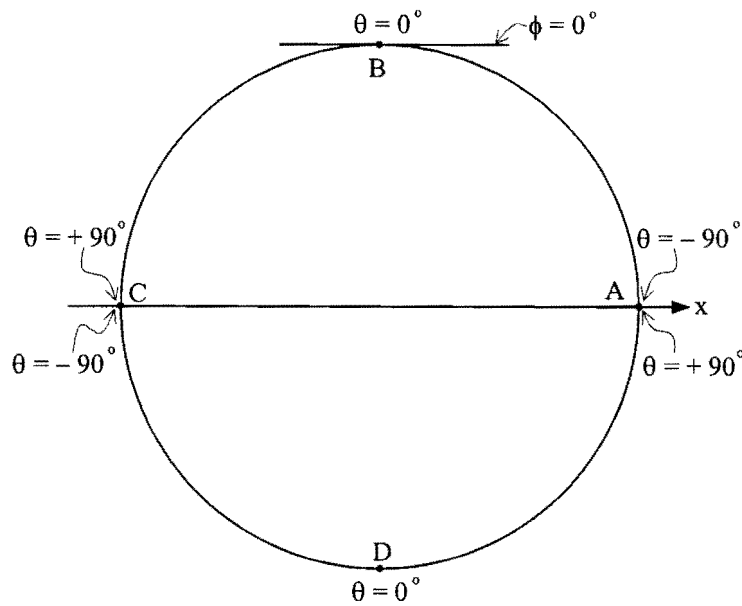
Figure 3.14: Circular prescribed curve.

Consider, for example, a prescribed circular curve as shown in Figure 3.14 with zero *orientation angle* ϕ at B. Starting at point A with θ and $\phi = -90°$ and progressing counterclockwise (CCW) around the circular curve the *gradient angle* θ computed via (3.60) or (3.61) gradually increases with ϕ from $-90°$ at A, to $0°$ at B, to $+90°$ at C. The CCW crossing of the x-axis at point C is however associated with a jump of $-180°$ in the computed *gradient angle* θ although ϕ is still clearly increasing continuously. Progressing CCW along the lower half of the circle again sees a gradual increase in the *gradient angle* θ from $-90°$ at C, to $0°$ at D, to $+90°$ at A, while ϕ continues to increase from $90°$ to $270°$ at A. At A where another jump of $-180°$ occurs in the computed value θ if the X-axis is crossed CCW.

A similar pattern is recognized using a clockwise (CW) tracing of the circular curve. Starting at point A, the computed *gradient angle* θ gradually decreases from $+90°$ at A, to $0°$ at D, to $-90°$ at C while ϕ decreases from $-90°$ at A to $-270°$ at C. The $+180°$ jump that occurs in θ with the CW crossing of the x-axis at C is followed by another gradual decrease in the *gradient angle* starting from $+90°$ at C, to $0°$ at B, to $-90°$ at A, while clearly ϕ continues to decrease from $-270°$ at C to $-450°$ at A.

The above-explained behavior of the *gradient angle* θ is used in establishing a procedure to determine the *orientation angle* ϕ:

If the jump between any two successive *gradient angles* θ_{i-1} and θ_i, $i = 1,2,...,N$ is smaller than $-90°$, i.e. $\theta_i - \theta_{i-1} \le -90°$, a CCW-counter I_{ccw} is incremented. Further reflection indicates that I_{ccw} should

also be incremented if $0 < \theta_i - \theta_{i-1} < 90°$. Similarly if $\theta_i - \theta_{i-1} \geq 90°$ or $-90° < \theta_i - \theta_{i-1} < 0$, a CW-counter I_{cw} is incremented. Using these counters, the true associated *orientation angles* ϕ_i, $i = 1, 2, ..., N$ are given by

$$\phi_i = \theta_i + (I_{ccw})(180°) \tag{3.62}$$

if $0 < \theta_i - \theta_{i-1} < 90°$, or $\theta_i - \theta_{i-1} \leq -90°$, and

$$\phi_i = \theta_i - (I_{cw})(180°) \tag{3.63}$$

if $-90° < \theta_i - \theta_{i-1} < 0$, or $\theta_i - \theta_{i-1} \geq 90°$

In general expressions (3.62) and (3.63) respectively are given by:

$$\phi_i = \theta_i + (I_{ccw})(180°) + \phi_{offset} \tag{3.64}$$

if $0 < \theta_i - \theta_{i-1} < 90°$, or $\theta_i - \theta_{i-1} \leq -90°$, and

$$\phi_i = \theta_i - (I_{cw})(180°) + \phi_{offset} \tag{3.65}$$

if $-90° < \theta_i - \theta_{i-1} < 0$, or $\theta_i - \theta_{i-1} \geq 90°$

The term ϕ_{offset} in expressions (3.64) and (3.65) is defined as the *offset orientation angle* of the end-effector measured in a CCW convention from the tangent to the prescribed path at the point of contact as shown in Figure 3.15.
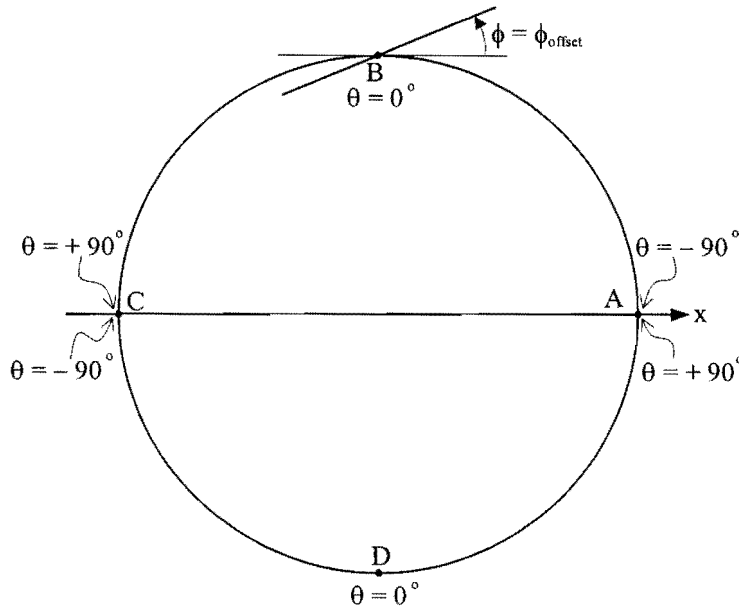
Figure 3.15: Circular prescribed curve with an angular offset added to the end-effector orientation.

Since the time instants t_i, $i = 0, 1, 2, ..., N$ are known (see Section 3.1.1.3), a cubic spline representation $\Phi(t)$ may now be determined in exactly the same way as the cubic spline representations $X(t)$ and

Y(t) (see Section 3.1.2). With the cubic spline $\Phi(t)$ known, the *continuous* first and second derivatives $\dot{\Phi}(t)$ and $\ddot{\Phi}(t)$ follow automatically.

Any prescribed path may also be traced with the end-effector posed in a specified fixed orientation ϕ_{fix}, thus eliminating the need to determine the cubic spline $\Phi(t)$ with its first and second derivatives $\dot{\Phi}(t)$ and $\ddot{\Phi}(t)$.

3.5 Test problems

The proposed trajectory planning methodology using Overlapping Cubic Arcs and (cubic) Splines (OCAS) is tested here on five different test functions. **Appendix B** contains a flow chart of the OCAS trajectory planning methodology.

3.5.1 Parabolic test function

The first test function is a parabola, where y is the quadratic function of x:

$$y(x) = \frac{x^2}{2} \tag{3.66}$$

The accuracy of the approximating fit is dependent on the number and distribution of the given nodal points $\{P_i = (x_i, y_i), i = 0,1,...,N\}$. The parabolic test function is approximated over the x-interval $x \in [-2,2]$ using 29 points spaced in such a way that they are more densely distributed at the beginning and end of the interval (see Figure 3.16). This is done to increase the accuracy of the calculation of the initial gradient $\frac{dy}{dx}$ at P_0 and final gradient $\frac{dy}{dx}$ at P_N as explained in Section 3.2. The nodal points are, for the obvious reason of greater accuracy, chosen more densely in neighborhood of the turning point where the greatest change in direction occurs.
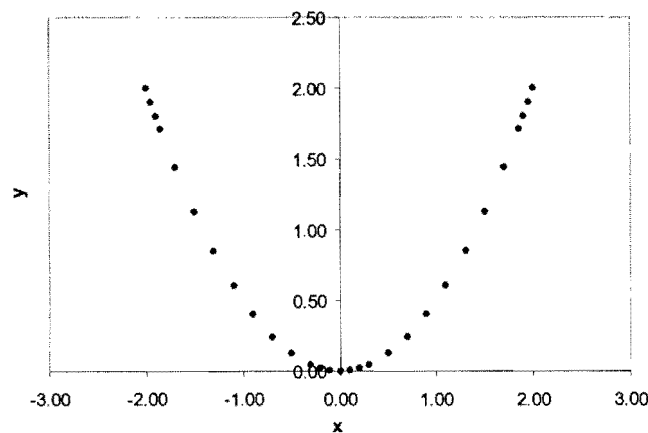
Figure 3.16: Nodal points used to approximate the parabolic test function.

In order to determine its accuracy, the fitted approximation is evaluated at chosen intermediate points between the pairs of consecutive nodes shown in Figure 3.16. Since the proposed OCAS-approach results in cubic spline representations for $X(t)$ and $Y(t)$ (see Section 3.1.2) over the time span between each pair of consecutive nodes, i.e. over $t_i - t_{i-1}$, $i = 1,2,...,28$, each interval may be subdivided to obtain a specified number of equally spaced additional *intermediate* time instants. The respective cubic spline representations $X(t)$ and $Y(t)$ are then evaluated at the *intermediate* time instants to give the corresponding *approximated intermediate* x- and y-values along the curve. Each approximated intermediate x-value lies in the interval $x \in [-2,2]$, and may therefore be substituted into (3.66) to find the corresponding *actual* y-value. For each intermediate x-value, the y-error is taken as the *absolute difference* between the *approximated* y-value and the *actual* y-value.
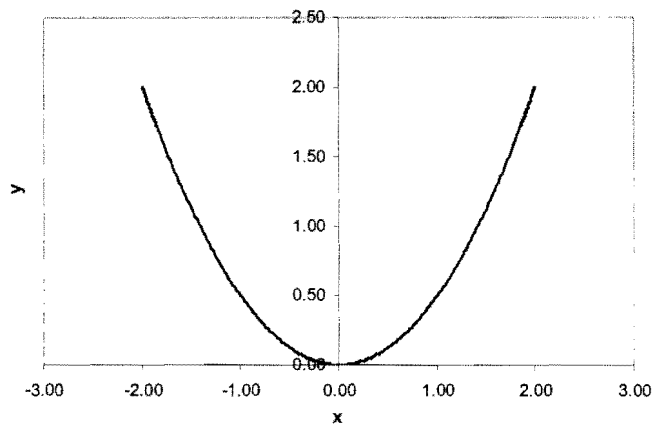
Figure 3.17: OCAS-approximation of parabolic test function.

Figure 3.17 shows the x-y profile obtained from the OCAS-approximation. Each consecutive time span $t_i - t_{i-1}$, $i = 1,2,...,28$ is divided into 10 equal subintervals and the curve in Figure 3.17 therefore represent a plot at 281 division points. The maximum absolute y-error over this set of points is 4.470×10^{-5} with an average error of 5.222×10^{-6}.

The trajectory planning along the parabolic profile was done by specifying a maximum allowable acceleration magnitude of 0.7 meter per second square, i.e. $\ddot{s}_{ALLOW} = 0.7$, and a specified central speed of 1.0 meter per second, i.e. $v^* = 1.0$. These specifications resulted in the LSCB-motion (see Section 3.3.1) shown in Figure 3.18. The blend times are $T_I = 2.922\,s$ and $T_{II} = 4.942\,s$ with the final time $T_{III} = 7.864\,s$. The initial acceleration is $\ddot{s}_I(0) = 0.684$ and the final acceleration is $\ddot{s}_{III}(T_{III}) = -0.684$ the magnitudes of which are both less than the specified maximum allowable acceleration magnitude $\ddot{s}_{ALLOW} = 0.7$.
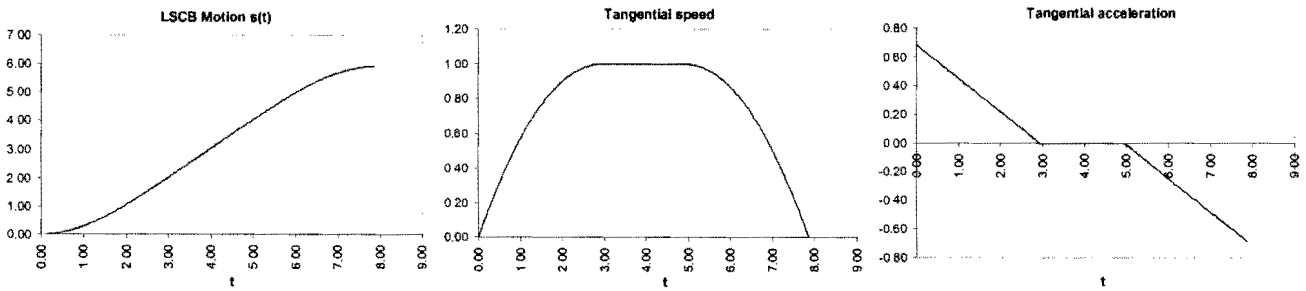
Figure 3.18: LSCB-motion for parabolic test function with its associated speed and acceleration curves.

The cubic spline representations $X(t)$ and $Y(t)$ that represent the x- and y-coordinate positions as functions of time, and plotted at the 281 time instants, are shown in Figure 3.19, together with the graphs of the continuous x- and y- velocities ($\dot{X}(t)$ and $\dot{Y}(t)$ designated as Vx and Vy) and accelerations ($\ddot{X}(t)$ and $\ddot{Y}(t)$ designated as Ax and Ay) over the total time interval $[0, 7.864]$. Note that the start point and end point of the prescribed trajectory follows from the cubic spline representations $X(t)$ and $Y(t)$, i.e. $(-2, 2)$ at $t = 0$ and $(2, 2)$ at $t = 7.864\,s$.
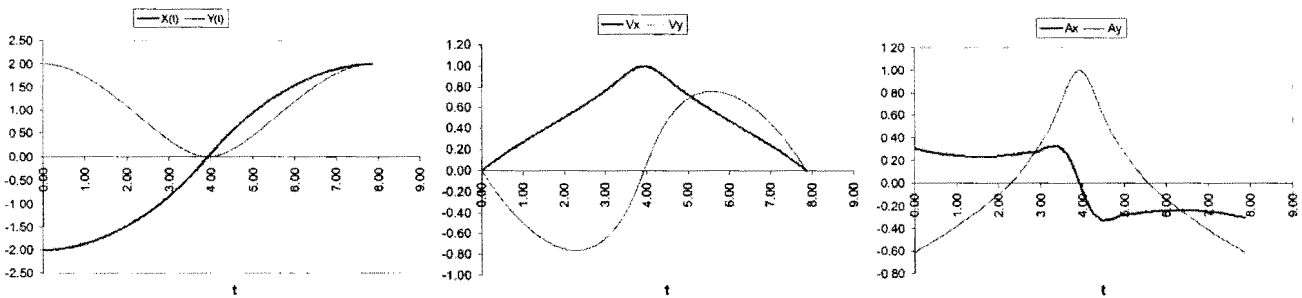
Figure 3.19: Plots of approximate coordinate positions, –velocities and –accelerations versus time for the parabolic test function.

With the specification that the end-effector be tangentially orientated with respect to the prescribed curve, (see Section 3.4), the cubic spline approximation $\Phi(t)$ representing the orientation angle ϕ [degrees] over the time interval $[0, 7.864]$ may be determined and is shown in Figure 3.20. Also shown in Figure 3.20 are the continuous orientation angular velocity curve $\dot{\Phi}(t)$ [rad/s] as well as the continuous orientation angular acceleration curve $\ddot{\Phi}(t)$ [rad/s^2].
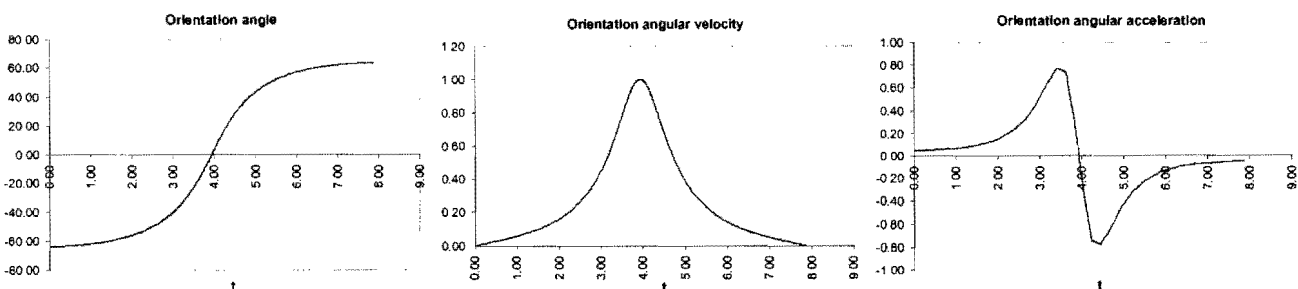
Figure 3.20: Plots of approximate orientation angle, orientation angular velocity and -acceleration for the parabolic test function.

3.5.2 Spike test function

The second test function is a spike test function taken from [68]:

$$y(x) = \frac{1}{1+x^2} \qquad (3.67)$$

This spike test function is also approximated over the x-interval $x \in [-2,2]$. The initial and final nodal points are $P_0 = (x_0, y_0) = (2, 0.2)$ and $P_N = (x_N, y_N) = (-2, 0.2)$ respectively. In total 27 nodal points are specified as shown in Figure 3.21, with denser distributions of nodal points at the end points of the interval, as well as at the midpoint as is evident in Figure 3.21.
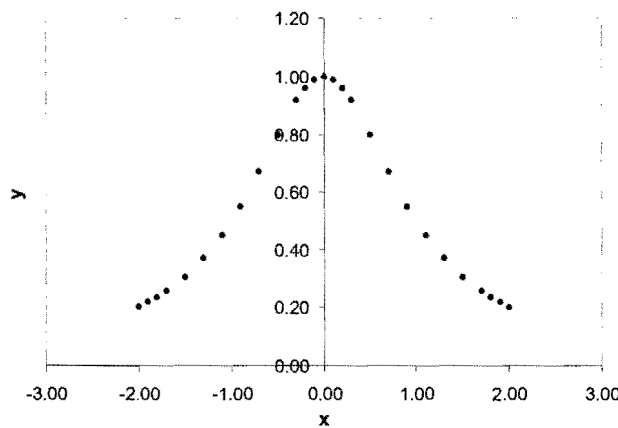
Figure 3.21: Nodal points used to specify the spike test function.

As in the case of the parabolic test function of Section 3.5.1, each consecutive time span $t_i - t_{i-1}$, $i = 1, 2, ..., 26$ is divided into 10 subintervals by equally spaced additional time instants. The approximate x-y profile is drawn by plotting the values at the 261 division points as shown in Figure 3.22. Here the absolute maximum y-error resulting from this approximation is 1.359×10^{-4} with average error 1.201×10^{-5}.
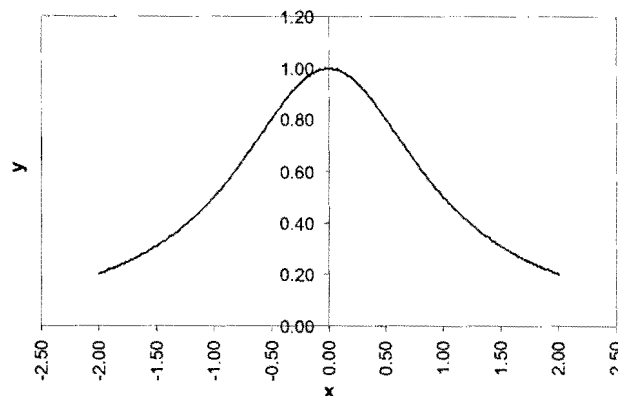
Figure 3.22: OCAS-approximation of spike test function.

With a specified central speed of $v^* = 1.0$ meter per second, and a specified maximum allowable acceleration $\ddot{s}_{ALLOW} = 0.5\,\text{m/s}^2$, the resulting motion is described by two blended cubic polynomials (see Section 3.3.2.2), as shown in Figure 3.23. The associated blend time is $T_{MID} = 3.6148\,\text{s}$, and from the tangential speeds graph in Figure 3.23 it is clear that the speed at the blend time, $v_{MID} = 0.9037\,\text{m/s}$, is slightly less that the desired speed of $v^* = 1.0\,\text{m/s}$. This is due to the fact that the magnitudes of both the initial and final curvature accelerations are equal to the maximum allowable acceleration of $\ddot{s}_{ALLOW} = 0.5\,\text{m/s}^2$.
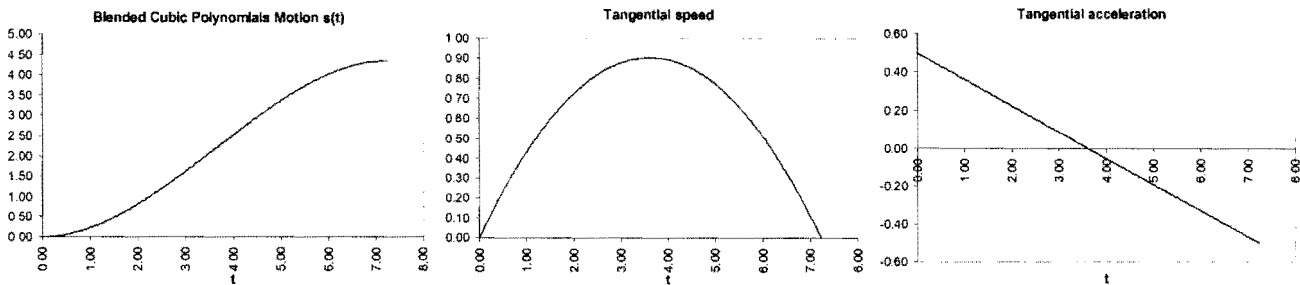
Figure 3.23: Blended cubic polynomials motion for spike test function with its associated speed and acceleration curves.

Figure 3.24 shows plots of the x- and y-positions $X(t)$ and $Y(t)$ (with start point $(2, 0.2)$ at $t = 0$ and end point $(-2, 0.2)$ at $t = 7.230\,\text{s}$), the x- and y-velocities $\dot{X}(t)$ and $\dot{Y}(t)$ (designated as Vx and Vy), and the x- and y-accelerations $\ddot{X}(t)$ and $\ddot{Y}(t)$ (designated as Ax and Ay) at the 261 time instants distributed over the time interval $[0, 7.230]$.
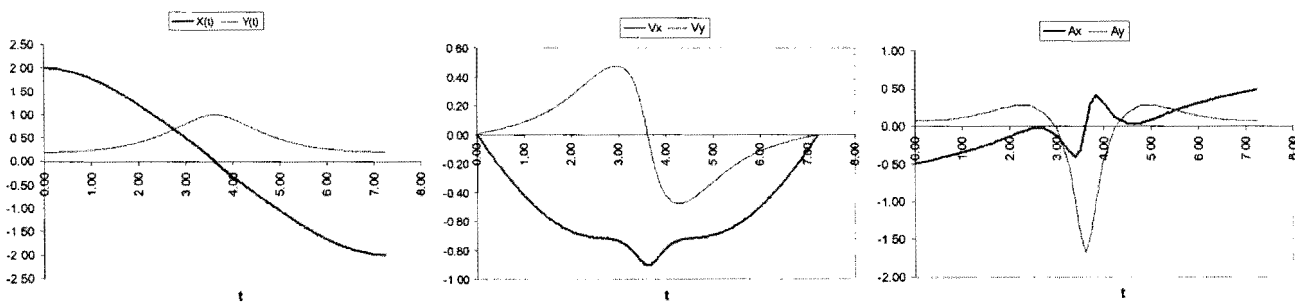
Figure 3.24: Plots of the approximate coordinates, velocities and accelerations versus time for the spike test function.

The tangentially orientated end-effector specification results in the cubic spline approximation $\Phi(t)$ [degrees] plotted in Figure 3.25, together with the corresponding plots of the continuous orientation angular velocity curve $\dot{\Phi}(t)$ [rad/s], and the continuous orientation angular acceleration curve $\ddot{\Phi}(t)$ [rad/s^2].
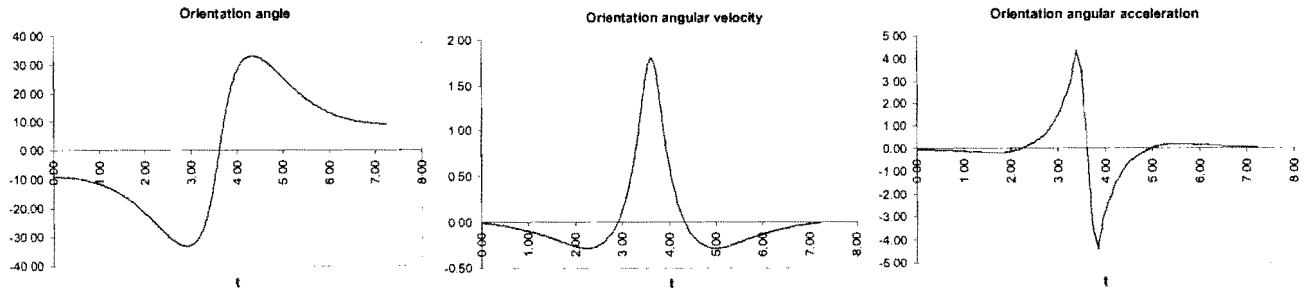
Figure 3.25: Plots of approximate orientation angle, orientation angular velocity and acceleration versus time for the spike test function.

In order to verify expressions (3.64) and (3.65), an orientation angle offset $\phi_{offset} = 30°$ is specified, and the associated cubic spline approximation $\Phi(t)$ [degrees] is plotted in Figure 3.26. Also shown in Figure 3.26 are the corresponding plots of the continuous orientation angular velocity curve $\dot{\Phi}(t)$ [rad/s], and the continuous angular acceleration curve $\ddot{\Phi}(t)$ [rad/s^2].
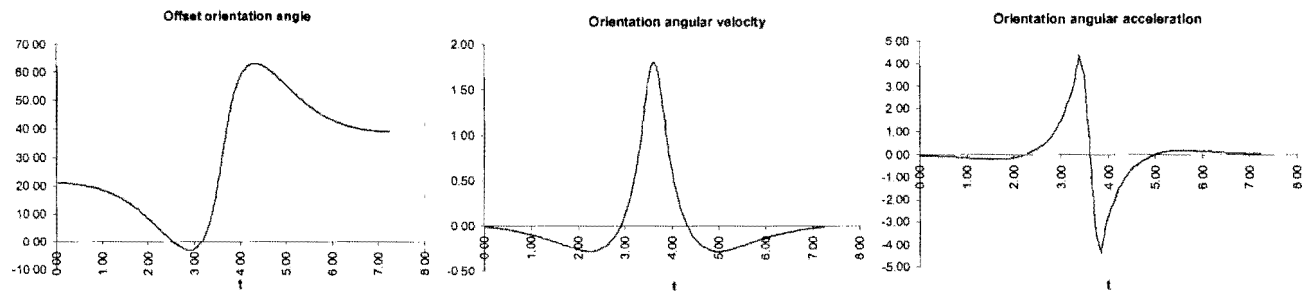
Figure 3.26: Plots of approximate offset orientation angle, orientation angular velocity and acceleration versus time for the spike test function.

Comparing the *offset* cubic spline approximation $\Phi(t)$ of Figure 3.26 with the *tangential* cubic spline approximation $\Phi(t)$ of Figure 3.25, it is clear that the specified offset ($\phi_{offset} = 30°$) resulted in an *upward* shift of the orientation angle curve. As expected, the orientation angular velocity and orientation angular acceleration curves of Figures 3.25 and 3.26 are in exact agreement.

3.5.3 Circular test curve

The ability of the proposed OCAS-approach to approximate curves that cannot be represented by unique-valued functions of one coordinate variable in terms of the other, is demonstrated here for the circle:

$$x^2 + y^2 = 9 \qquad (3.68)$$

The nodal points $\{P_i = (x_i, y_i), i = 0,1,...,N\}$ are specified using corresponding sweep angles $\beta_i \in [0°, 720°]$, where the sweep angle is measured clockwise from the positive x-axis. For any specific

sweep angle β_i, $i = 0,1,...,N$ the corresponding x- and y-values are given by $x_i = 3\cos\beta_i$, and $y_i = 3\sin\beta_i$ respectively. Here the sequence of sweep angles $\{\beta_i\}$ is chosen such that starting at $\beta = 0°$, two complete CCW revolutions are followed.

The spacing of the nodal points is again clustered around the beginning and end of the total interval as can be seen in Figure 3.27. A total of 79 nodal points cover the two revolutions of the circular path. The nodes for each revolution are shown separately in Figure 3.27. In particular, the first revolution ($\beta \in [0, 360°]$) is shown on the left-hand side of Figure 3.27, and the second revolution ($\beta \in [360°, 720°]$) is shown on the right-hand side of Figure 3.27.
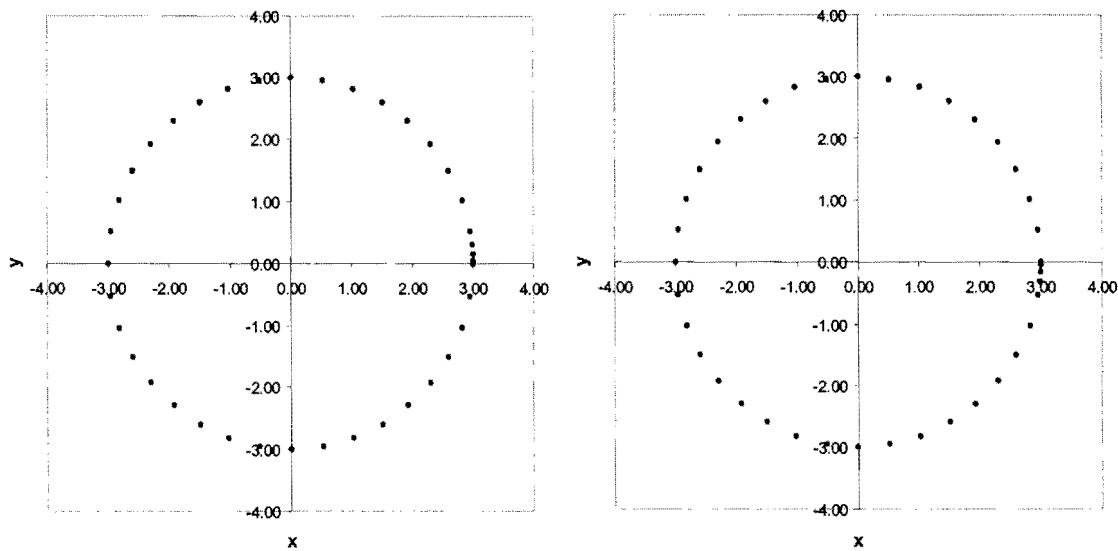
Figure 3.27: Nodal points used to approximate two revolutions of the circular curve.

As before, each time span $t_i - t_{i-1}$, $i = 1,2,...,78$ is divided into 10 equal subintervals for the purpose of mapping the computed approximation at the division points (see Section 3.5.1). The x-y-profile obtained from the OCAS-approximation at the specified division points is shown in Figure 3.28. For any given time instant the approximated x- and y-coordinates correspond to an *approximated* radius, from which the absolute radius error can be calculated. The maximum absolute radius error computed over the 781 division points is 5.27×10^{-5} with an average error of 6.27×10^{-6}.
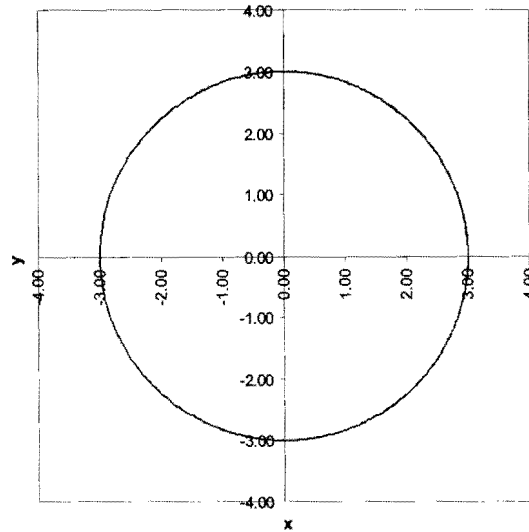
Figure 3.28: OCAS-approximation of circular test curve.

The trajectory planning is done by limiting the maximum allowable acceleration to 0.5 meter per second square, i.e. $\ddot{s}_{ALLOW} = 0.5 \, \text{m/s}^2$, and by specifying a central speed of 1.0 meter per second, i.e. $v^* = 1.0 \, \text{m/s}$. These specifications resulted in a LSCB- motion with corresponding blend times $T_I = 4.712 \, \text{s}$ and $T_{II} = 36.127 \, \text{s}$ (see Figure 3.29) and total path time $T_{III} = 40.841 \, \text{s}$. The initial and final tangential accelerations are $\ddot{s}_I(0) = 0.424 \, \text{m/s}^2$ and $\ddot{s}_{III}(T_{III}) = -0.424 \, \text{m/s}^2$ both satisfying the bound on the magnitude of accelerations.
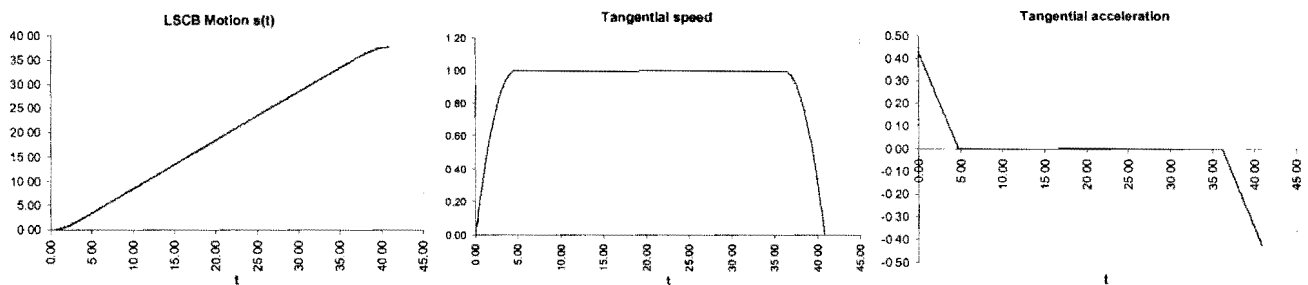
Figure 3.29: LSCB-motion for the circular curve with its accompanying speed and acceleration curves.

Figure 3.30 shows the x- and y-positions $X(t)$ and $Y(t)$ (with start point $(3,0)$ at $t = 0$ and end point $(3,0)$ at $t = 40.841 \, \text{s}$), the x- and y-velocities $\dot{X}(t)$ and $\dot{Y}(t)$ (designated as Vx and Vy), and the x- and y-accelerations $\ddot{X}(t)$ and $\ddot{Y}(t)$ (designated as Ax and Ay) over the time interval $[0, 40.841]$.
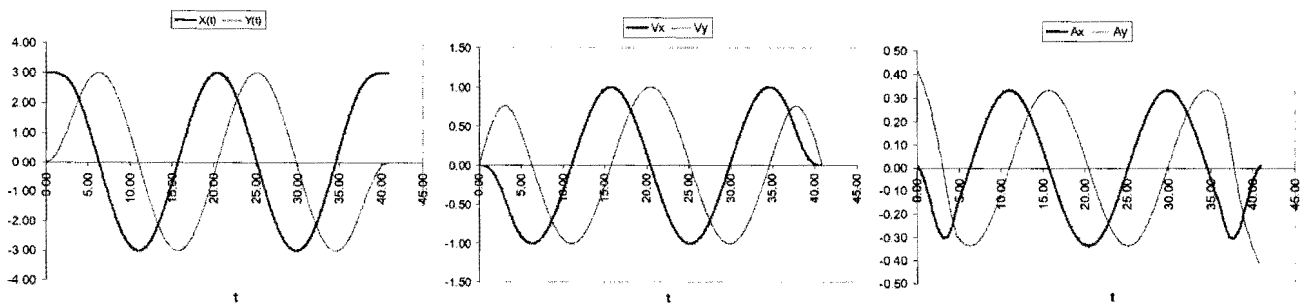
Figure 3.30: Plots of the approximate coordinates, velocities and accelerations versus time for the circular curve.

For the circular test curve, the situation depicted in Figure 3.14 occurs, where the specification of a tangentially orientated end-effector necessitates the monitoring of the behavior of the *calculated gradient angle* θ to keep track of the end-effector *orientation angle* ϕ (see Section 3.4). The corresponding cubic spline approximation $\Phi(t)$ [degrees] that results from the monitoring procedure outlined in Section 3.4 is shown in Figure 3.31. Since the nodal points were specified within the sweep angle range of $[0°,720°]$, the *orientation angle* varies from $-90°$ to $630°$. The corresponding orientation angular velocity curve $\dot{\Phi}(t)$ [rad/s] and the orientation angular accelerations $\ddot{\Phi}(t)$ [rad/s^2] are also shown in Figure 3.31.
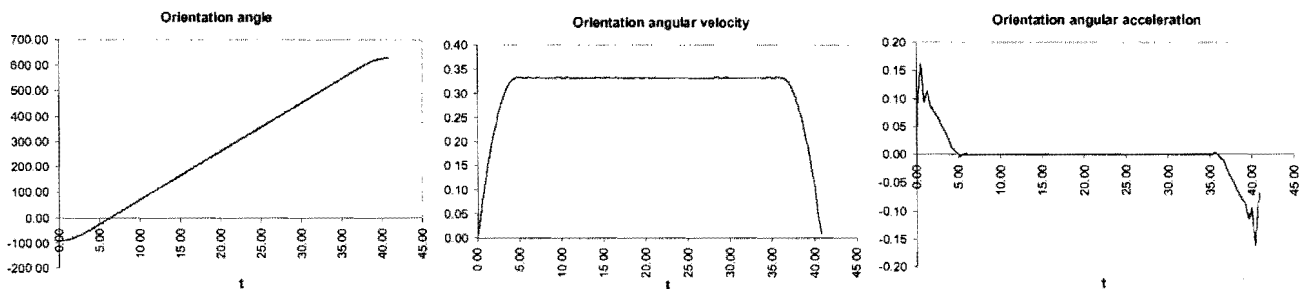
Figure 3.31: Plots of the approximate orientation angle, orientation angular velocity and orientation angular acceleration versus time for the circular test curve.

The unexpected spikes at the beginning- and endpoints of the angular acceleration curve, as opposed to the smooth behavior of both $\ddot{X}(t)$ and $\ddot{Y}(t)$ in the same regions, are probably due to the slight inaccuracies introduced in the calculation of the gradient angle via expressions (3.60) and (3.61). Expression (3.60) uses the *approximated* gradient, while expression (3.61) uses the *approximated* x- and y-velocities to find the gradient angle θ.

For the circular test curve under consideration, the exact gradient angle θ (and orientation angle ϕ) corresponding to a given *sweep angle* β may be determined (see Figure 3.32).
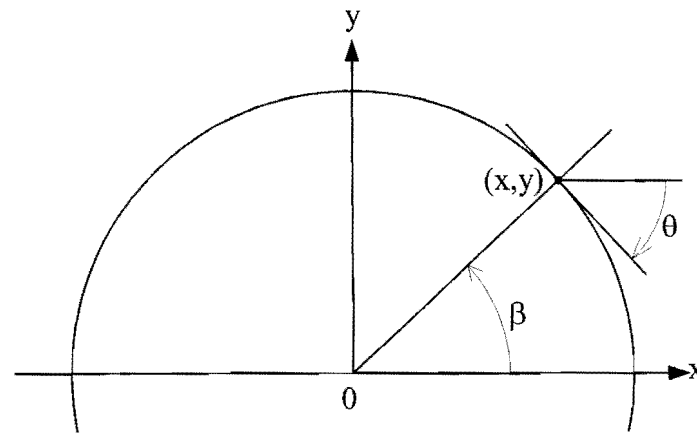
Figure 3.32: Exact gradient angle for a given sweep angle.

The figure clearly shows that the relationship $\tan\beta = \frac{y}{x}$ applies, from which it follows that the exact

gradient angle is $\theta = \beta - 90°$, which also allows for the exact determination of ϕ. With this information

available a comparison can be made between the approximated and exact orientation angle at any point

along the curve.

Corresponding to the determination of the absolute radius error, the absolute difference between the

approximated orientation angle, and the exact orientation angle is referred to as the orientation angle

error. For the circular test curve, the maximum absolute orientation angle error over all the 781 division

points is 5.714×10^{-4} rad, i.e. $0.03274°$ with an average error 3.742×10^{-5} rad, i.e. $0.00214°$.

3.5.4 Logarithmic spiral test curve

The final analytical test curve is the logarithmic spiral taken from [69]:

$$\rho = e^{0.1\beta} \tag{3.69}$$

which specifies the relationship between the polar coordinates (ρ, β) of any point on the curve.

As in the case of the circular curve of Section 3.5.3, the spiral curve can also not be expressed as a

function of one coordinate variable in terms of the other. The nodal points $\{P_i = (x_i, y_i), i = 0,1,...N\}$ are

generated via (3.69) where the polar angle plays the role of a sweep angle β_i. For the spiral test curve

the sweep angle ranges from $-\pi$ to -5π, i.e. $\beta \in [-\pi, -5\pi]$. Note that the sweep angle is incremented

such that the logarithmic spiral curve is traced in a CW manner, as opposed to the CCW-tracing of the

circular test curve (see Section 3.5.3). The 79 nodal points specified are shown in Figure 3.33
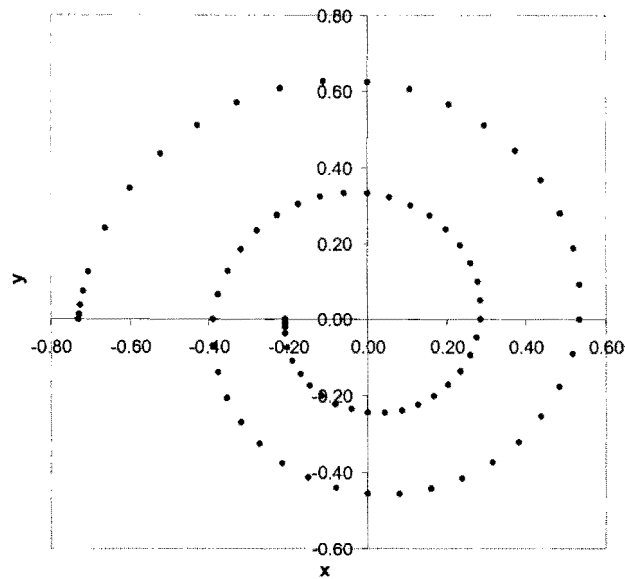
Figure 3.33: Nodal points used to approximate the spiral test curve.

Using the same procedure as outlined before, the x-y profile may be mapped at 781 division points as shown in Figure 3.34. For each interpolated point the x and y coordinates yield an interpolated radius, i.e. $r = \sqrt{x^2 + y^2}$. Furthermore, for each interpolated point the relationship $\tan\beta = \dfrac{y}{x}$ applies as it does for the circular test curve (see Figure 3.32). The calculated β-angle is used in a special procedure similar to the one explained in Section 3.4, to determine the exact β-polar coordinate associated with the interpolated point. Hence, by substituting the exact β-polar coordinate into expression (3.69), the ρ-polar coordinate as well as the absolute radius error $|\rho - r|$ associated with the interpolated point may be determined. The maximum absolute radius error for the spiral test curve over the 781 division points is 1.361×10^{-5} with average error 7.258×10^{-7}.
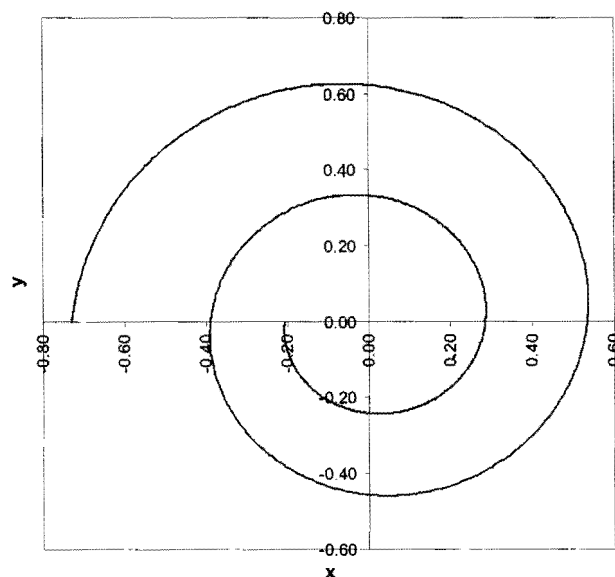
Figure 3.34: OCAS-approximation of spiral test curve.

Here the bound on the maximum allowable acceleration is 0.7 meter per second square, and a central speed of $v^* = 1\,m/s$ is specified. The resulting LSCB motion is shown in Figure 3.35, for which the respective blend times are $T_I = 2.968\,s$ and $T_{II} = 4.275\,s$ with total path time $T_{III} = 7.224\,s$. The tangential accelerations are within the specified limits, since $\ddot{s}_I(0) = 0.674 < 0.7$ and $\left|\ddot{s}_{III}(T_{III})\right| = \left|-0.678\right| < 0.7$.
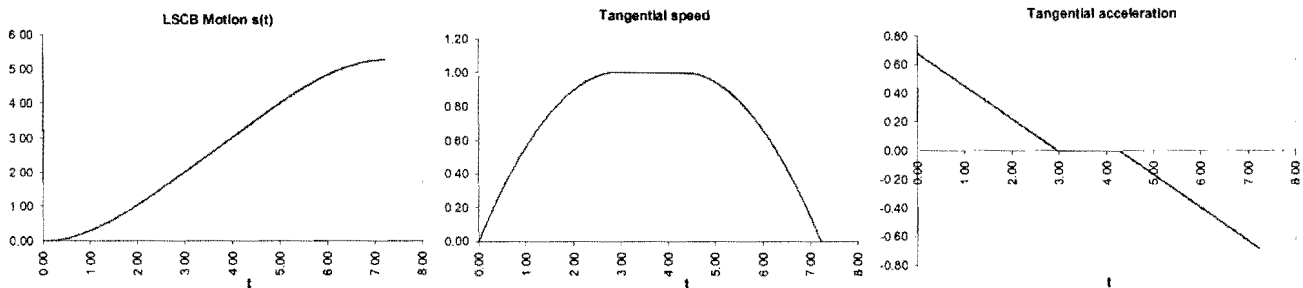
Figure 3.35: LSCB-motion for the spiral test curve with its accompanying speed and acceleration curves.

The corresponding approximated x- and y-positions $X(t)$ and $Y(t)$ (with start point $(-0.730, 0)$ at $t = 0$ and end point $(-0.208, 0)$ at $t = 7.224\,s$), x- and y-velocities $\dot{X}(t)$ and $\dot{Y}(t)$ (designated as Vx and Vy), and x- and y-accelerations $\ddot{X}(t)$ and $\ddot{Y}(t)$ (designated as Ax and Ay) computed at the 781 division points are plotted in Figure 3.36.
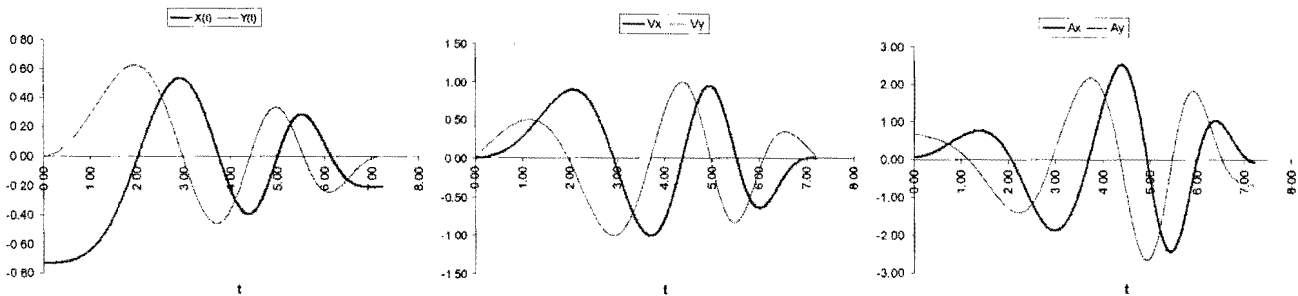
Figure 3.36: Plots of the approximate coordinates, velocities and accelerations versus time for the spiral test curve.

As for the circular test curve, the orientation angles of the spiral test curve are determined using the monitoring procedure outlined in Section 3.4. The end-effector orientation angle of the spiral test curve varies between $84.29°$ and $-635.71°$ as shown in Figure 3.37.
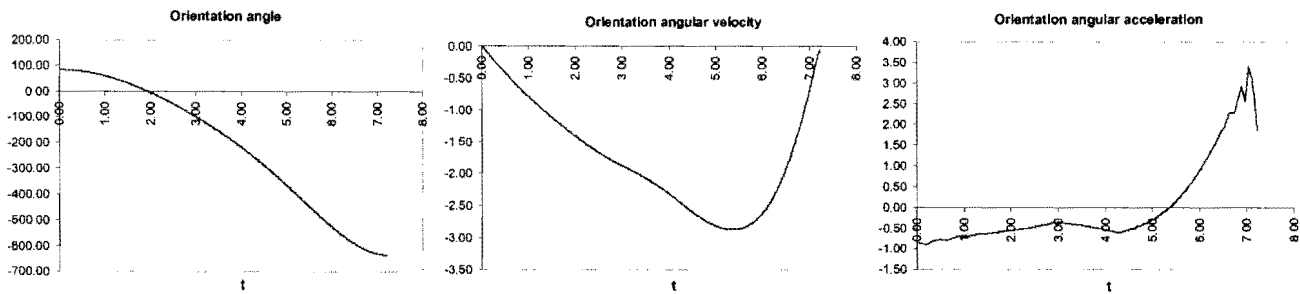
Figure 3.37: Plots of the approximate orientation angle, orientation angular velocity and orientation angular acceleration versus time for the spiral test curve.

The orientation angular velocities [$\mathrm{rad/s}$] and the orientation angular accelerations [$\mathrm{rad/s^2}$] are also shown in Figure 3.37. Again the spikes at end point of the angular acceleration curve are probably due to slight inaccuracies in the determination of the orientation angle (see Section 3.5.3).

Although specifying an angular offset $\phi_{\mathrm{offset}} = -45°$ shifts the orientation angle curve *down* as shown in Figure 3.38, the orientation angular velocity and orientation angular acceleration curves remain unchanged. In particular, the *offset* orientation angle of the spiral test curve varies between $39.29°$ and $-680.71°$.
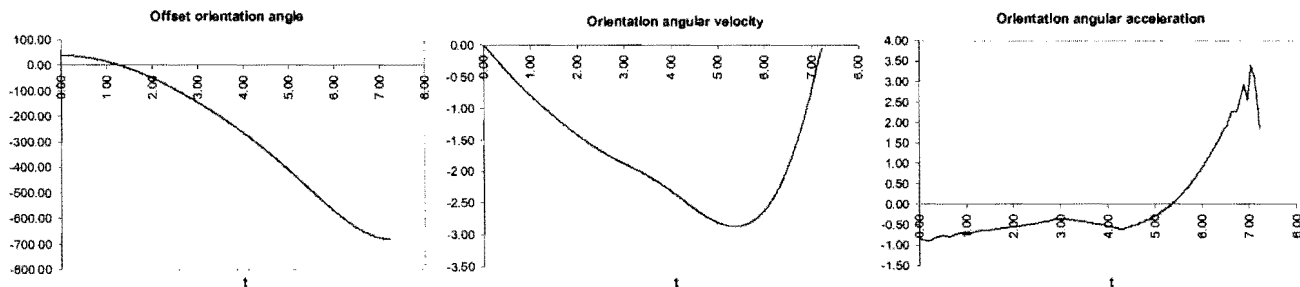
Figure 3.38: Plots of the approximate offset orientation angle, orientation angular velocity and orientation angular acceleration versus time for the spiral test curve.

3.5.5 Non-analytical test curve

The final test curve is the non-analytical treble clef shown in Figure 3.39. The particular curve is a Non-Uniform Rational B-Spline (NURBS) generated with commercial Computer Aided Design (CAD) software, and fitted through the 42 nodal points also indicated in Figure 3.39. For trajectory planning purposes, the start- and end points are as indicated in Figure 3.39.

This illustrative example is typical of a real life situation where the prescribed curve is an arbitrary smooth curve for which no analytical expression exists.
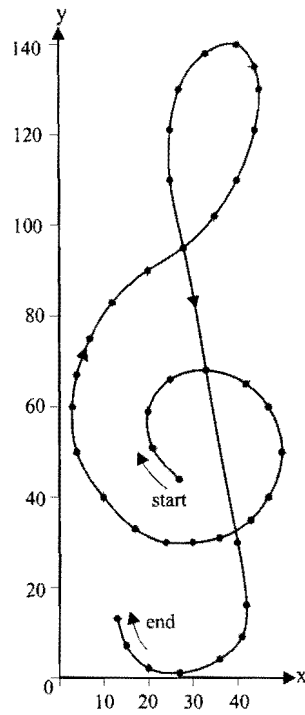
Figure 3.39: CAD-spline drawing through specified points of the treble clef test curve.

The OCAS trajectory planning methodology is tested by specifying different sets of nodal points, where the nodal points of each set are differently spread along the CAD spline treble clef. In particular, three different sets of nodal points are chosen with respectively 22, 31 and 49 nodal points. The approximated OCAS x-y profiles computed at respectively 211, 301 and 481 division points are shown in Figure 3.40.
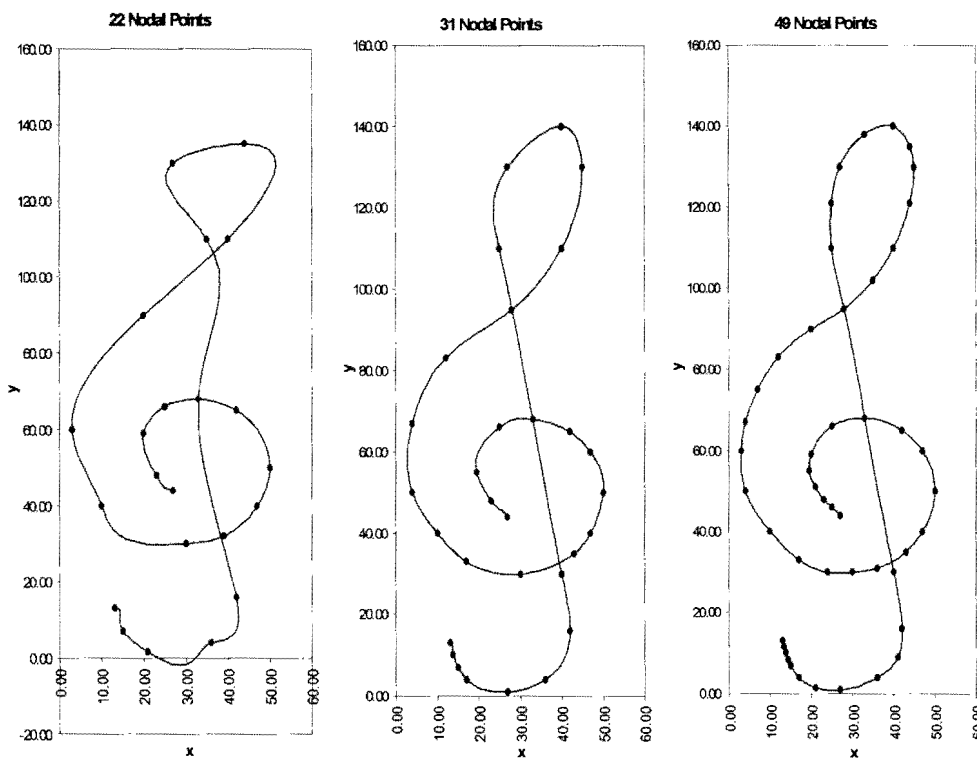
Figure 3.40: Three OCAS approximations of treble clef test curve.

By comparing Figure 3.40 with Figure 3.39, it is evident that the approximation capability of the OCAS trajectory planning methodology is accurate with relatively few specified nodal points. Using only 31 nodal points yields a reasonably accurate fit, while using 49 nodal points yields an approximation which by inspection shows no deviation from the original CAD-spline treble clef. However, specifying too few nodal points, and in an injudicious manner, results in a poor approximation as can be seen from the x-y profile computed for the 22 chosen nodal points in Figure 3.40.

The results presented in Figure 3.40 also emphasize the importance of clustered distributions of nodal points near the extreme points (especially the end point) of the prescribed curve, which ensure accurate approximations to $\dfrac{dy}{dx}$ at P_0 and P_N.

Since the choice of 49 nodal points gives the best approximation, its associated trajectory planning results are also shown. Here the bound on the maximum allowable acceleration is $5 \, mm/s^2$, and a central speed of $v^* = 10 \, mm/s$ is specified. The resulting LSCB motion is shown in Figure 3.41, for which the respective blend times are $T_I = 5.126 \, s$ and $T_{II} = 40.1435 \, s$ with total path time $T_{III} = 44.693 \, s$. The tangential accelerations are within the specified limits, since $\ddot{s}_I(0) = 3.834 < 5$ and $|\ddot{s}_{III}(T_{III})| = |-4.396| < 5$.
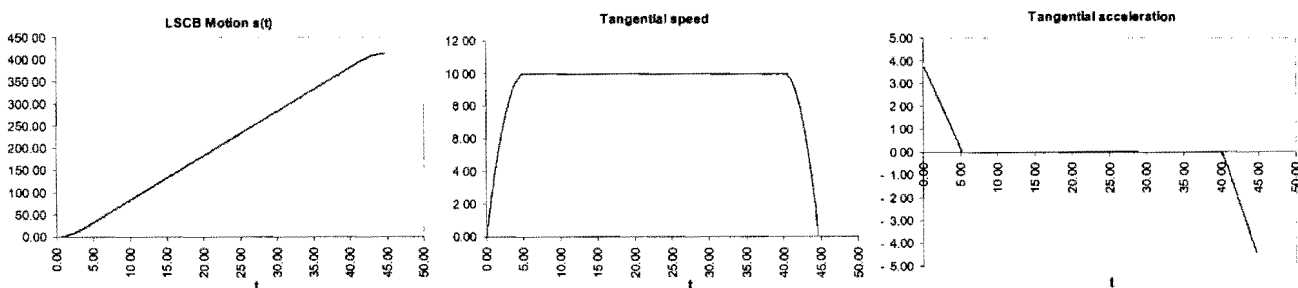

Figure 3.41: LSCB-motion for the treble clef test curve with its accompanying speed and acceleration curves.

The corresponding approximated x- and y-positions $X(t)$ and $Y(t)$ (with start point $(27.0, 44.0)$ at $t = 0$ and end point $(13.0, 13.0)$ at $t = 44.693 \, s$), x- and y-velocities $\dot{X}(t)$ and $\dot{Y}(t)$ (designated as Vx and Vy), and x- and y-accelerations $\ddot{X}(t)$ and $\ddot{Y}(t)$ (designated as Ax and Ay) computed at the 481 division points are plotted in Figure 3.42.
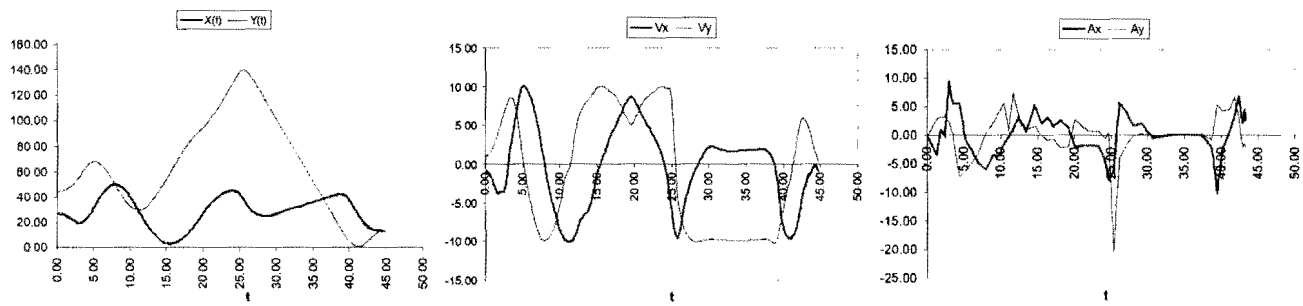
Figure 3.42: Plots of the approximate coordinates, velocities and accelerations versus time for the treble clef test curve.

The treble clef prescribed curve is traced with the end-effector in a fixed horizontal orientation $\phi = 0°$, hence the orientation angle curves are omitted here.

4 THE DETERMINATION OF OPTIMUM PLATFORM GEOMETRIES FOR PRESCRIBED MACHINING TASKS

4.1 Introduction

Du Plessis et al. [70] introduced the unique concept of an *adjustable geometry* planar Gough-Stewart platform machining center, where the geometry of the planar machining center is *optimized* using the LFOPC-algorithm [64]. The geometry was optimized with respect to the *static actuator forces* required to hold the mechanism in static equilibrium at each instant along the prescribed path. The *dynamic actuator forces* were also taken into account in the work by Snyman and Smit [71], in which the manipulator dynamics were simulated using the *Dynamic Analysis Design System* (DADS v. 9.0) [72]. They found that optimizing the platform geometry using the DADS software for the dynamics was computationally expensive if excessive numerical noise in the objective functions was to be avoided.

This chapter now explains how the LFOPC-algorithm [64] may be used to *optimize* the adjustable geometry of the planar Gough-Stewart platform machining center for any reasonably prescribed path using the stand-alone and *fundamentally based inverse dynamic analysis* procedure developed in **Chapter 2**. Here the actuator forces are determined as the manipulator moves in a prescribed manner along the specified path. In this study, the path specification is done using to the OCAS trajectory-planning methodology as explained in **Chapter 3**.

Minimizing the dynamic actuator forces required for executing the prescribed path with respect to the geometry, results in the avoidance of the very large actuator forces associated with singularities. Furthermore, as a by-product of the *constrained* optimization procedure, a *positioning* of the planar Gough-Stewart platform relative to the prescribed path is obtained that automatically ensures that the tool path is *feasibly placed* within the *workspace* of the mechanism. If it is not possible to place the prescribed path inside the workspace of the manipulator, the optimization algorithm yields an optimum compromised design geometry which allows the user to intervene in a rational manner.

Section 4.2 explains the formulation of the basic constrained optimization problem, while Section 4.3 gives details regarding the evaluation of the objective and constraint functions. The procedure for solving the optimization problem is explained in Section 4.4. Finally, the results of a representative optimization test run are shown and discussed in Section 4.5.

4.2 Formulation of the constrained optimization problem

In general, any conceptual design, dependent on n real *design variables* $\mathbf{X} = [X_1, X_2, X_3, ..., X_n]^T$, can be optimized by firstly defining an appropriate *objective function* $F(\mathbf{X})$, and where applicable, additional *inequality constraints* $C_j(\mathbf{X}) \leq 0$ ($j = 1,2,3,...m$) and *equality constraints* $H_k(\mathbf{X}) = 0$ ($k = 1,2,3,...p < n$). The optimum design $\mathbf{X}^*$ and optimum objective function value $F(\mathbf{X}^*)$ can then be found by applying any one of several available optimization techniques or algorithms, to solve the following mathematically formulated (constrained) optimization problem:

$$\underset{\mathbf{X}}{\text{minimize}} \ F(\mathbf{X})$$

$$\text{with } \mathbf{X} = [X_1, X_2, X_3, ..., X_n]^T \tag{4.1}$$

$$\text{such that } C_j(\mathbf{X}) \leq 0 \quad j = 1,2,3,...m \text{ and } H_k(\mathbf{X}) = 0 \ ; \ k = 1,2,3,...p < n$$

The selection of the design variables must be such that the objective function $F(\mathbf{X})$, the inequality constraint functions $C_j(\mathbf{X})$ ($j = 1,2,3,...m$) and the equality constraint functions $H_k(\mathbf{X})$ ($k = 1,2,3,...p < n$) are all dependent on $\mathbf{X} = [X_1, X_2, X_3, ..., X_n]^T$.

4.2.1 Design variables describing the adjustable geometry of the planar Gough-Stewart platform machining center

With reference to **Chapter 2**, where the planar Gough-Stewart platform machining center was introduced (see Figure 2.2 and 2.5), the positioning of the actuator joints on the base and on the moving platform may easily be adjusted. This feature is also incorporated in the practical design of the planar Gough-Stewart platform test-model with *continuously* adjustable geometry (see **Appendix D**). In particular the five design variables $\mathbf{X} = [X_1, X_2, X_3, X_4, X_5]^T$, indicated by the arrows in Figure 4.1, are used to describe the proposed adjustable geometry.
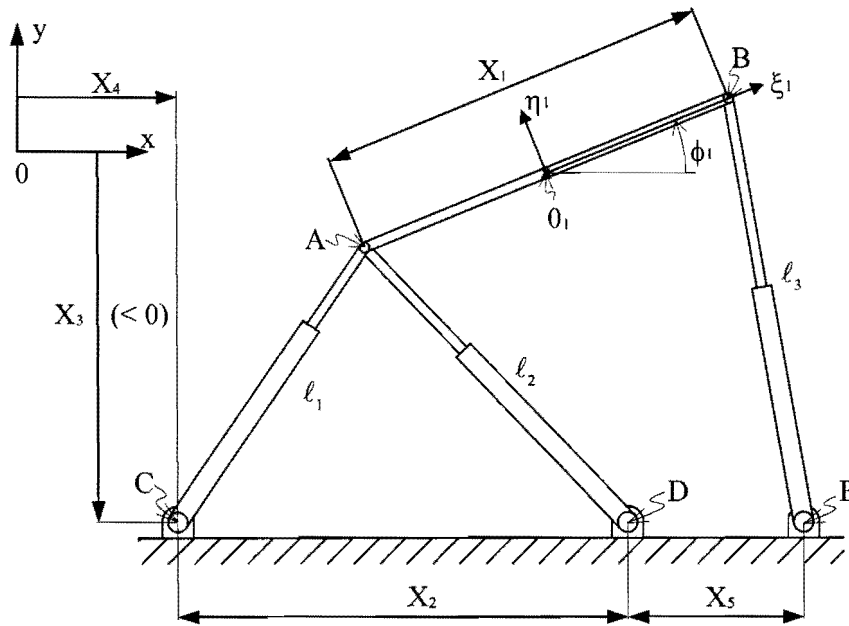
Figure 4.1: Five design variables describing the adjustable geometry planar Gough-Stewart platform machining center.

The two design variables X_3 and X_4 represent the coordinates of the left most revolute joint C on the horizontal base relative to the fixed global reference frame. In practical terms this implies that the position of point C on the base of the planar Gough-Stewart platform must be adjustable. This required positional adjustment may of course also be accomplished in practice by shifting the position of the global origin 0 relative to the fixed horizontal base (see Figure 2.8 and 2.10 for the *fixed workpiece* and *fixed cutting tool* cases respectively). The tool path is described relative to the global origin 0, and the kinematic and kinetic analysis of the mechanism is also done relative to its position (**Chapter 2**).

The remaining three design variables X_1, X_2 and X_5 indicate the relative distances between the linearly adjustable revolute joints of the fixed base (X_2 and X_5) and the moving platform (X_1).

In summary, and with reference to Figure 4.1,

$$\left| \xi_{\tilde{\jmath}i}^{A} \right| + \xi_{\tilde{\jmath}i}^{B} = X_1 \tag{4.2}$$

and

$$
\begin{array}{lll}
x^{C} = X_4 & x^{D} = X_4 + X_2 & x^{E} = X_4 + X_2 + X_5 \\
y^{C} = X_3 & y^{D} = X_3 & y^{E} = X_3
\end{array}
\tag{4.3}
$$

In order to solve for expression (4.2), one of the two local coordinates ξ_1^A or ξ_1^B must be known. If the center of mass of the moving platform is midway between revolute joints A and B, expression (4.2) reduces to $\left|\xi_1^A\right| = \xi_1^B = \dfrac{X_1}{2}$.

4.2.2 Objective function used to optimize the planar machining center geometry

The objective function used here, is the *overall maximum magnitude of the individual actuator forces* f_k, $k = 1,2,3$ (see expression (2.124)), as the planar Gough-Stewart platform moves along a prescribed tool path.

Using to the OCAS trajectory-planning algorithm, the prescribed path is specified by a set of nodal points $\left\{P_i = (x_i, y_i), i = 0,1,...,N\right\}$ (see Section 3.1). Time instants are then allocated to the consecutive nodal points according to the specified tangential "cutting speed", as well as the magnitude of the maximum allowable tangential acceleration. Each consecutive time span $[t_i, t_{i+1}]$, $i = 0,1,...,N-1$, with associated magnitudes $\Delta t_i = t_{i+1} - t_i$ is then subdivided into an additional number of equally spaced intermediate time instants, using the parameter n_{time} (see **Appendix B**). This intermediate time parameter is used in the OCAS-algorithm for the graphical representation of the results as is explained in Section 3.5.1.

In determining the overall maximum magnitude of the individual actuator forces f_k, $k = 1,2,3$, for a specific prescribed tool path, the additional *time discretization parameter* n_{time} is again utilized. This allows for a further discretization of the interval $[t_i, t_{i+1}]$ into time instants $t_{i,j} = t_i + \dfrac{j}{n_{time}}\Delta t_i$, $i = 0,1,2,...,N-1$, $j = 0,1,2,...,n_{time}$. Hence, for a sufficiently refined time discretization $\{t_{i,j}, i = 0,1,2,...,N-1; j = 0,1,2,...,n_{time}\}$ * over $[0,T] = [0, t_{N-1, n_{time}}]$, the objective function may be taken as

$$F(\mathbf{X}) = \max_{k=1,2,3}\{\max_{i,j}\left|f_k(t_{i,j})\right| , i = 0,1,2,...,N-1; j = 0,1,2,...,n_{time}\} \qquad (4.4)$$

The occurrence of singularities inside the workspace of Gough-Stewart platforms is associated with dramatic increases in actuator forces [59]. Minimizing the above objective function will push the design

---

* note that $t_{i,0} = t_{i-1, n_{time}}$

towards an optimum platform geometry which avoids close proximity to singularities as a specific prescribed path is traced.

Apart from the fact that the objective function is dependent on the prescribed path, it is also shown in Section 4.3 that expression (2.124) is indeed an implicit function of the vector of design variables $\mathbf{X} = \left[X_1, X_2, X_3, X_4, X_5 \right]^T$, and that the objective function is therefore well defined.

4.2.3 Constraints applicable on the planar machining center

With reference to Figure 4.1, the allowable relative distances between the linearly adjustable revolute joints of the fixed base (X_2 and X_5) and the moving platform (X_1) are subject to physical *lower* ($\underline{X}_i$, $i = 1,2,5$) and *upper* ($\overline{X}_i, i = 1,2,5$) bounds, i.e.

$$\underline{X}_i \leq X_i \leq \overline{X}_i, \; i = 1,2,5 \tag{4.5}$$

Similarly, the actuator leg lengths ($\ell_i, i = 1,2,3$) are bounded by *minimum* ($\underline{\ell}_i$, $i = 1,2,3$) and *maximum* ($\overline{\ell}_i, i = 1,2,3$) leg length limits:

$$\underline{\ell}_i \leq \ell_i \leq \overline{\ell}_i, \; i = 1,2,3 \tag{4.6}$$

These bounds are defined as the *mechanism configurational constraints*, and determine its *working capability*, since for any specific *operational geometry* $\mathbf{X} = \left[X_1, X_2, X_3, X_4, X_5 \right]^T$ to be feasible, the *mechanism configurational constraints* (4.5) and (4.6) must be satisfied.

The formulation of the constrained optimization problem (expression (4.1)) allows for the easy imposition of the above configurational constraints, since they may readily be expressed as general inequality constraints of the form $C_j(\mathbf{X}) \leq 0$, ($j = 1,2,3,...,m$).

In particular, expression (4.5) represents the first six inequality constraints $C_j(\mathbf{X}) \leq 0$, ($j = 1,2,3,...,6$) :

$$
\begin{aligned}
C_1(\mathbf{X}) &\equiv X_1 - \overline{X}_1 \leq 0 \\
C_2(\mathbf{X}) &\equiv \underline{X}_1 - X_1 \leq 0 \\
C_3(\mathbf{X}) &\equiv X_2 - \overline{X}_2 \leq 0 \\
C_4(\mathbf{X}) &\equiv \underline{X}_2 - X_2 \leq 0 \\
C_5(\mathbf{X}) &\equiv X_5 - \overline{X}_5 \leq 0 \\
C_6(\mathbf{X}) &\equiv \underline{X}_5 - X_5 \leq 0
\end{aligned}
\tag{4.7}
$$

The leg length limits $\underline{\ell}_i \leq \ell_i \leq \bar{\ell}_i$, $i = 1,2,3$ (expression (4.6)) represent an additional six inequality constraints $C_{j+6}(\mathbf{X}) \leq 0$, $(j = 1,2,3,...,6)$. As with the objective function (4.4), these six inequality constraints are dependent on the prescribed path, as well as the design variables $\mathbf{X} = [X_1, X_2, X_3, X_4, X_5]^T$ (see Section 4.3). Monitoring the prescribed path and corresponding platform geometry at discrete time instants $t_{i,j}$, the overall maximum and minimum actuator leg lengths may be obtained. They are respectively given by $\ell_k^{max}(\mathbf{X}) = \max_{i,j}[\ell_k(t_{i,j}, \mathbf{X})]$ and $\ell_k^{min}(\mathbf{X}) = \min_{i,j}[\ell_k(t_{i,j}, \mathbf{X})]$ for $k = 1,2,3$ and $\{t_{i,j}, i = 0,1,2,...,N-1; j = 0,1,2,...,n_{time}\}$ suitably small *monitoring* time intervals as previously defined in Section 4.2.2. The *allowable* maximum and minimum actuator leg lengths are respectively denoted by $\bar{\ell}_k$ and $\underline{\ell}_k$, $k = 1,2,3$, resulting in the following six mathematically expressed inequality constraints:

$$C_{k+6}(\mathbf{X}) \equiv \ell_k^{max}(\mathbf{X}) - \bar{\ell}_k \leq 0, \quad k = 1,2,3$$

$$\text{and } C_{k+9}(\mathbf{X}) \equiv \underline{\ell}_k - \ell_k^{min}(\mathbf{X}) \leq 0, \quad k = 1,2,3$$

$$(4.8)$$

4.3 Evaluation of the constrained optimization problem

The formulated constrained optimization problem (Section 4.2) is evaluated for a specific prescribed path, given any arbitrary design $\mathbf{X} = [X_1, X_2, X_3, X_4, X_5]^T$. The design vector $\mathbf{X}$ fixes the operational geometry of the platform.

4.3.1 Evaluation of the objective function

Evaluating the objective function (4.4), involves performing a kinematic and kinetic analysis of the planar Gough-Stewart platform as explained in **Chapter 2**. In particular, for any time instant along the prescribed path, the position (x_1, y_1) and orientation (ϕ_1) of the moving platform (body 1 in Figure 2.5) are known (see Section 2.4). Furthermore, with the *operational geometry* $(\mathbf{X})$ fixed, expression (4.2) yields the local ξ_1^A- and ξ_1^B-coordinates while expression (4.3) yields global coordinates (x^C, y^C), (x^D, y^D) and (x^E, y^E). Note that since the coordinates (x^A, y^A) and (x^B, y^B) follow from (x_1, y_1, ϕ_1), ξ_1^A and ξ_1^B in expression (2.57), expressions (2.58) – (2.61) may be solved for. Expressions (2.57) – (2.61) uniquely define the coordinate vector $\mathbf{q} = [x_1, y_1, \phi_1, x_2, y_2, \phi_2, ..., x_8, y_8, \phi_8]^T$, which uniquely defines the Jacobian matrix of the planar Gough-Stewart platform given by expression (2.62). The Jacobian matrix is used to find the accelerations of the individual bodies (expression (2.56)). With these

accelerations known, the Jacobian matrix is again used to solve the inverse dynamic equations of motion (expression (2.124)) for the unknown LaGrange multipliers λ and actuator forces $\mathbf{ff}$.

The sensitivity of the objective function (4.4) to each of the design variable X_i, $i = 1,2,...,5$ may also be graphically determined. This is done by fixing four of the five design variables, and varying the fifth while evaluating the objective function value.

As an example, the sensitivity analysis is done for a path where the center of mass of the moving platform follows a straight-line prescribed path inclined at $60°$ to the horizontal as shown in Figure 4.2. Five equally spaced nodal points are used to specify the path, and using the OCAS-algorithm, the trajectory-planning is done for a specified constant tangential speed of $0.01\,\text{m/s}$. Furthermore, the default time discretization parameter, $n_{\text{time}} = 10$, is used resulting in a total of 41 monitoring time intervals.

The direction of travel is such that the initial configuration of the mechanism corresponds to the one shown in dashed lines in Figure 4.2 and the final configuration to the one in solid lines. Furthermore, the moving platform remains horizontal as the straight-line path is traced. The fixed values of the respective design variables are

$$X_1 = 0.4\,\text{m} \qquad X_2 = 0.4\,\text{m} \qquad X_3 = -0.4\,\text{m} \qquad X_4 = -0.4\,\text{m} \qquad X_5 = 0.2\,\text{m} \qquad (4.9)$$

and the mass matrix of this example platform is given by expression (2.132).
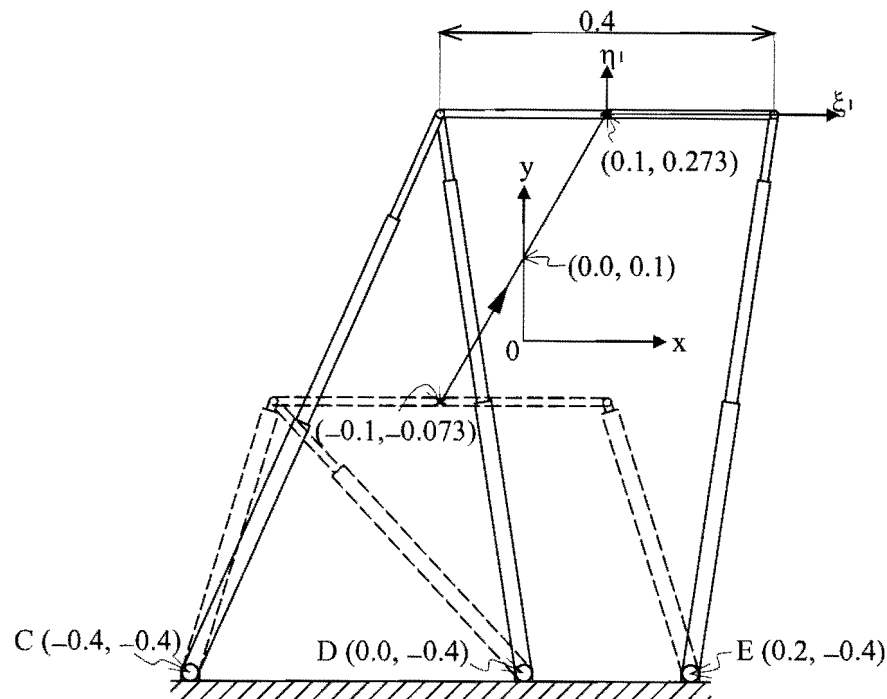
Figure 4.2: Straight-line prescribed path.

The sensitivity of the objective function to design variable X_1 is shown in Figure 4.3. Here X_1 is varied with a step size of $0.0025\,m$ between $0.1\,m$ and $1.0\,m$, while design variables X_2, X_3, X_4 and X_5 remain fixed (see expression (4.9)).
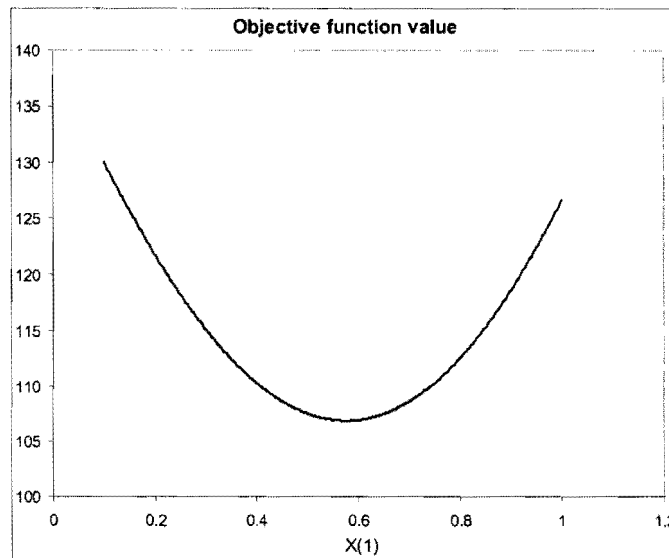
Figure 4.3: Objective function (4.4) versus design variable X_1.

Figure 4.3 consists of a *single smooth* curve, indicating that as X_1 varies, a *single* actuator is responsible for carrying the maximum magnitude actuator force. For the example prescribed path considered here (Figure 4.2), actuator leg ℓ_1 (see Figure 4.1) carries the maximum magnitude actuator force.

Evaluating the objective function while varying design variable X_1 with a step size of $0.000001\,m$ between $0.5756\,m$ and $0.576\,m$, magnifies the curve as shown in Figure 4.4. This curve demonstrates the effective absence of any numerical noise in the analysis.
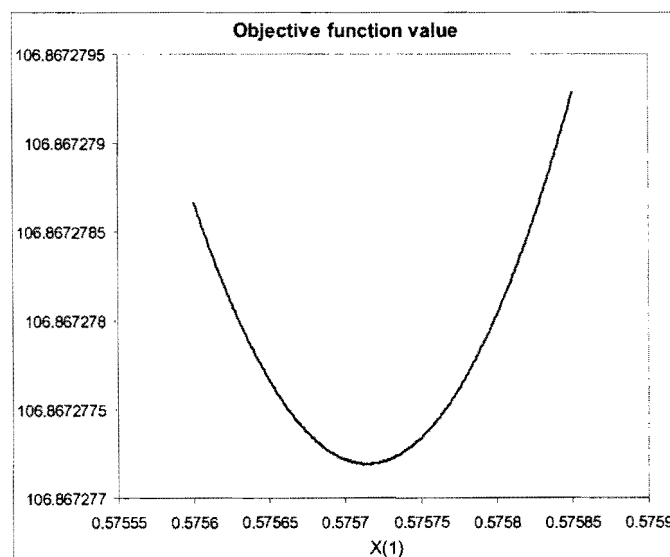
Figure 4.4: Close-up of objective function (4.4) versus design variable X_1.

This absence of noise is due to the fact that the objective function (expression (4.4)) is determined with high accuracy using the fundamentally based inverse dynamic analysis procedure explained in **Chapter 2**.

The sensitivity of the objective function to X_2 is shown in Figure 4.5. Here design variables X_1, X_3, X_4 and X_5 remain fixed (see expression (4.9)) while X_2 is varied with a step size of $0.0025\,\text{m}$ between $0.1\,\text{m}$ and $1.0\,\text{m}$.
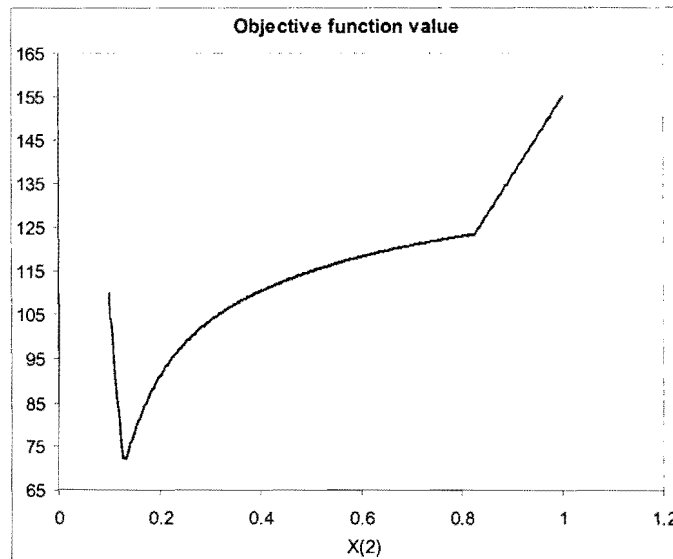
Figure 4.5: Objective function (4.4) versus design variable X_2.

In contrast to Figure 4.3 which consists of a *single* smooth curve, Figure 4.5 consists of *four* smooth curves linked to each other at three points where discontinuities in the slope (kinks) occur. Each of the three kinks in the above graph is due to a *switch* in the actuator leg responsible for the maximum magnitude actuator force.
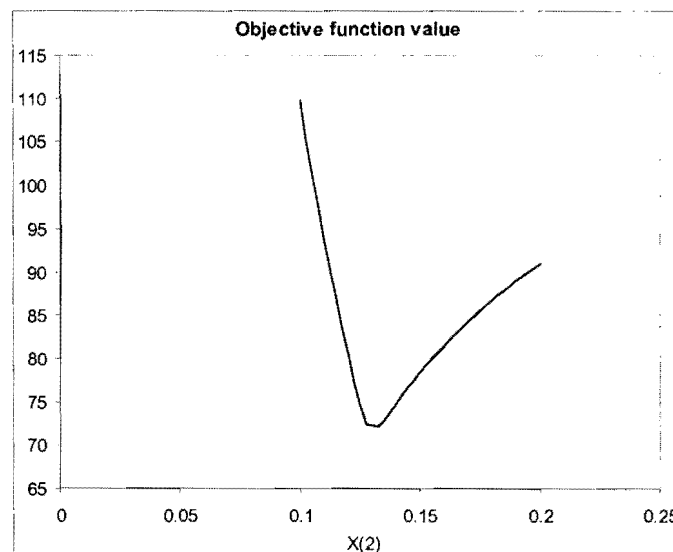
Figure 4.6: Close-up of objective function (4.4) versus design variable X_2.

Figure 4.6 shows a close-up view of the first two kinks, where the *left most* smooth curve represents actuator leg ℓ_2 (see Figure 4.1) carrying the maximum magnitude actuator force, the *middle* smooth curve represents actuator leg ℓ_3 carrying the maximum magnitude actuator force, and the *right most* smooth curve represents actuator leg ℓ_1 carrying the maximum magnitude actuator force. The isolated discontinuity in Figure 4.5 occurring near $X_2 = 0.8\,\text{m}$ is due to the switch between actuator legs ℓ_1 and ℓ_2 in carrying the maximum magnitude actuator force.

The respective sensitivities of the objective function (4.4) to design variables X_3, X_4 and X_5 are as shown in, Figures 4.7 – 4.9.
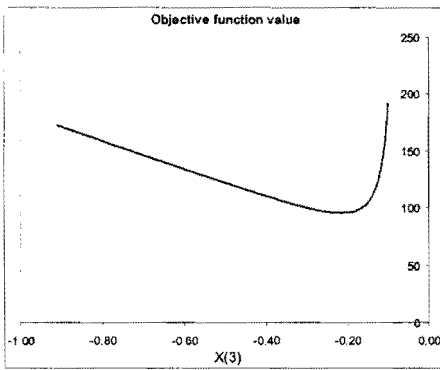
Figure 4.7: Objective function (4.4) versus design variable X_3.
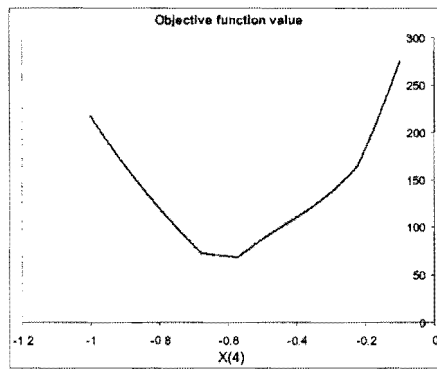
Figure 4.8: Objective function (4.4) versus design variable X_4.
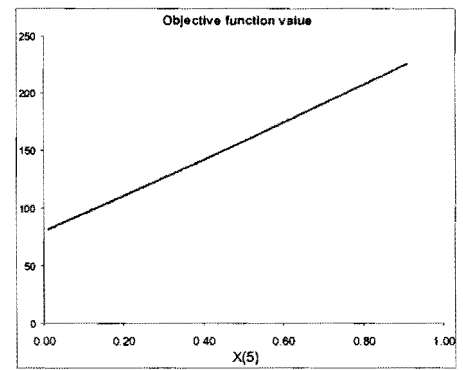
Figure 4.9: Objective function (4.4) versus design variable X_5.

4.3.2 Evaluation of the inequality constraints

Inequality constraints (4.7) may, of course, be explicitly evaluated. The evaluation of the inequality constraints (4.8) follow from the kinematic and kinetic analysis mentioned in Section 4.3.1. With the global coordinates of points A, B, C, D and E known at any time instant t, actuator leg lengths $\ell_1(\mathbf{X},t)$, $\ell_2(\mathbf{X},t)$ and $\ell_3(\mathbf{X},t)$ are the magnitudes of respective vectors $\overrightarrow{CA}$, $\overrightarrow{DA}$ and $\overrightarrow{EB}$ (see Figure 4.1):

$$\ell_1(\mathbf{X},t) = \left|\overrightarrow{CA}\right| = \sqrt{(x^A - x^C)^2 + (y^A - y^C)^2}$$

$$\ell_2(\mathbf{X},t) = \left|\overrightarrow{DA}\right| = \sqrt{(x^A - x^D)^2 + (y^A - y^D)^2} \qquad (4.10)$$

$$\ell_3(\mathbf{X},t) = \left|\overrightarrow{EB}\right| = \sqrt{(x^B - x^E)^2 + (y^B - y^E)^2}$$

Note that mechanism configurational constraint (4.6), not only fixes the *allowable* maximum and minimum actuator leg lengths, but also influences the kinematic and kinetic performance of the planar

Gough-Stewart platform. This follows from the relationship existing between the physical dimensions of the two bodies comprising an actuator leg, and the allowable relative actuator displacement.

Consider translational joint $2-5$, which is the left most actuator leg of the planar Gough-Stewart platform as shown in Figure 2.5 (actuator leg ℓ_1 in Figure 4.1). The physical dimensions of bodies 2 and 5 determine the allowable actuator displacement of leg 1. Furthermore, the local $0_2\xi_2\eta_2$ and $0_5\xi_5\eta_5$ coordinate systems are chosen with 0_2 and 0_5 respectively coinciding with the centers of mass of bodies 2 and 5, the positions of which are also determined by the physical dimensions of these two bodies. With the positions of the respective centers of mass of bodies 2 and 5 known, local coordinates ξ_2^A and ξ_5^C are also known. Similar arguments apply for translational joints $3-6$ and $4-7$.

With reference to Figure 2.5, local coordinates ξ_3^A and ξ_6^D of translational joint $3-6$, ξ_4^B and ξ_7^D of translational joint $4-7$, together with local coordinates ξ_2^A and ξ_5^C of translational joint $2-5$ are required to solve for expression (2.61).

4.4 Solving the constrained optimization problem

As mentioned in Section 4.1, the LFOPC-algorithm [64] is used here to optimize the adjustable geometry of the planar Gough-Stewart platform machining center for any specific prescribed path. The optimization procedure is schematically represented in Figure 4.10.
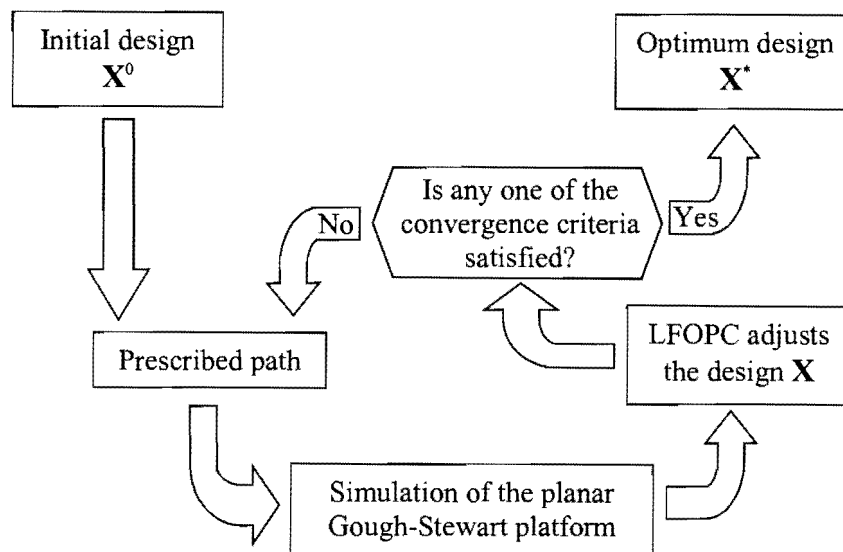
Figure 4.10: Optimization of the adjustable geometry of the planar platform machining center.

The user specifies the initial design $\mathbf{X}^0$ as well as the prescribed path. The simulation of the planar Gough-Stewart platform involves the OCAS trajectory-planning algorithm presented in **Chapter 3**, as well as the kinematic and kinetic analysis of **Chapter 2**.

The LFOPC optimization algorithm [64] used here is a *gradient-based* method for unconstrained minimization applied to a *penalty function* formulation of the constrained optimization problem. A more detailed description of the LFOPC-algorithm is given in **Appendix C**. In short, a *penalty function* is created by combining the objective function (4.4) and the inequality constraint equations (4.7) and (4.8). Furthermore, the *gradient vector* of the penalty function determines the adjustment of the design vector $\mathbf{X}$ as the LFOPC-algorithm searches iteratively for an optimum design $\mathbf{X}^*$. These optimization iterations continue until one of the following two *convergence criteria* (see Figure 4.10) is satisfied:

1. The norm of the penalty function gradient vector is below a specified value ε_g

2. The norm of the relative design vector, given by $\left\| \mathbf{X}^{\text{"Current"}} - \mathbf{X}^{\text{"Previous"}} \right\|$, is below a specified tolerance ε_x.

In determining the gradient vector of the penalty function, LFOPC requires the gradient vector of the objective function with respect to the design variables, as well as the gradient vectors of each inequality constraint with respect to the design variables.

The gradient vector of the objective function (4.1) with respect to the design variables is obtained by differentiating numerically using forward finite differences [55]. The components of the objective function gradient vector at any specific design $\mathbf{X} = [X_1, X_2, X_3, X_4, X_5]^T$ is approximated by

$$\frac{\partial F(\mathbf{X})}{\partial X_i} \approx F[\mathbf{X} + \Delta \mathbf{X}_i, \mathbf{X}] = \frac{F(\mathbf{X} + \Delta \mathbf{X}_i) - F(\mathbf{X})}{\varepsilon_i} \tag{4.11}$$

where $\Delta \mathbf{X}_i = [0, 0, \ldots, \varepsilon_i, \ldots, 0]^T$ with $\varepsilon_i > 0$ in the ith position, and $i = 1, 2, \ldots, 5$.

With reference to the optimization flowchart given in Figure 4.10, six simulation runs of the planar Gough-Stewart platform are required per iteration. This is because at each design point forward finite differences are used in computing the gradient components of the objective function, requiring five *perturbed* objective function values, and one *unperturbed* objective function value as is apparent from expression (4.11).

The appropriate values of ε_i to be used may be determined from an experimental sensitivity study of the approximate gradients with respect to different step sizes ε_i of the five design variables. For any chosen design $\mathbf{X}$, the objective function may be determined as the platform traces the prescribed path. The

sensitivity of, for example the variation of the approximation $F[X + \Delta X_i, X]$ to $\dfrac{\partial F(X)}{\partial X_i}$ with respect to

different orders of magnitude of ε_i, may be represented by an exponential graph. The graph of $F[X + \Delta X_i, X]$ versus ε_i is expected to show a stable plateau, the mid ε-value of which is the most suitable value to be used in expression (4.11).

A sensitivity analysis of $F[X + \Delta X_i, X]$ versus ε_i is performed here for the example straight-line prescribed path shown in Figure 4.2. For this sensitivity analysis, a constant tangential speed of 0.1 m/s is specified, and the moving platform remains horizontal as the prescribed path is traced. The fixed design of the adjustable geometry planar Gough-Stewart platform at which the sensitivity analysis is performed is $X = [0.4, 0.4, -0.4, -0.4, 0.2]^T$ (see Figure 4.2) and the mass matrix of this example platform is given by expression (2.132).

The computed approximations $F[X + \Delta X_i, X]$ (denoted by $F[X + \Delta X\_i, X]$) to the gradients $\dfrac{\partial F(X)}{\partial X_i}$, $i = 1, 2, ..., 5$ are plotted versus ε in Figure 4.11.
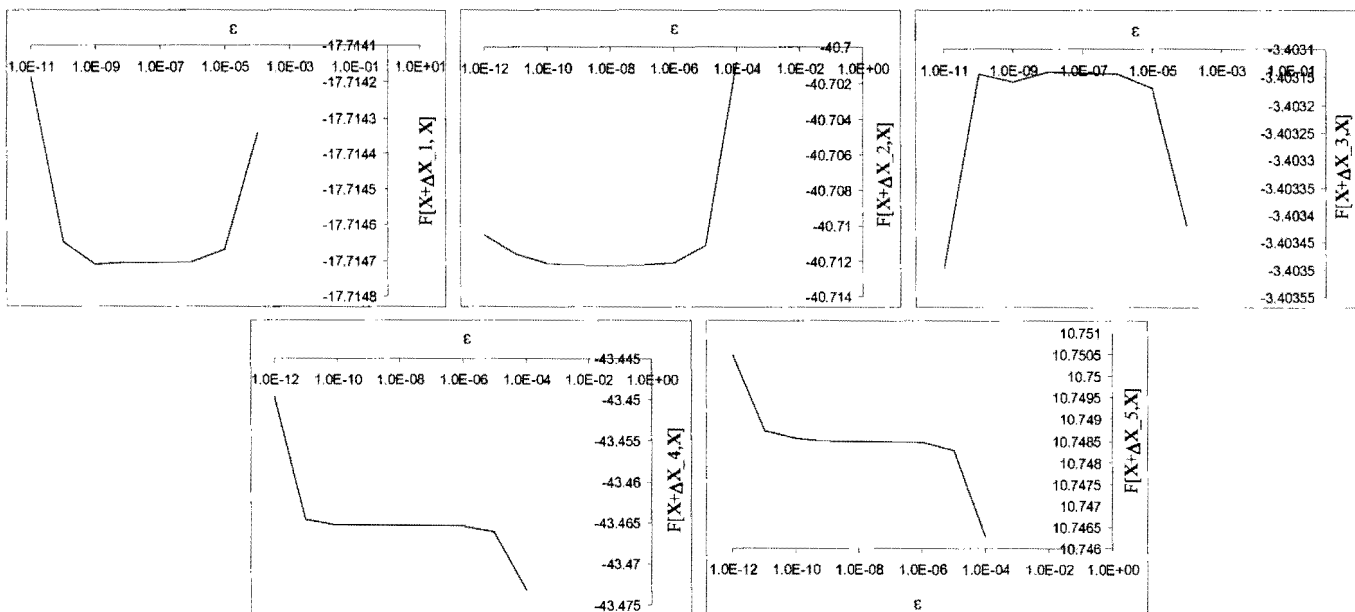
Figure 4.11: **Sensitivity of** $F[X + \Delta X_i, X]$ **to step size** ε, **for** $i = 1, 2, ..., 5$.

The above sensitivity analyses show that the choice $\varepsilon_i \equiv \varepsilon = 10^{-8}$, $i = 1, 2, ..., 5$ will result in reliable computed gradients.

The components of the gradient vectors of each inequality constraint function in (4.7) are, of course, analytically known and given by:

$$
\begin{array}{lllll}
\dfrac{\partial C_1(\mathbf{X})}{\partial X_1} = 1 & \dfrac{\partial C_1(\mathbf{X})}{\partial X_2} = 0 & \dfrac{\partial C_1(\mathbf{X})}{\partial X_3} = 0 & \dfrac{\partial C_1(\mathbf{X})}{\partial X_4} = 0 & \dfrac{\partial C_1(\mathbf{X})}{\partial X_5} = 0 \\[2mm]
\dfrac{\partial C_2(\mathbf{X})}{\partial X_1} = -1 & \dfrac{\partial C_2(\mathbf{X})}{\partial X_2} = 0 & \dfrac{\partial C_2(\mathbf{X})}{\partial X_3} = 0 & \dfrac{\partial C_2(\mathbf{X})}{\partial X_4} = 0 & \dfrac{\partial C_2(\mathbf{X})}{\partial X_5} = 0 \\[2mm]
\dfrac{\partial C_3(\mathbf{X})}{\partial X_1} = 0 & \dfrac{\partial C_3(\mathbf{X})}{\partial X_2} = 1 & \dfrac{\partial C_3(\mathbf{X})}{\partial X_3} = 0 & \dfrac{\partial C_3(\mathbf{X})}{\partial X_4} = 0 & \dfrac{\partial C_3(\mathbf{X})}{\partial X_5} = 0 \\[2mm]
\dfrac{\partial C_4(\mathbf{X})}{\partial X_1} = 0 & \dfrac{\partial C_4(\mathbf{X})}{\partial X_2} = -1 & \dfrac{\partial C_4(\mathbf{X})}{\partial X_3} = 0 & \dfrac{\partial C_4(\mathbf{X})}{\partial X_4} = 0 & \dfrac{\partial C_4(\mathbf{X})}{\partial X_5} = 0 \\[2mm]
\dfrac{\partial C_5(\mathbf{X})}{\partial X_1} = 0 & \dfrac{\partial C_5(\mathbf{X})}{\partial X_2} = 0 & \dfrac{\partial C_5(\mathbf{X})}{\partial X_3} = 0 & \dfrac{\partial C_5(\mathbf{X})}{\partial X_4} = 0 & \dfrac{\partial C_5(\mathbf{X})}{\partial X_5} = 1 \\[2mm]
\dfrac{\partial C_6(\mathbf{X})}{\partial X_1} = 0 & \dfrac{\partial C_6(\mathbf{X})}{\partial X_2} = 0 & \dfrac{\partial C_6(\mathbf{X})}{\partial X_3} = 0 & \dfrac{\partial C_6(\mathbf{X})}{\partial X_4} = 0 & \dfrac{\partial C_6(\mathbf{X})}{\partial X_5} = -1
\end{array}
\tag{4.12}
$$

On the other hand, the forward finite difference formula is again used to numerically approximate the derivatives of the inequality constraint functions in (4.8) at any given design $\mathbf{X} = [X_1, X_2, X_3, X_4, X_5]^T$:

$$
\frac{\partial C_{j+6}(\mathbf{X})}{\partial X_i} \approx C_{j+6}[\mathbf{X} + \Delta\mathbf{X}_i, \mathbf{X}] = \frac{C_{j+6}(\mathbf{X} + \Delta\mathbf{X}_i) - C_{j+6}(\mathbf{X})}{\varepsilon_i}
\tag{4.13}
$$

where $\Delta\mathbf{X}_i = [0,0,...,\varepsilon_i,...,0]^T$ with $\varepsilon_i > 0$ in the ith position, and $j = 1,2,...,6$.

The same six simulation runs of the planar Gough-Stewart platform required to determine the objective function gradient vector, are utilized to evaluate expression (4.13).

The gradients of the inequality constraint functions are expected to have similar sensitivities with respect to the order of magnitude of ε_i as the objective function gradients (see Figure 4.11), hence $\varepsilon_i \equiv \varepsilon = 10^{-8}$ is used in expression (4.13), for all j.

4.5 Discussion of optimization results

The prescribed straight-line path of Figure 4.2 is used here to *illustrate* the determination of the optimum geometry of the planar Gough-Stewart platform machining center for a given task path. Using the *general* OCAS trajectory-planning methodology (see **Chapter 3**), the straight-line path is prescribed by specifying 5 nodal points as shown in Figure 4.12. Again the default value of $n_{time} = 10$ is used for the discretization parameter in the analysis of the straight-line path.
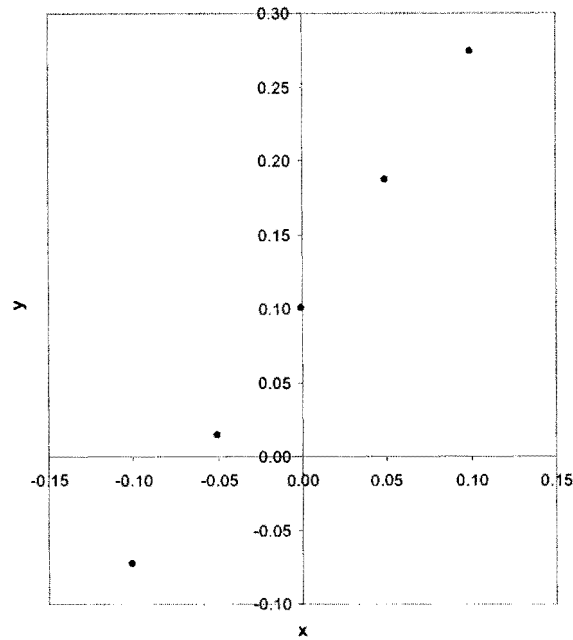
Figure 4.12: Nodal points specified for the straight-line prescribed path.

For this illustrative example, the "fixed workpiece" mode of operation of the machining center, as explained in Sections 2.4.1 and 2.6.4.2.1, is used with a zero tool length $\eta_1^P = 0.0$. Specifying a zero tool length enforces the center of mass of the moving platform to trace the prescribed straight-line path, as was done for the sensitivity analysis explained in Section 4.3.1. Furthermore, a fixed moving platform orientation $\phi_1 \equiv 0$ (see Figure 4.2) is maintained with a *constant* tangential cutting speed of $0.01\,\mathrm{m/s}$ and a "cutting force constant" $C_{cut} = 10000\,\mathrm{Ns/m}$ (see expression (2.107)). Since the length of the prescribed straight-line path is $0.4\,\mathrm{m}$, the motion takes $40\,\mathrm{s}$ to complete.

With reference to Figure 4.1 the initial configuration of the planar machining center is $\mathbf{X}^0 = [0.4,\ 0.4,\ -0.4,\ -0.4,\ 0.2]^T$, where the design variables X_1^0, X_2^0 and X_5^0 (given in m) are in scaled agreement with the geometry of Haug et al.'s [73] planar Gough-Stewart platform. The initial coordinates $(X_4^0;\ X_3^0)$ of the left- most revolute joint on the horizontal base are arbitrarily chosen as $(-0.4;\ -0.4)$. Figure 4.2 is a *scaled* schematic representation of the machining center fixed to these initial geometry settings $\mathbf{X}^0 = [0.4,\ 0.4,\ -0.4,\ -0.4,\ 0.2]^T$ at the start and end points of the prescribed straight-line path. The mass matrix of this platform is again given by expression (2.132).

Figure 4.14 shows the variation in the respective actuator lengths (designated by L1, L2 and L3) as the prescribed path is followed using the initial design, while Figure 4.16 shows the variation of corresponding actuator forces f_k, $k = 1,2,3$ (designated by f1, f2 and f3) for the prescribed path.

It is important to note that the allowable maximum actuator lengths $\bar{\ell}_k = 0.525$ m, $k = 1,2,3$ designated by Lmax in Figure 4.14 are violated if the initial design is used to trace the prescribed path. These violations imply that the specified tool path lies outside the workspace of the platform and that the initial geometry settings are therefore *infeasible* for carrying out the prescribed task. The specific bounds of the *mechanism configurational constraints*, given in meters, (see Section 4.2.3, expressions (4.5) and (4.6)), are

$$0.1 \le X_1 \le 0.45$$
$$0.113 \le X_2 \le 0.465 \tag{4.14}$$
$$0.113 \le X_5 \le 0.27$$

and

$$0.075 \le \ell_i \le 0.525, \; i = 1,2,3 \tag{4.15}$$

In particular, the inequality constraint function values for tracing the straight-line prescribed tool path using the initial design X^0, are

$$C_1(X^0) = -0.05 \quad C_2(X^0) = -0.3 \quad C_3(X^0) = -0.065$$
$$C_4(X^0) = -0.287 \quad C_5(X^0) = -0.07 \quad C_6(X^0) = -0.087$$
$$\rightarrow C_7(X^0) = 0.21202 \quad \rightarrow C_8(X^0) = 0.15559 \quad \rightarrow C_9(X^0) = 0.15559$$
$$C_{10}(X^0) = -0.26675 \quad C_{11}(X^0) = -0.36862 \quad C_{12}(X^0) = -0.26675$$

where the violated inequality constraints associated with the initial design X^0 have function values greater than zero, and are indicated by a *single* arrow $\rightarrow$.

The optimized geometry settings for the straight-line prescribed path are: $X^* = [0.44978, 0.34151, -0.14924, -0.38010, 0.13973]^T$. Figure 4.13 shows a scaled schematic representation of the machining center fixed to these optimal geometry settings at the start and end points of the prescribed straight-line path. Figure 4.15 shows the variation in the actuator lengths for the optimum platform design. The varying actuator lengths lie well within the minimum and maximum bounds specified, demonstrating the feasibility of the optimum design X^*. The particular inequality constraint function values for tracing the straight-line prescribed tool path using the optimum design X^*, are

$$C_1(X^*) = -0.223 \times 10^{-3} \quad C_2(X^*) = -0.34978 \quad C_3(X^*) = -0.12349$$
$$C_4(X^*) = -0.22851 \quad C_5(X^*) = -0.13027 \quad C_6(X^*) = -0.02673$$
$$C_7(X^*) = -0.03145 \quad C_8(X^*) = -0.09383 \quad C_9(X^*) = -0.04696$$
$$C_{10}(X^*) = -0.01897 \quad C_{11}(X^*) = -0.21098 \quad C_{12}(X^*) = -0.00466$$

Note that since all the above inequality constraint function values are less than zero, the optimum design found by the LFOPC-algorithm is referred to as an *unconstrained optimum*. In the event that the optimum solution corresponds to a design where one or more inequality constraint function values are equal to zero, the associated constraints are considered *active*, and the design $\mathbf{X}^*$ is known as a *constrained optimum*. In the actual practical numerical identification of active constraints, the condition *equal to zero* is relaxed to *approximately equal to zero*.
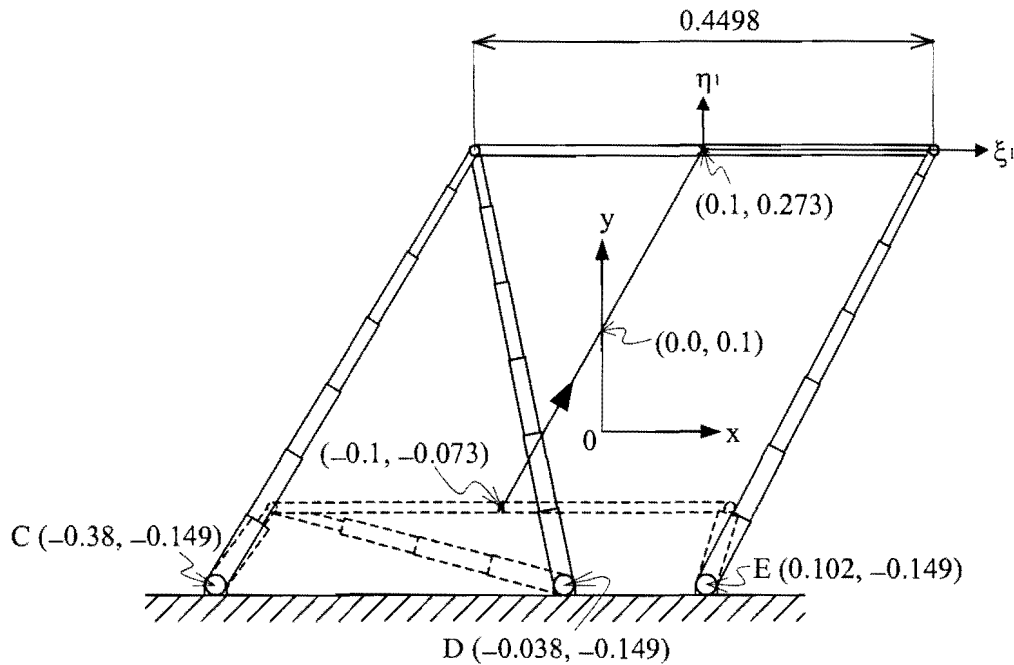
Figure 4.13: Scaled schematic representation of optimum machining center geometry settings.
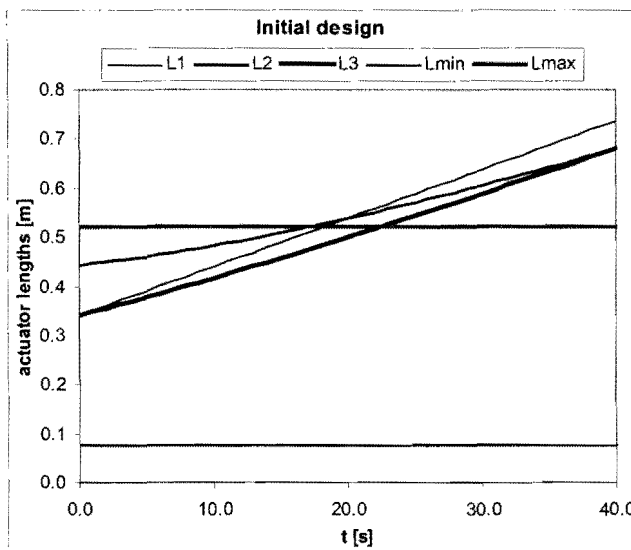
| **Figure 4.14: Initial design: variation of actuator lengths along tool path.** | **Figure 4.15: Optimum design: variation of actuator lengths along tool path.** |
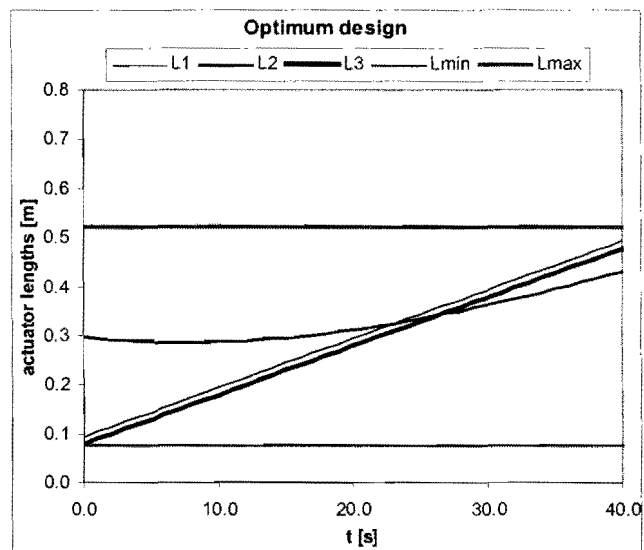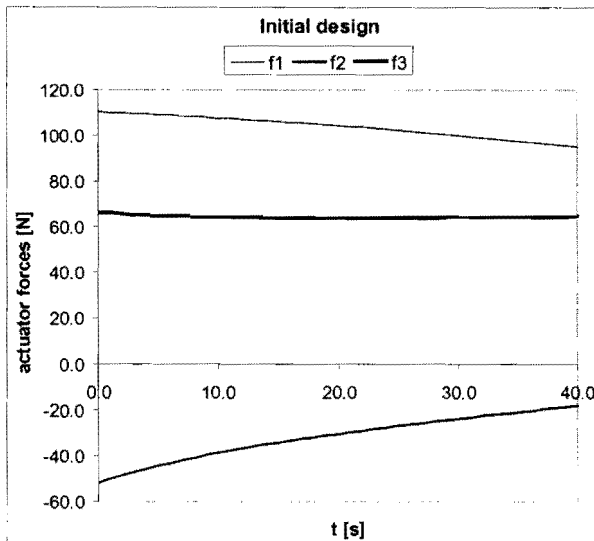
Figure 4.16: Initial design: variation of actuator forces along tool path.
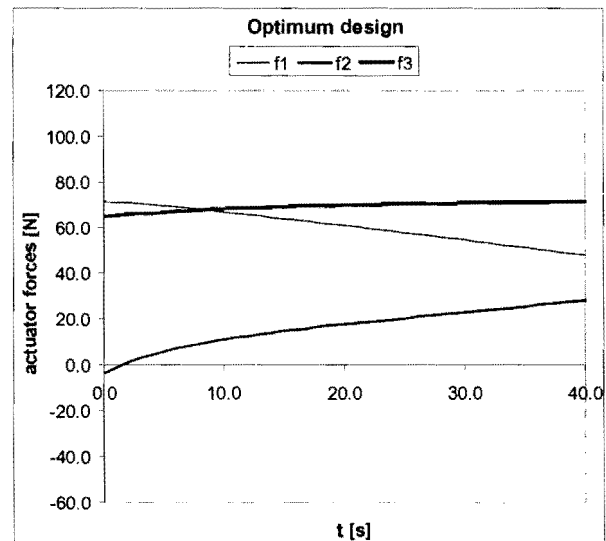
Figure 4.17: Optimum design: variation of actuator forces along tool path.

The effectiveness of the optimization procedure is further borne out by comparing Figure 4.16, with Figure 4.17, showing the variations in actuator forces for the optimum and initial designs respectively. For this simple illustrative example, the objective function value (expression (4.4)) is reduced by approximately 35% by optimizing the geometry of the platform. The initial objective function value is $F(\mathbf{X}^0) = 110.28$ N in actuator leg 1, compared to the optimum objective function value of $F(\mathbf{X}^*) = 71.32$ N, also in actuator leg 1.

The objective function convergence history is depicted in Figure 4.18.
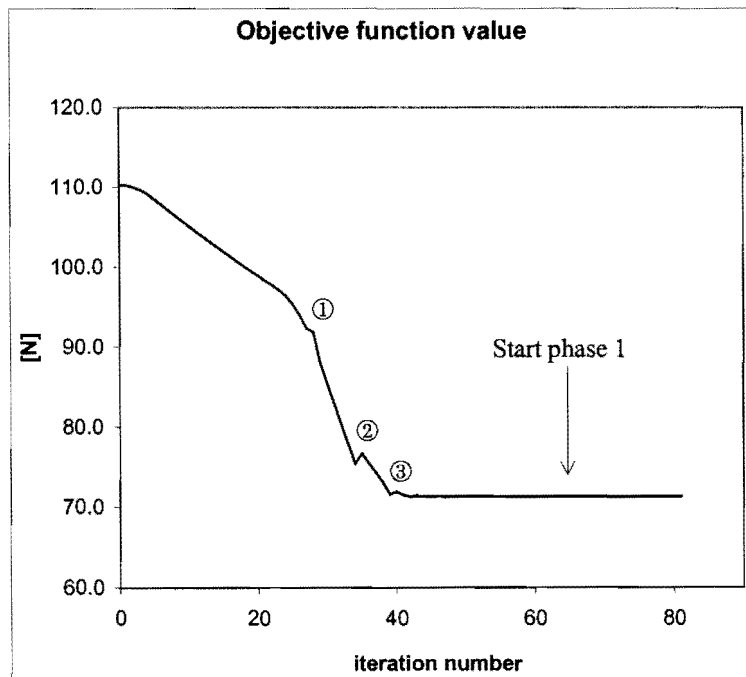
Figure 4.18: Objective function convergence history.

The labels ① – ③ in Figure 4.18 are used in Table 4.1 to relate the *iteration number* and *phase* of the LFOPC-algorithm (see **Appendix C**) to the actuator leg responsible for the *maximum magnitude actuator force* (see Section 4.2.2) and the violated inequality constraints at the indicated regions of the convergence curve.

Labels	Iter. No.	LFOPC-Phase	Act. Leg	Violated Inequality Constraints
$\mathbf{X}^0$	0	0	ℓ_1	$C_7 \quad C_8 \quad C_9$
①	25-26	0	ℓ_1	None
	27	0	ℓ_1	None
	28	0	ℓ_3	None
	29	0	ℓ_1	None
	30-32	0	ℓ_1	None
②	33	0	ℓ_1	$C_1 \quad\quad C_{12}$
	34	0	ℓ_1	$C_1 \quad\quad C_{12}$
	35	0	ℓ_1	$C_1 \quad\quad C_{12}$
	36	0	ℓ_1	$C_1 \quad\quad C_{12}$
③	39	0	ℓ_1	C_1
	40-42	0	ℓ_3	C_1
	43	0	ℓ_1	C_1
	44	0	ℓ_3	C_1
	45	0	ℓ_3	C_1
	46	0	ℓ_1	C_1
LFOPC-phase change	64	0	ℓ_3	C_1
	65	0	ℓ_1	C_1 violated constraint value $C_1(\mathbf{X}^{65}) = 0.570 \times 10^{-3}$
	65	1	ℓ_1	C_1
	66	1	ℓ_1	C_1
	80	1	ℓ_3	None
$\mathbf{X}^*$	81	1	ℓ_1	None

Table 4.1: Comparative table for the parabolic tool path objective function vs. iteration number curve (see Figure 4.18).

Note that there are switches between actuator legs ℓ_1 and ℓ_3 in being responsible for the maximum magnitude actuator force at labels ① and ③. The discontinuities in the objective function gradient vector (4.11) associated with these switches (see Section 4.3.1) are responsible for the unsmooth behavior of objective function convergence graph in these regions. The slight spiked behavior occurring at label ② can be attributed to inequality constraints C_1 and C_{12} being violated during iterations $\mathbf{X}^{33} - \mathbf{X}^{38}$.

Figure 4.19 shows the corresponding convergence histories for the design variables X_i, $i = 1,2,...,5$.
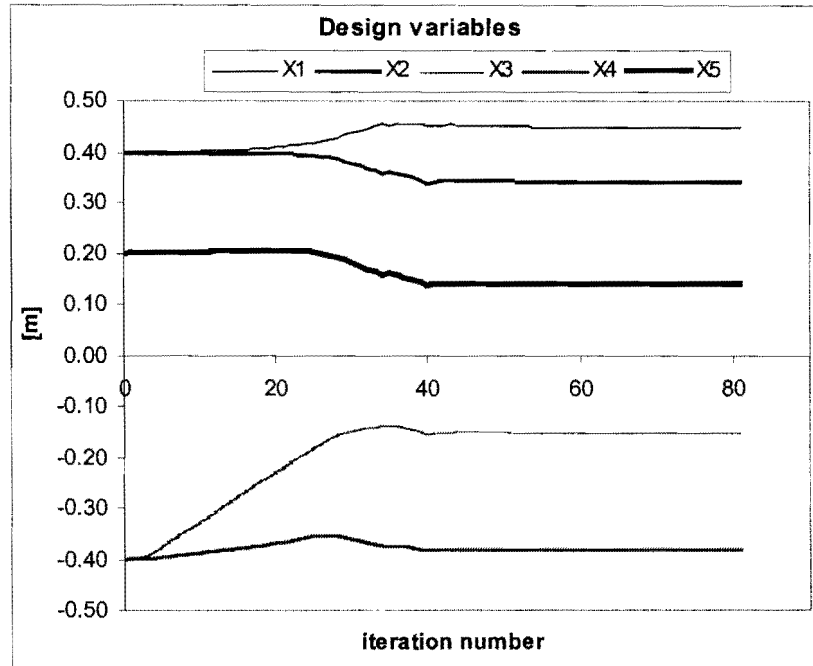
Figure 4.19: Convergence histories of design variables X_i, $i = 1,2,...,5$.

When comparing Figure 4.18 with Figure 4.19, it is evident that the LFOPC optimization algorithm [64] used here effectively converges to the optimum solution after only 50 optimization iterations. In particular, Table 4.1 shows that the end of phase 0 of the LFOPC-algorithm, the only violated constraint is C_1 with an associated constraint function value of $C_1(\mathbf{X}^{65}) = 0.570 \times 10^{-3}$ m (0.570 mm). This violation is of such small magnitude that it is negligible.

The optimum solution, corresponding to the specification of extremely accurate convergence tolerances ($\varepsilon_g = 10^{-5}$ for criterion 1; and $\varepsilon_x = 10^{-5}$ for criterion 2 in Section 4.4), is found after 81 optimization iterations and utilizing 53 seconds computational time on a Pentium IV 1.5 GHz computer with 640 MB DDRAM. The specific criterion that the LFOPC-algorithm terminated on is criterion 2, $\varepsilon_x \leq 10^{-5}$ (see Section 4.4). Throughout the choice DELT = 0.01 was used for the LFOPC maximum stepsize parameter (see **Appendix C**).

5 DEMONSTRATION OF THE OPTIMUM EXECUTION OF REPRESENTATIVE PRESCRIBED MACHINING PATHS

5.1 Introduction

In this chapter, optimum platform geometries of the re-configurable planar Gough-Stewart platform test-model are determined for different prescribed machining tasks.

The determination of the optimum platform geometries is done using the *simulation-based* optimization methodology developed in **Chapter 4**. The feasibility of this approach was illustrated in **Chapter 4** by optimizing the geometry of a *hypothetical* planar Gough-Stewart platform for a simple straight-line prescribed path, taking into consideration the mechanism's configurational constraints. In applying the methodology to a *physically real* platform, however, the physical operational constraints specified in Section D.3 are required to prevent mechanical interference. The respective masses and moments of inertia of the seven bodies comprising the physical test-model are also determined in **Appendix D** (Section D.2.3). These seven bodies are numbered below in Figure 5.1 which corresponds to Figure 2.5 and Figure D.2.

5.4.4 Execution of the circular tool path

The series of photographs shown in Figure 5.18 is of different instants during the execution of the first revolution of the circular tool path.

Figure 5.18: Execution of the circular tool path.

Figure 5.19 is a close-up of the traced circular tool path, showing that the diameter of the traced circle is approximately 350 mm (35 cm), and that the circle is smoothly traced.

Figure 5.19: Close-up view of the executed circular tool path.

5.5 Spiral tool path

5.5.1 Nodal points and orientation angle

The spiral tool path is a scaled version of the logarithmic spiral test curve $\rho = e^{0.1\beta}$ of Section 3.5.4. Using a scale factor of 0.285, the 79 spiral tool path nodal points are as shown in Figure 5.20.

The motion time along the spiral tool path is 93.24 seconds with the specification of $\ddot{s}_{ALLOW} = 0.01\,m/s^2$, $v^* = 1.0\,m/min$ and $n_{time} = 5$ for the use of the OCAS trajectory-planning algorithm.

Figure 5.1: Photograph of the physical planar Gough-Stewart platform test-model.

The moving platform is in contact with the Perspex side panels via the Teflon stabilizers and the pen shown in Figure 5.1. Section D.2.3 shows how the resulting *frictional* force was experimentally determined. This external frictional force represents the *cutting force* incorporated in the kinematic and kinetic model of the planar Gough-Stewart machining platform. In fact, the test-model is used here to demonstrate the "fixed workpiece scenario" (see Sections 2.4.1 and 2.6.4.2.1), with specifically a *zero tool length* ($\eta_1^p = 0$), since the pen is mounted to coincide with the *assumed* center of mass of the moving platform.

Furthermore, in this chapter, non-trivial prescribed paths are specified for the physical test-model using the OCAS trajectory-planning technique described in **Chapter 3**. The five different test functions discussed in Section 3.5 are used as prescribed tool paths, to illustrate the application of the proposed optimization methodology to obtain optimum operational geometries.

Once the *simulation-based* numerical optimization of the physical test-model is done for each prescribed path, the *execution* of each path follows through the control commands generated by the computer simulation for controlling the required variation of the actuator leg lengths. These lengths are found by solving the three closed-form inverse kinematic equations relating the position and orientation of the moving platform to the actuator leg lengths. The position and orientation of the moving platform follows

directly from the prescribed trajectory, and hence the required actuator leg lengths may easily be determined (see expression (4.10)).

Since the purpose of the test-model is only to demonstrate the new technology, visual inspection is used to verify that each executed path indeed corresponds to the prescribed path. Photographs are included in this chapter to show the successful execution of the prescribed paths, for the respective optimum and feasible settings of the planar machine.

Sections 5.2 – 5.6 respectively deal with the five different prescribed paths all of which are scaled for *continuous* execution. Section 5.7 shows how the proposed optimization methodology may be applied in the *piece-wise* execution of the "bigger parabolic tool path".

5.2 Parabolic tool path

5.2.1 Nodal points and orientation angle

The parabolic test function used in Section 3.5.1, $y(x) = \dfrac{x^2}{2}$, was approximated over the x-interval, $x \in [-2, 2]$, using 29 nodal points as shown in Figure 3.16. Here a *scaled mirror image* of this quadratic function is used as prescribed path. The *mirror image* of the original parabola (expression (3.66)) is given by

$$y(x) = -\frac{x^2}{2} \qquad (5.1)$$

over the x-interval, $x \in [-2, 2]$. Substituting the *unscaled* x-values into (5.1) gives the *unscaled* y-values. The scale factor used here is 0.075, and the resulting 27 nodal points are shown in Figure 5.2.
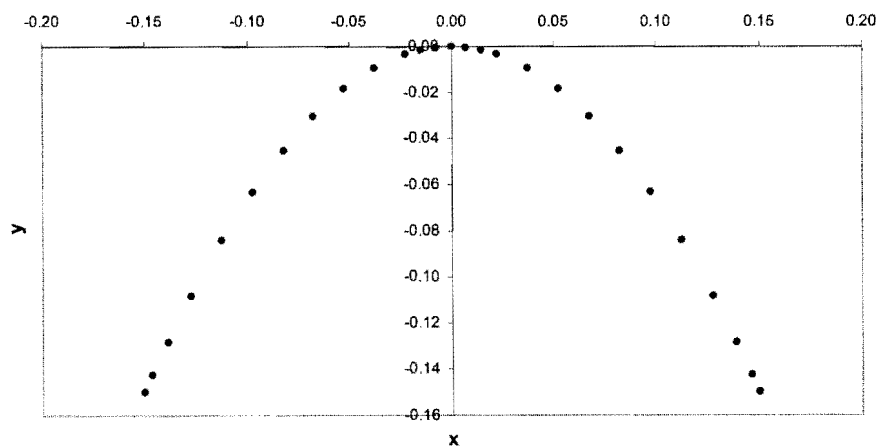
Figure 5.2: Nodal points used to approximate the parabolic tool path.

For the OCAS trajectory-planning methodology (**Chapter 3**), the maximum allowable acceleration is limited to 0.01 meter per second square ($\ddot{s}_{allow} = 0.01\,\text{m}/\text{s}^2$), and a cutting speed of 1.0 m/min ($v^* = 1.0\,\text{m}/\text{min}$) is specified. With these specifications, the *simulated* prescribed motion is completed in 29.46 s. The simulation is furthermore carried out with the number of additional intermediate time instants, $n_{time} = 5$ (see **Appendix B**).

It is also required that the moving platform of the test-model be tangentially orientated with respect to the prescribed curve. With this specification the moving platform orientation angle varies from $63.43°$ at the starting point $(-0.15, -0.15)$, to $-63.43°$ at the end point $(0.15, -0.15)$ (see Figure 5.3).
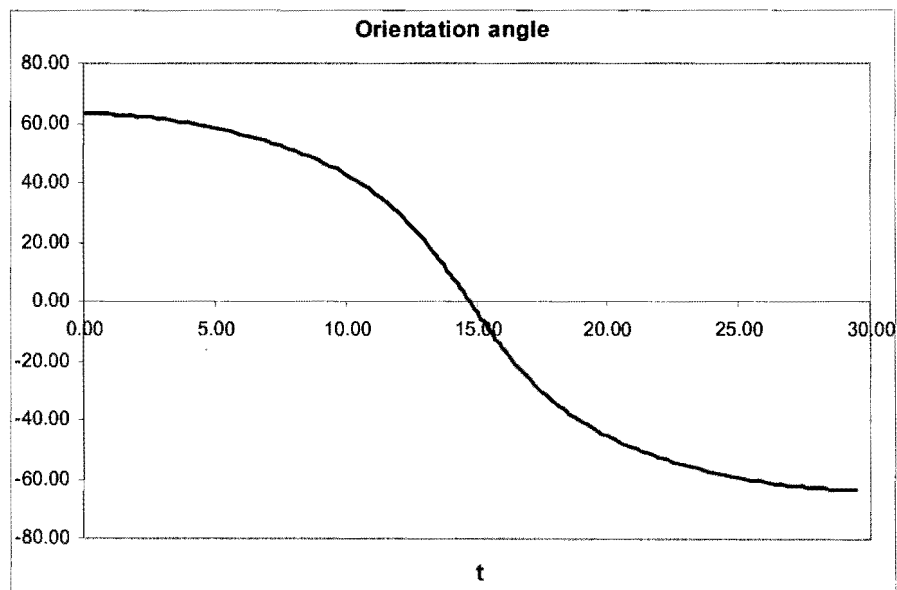
Figure 5.3: Variation in the orientation angle for the parabolic tool path.

5.2.2 Optimization results

A comparison between the initial test-model design and optimum test-model design for the parabolic prescribed tool path is given in Table 5.1, with figure insets 1(a) – 1(d).

Initial design	Optimum design
$\mathbf{X}^0 = [0.4, 0.4, -0.4, -0.4, 0.2]^T$	$\mathbf{X}^* = [0.1, 0.19387, -0.47769, -0.18012, 0.113]^T$

Inequality constraint values (see Section D.3):

$C_1(\mathbf{X}^0) = -0.05$	$C_2(\mathbf{X}^0) = -0.3$	$C_1(\mathbf{X}^*) = -0.35$	$\Rightarrow C_2(\mathbf{X}^*) = -0.363 \times 10^{-6}$
$C_3(\mathbf{X}^0) = -0.065$	$C_4(\mathbf{X}^0) = -0.287$	$C_3(\mathbf{X}^*) = -0.27113$	$C_4(\mathbf{X}^*) = -0.08087$
$C_5(\mathbf{X}^0) = -0.07$	$C_6(\mathbf{X}^0) = -0.087$	$C_5(\mathbf{X}^*) = -0.157$	$\Rightarrow C_6(\mathbf{X}^*) = 0.624 \times 10^{-6}$
$\rightarrow C_7(\mathbf{X}^0) = 0.10533$	$C_8(\mathbf{X}^0) = -0.01481$	$\Rightarrow C_7(\mathbf{X}^*) = -0.784 \times 10^{-6}$	$C_8(\mathbf{X}^*) = -0.03374$
$\rightarrow C_9(\mathbf{X}^0) = 0.00045$	$\rightarrow C_{10}(\mathbf{X}^0) = 0.07769$	$C_9(\mathbf{X}^*) = -0.01780$	$\Rightarrow C_{10}(\mathbf{X}^*) = -0.616 \times 10^{-6}$
$\rightarrow C_{11}(\mathbf{X}^0) = 0.07769$	$C_{12}(\mathbf{X}^0) = -0.34542$	$\Rightarrow C_{11}(\mathbf{X}^*) = -0.616 \times 10^{-6}$	$C_{12}(\mathbf{X}^*) = -0.39888$
$C_{13}(\mathbf{X}^0) = -0.14542$	$\rightarrow C_{14}(\mathbf{X}^0) = 0.00109$	$C_{13}(\mathbf{X}^*) = -0.22639$	$C_{14}(\mathbf{X}^*) = -0.04907$
$C_{15}(\mathbf{X}^0) = -0.00493$	$\rightarrow C_{16}(\mathbf{X}^0) = 0.01619$	$C_{15}(\mathbf{X}^*) = -0.22745$	$C_{16}(\mathbf{X}^*) = -0.05909$
$\rightarrow C_{17}(\mathbf{X}^0) = 0.01727$	$\rightarrow C_{18}(\mathbf{X}^0) = 0.04250$	$C_{17}(\mathbf{X}^*) = -0.01676$	$C_{18}(\mathbf{X}^*) = -0.05310$
$C_{19}(\mathbf{X}^0) = -0.06220$	$C_{20}(\mathbf{X}^0) = -0.08449$	$C_{19}(\mathbf{X}^*) = -0.05754$	$C_{20}(\mathbf{X}^*) = -0.15073$
$C_{21}(\mathbf{X}^0) = -0.07149$	$\rightarrow C_{22}(\mathbf{X}^0) = 0.03098$	$C_{21}(\mathbf{X}^*) = -0.05200$	$C_{22}(\mathbf{X}^*) = -0.11672$

$\rightarrow$ constraint violation	$\Rightarrow$ constraint active

Variation of actuator leg lengths along the parabolic tool path:

1(a)

1(b)

Variation of actuator forces along the parabolic tool path:	

1(c)

1(d)

$F(\mathbf{X}^0) = 22.066\,\text{N}$	$F(\mathbf{X}^*) = 31.936\,\text{N}$
Actuator leg 3	Actuator leg 1
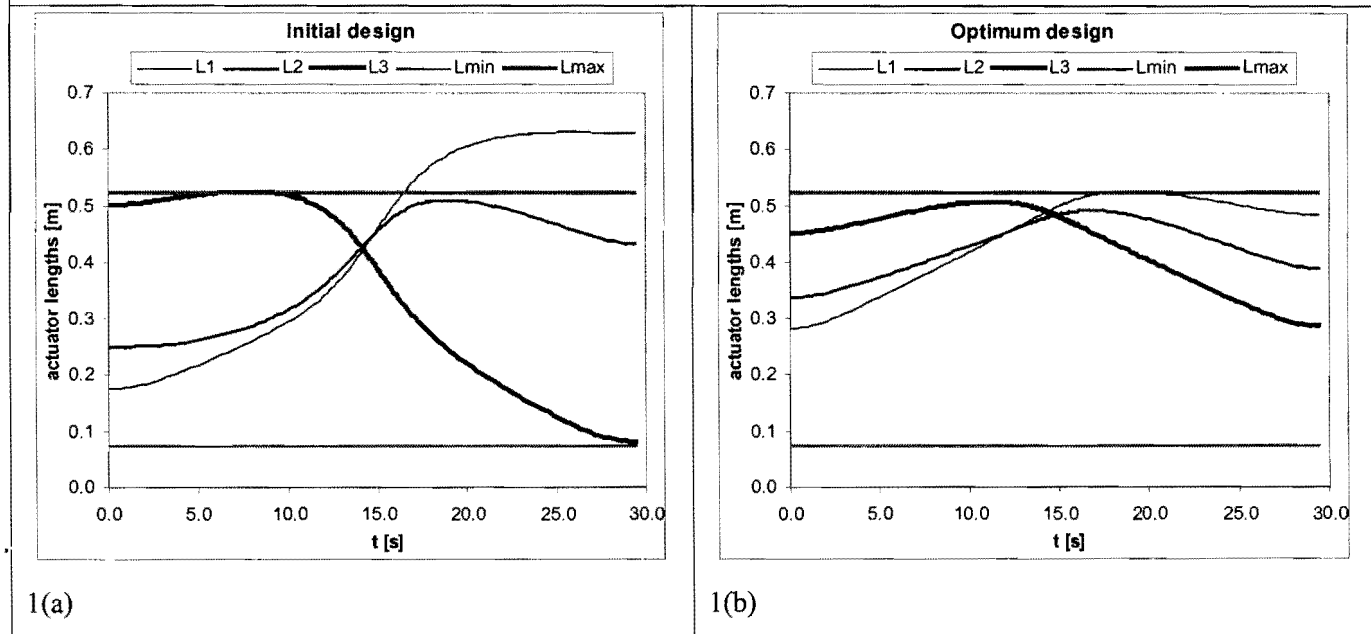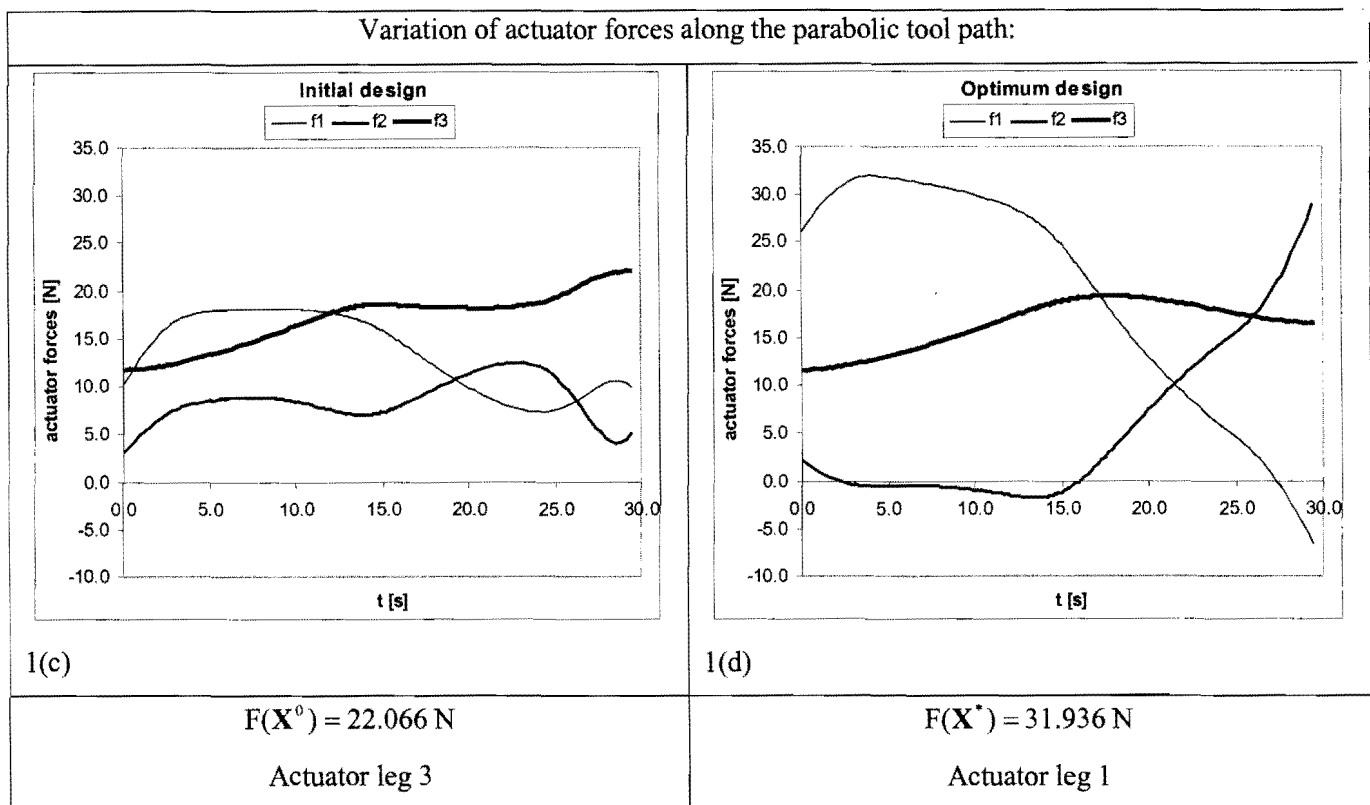
Table 5.1: Comparison between the initial and optimum designs for the parabolic tool path.

Although the initial objective function value $F(\mathbf{X}^0) = 22.066\,\text{N}$ is lower than the optimum objective function value $F(\mathbf{X}^*) = 31.936\,\text{N}$, the *initial design is infeasible*. In fact, nine of the 22 inequality constraints are *violated* when the parabolic test function is traced with the initial design $\mathbf{X}^0$. Table 5.1 lists the initial values of the inequality constraint functions $C_i(\mathbf{X}^0)$, $i = 1,2,3,...,22$, as well as their optimum values $C_i(\mathbf{X}^*)$, $i = 1,2,3,...,22$. The violated inequality constraints associated with the initial design $\mathbf{X}^0$ have function values greater than zero, and are indicated by a *single* arrow $\rightarrow$ in Table 5.1. Similarly, the *active* inequality constraints associated with the optimum design $\mathbf{X}^*$ have *approximately* zero function values, and are indicated by a *double* arrow $\Rightarrow$ in Table 5.1.

The variation in the actuator leg lengths depicted in figure inset 1(a) clearly show that both actuator legs ℓ_1 and ℓ_3 initially violate the allowable maximum leg length, explaining the positive constraint function values of C_7 and C_9 (expression (D.11)). Inequality constraints corresponding to C_{10} and C_{11} (expression (D.12)) are violated even though the allowable minimum leg length is not violated (see figure inset 1(a)). Indeed, these two inequality constraints are violated as a result of the specification of tangential orientation of the moving platform with respect to the parabolic tool path (see Figure 5.3). The remaining violated inequality constraints, corresponding to the positive function values of C_{14}, C_{16},

C_{17}, C_{18} and C_{22}, indicate that the parabolic tool path cannot be followed with the initial design $\mathbf{X}^0$, due to mechanical interference (see respective expressions (D.15), (D.17), (D.18), (D.19) and (D.23)).

On the other hand, figure inset 1(b) clearly shows that for the optimum design $\mathbf{X}^*$, the variation in actuator leg lengths as the parabolic tool path is followed, lies within the minimum and maximum allowable lengths. The *feasibility* of the optimum design $\mathbf{X}^*$ is further borne out by the fact that the optimum inequality constraint function values $C_i(\mathbf{X}^*)$, $i = 1,2,3,...,22$ are all less than, or approximately equal to zero. In particular, the inequality constraints corresponding to C_2, C_6, C_7, C_{10} and C_{11} are considered to be *active* (see expressions (D.10), (D.11) and (D.12)). The optimum solution is found after 227 optimization iterations and utilizing 6 minutes and 58 seconds computational time on a Pentium IV 1.5 GHz computer with 640 MB DDRAM. LFOPC terminated on criterion 2 ($\varepsilon_x \leq 10^{-5}$) listed in Section 4.4.

5.2.3 Analysis of convergence to optimum

Figure 5.4 shows the convergence history of the objective function.
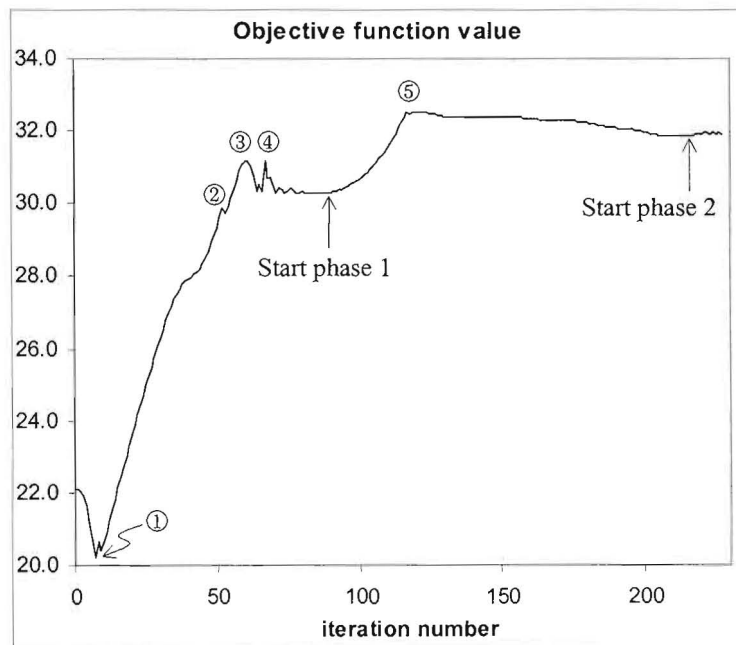
Figure 5.4: Convergence history of the objective function for the parabolic tool path.

The behavior of the above objective function vs. iteration number curve is of course dependent on the iterative search generated by the LFOPC algorithm in the five dimensional design space (see Figure 4.10). The choice of the initial design $\mathbf{X}^0$ obviously plays an important role in the nature of the convergence history of the objective function. In correspondence with Section 4.5, the initial configuration of the planar machining center is chosen as $\mathbf{X}^0 = [0.4, 0.4, -0.4, -0.4, 0.2]^T$ for all the

machining paths investigated in this chapter. Initial design variable values $X_1^0 = 0.4\,\text{m}$, $X_2^0 = 0.4\,\text{m}$ and $X_5^0 = 0.2\,\text{m}$ are in scaled agreement with the geometry of Haug et al.'s [73] planar Gough-Stewart platform. Setting design variables $X_4^0 = -0.4\,\text{m}$ and $X_3^0 = -0.4\,\text{m}$ corresponds to a random choice for the position of the origin of the global 0xy-coordinate system, relative to which the tool path is described, and the kinematic and kinetic analysis (**Chapter 2**) is done.
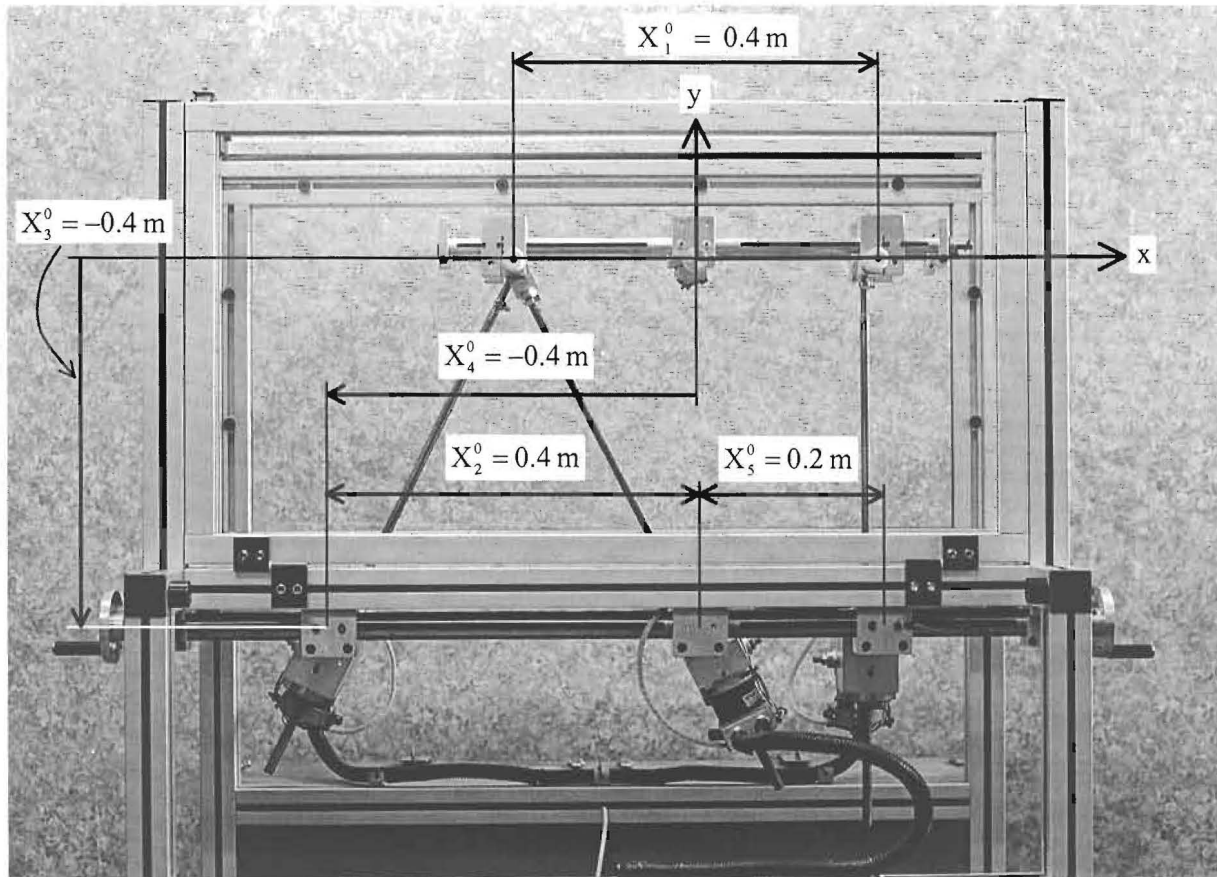
Figure 5.5: Photograph of the initial test-model design $X^0 = [0.4, 0.4, -0.4, -0.4, 0.2]^T$.

With specific reference to Figure 5.4, the labels ① – ⑤ are used in Table 5.2 to relate the *iteration number* and *phase* of the LFOPC-algorithm (see **Appendix C**) to the actuator leg responsible for the *maximum magnitude actuator force* (see Section 4.2.2) and the violated inequality constraints at the indicated regions of the convergence curve.

Labels	Iter. No.	LFOPC-Phase	Act. leg	Violated Inequality Constraints
$\mathbf{X}^0$	0	0	ℓ_3	$C_7 \quad C_9 \quad C_{10} \quad C_{11} \quad C_{14} \quad C_{16} \quad C_{17} \quad C_{18} \quad C_{22}$
①	7	0	ℓ_3	$C_7 \quad C_8 \quad C_9 \quad C_{10} \quad C_{11} \quad C_{16} \quad C_{18} \quad C_{22}$
	8	0	ℓ_1	$C_7 \quad C_8 \quad C_9 \quad C_{10} \quad C_{11} \quad C_{18} \quad C_{22}$
	9	0	ℓ_1	$C_7 \quad C_8 \quad C_9 \quad C_{10} \quad C_{11} \quad C_{16} \quad C_{18} \quad C_{22}$
②	52	0	ℓ_1	$C_6 \quad C_7 \quad C_{10} \quad C_{11} \quad C_{17}$
	53	0	ℓ_1	$C_6 \quad C_7 \quad C_{10} \quad C_{11} \quad C_{17}$
	54	0	ℓ_1	$C_6 \quad C_7 \quad C_{10} \quad C_{11} \quad C_{17}$
③	60	0	ℓ_1	$C_7 \quad C_{10} \quad C_{11}$
	61	0	ℓ_1	$C_7 \quad C_{10} \quad C_{11}$
④	63	0	ℓ_1	$C_7 \quad C_{10} \quad C_{11}$
	64	0	ℓ_2	$C_7 \quad C_{10} \quad C_{11}$
	65	0	ℓ_1	$C_7 \quad C_{10} \quad C_{11}$
	66	0	ℓ_1	$C_7 \quad C_{10} \quad C_{11}$
	67	0	ℓ_2	$C_7 \quad C_{10} \quad C_{11}$
	68	0	ℓ_2	$C_7 \quad C_{10} \quad C_{11}$
	69	0	ℓ_1	$C_7 \quad C_{10} \quad C_{11}$
LFOPC phase-change	86	0	ℓ_1	$C_7 \quad C_{10} \quad C_{11}$
	87	0	ℓ_2	$C_7 \quad C_{10} \quad C_{11}$ maximum violated constraint value $C_7(\mathbf{X}^{87}) = 0.00496$
	87	1	ℓ_2	$C_7 \quad C_{10} \quad C_{11}$
	88	1	ℓ_1	$C_7 \quad C_{10} \quad C_{11}$
⑤	121	1	ℓ_1	none
	122	1	ℓ_1	none
	123	1	ℓ_1	$C_2 \quad C_7$
LFOPC phase-change	215	1	ℓ_1	$C_2 \quad C_6 \quad C_7 \quad C_{10} \quad C_{11}$
	215	2	ℓ_1	$C_2 \quad C_6 \quad C_7 \quad C_{10} \quad C_{11}$
$\mathbf{X}^*$	227	2	ℓ_1	$C_2 \quad C_6 \quad C_7 \quad C_{10} \quad C_{11}$ (active)

Table 5.2: Comparative table for the parabolic tool path objective function vs. iteration number curve (see Figure 5.4).

The increase in the objective function value between labels ④ and ⑤ in Figure 5.4 is a result of the LFOPC phase-change occurring at iteration number 87 (see **Appendix C**) at which point the penalty parameter is increased. Furthermore, Table 5.2 shows that the actuator leg responsible for the maximum magnitude actuator force switches from actuator leg ℓ_3 to ℓ_1 at label ①. It was shown in Section 4.3.1 that a switch in the actuator legs responsible for the maximum magnitude actuator force is associated with a kink in the objective function, and hence a discontinuity in its slope. This results in the spiky behavior of the objective function in these regions.

The switches involving actuator legs ℓ_1 and ℓ_2 that occur as the LFOPC-algorithm changes from phase 0 to phase 1 show that the associated design is close to the optimum. Consider figure inset 1(d) showing the variation in actuator forces associated with the optimum design $\mathbf{X}^*$. The maximum magnitude of the force in actuator leg ℓ_1, $f_1 = 31.936\,\text{N}$ occurring at time instant $t = 3.97\,\text{s}$, is only slightly larger than the maximum magnitude of the force in actuator leg ℓ_2, $f_2 = 28.774\,\text{N}$ occurring at time instant $t = 29.46\,\text{s}$.

The fact that the final design of phase 0 (iteration number 87 in Table 5.2) is indeed relatively close with respect to feasibility to the optimum design, is evident from the convergence histories of the respective design variables X_i, $i = 1,2,...,5$ as shown in Figure 5.6. It is of interest to note that for the design variables the convergence is considerably smoother. In practical terms, convergence is effectively achieved at the end of phase 0 after only 87 iterations where the maximum violated constraint is C_7 with a function value of $C_7(\mathbf{X}^{87}) = 0.00496\,\text{m} = 4.96\,\text{mm}$.
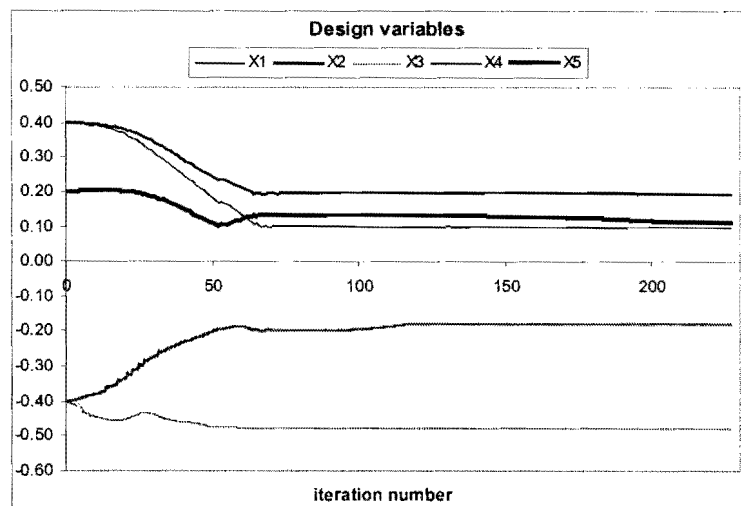
Figure 5.6: Convergence histories of design variables X_i, $i = 1,2,...,5$ for the parabolic tool path.

5.2.4 *Execution of parabolic tool path*

Figure 5.7 shows a series of photographs taken at different time instants as the parabolic tool path is traced. The tangential orientation of the moving platform along the curve is clearly visible from the photographs.
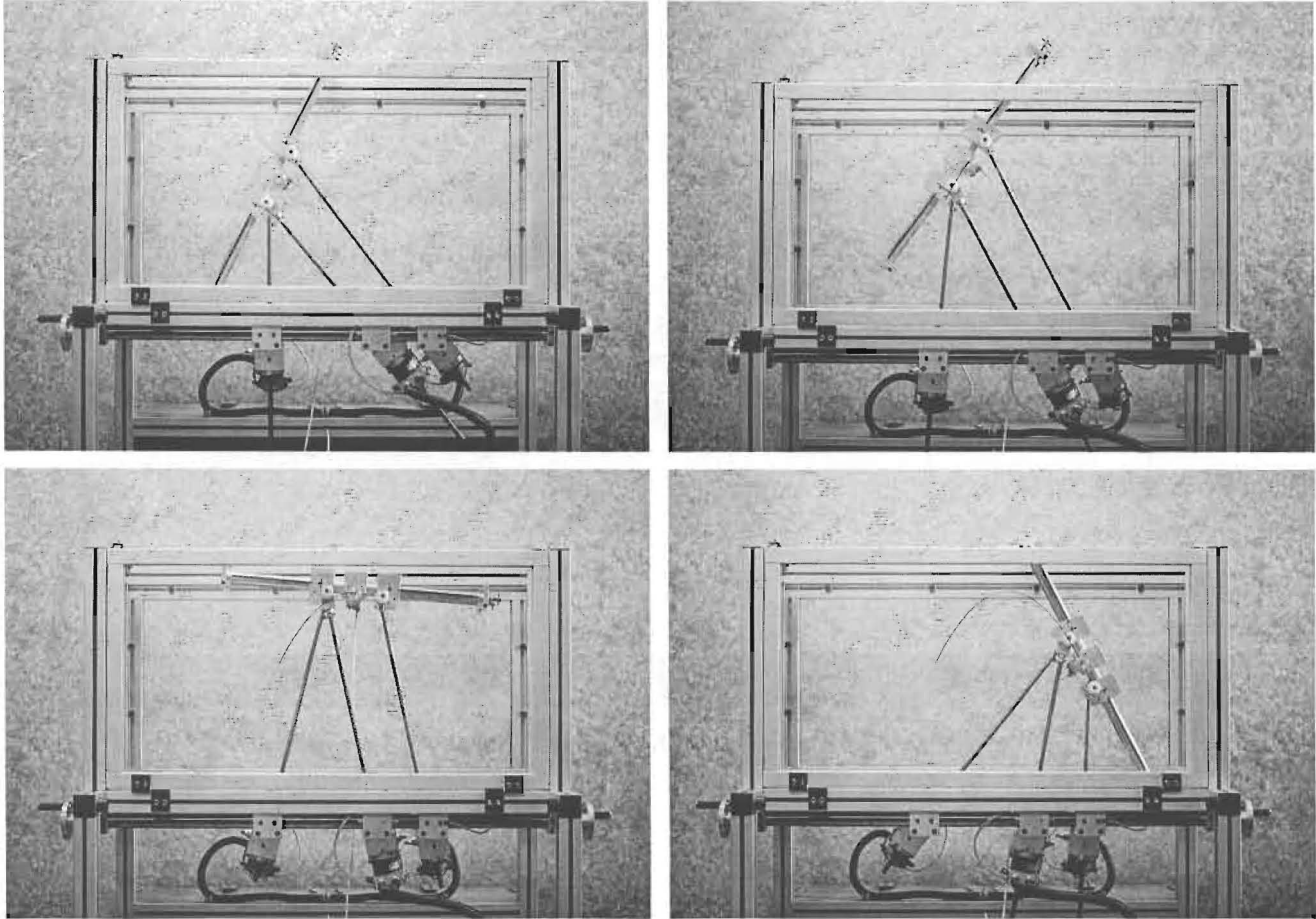
Figure 5.7: Execution of parabolic tool path.

A close-up view of the executed parabolic tool path is shown in Figure 5.8. Inspection shows that the actual executed tool path accurately resembles the prescribed tool path (see Figure 5.2). It is evident that the distance between the end points of the traced parabolic tool path is approximately $300\,\mathrm{mm}$ ($30\,\mathrm{cm}$) and that the traced parabolic tool path is proportionally shaped and smooth in agreement with the prescribed path specified by Figure 5.2.
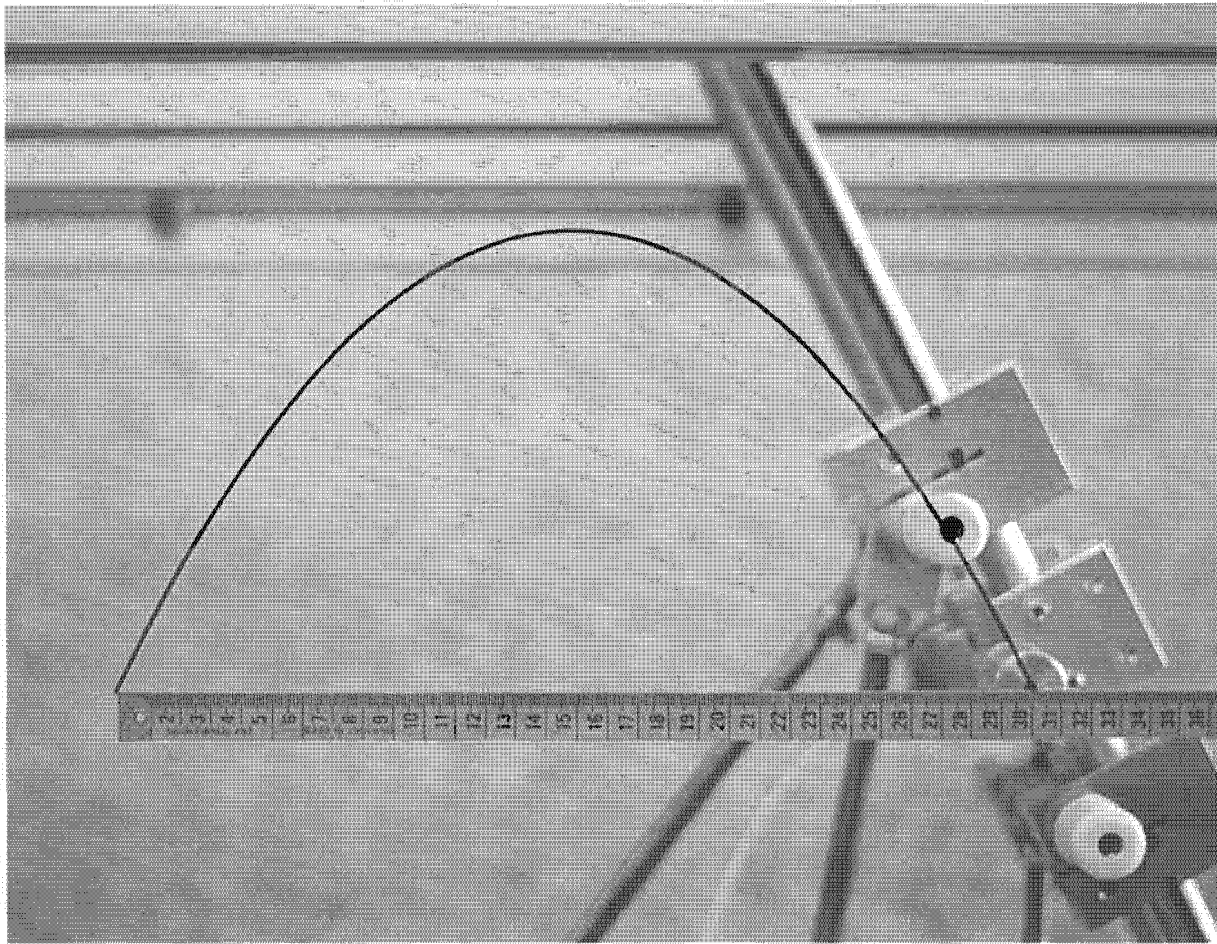
Figure 5.8: Close-up view of the executed parabolic tool path.

5.3 Spike tool path

5.3.1 Nodal points and orientation angle

The spike test function of Section 3.5.2, $y(x) = \dfrac{1}{1+x^2}$ (see expression 3.67) was approximated over the x-interval, $x \in [-2, 2]$, using 27 nodal points. Note that the initial and final nodal points are $P_0 = (x_0, y_0) = (2, 0.2)$ and $P_N = (x_N, y_N) = (-2, 0.2)$ respectively.

The spike tool path is a *scaled* version of the original spike test function using a scale factor of 0.15. In particular, the initial and final nodal points are thus $P_0 = (x_0, y_0) = (0.3, 0.03)$ and $P_N = (x_N, y_N) = (-0.3, 0.03)$ respectively. Figure 5.9 shows the 27 nodal points used to approximate the spike tool path.
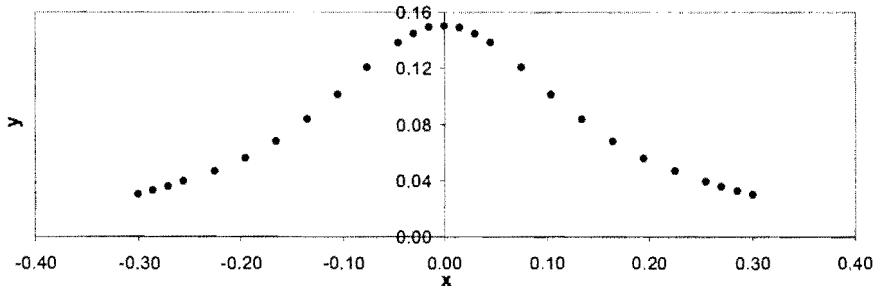
Figure 5.9: Nodal points used to approximate the spike tool path.

The OCAS trajectory-planning methodology (**Chapter 3**) is again used to approximate the spike tool path with $\ddot{s}_{allow} = 0.01\,\text{m}/\text{s}^2$ and $v^* = 1.0\,\text{m}/\text{min}$ resulting in a total motion time of $41.95\,\text{s}$. The simulation is again done with $n_{time} = 5$.
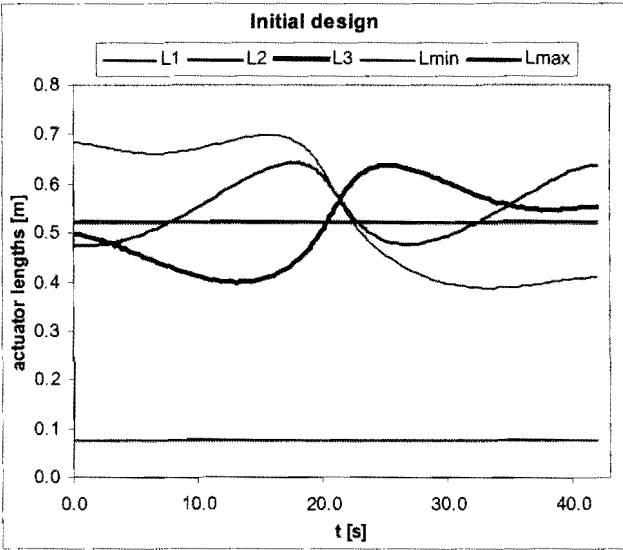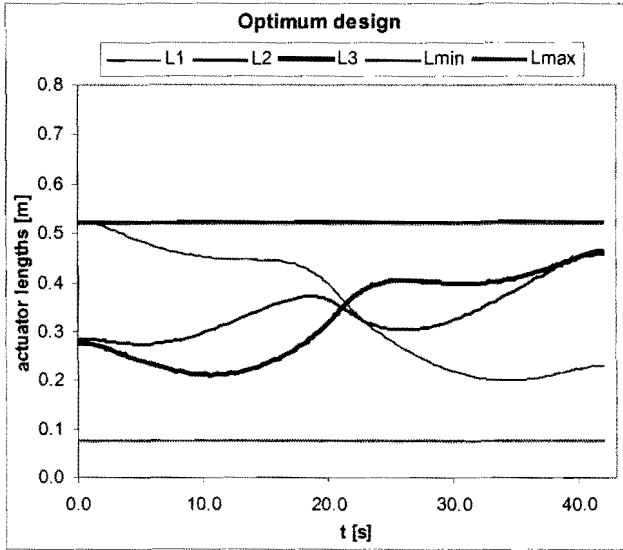
As in the case of the parabolic tool path, the moving platform of the test-model must maintain a tangential orientation with respect to the prescribed spike tool path. The variation of the orientation angle [degrees] as the moving platform traces the spike tool path, is depicted in Figure 5.10.
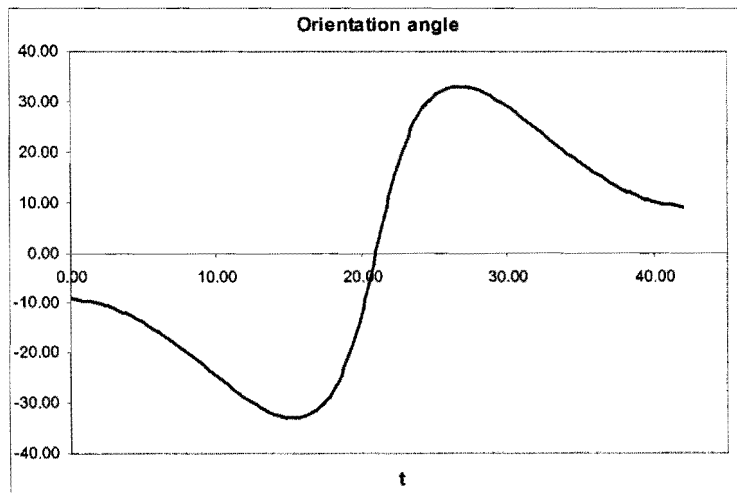
Figure 5.10: Variation in the orientation angle for the spike tool path.

5.3.2 Optimization results

The initial and optimum test-model designs for the spike tool path are compared in Table 5.3, with graphical insets 2(a) – 2(d).

Initial design	Optimum design
$\mathbf{X}^0 = [0.4, 0.4, -0.4, -0.4, 0.2]^T$	$\mathbf{X}^* = [0.21174, 0.29788, -0.17937, -0.27835, 0.18509]^T$

Inequality constraint values (see Section D.3):	
$C_1(\mathbf{X}^0) = -0.05 \qquad C_2(\mathbf{X}^0) = -0.3$ $C_3(\mathbf{X}^0) = -0.065 \qquad C_4(\mathbf{X}^0) = -0.287$ $C_5(\mathbf{X}^0) = -0.07 \qquad C_6(\mathbf{X}^0) = -0.087$ $\rightarrow C_7(\mathbf{X}^0) = 0.17403 \quad \rightarrow C_8(\mathbf{X}^0) = 0.11745$ $\rightarrow C_9(\mathbf{X}^0) = 0.11302 \quad C_{10}(\mathbf{X}^0) = -0.27092$ $C_{11}(\mathbf{X}^0) = -0.27092 \quad C_{12}(\mathbf{X}^0) = -0.08751$ $\rightarrow C_{13}(\mathbf{X}^0) = 0.11249 \quad C_{14}(\mathbf{X}^0) = -0.03529$ $C_{15}(\mathbf{X}^0) = -0.05145 \quad C_{16}(\mathbf{X}^0) = -0.02809$ $C_{17}(\mathbf{X}^0) = -0.04628 \quad C_{18}(\mathbf{X}^0) = -0.05358$ $C_{19}(\mathbf{X}^0) = -0.05924 \quad C_{20}(\mathbf{X}^0) = -0.08094$ $C_{21}(\mathbf{X}^0) = -0.08051 \quad C_{22}(\mathbf{X}^0) = -0.05931$	$C_1(\mathbf{X}^*) = -0.23826 \qquad C_2(\mathbf{X}^*) = -0.11174$ $C_3(\mathbf{X}^*) = -0.16712 \qquad C_4(\mathbf{X}^*) = -0.18488$ $C_5(\mathbf{X}^*) = -0.08491 \qquad C_6(\mathbf{X}^*) = -0.07209$ $\Rightarrow C_7(\mathbf{X}^*) = -0.511 \times 10^{-5} \quad C_8(\mathbf{X}^*) = -0.05923$ $C_9(\mathbf{X}^*) = -0.06545 \qquad C_{10}(\mathbf{X}^*) = -0.05029$ $C_{11}(\mathbf{X}^*) = -0.05029 \qquad C_{12}(\mathbf{X}^*) = -0.16093$ $\Rightarrow C_{13}(\mathbf{X}^*) = 0.687 \times 10^{-5} \quad C_{14}(\mathbf{X}^*) = -0.00220$ $C_{15}(\mathbf{X}^*) = -0.05317 \quad \Rightarrow C_{16}(\mathbf{X}^*) = 0.281 \times 10^{-6}$ $\Rightarrow C_{17}(\mathbf{X}^*) = -0.535 \times 10^{-5} \quad C_{18}(\mathbf{X}^*) = -0.02511$ $C_{19}(\mathbf{X}^*) = -0.01017 \qquad C_{20}(\mathbf{X}^*) = -0.02684$ $C_{21}(\mathbf{X}^*) = -0.03971 \qquad C_{22}(\mathbf{X}^*) = -0.10923$
$\rightarrow$ constraint violation	$\Rightarrow$ constraint active

Variation of actuator leg lengths along the spike tool path:	

2(a)

2(b)

Variation of actuator forces along the spike tool path:	
2(c)	2(d)
$F(\mathbf{X}^0) = 37.884$ N	$F(\mathbf{X}^*) = 35.160$ N
Actuator leg 2	Actuator leg 1

Table 5.3: Comparison between the initial and optimum designs for the spike tool path.

The violated inequality constraints associated with the *infeasible initial design* correspond to constraint functions C_7, C_8, C_9 and C_{13} (see expressions (D.11) and (D.14)). Again looking at figure inset 2(a), it is evident that all three actuator legs ℓ_1, ℓ_2 and ℓ_3 will violate the maximum allowable actuator leg length if the spike tool path is to be traced with the initial design $\mathbf{X}^0$, explaining why the inequality constraint function values $C_7(\mathbf{X}^0)$, $C_8(\mathbf{X}^0)$, $C_9(\mathbf{X}^0)$ are greater than zero. The inequality constraint corresponding to C_{13} prevents the excessive side way movement of the moving platform towards the right hand side as explained in Section D.3.3.4.

Figure inset 2(b) shows that in the case of the *feasible optimum design* $\mathbf{X}^*$, the variation in the actuator legs lies within the specified minimum and maximum allowable bounds. The active constraints correspond to C_7, C_{13}, C_{16} and C_{17} (see respective expressions (D.11), (D.14), (D.17) and (D.18)). The optimum solution is found after 156 optimization iterations and utilizing 4 minutes and 53 seconds computational time on a Pentium IV 1.5 GHz computer with 640 MB DDRAM. LFOPC again terminated on criterion 2 ($\varepsilon_x \leq 10^{-5}$).

5.3.3 Analysis of convergence to optimum

Figure 5.11 shows the convergence history of the objective function.
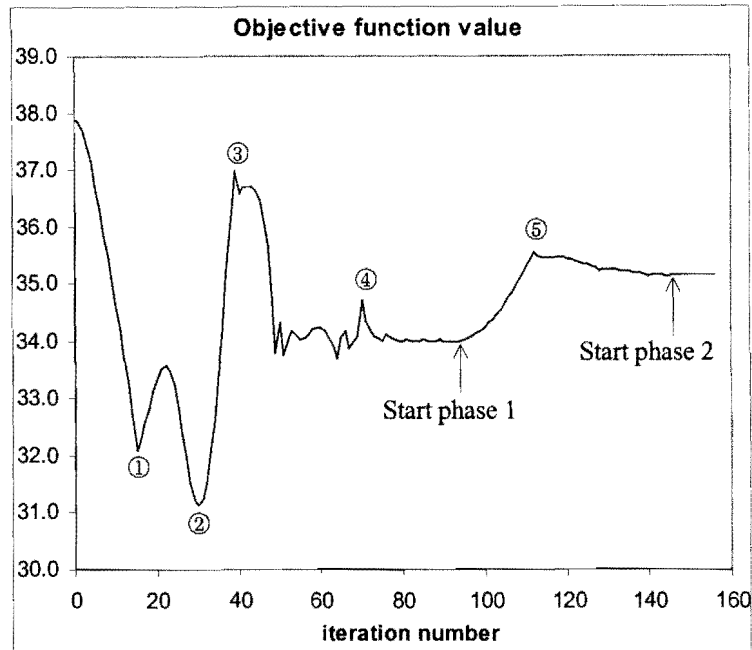
Figure 5.11: Convergence history of the objective function for the spike tool path.

Labels ① – ⑤ in Figure 5.11 are used in Table 5.4 to relate the *iteration number* and *phase* of the LFOPC-algorithm (see **Appendix C**) to the actuator leg responsible for the *maximum magnitude actuator force* (see Section 4.2.2) and the violated inequality constraints in the respectively indicated regions.

Labels	Iteration No.	LFOPC-Phase	Act. leg	Violated Inequality Constraints			
$\mathbf{X}^0$	0	0	ℓ_2	C_7 C_8 C_9 C_{13}			
①	15	0	ℓ_2	C_7 C_8 C_9 C_{13}			
	16	0	ℓ_1	C_7 C_8 C_{13}			
	17	0	ℓ_1	C_7 C_8 C_{13}			
②	30	0	ℓ_1	C_7	C_{13}	C_{16}	C_{17}
	31	0	ℓ_1	C_7	C_{13}	C_{16}	
③	39	0	ℓ_1	C_7	C_{16}		
	40	0	ℓ_1	C_7	C_{16}		
	41	0	ℓ_1	C_7	C_{16}		
	42	0	ℓ_1	C_7			

	64	0	ℓ_1	C_7		C_{13}	C_{16}	C_{17}
	65	0	ℓ_2	C_7		C_{13}	C_{16}	C_{17}
	66	0	ℓ_1	C_7			C_{16}	C_{17}
④	67	0	ℓ_1	C_7		C_{13}	C_{16}	C_{17}
	68	0	ℓ_1	C_7		C_{13}	C_{16}	C_{17}
	69	0	ℓ_2	C_7		C_{13}	C_{16}	
	70	0	ℓ_1	C_7			C_{16}	C_{17}
	87	0	ℓ_1	C_7		C_{13}	C_{16}	C_{17}
	88	0	ℓ_2	C_7		C_{13}	C_{16}	C_{17}
	89	0	ℓ_1	C_7		C_{13}	C_{16}	C_{17}
LFOPC	90	0	ℓ_1	C_7		C_{13}	C_{16}	C_{17}
phase-	91	0	ℓ_1	C_7		C_{13}	C_{16}	C_{17}
change	92	0	ℓ_1	C_7 C_{13} C_{16} C_{17} maximum violated constraint value: $C_7(\mathbf{X}^{92}) = 0.00436$				
	92	1	ℓ_1	C_7		C_{13}	C_{16}	C_{17}
	93	1	ℓ_1	C_7		C_{13}	C_{16}	C_{17}
	112–114	1	ℓ_1	none				
⑤	115	1	ℓ_1	C_7				
	116	1	ℓ_1	C_7				
LFOPC	145	1	ℓ_1	C_7		C_{13}		C_{17}
phase-	146	1	ℓ_1	C_7		C_{13}	C_{16}	C_{17}
change	146	2	ℓ_1	C_7		C_{13}	C_{16}	C_{17}
	147	2	ℓ_1	C_7		C_{13}	C_{16}	C_{17}
$\mathbf{X}^{*}$	156	2	ℓ_1	C_7		C_{13}	C_{16}	C_{17} (active)

Table 5.4: Comparative table for the spike tool path objective function vs. iteration number curve (see Figure 5.11).

The first LFOPC phase-change from phase 0 to phase 1 occurs at iteration number 92, hence the resulting increase in the objective function value between labels ④ and ⑤ in Figure 5.11 as the penalty parameter is increased at the start of phase 1. The spiky behavior of the objective function value at labels ① and ④ can again be explained by the switch in the actuator leg responsible for the maximum magnitude actuator force, that occur in these regions.

The convergence histories of the respective design variables x_i, $i = 1,2,...,5$ are shown in Figure 5.12. Again effective convergence with respect to feasibility is obtained at the end of phase 0 after only 92 iterations with the maximum violated constraint value $C_7(\mathbf{X}^{92}) = 0.00436 \text{ m} = 4.36 \text{ mm}$. Note also, that there is a switch between actuator legs ℓ_1 and ℓ_2 responsible for the maximum magnitude actuator force at iteration number 88, just before the end of phase 0. This corresponds to the behavior of the actuator leg forces associated with the optimum design $\mathbf{X}^*$ (figure inset 2(d)). The maximum magnitude of the force in actuator leg ℓ_1, $f_1 = 35.160 \text{ N}$ occurring at time instant $t = 41.95 \text{ s}$, is only slightly larger than the maximum magnitude of the force in actuator leg ℓ_2, $f_2 = 33.838 \text{ N}$ occurring at time instant $t = 1.71 \text{ s}$.
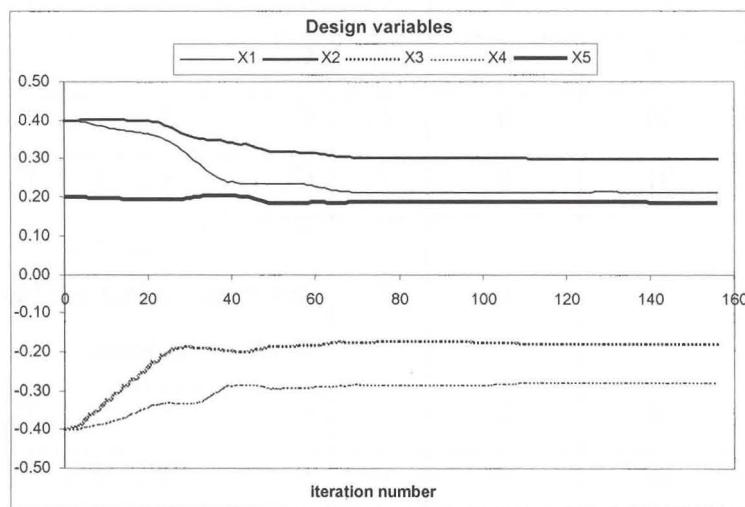
Figure 5.12: Convergence histories of design variables X_i, $i = 1,2,...,5$ for the spike tool path.

5.3.4 Execution of the spike tool path

Figure 5.13 shows a series of photographs taken at different time instants as the spike tool path is traced. Similarly to the parabolic tool path, the spike tool path is executed with a tangentially orientated moving platform (see Figure 5.10).
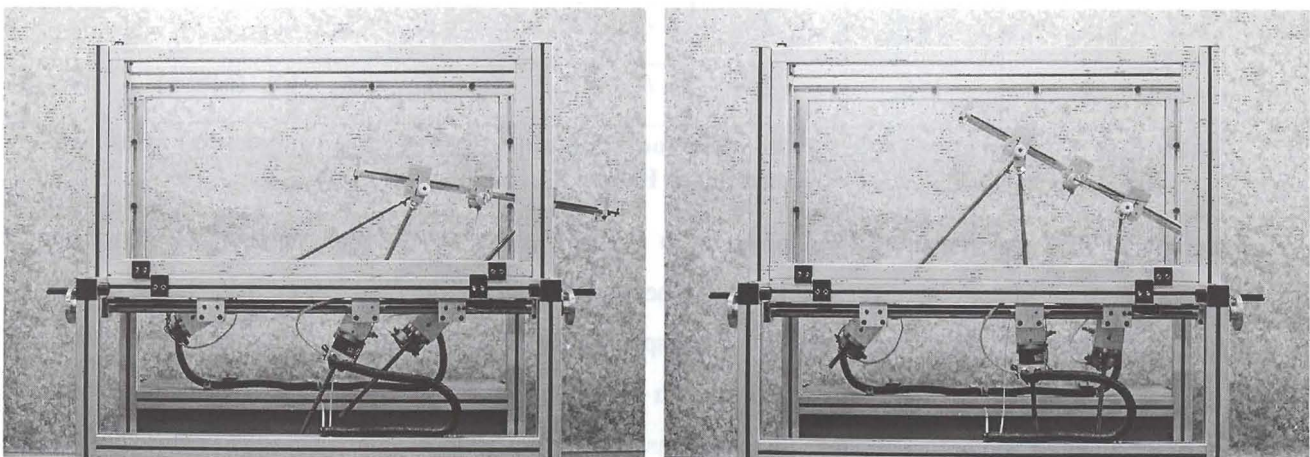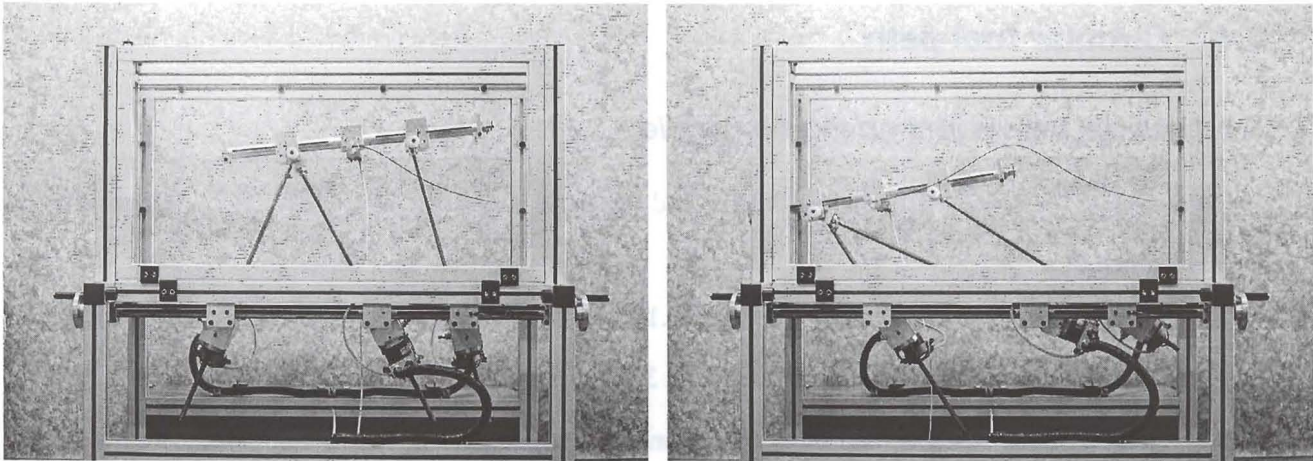
Figure 5.13: Execution of the spike tool path.

The close-up view of the executed spike tool path (Figure 5.14) shows that the traced spike tool path closely resembles the prescribed spike tool path specified by Figure 5.9.
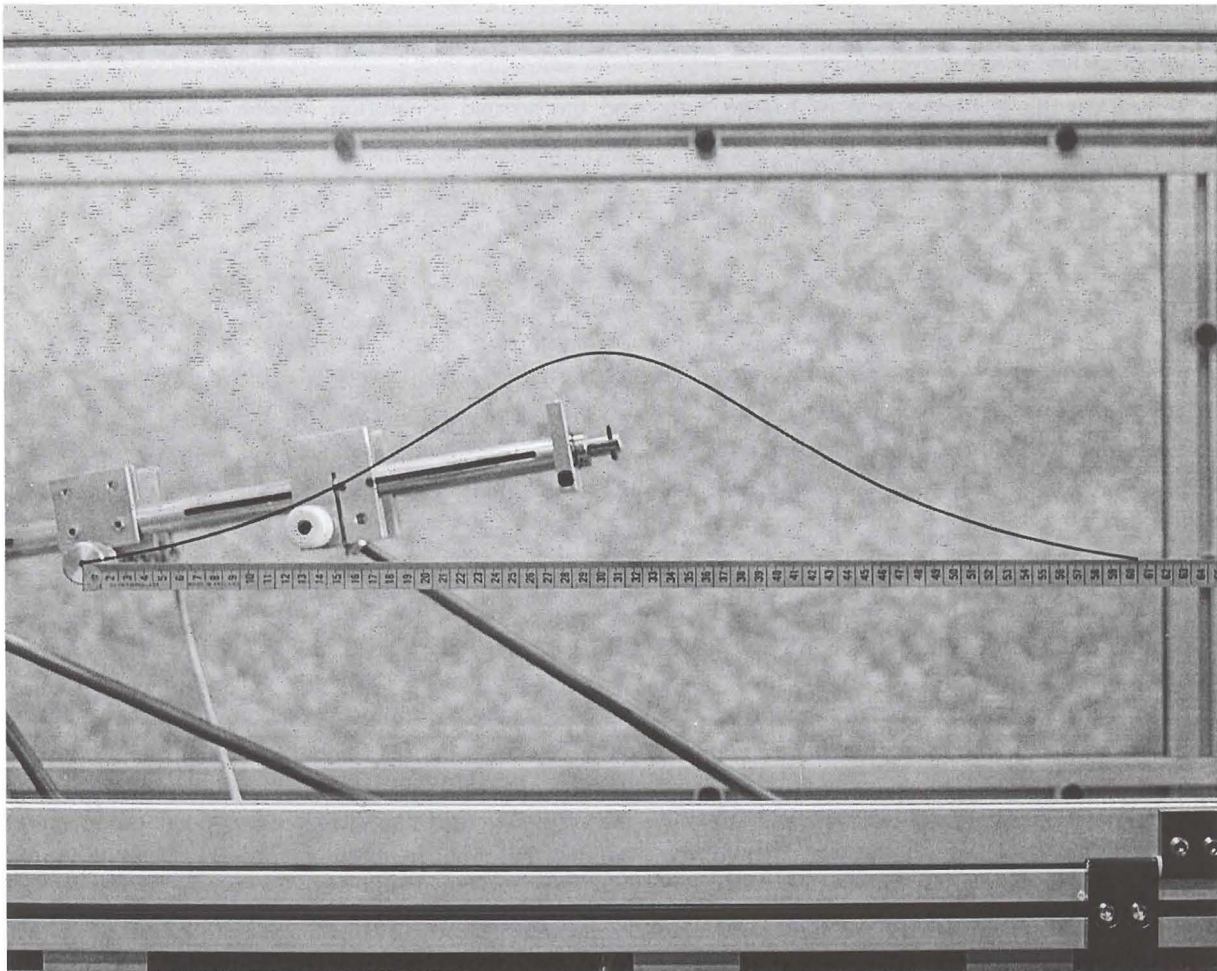
Figure 5.14: Close-up view of the executed spike tool path.

5.4 Circular tool path

5.4.1 Nodal points and orientation angle

The diameter of the circular tool path is $0.35\,\text{m}$ and the circle is centered at $(x,y)=(0,0)$. Hence the path is defined by

$$x^2 + y^2 = (0.175)^2 \qquad\qquad (5.2)$$

In agreement with the circular *test curve* of Section 3.5.3, the nodal points $\{P_i = (x_i, y_i), i = 0,1,2,...,N\}$ of the circular *tool path* are specified using corresponding sweep angles $\beta_i \in [0°,720°]$, where the sweep angle is measured clockwise from the positive x-axis. For any specific sweep angle β_i, $i = 0,1,2,...,N$, the corresponding x- and y-values are given by $x_i = 0.175\cos\beta_i$, and $y_i = 0.175\sin\beta_i$ respectively. The sequence of sweep angles $\{\beta_i\}$, is chosen such that starting at $\beta = 0°$, two CCW revolutions are followed. A total of 79 nodal points cover the two revolutions. The first revolution where $\beta \in [0°,360°]$ is shown on the left-hand side of Figure 5.15, and the second revolution, where $\beta \in [360°,720°]$ is shown on the right-hand side of Figure 5.15.
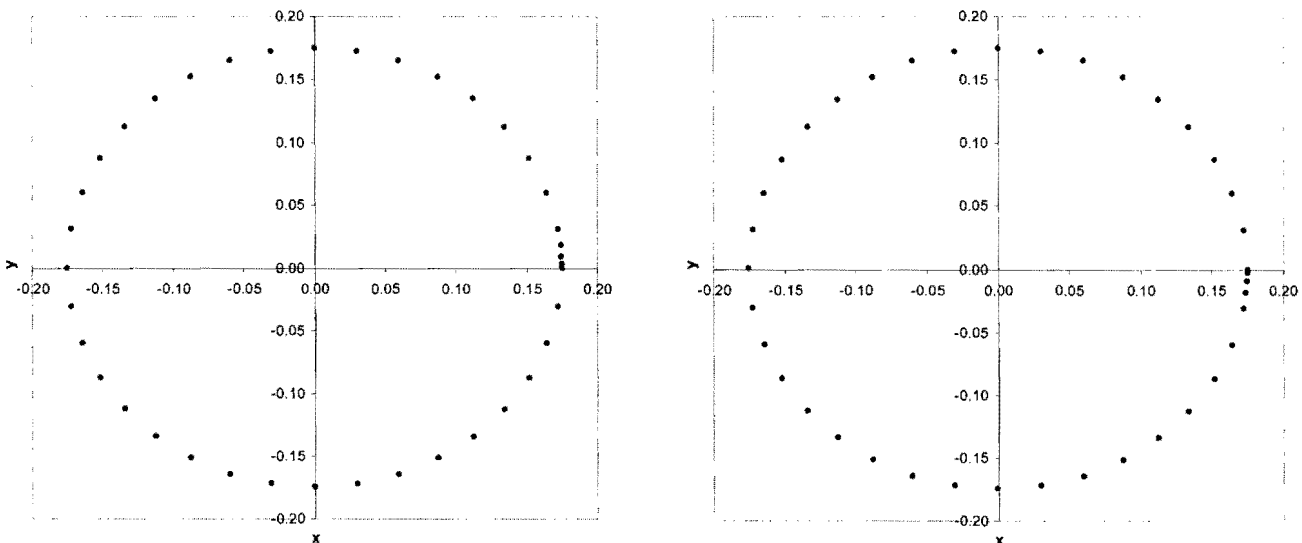
Figure 5.15: Nodal points used to approximate the two revolutions of the circular tool path.

The total time required to complete the two revolutions is $135.61\,\text{s}$, using the OCAS trajectory-planning methodology with $\ddot{s}_{\text{allow}} = 0.01\,\text{m/s}^2$, $v^* = 1.0\,\text{m/min}$ and $n_{\text{time}} = 5$.

Other than in the cases of the parabolic and spike tool paths, a fixed moving platform orientation $\phi_i = 0$ is maintained as the circular tool path is traced.

5.4.2 Optimization results

A comparison between the initial and optimum test-model designs for the circular tool path is shown in Table 5.5, with figure insets 3(a) – 3(d).

Note that the kinematics and kinetics of the two revolutions are *not identical*. The distribution of the nodal points is specifically chosen to accommodate acceleration at the start of the first revolution, and deceleration at the end of the second revolution (see Figure 5.15). The effect of this on figure insets 3(a) – 3(d) are the slight differences between the respective curves at time instants $t = 0\,\text{s}$ and $t = 135.61\,\text{s}$.

Initial design		Optimum design	
$\mathbf{X}^0 = [0.4, 0.4, -0.4, -0.4, 0.2]^\mathsf{T}$		$\mathbf{X}^* = [0.34476, 0.39829, -0.28487, -0.36676, 0.25238]^\mathsf{T}$	
Inequality constraint values (see Section D.3):			
$C_1(\mathbf{X}^0) = -0.05$	$C_2(\mathbf{X}^0) = -0.3$	$C_1(\mathbf{X}^*) = -0.10524$	$C_2(\mathbf{X}^*) = -0.24476$
$C_3(\mathbf{X}^0) = -0.065$	$C_4(\mathbf{X}^0) = -0.287$	$C_3(\mathbf{X}^*) = -0.06671$	$C_4(\mathbf{X}^*) = -0.28529$
$C_5(\mathbf{X}^0) = -0.07$	$C_6(\mathbf{X}^0) = -0.087$	$C_5(\mathbf{X}^*) = -0.01762$	$C_6(\mathbf{X}^*) = -0.13938$
$\rightarrow C_7(\mathbf{X}^0) = 0.09721$	$\rightarrow C_8(\mathbf{X}^0) = 0.09721$	$C_7(\mathbf{X}^*) = -0.00514$	$\Rightarrow C_8(\mathbf{X}^*) = 0.326 \times 10^{-3}$
$\rightarrow C_9(\mathbf{X}^0) = 0.05$	$C_{10}(\mathbf{X}^0) = -0.15$	$C_9(\mathbf{X}^*) = -0.04408$	$C_{10}(\mathbf{X}^*) = -0.03487$
$C_{11}(\mathbf{X}^0) = -0.15$	$C_{12}(\mathbf{X}^0) = -0.21$	$C_{11}(\mathbf{X}^*) = -0.03487$	$C_{12}(\mathbf{X}^*) = -0.20608$
$C_{13}(\mathbf{X}^0) = -0.01$	$C_{14}(\mathbf{X}^0) = -0.03130$	$C_{13}(\mathbf{X}^*) = -0.06916$	$C_{14}(\mathbf{X}^*) = -0.00157$
$C_{15}(\mathbf{X}^0) = -0.04642$	$C_{16}(\mathbf{X}^0) = -0.03130$	$C_{15}(\mathbf{X}^*) = -0.00911$	$\Rightarrow C_{16}(\mathbf{X}^*) = -0.114 \times 10^{-4}$
$C_{17}(\mathbf{X}^0) = -0.05081$	$C_{18}(\mathbf{X}^0) = -0.04334$	$C_{17}(\mathbf{X}^*) = -0.02786$	$C_{18}(\mathbf{X}^*) = -0.04462$
$C_{19}(\mathbf{X}^0) = -0.06975$	$C_{20}(\mathbf{X}^0) = -0.09344$	$C_{19}(\mathbf{X}^*) = -0.01857$	$C_{20}(\mathbf{X}^*) = -0.00119$
$C_{21}(\mathbf{X}^0) = -0.08546$	$C_{22}(\mathbf{X}^0) = -0.06502$	$C_{21}(\mathbf{X}^*) = -0.08240$	$C_{22}(\mathbf{X}^*) = -0.06527$
$\rightarrow$ constraint violation		$\Rightarrow$ constraint active	

Variation of actuator leg lengths along the circular tool path:	
3(a)	3(b)
Variation of actuator forces along the circular tool path:	
3(c)	3(d)
$F(\mathbf{X}^0) = 26.976\,\text{N}$	$F(\mathbf{X}^*) = 21.431\,\text{N}$
Actuator leg 2	Actuator leg 2
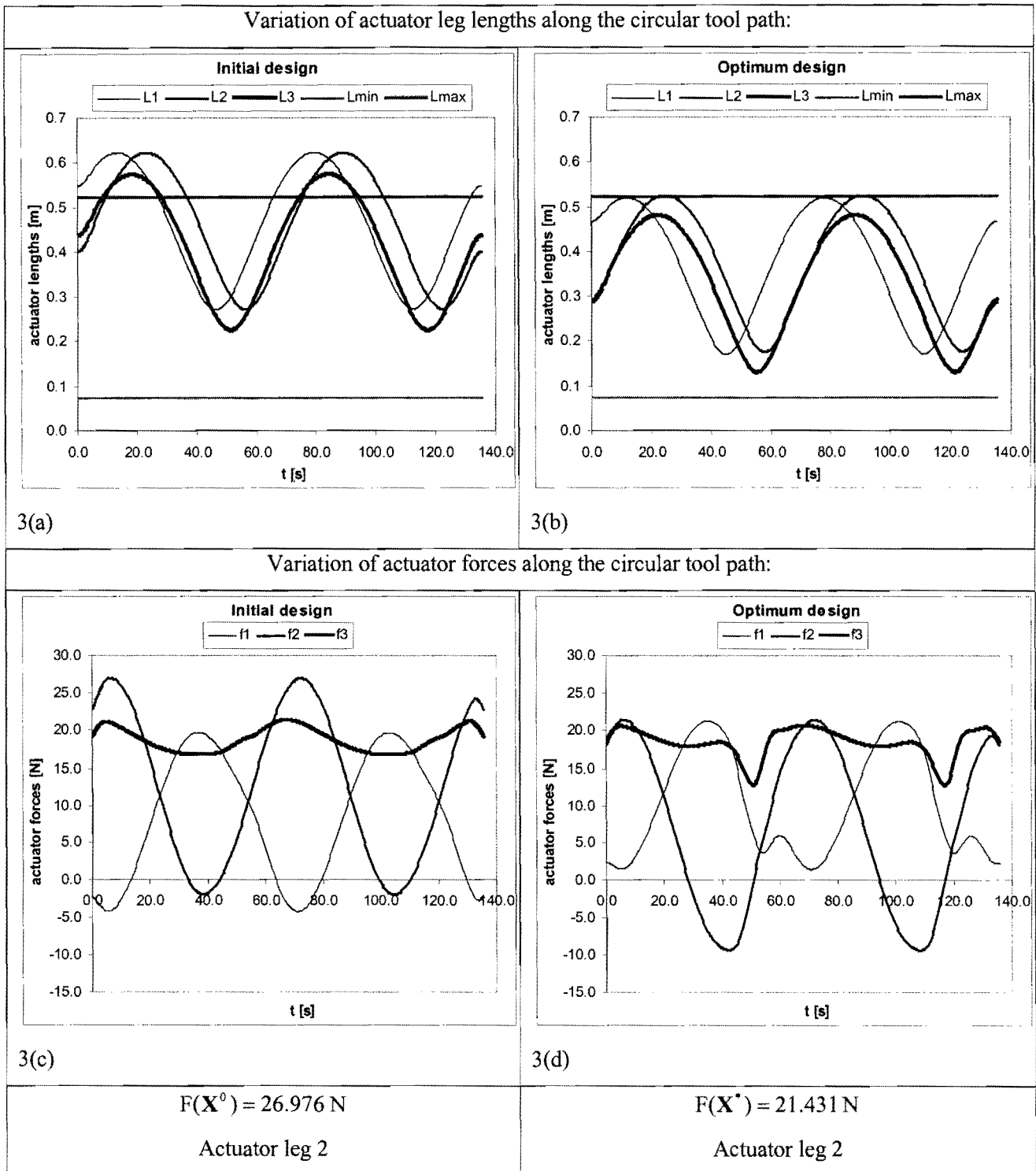
Table 5.5: Comparison between the initial and optimum designs for the circular tool path.

Starting with the infeasible initial design $\mathbf{X}^0$ (see the unallowable variation in actuator leg lengths in inset 3(a), and associated positive inequality constraint function values $C_7(\mathbf{X}^0)$, $C_8(\mathbf{X}^0)$ and $C_9(\mathbf{X}^0)$), the optimum design $\mathbf{X}^*$ is found in 73 optimization iterations. This requires 6 minutes and 35 seconds computational time on a Pentium IV 1.5 GHz computer with 640 MB DDRAM. The LFOPC-algorithm again terminated on criterion 2 ($\varepsilon_x \leq 10^{-5}$) listed in Section 4.4.

Note that the absolute values of the two active constraints, identified from the positive values of $C_8(\mathbf{X}^*)$ and $C_{16}(\mathbf{X}^*)$ (expressions (D.11) and (D.17)) are at least one order of magnitude larger than the absolute values of the active constraints for the optimization of the parabolic and spike test functions. In spite of the fact that inequality constraint C_8 is violated by 0.326×10^{-3} m (0.326 mm), this violation lies well within the minimum safety margin of 5 mm that was used during the formulation of the inequality constraints.

The effectiveness of the chosen "maximum magnitude actuator force" objective function (see Section 4.2.2) is borne out by comparing figure insets 3(c) and 3(d). In figure inset 3(c) showing the actuator force variations for the initial design $\mathbf{X}^0$, actuator force f_2 is predominant with significant elevations at time instants $t = 6.23$ s, $t = 72.20$ s and $t = 132.45$ s. On the other hand, the actuator force variations associated with the optimum design $\mathbf{X}^*$ in figure inset 3(d) shows a much more level distribution in terms of the maximum forces in all three actuator legs.

5.4.3 Analysis of convergence to optimum

Figure 5.16 shows the convergence history of the objective function.
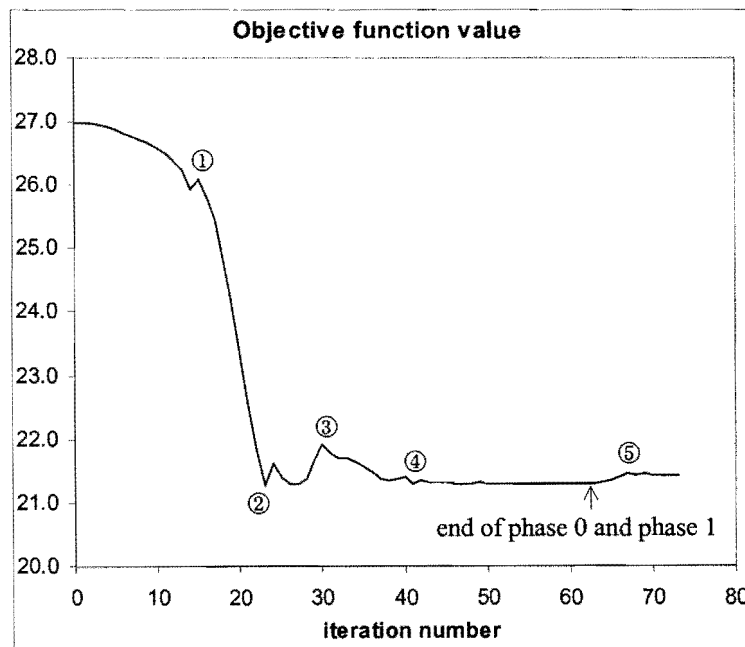
Figure 5.16: Convergence history of the objective function for the circular tool path.

Labels ① – ⑤ in Figure 5.16 are used in Table 5.6 to relate the behavior of the convergence curve of the objective function in the respective indicated regions to the iteration number and phase of the LFOPC-algorithm, the actuator leg responsible for the maximum magnitude actuator force and the violated inequality constraints.

Labels	Iteration No.	LFOPC-Phase	Act. leg	Violated Inequality Constraints		
$\mathbf{X}^0$	0	0	ℓ_2	C_7 C_8 C_9		
①	14	0	ℓ_2	C_{18}		
	15	0	ℓ_2	C_{18}		
	16	0	ℓ_2	C_{18}		
②	23	0	ℓ_2	C_8	C_{16}	
	24	0	ℓ_1	C_8	C_{16}	C_{20}
	25	0	ℓ_1	C_8	C_{16}	C_{20}
	26	0	ℓ_1	C_8	C_{16}	
	27	0	ℓ_1	C_8	C_{16}	C_{20}
	28	0	ℓ_2	C_8	C_{16}	C_{20}
	29	0	ℓ_2	C_8	C_{16}	C_{20}
③	30	0	ℓ_2	C_8	C_{16}	C_{20}
	31	0	ℓ_2	C_8	C_{16}	C_{20}
④	39	0	ℓ_2	C_8	C_{16}	C_{20}
	40	0	ℓ_2	C_8	C_{16}	
	41	0	ℓ_1	C_8	C_{16}	C_{20}
	42	0	ℓ_2	C_8 C_{16} maximum violated constraint value $C_{16}(\mathbf{X}^{42}) = 0.00110$		
	43	0	ℓ_1	C_{16}		

LFOPC Phase-changes	60	0	ℓ_2	C_{16}
	61	0	ℓ_1	C_{16}
	62	0	ℓ_2	C_{16} $C_{16}(\mathbf{X}^{62}) = 0.936 \times 10^{-3}$
	62	1	ℓ_2	C_{16}
	63	1	ℓ_2	C_{16} (only active constraint) see footnote * at the end of Table 5.6
	63	2	ℓ_2	C_{16}
	64	2	ℓ_2	C_{16}
⑤	67	2	ℓ_2	C_8
	68	2	ℓ_2	C_8 C_{16}
	69	2	ℓ_2	C_8
	70	2	ℓ_2	C_8
	71	2	ℓ_2	C_8
	72	2	ℓ_2	C_8
$\mathbf{X}^*$	73	2	ℓ_2	C_8 C_{16} (active) (only $C_{16} = 0$ enforced in LFOPC- phase 2)

* Note that at the end of phase 1 only one constraint, corresponding to C_{16}, is identified to be active. In the subsequent stringent enforcement of this constraint in phase 2, the constraint corresponding to C_8 also incidentally becomes active. This explains the relative large value (but nevertheless of insignificant magnitude) of $C_8(\mathbf{X}^*)$ in Table 5.5. A diagrammatical representation of the situation that arises is sketched below

As is evident from the convergence histories of the $\mathbf{X}_i$ ($i = 1,2,\ldots,5$), this distance $\| \mathbf{X}^* - \mathbf{X}^{62} \|$ is extremely small (negligible) and does not affect the reliability and accuracy of the computed solution.

$\mathbf{X}^{62}$ at the end of phase 1 is infeasible because LFOPC is essentially an *exterior* penalty function method
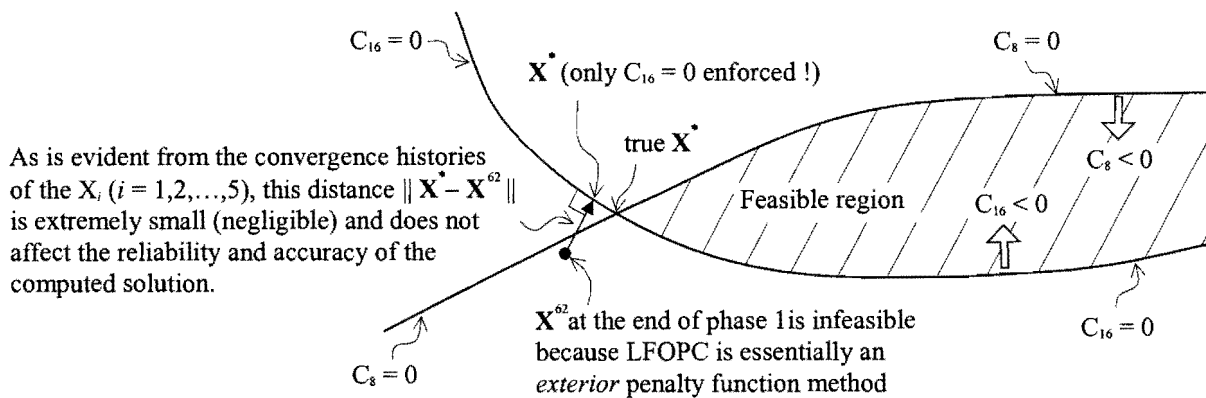
Table 5.6: Comparative table for the circular tool path objective function vs. iteration number curve (see Figure 5.16).

A switch in the actuator leg responsible for the maximum magnitude actuator force occurs in the vicinity of label ②. This again explains the non-smooth nature of the objective function vs. iteration number curve in this area (see Figure 5.16).

Note that since the initial design only violates the "allowable maximum leg length" inequality constraints (expression (D.11)), it may be possible to *intuitively* adjust the position of the prescribed tool path *relative* to the position of the planar machine in order to achieve feasibility. In terms of the set of design variables, this implies that *only* two design variables, X_3 and X_4, need to be changed until the prescribed circular tool path is *feasibly* traced. Although this might seem to be an easier option, the inherent danger of this approach is the unknown occurrence of mechanical interference. This danger is evident from the fact that the optimum design $\mathbf{X}^*$ found by LFOPC is associated with the two active constraints:

- C_8 an "allowable maximum leg length" inequality constraint (expression (D.11)), and

- C_{16} a "mechanical interference" inequality constraint (expression (D.17)).

The convergence histories of the respective design variables X_i, $i = 1,2,...,5$ are shown in Figure 5.17. Practical convergence (both with respect to feasibility and optimum objective function value), has already been achieved as early as iteration 42 with a maximum violated constraint function value of $C_{16}(\mathbf{X}^{42}) = 0.00110\,\text{m}$ (1.10 mm), and with the associated design vector given by $\mathbf{X}^{42} = [0.34901, 0.39819, -0.28277, -0.36638, 0.25303]^T$. Note that no significant changes in the values of the design variables occur after iteration 42 as can be seen from the optimum values of the design variables, $\mathbf{X}^* = [0.34476, 0.39829, -0.28487, -0.36676, 0.25238]^T$.
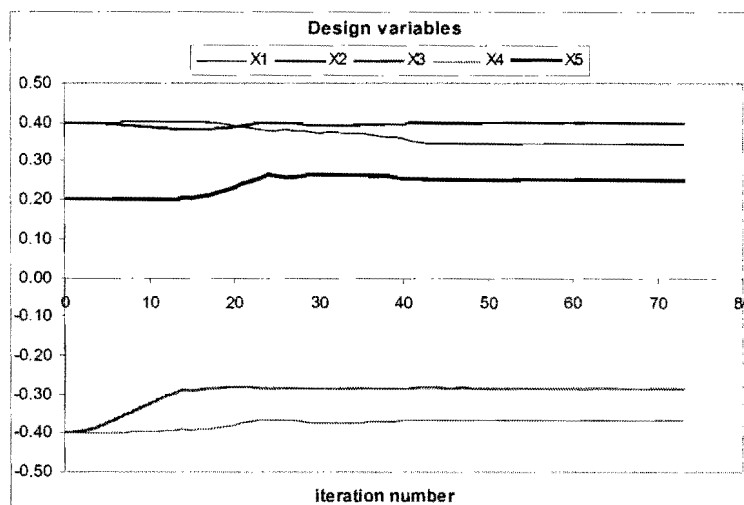
Figure 5.17: Convergence histories of design variables X_i, $i = 1,2,...,5$ **for the circular tool path.**

5.4.4 Execution of the circular tool path

The series of photographs shown in Figure 5.18 is of different instants during the execution of the first revolution of the circular tool path.

Figure 5.18: Execution of the circular tool path.

Figure 5.19 is a close-up of the traced circular tool path, showing that the diameter of the traced circle is approximately 350 mm (35 cm), and that the circle is smoothly traced.

Figure 5.19: Close-up view of the executed circular tool path.

5.5 Spiral tool path

5.5.1 Nodal points and orientation angle

The spiral tool path is a scaled version of the logarithmic spiral test curve $\rho = e^{0.1\beta}$ of Section 3.5.4. Using a scale factor of 0.285, the 79 spiral tool path nodal points are as shown in Figure 5.20.

The motion time along the spiral tool path is 93.24 seconds with the specification of $\ddot{s}_{ALLOW} = 0.01\,m/s^2$, $v^* = 1.0\,m/min$ and $n_{time} = 5$ for the use of the OCAS trajectory-planning algorithm.

Figure 5.20: Nodal points used to approximate the spiral tool path.

As for the circular tool path, the spiral tool path is traced with a fixed moving platform orientation $\phi_1 \equiv 0$.

5.5.2 Optimization results

The initial and optimum test-model designs for the spiral tool path are compared in Table 5.7 (with figure insets 4(a) – 4(d)).

Initial design	Optimum design
$\mathbf{X}^0 = [0.4, 0.4, -0.4, -0.4, 0.2]^T$	$\mathbf{X}^* = [0.32686, 0.34053, -0.26137, -0.40930, 0.15538]^T$
Inequality constraint values (see Section D.3):	

$C_1(\mathbf{X}^0) = -0.05$	$C_2(\mathbf{X}^0) = -0.3$	$C_1(\mathbf{X}^*) = -0.12314$	$C_2(\mathbf{X}^*) = -0.22686$
$C_3(\mathbf{X}^0) = -0.065$	$C_4(\mathbf{X}^0) = -0.287$	$C_3(\mathbf{X}^*) = -0.12447$	$C_4(\mathbf{X}^*) = -0.22753$
$C_5(\mathbf{X}^0) = -0.07$	$C_6(\mathbf{X}^0) = -0.087$	$C_5(\mathbf{X}^*) = -0.11462$	$C_6(\mathbf{X}^*) = -0.04238$
$\rightarrow C_7(\mathbf{X}^0) = 0.09323$	$\rightarrow C_8(\mathbf{X}^0) = 0.10988$	$\Rightarrow C_7(\mathbf{X}^*) = 0.347 \times 10^{-6}$	$C_8(\mathbf{X}^*) = -0.06128$
$\rightarrow C_9(\mathbf{X}^0) = 0.05420$	$C_{10}(\mathbf{X}^0) = -0.19441$	$C_9(\mathbf{X}^*) = -0.07828$	$C_{10}(\mathbf{X}^*) = -0.05578$
$C_{11}(\mathbf{X}^0) = -0.19441$	$C_{12}(\mathbf{X}^0) = -0.17684$	$C_{11}(\mathbf{X}^*) = -0.05578$	$C_{12}(\mathbf{X}^*) = -0.28217$
$C_{13}(\mathbf{X}^0) = -0.03220$	$C_{14}(\mathbf{X}^0) = -0.03972$	$\Rightarrow C_{13}(\mathbf{X}^*) = 0.108 \times 10^{-5}$	$\Rightarrow C_{14}(\mathbf{X}^*) = 0.700 \times 10^{-6}$
$C_{15}(\mathbf{X}^0) = -0.05697$	$C_{16}(\mathbf{X}^0) = -0.03865$	$C_{15}(\mathbf{X}^*) = -0.03094$	$C_{16}(\mathbf{X}^*) = -0.03204$
$C_{17}(\mathbf{X}^0) = -0.06113$	$C_{18}(\mathbf{X}^0) = -0.06216$	$C_{17}(\mathbf{X}^*) = -0.02269$	$C_{18}(\mathbf{X}^*) = -0.00256$
$C_{19}(\mathbf{X}^0) = -0.06763$	$C_{20}(\mathbf{X}^0) = -0.09095$	$C_{19}(\mathbf{X}^*) = -0.06875$	$C_{20}(\mathbf{X}^*) = -0.11837$
$C_{21}(\mathbf{X}^0) = -0.09526$	$C_{22}(\mathbf{X}^0) = -0.06325$	$\Rightarrow C_{21}(\mathbf{X}^*) = 0.345 \times 10^{-5}$	$C_{22}(\mathbf{X}^*) = -0.06792$
$\rightarrow$ constraint violation		$\Rightarrow$ constraint active	

Variation of actuator leg lengths along the spiral tool path:

4(a)

4(b)
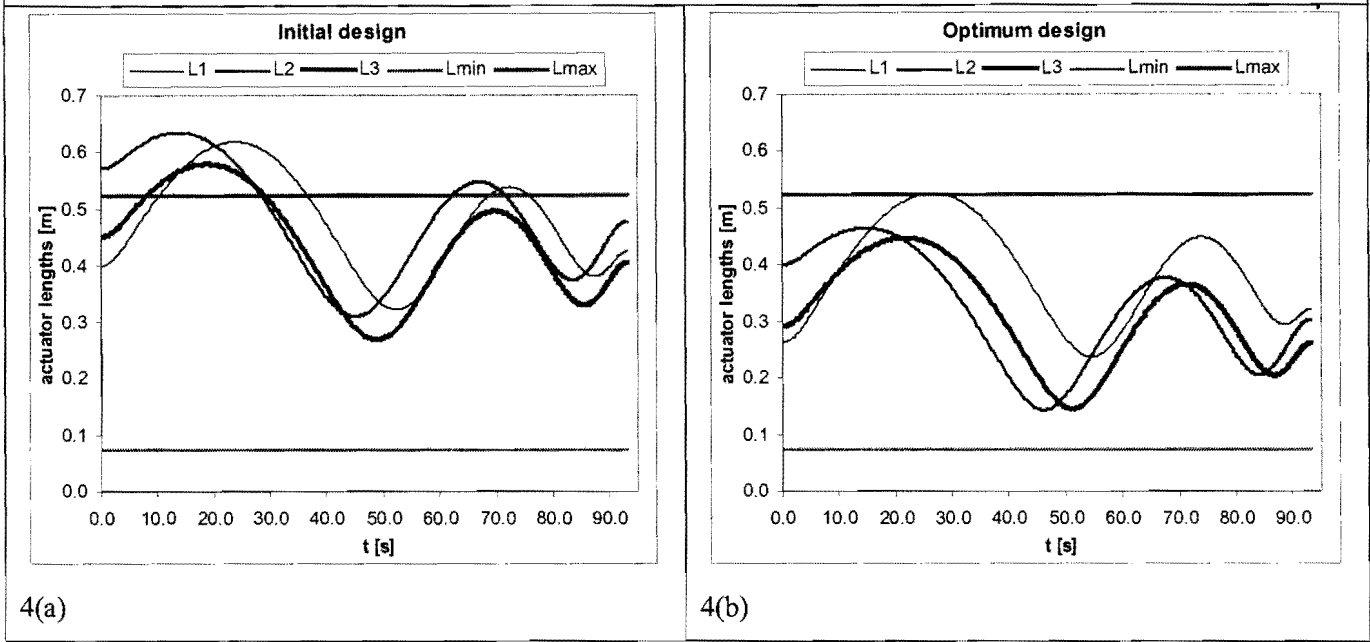
Variation of actuator forces along the spiral tool path:

4(c)

4(d)
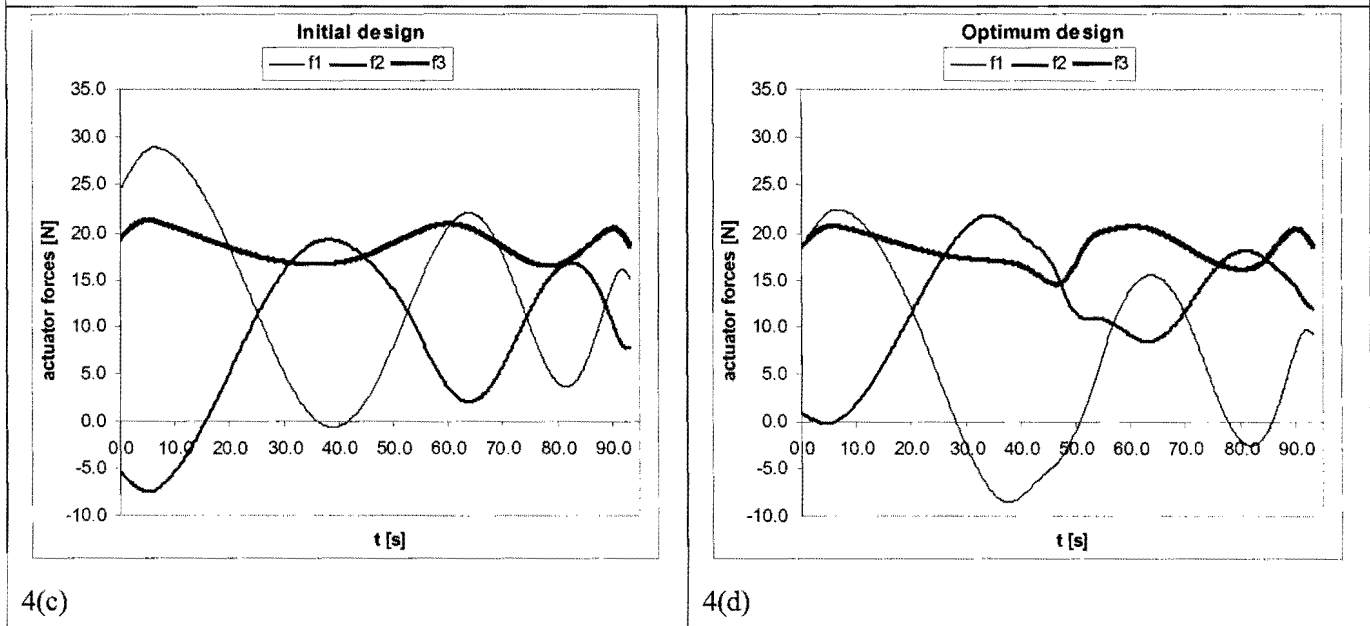
$F(\mathbf{X}^0) = 28.914\,\text{N}$	$F(\mathbf{X}^*) = 22.409\,\text{N}$
Actuator leg 1	Actuator leg 1

Table 5.7: Comparison between the initial and optimum designs for the spiral tool path.

The initial design is *again infeasible* (see the variation in actuator leg lengths in inset 4(a) and the corresponding *positive* inequality constraint function values $C_7(\mathbf{X}^0)$, $C_8(\mathbf{X}^0)$ and $C_9(\mathbf{X}^0)$). The *feasible* optimum design (see figure inset 4(b)) is associated with active constraints corresponding to C_7, C_{13}, C_{14} and C_{21} (see respective expressions (D.10), (D.14), (D.15) and (D.22)). Note that

---

corresponding to the circular tool path, the optimum variation in actuator forces of figure inset 4(d) shows a level distribution in terms of the maximum forces in all three actuator legs.

The optimum design, $\mathbf{X}^*$, is found in 133 optimization iterations and utilizing 11 minutes and 46 seconds computational time on a Pentium IV 1.5 GHz computer with 640 MB DDRAM. As before, LFOPC terminated on criterion 2 ($\varepsilon_x \le 10^{-5}$) listed in Section 4.4.

5.5.3 Analysis of convergence to optimum

Figure 5.21 shows the convergence history of the objective function.
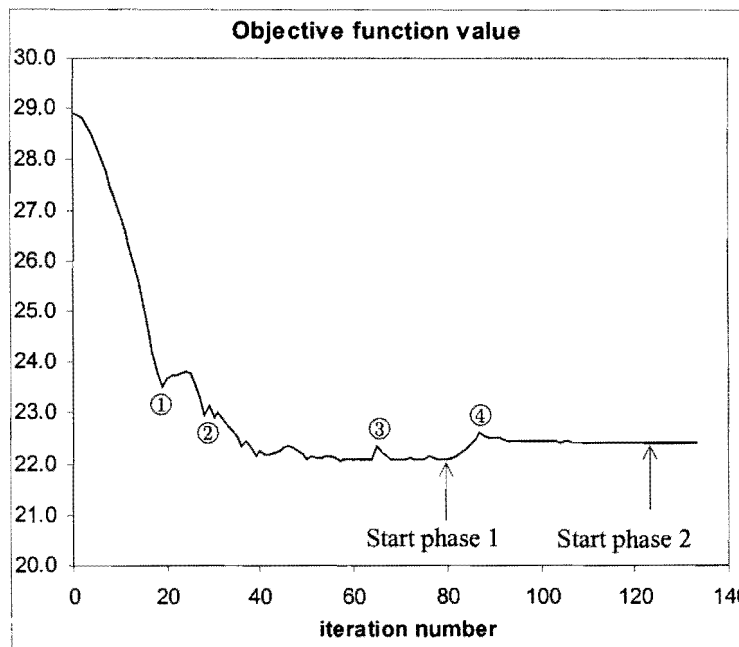
Figure 5.21: Convergence history of the objective function for the spiral tool path.

Table 5.8 with labels ① – ④ relate the behavior of the convergence curve of the objective function to iteration number, the LFOPC phases, the actuator leg responsible for the maximum magnitude actuator force, and the violated inequality constraints in the respectively indicated regions of the curve.

Labels	Iteration No.	LFOPC-Phase	Act. leg	Violated Inequality Constraints
$\mathbf{X}^0$	0	0	ℓ_1	C_7 C_8 C_9
①	18	0	ℓ_1	C_{13} C_{18}
①	19	0	ℓ_1	C_{13} C_{14} C_{18}
①	20	0	ℓ_1	C_{13} C_{14} C_{18}
①	21	0	ℓ_1	C_{13} C_{18}
②	28-31	0	ℓ_1	C_7 C_{13} C_{14}
③	63	0	ℓ_1	C_7 C_{13} C_{14} C_{21}
③	64	0	ℓ_2	C_7 C_{13} C_{14} C_{21}
③	65	0	ℓ_1	C_7 C_{14} C_{21}
③	66	0	ℓ_1	C_7 C_{13} C_{14} C_{21}
LFOPC phase-change	78	0	ℓ_1	C_7 C_{13} C_{14} C_{21}
LFOPC phase-change	79	0	ℓ_1	C_7 C_{13} C_{14} C_{21} maximum violated constraint value $C_{21}(\mathbf{X}^{79}) = 0.00316$
LFOPC phase-change	79	1	ℓ_1	C_7 C_{13} C_{14} C_{21}
LFOPC phase-change	80	1	ℓ_1	C_7 C_{13} C_{14} C_{21}
④	87–89	1	ℓ_1	none
④	90	1	ℓ_1	C_7
LFOPC phase-change	125	1	ℓ_1	C_7 C_{13} C_{14} C_{21}
LFOPC phase-change	126	1	ℓ_1	C_7 C_{13} C_{14} C_{21}
LFOPC phase-change	126	2	ℓ_1	C_7 C_{13} C_{14} C_{21}
LFOPC phase-change	127	2	ℓ_1	C_7 C_{14} C_{21}
$\mathbf{X}^*$	133	2	ℓ_1	C_7 C_{13} C_{14} C_{21} (active)

Table 5.8: Comparative table for the spiral tool path objective function vs. iteration number curve (see Figure 5.21)

Note that the actuator leg responsible for the maximum magnitude actuator force switches between ℓ_1 and ℓ_2 in the vicinity of label ③.

The convergence histories of the respective design variables X_i, $i = 1,2,...,5$ are shown in Figure 5.22. Again convergence (with respect to feasibility and objective function value), is effectively achieved at

the end of phase 0, after 79 iterations with the maximum violated constraint value $C_{21}(\mathbf{X}^{79}) = 0.00316\,\text{m}$ ($3.16\,\text{mm}$).
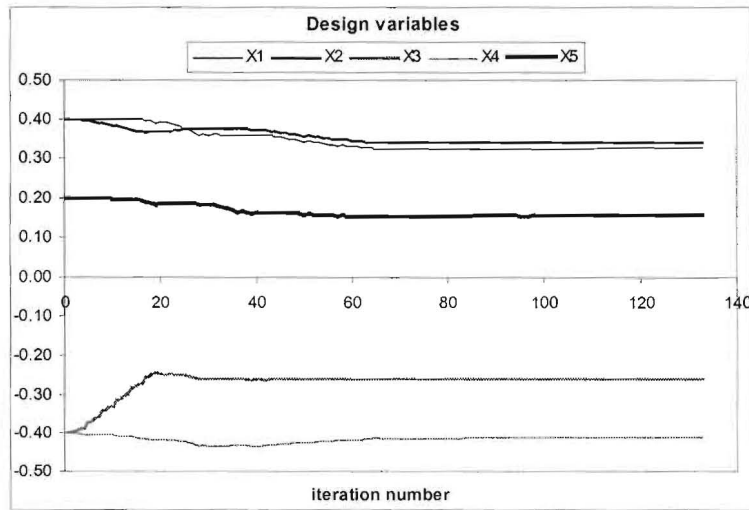
Figure 5.22: **Convergence histories of design variables** X_i , $i = 1,2,...,5$ **for the spiral tool path.**

5.5.4 Execution of the spiral tool path

The series of five photographs in Figure 5.23 depicts the tracing of the spiral tool path with a horizontally orientated moving platform ($\phi_1 \equiv 0$).
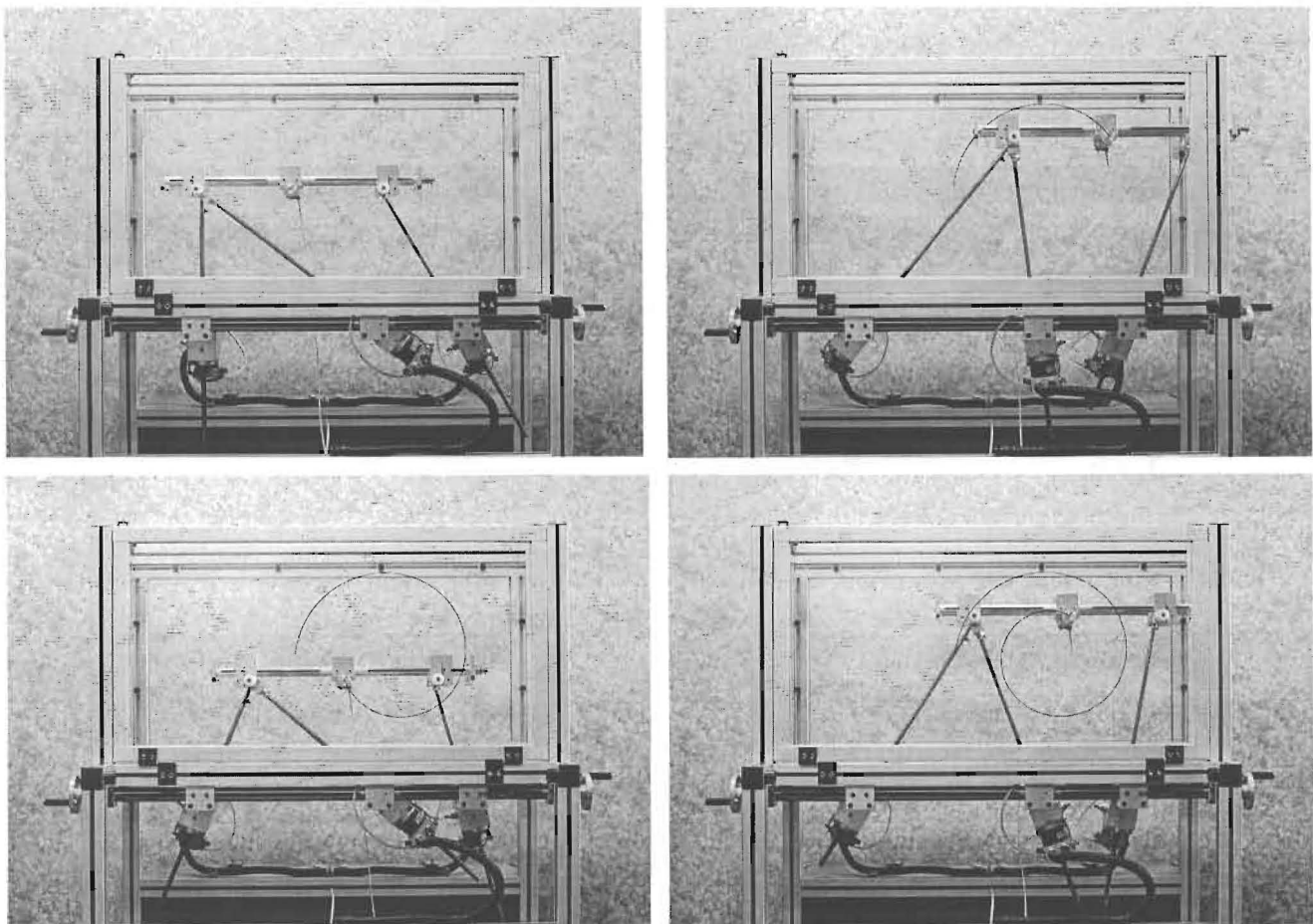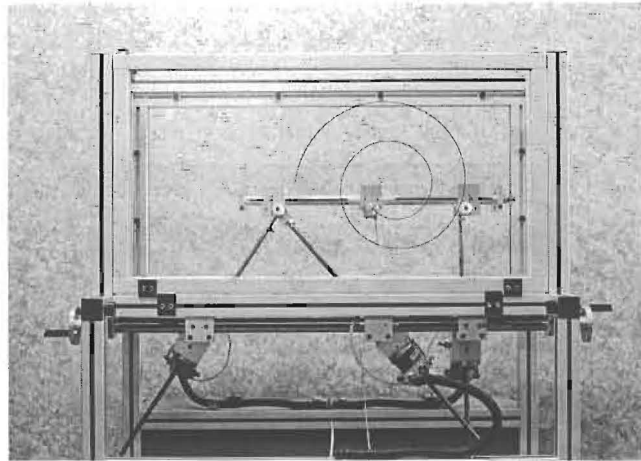
Figure 5.23: Execution of the spiral tool path.

The close-up view of the executed spiral tool path in Figure 5.24 shows its relative size and proportional shape. For all practical purposes the executed path corresponds accurately and smoothly to the spiral tool path prescribed by Figure 5.20.
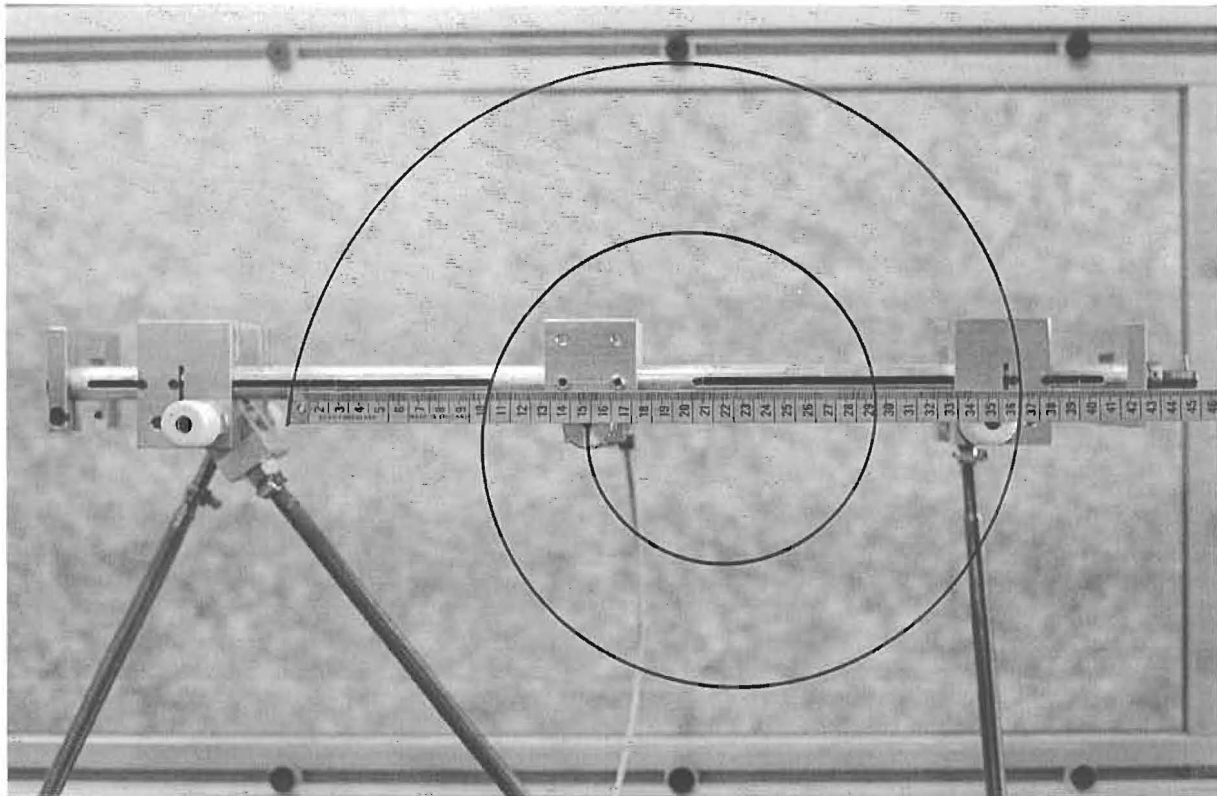
Figure 5.24: Close-up view of the executed spiral tool path.

5.6 Treble clef tool path

5.6.1 Nodal points and orientation angle

The treble clef tool path used here is a scaled version of the treble clef test curve of Section 3.5.5. Figure 5.25 shows the 49 scaled nodal points generated with a scale factor of 0.00285.
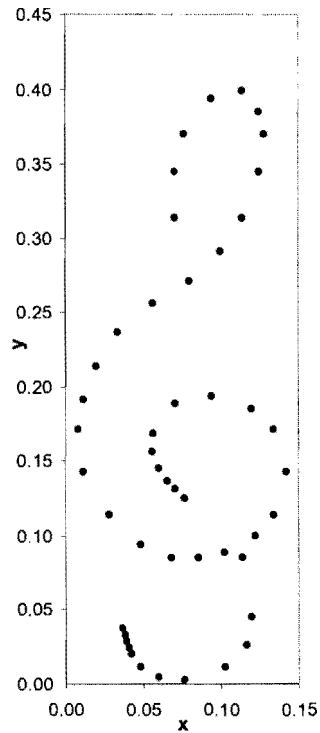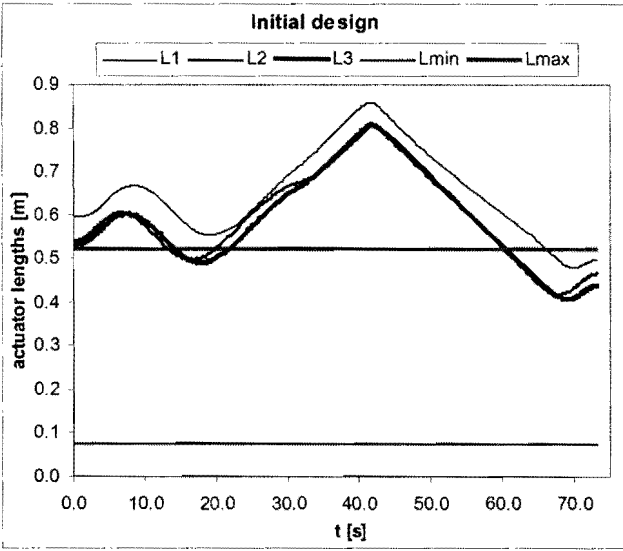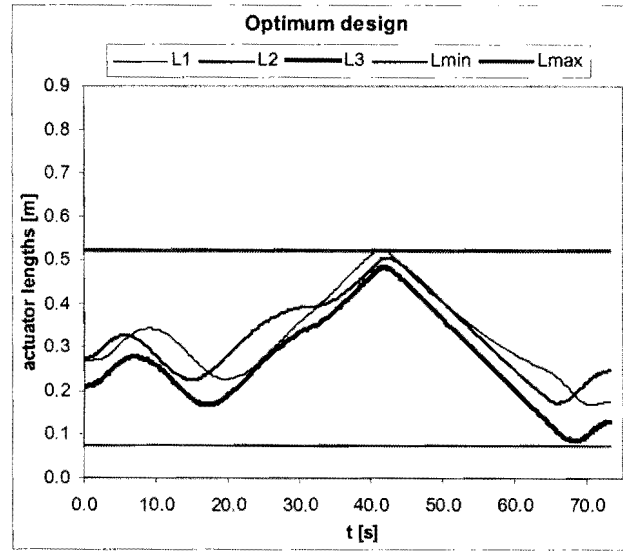
Figure 5.25: Nodal points used to approximate the treble clef tool path.

The OCAS trajectory-planning methodology is again utilized here with the specification of $\ddot{s}_{ALLOW} = 0.01 \, \text{m/s}^2$, $v^* = 1.0 \, \text{m/min}$ and $n_{time} = 5$, resulting in a total motion time along the treble clef tool path of 73.28 seconds.

The treble clef tool path is also traced with a fixed moving platform orientation $\phi_1 \equiv 0$.

5.6.2 Optimization results

The initial and optimum test-model designs for the treble clef tool path are compared in Table 5.9.

Initial design	Optimum design
$\mathbf{X}^0 = [0.4, 0.4, -0.4, -0.4, 0.2]^T$	$\mathbf{X}^* = [0.42327, 0.34561, -0.08380, -0.30386, 0.25886]^T$

<table>
<tr><td colspan="2" align="center">Inequality constraint values (see Section D.3):</td></tr>
<tr>
<td>

$C_1(\mathbf{X}^0) = -0.05 \qquad C_2(\mathbf{X}^0) = -0.3$

$C_3(\mathbf{X}^0) = -0.065 \qquad C_4(\mathbf{X}^0) = -0.287$

$C_5(\mathbf{X}^0) = -0.07 \qquad C_6(\mathbf{X}^0) = -0.087$

$\rightarrow C_7(\mathbf{X}^0) = 0.33349 \quad \rightarrow C_8(\mathbf{X}^0) = 0.27978$

$\rightarrow C_9(\mathbf{X}^0) = 0.28228 \quad C_{10}(\mathbf{X}^0) = -0.32755$

$C_{11}(\mathbf{X}^0) = -0.32755 \quad C_{12}(\mathbf{X}^0) = -0.39335$

$C_{13}(\mathbf{X}^0) = -0.0425 \quad C_{14}(\mathbf{X}^0) = -0.05377$

$C_{15}(\mathbf{X}^0) = -0.07431 \quad C_{16}(\mathbf{X}^0) = -0.07656$

$C_{17}(\mathbf{X}^0) = -0.11291 \quad C_{18}(\mathbf{X}^0) = -0.10447$

$C_{19}(\mathbf{X}^0) = -0.09483 \quad C_{20}(\mathbf{X}^0) = -0.12035$

$C_{21}(\mathbf{X}^0) = -0.11013 \quad C_{22}(\mathbf{X}^0) = -0.07064$

<div align="center">$\rightarrow$ constraint violation</div>

</td>
<td>

$C_1(\mathbf{X}^*) = -0.02673 \qquad C_2(\mathbf{X}^*) = -0.32327$

$C_3(\mathbf{X}^*) = -0.11939 \qquad C_4(\mathbf{X}^*) = -0.23261$

$C_5(\mathbf{X}^*) = -0.01114 \qquad C_6(\mathbf{X}^*) = -0.14586$

$\Rightarrow C_7(\mathbf{X}^*) = 0.221 \times 10^{-5} \quad C_8(\mathbf{X}^*) = -0.01996$

$C_9(\mathbf{X}^*) = -0.04101 \quad C_{10}(\mathbf{X}^*) = -0.01136$

$C_{11}(\mathbf{X}^*) = -0.01136 \quad C_{12}(\mathbf{X}^*) = -0.33997$

$C_{13}(\mathbf{X}^*) = -0.07261 \quad C_{14}(\mathbf{X}^*) = -0.00315$

$C_{15}(\mathbf{X}^*) = -0.03426 \quad \Rightarrow C_{16}(\mathbf{X}^*) = -0.774 \times 10^{-6}$

$C_{17}(\mathbf{X}^*) = -0.03052 \quad C_{18}(\mathbf{X}^*) = -0.00305$

$C_{19}(\mathbf{X}^*) = -0.07222 \quad C_{20}(\mathbf{X}^*) = -0.04259$

$C_{21}(\mathbf{X}^*) = -0.13874 \quad C_{22}(\mathbf{X}^*) = -0.04912$

<div align="center">$\Rightarrow$ constraint active</div>

</td>
</tr>
<tr><td colspan="2" align="center">Variation of actuator leg lengths along the treble clef tool path:</td></tr>
</table>

5(a)

5(b)

Variation of actuator forces along the treble clef tool path:	
Initial design	**Optimum design**
5(c)	5(d)
$F(\mathbf{X}^0) = 29.586\,\mathrm{N}$	$F(\mathbf{X}^*) = 20.715\,\mathrm{N}$
Actuator leg 2	Actuator leg 3

Table 5.9: Comparison between the initial and optimum designs for the treble clef tool path.

The initial design is *severely infeasible* (see the unallowable variations in actuator leg lengths shown in inset 5(a) and which correspond to the positive inequality constraint function values $C_7(\mathbf{X}^0)$, $C_8(\mathbf{X}^0)$ and $C_9(\mathbf{X}^0)$). The optimum and *feasible* (see inset 5(b)) design $\mathbf{X}^*$ with *active* inequality constraints corresponding to C_7 and C_{16}, and a level maximum magnitude actuator force distribution (see inset 5(d)) is found in 127 optimization iterations and utilizing 6 minutes and 57 seconds computational time on a Pentium IV 1.5 GHz computer with 640 MB DDRAM. Once again, LFOPC terminated on criterion 2 ($\varepsilon_x \leq 10^{-5}$) listed in Section 4.4.

5.6.3 Analysis of convergence to optimum

Figure 5.26 shows the convergence history of the objective function.
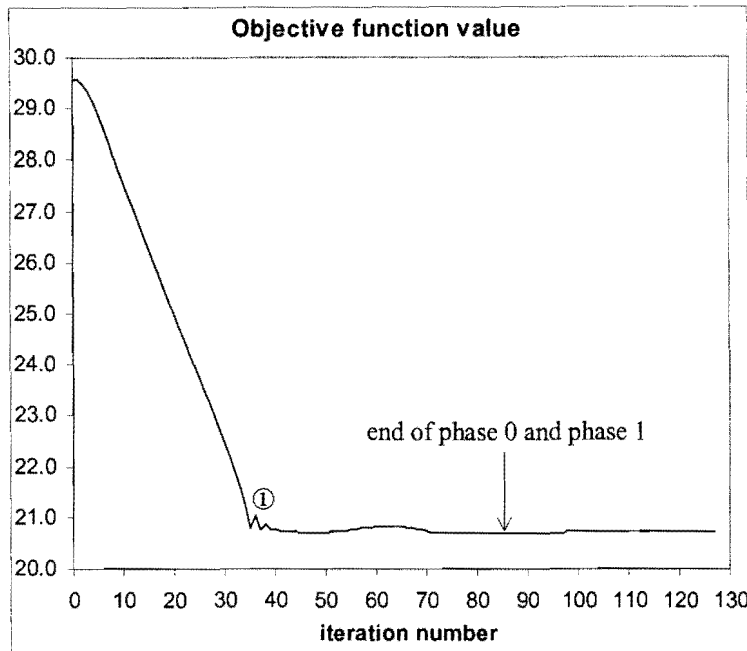
Figure 5.26: Convergence history of the objective function for the treble clef tool path.

The relatively smooth convergence graph of the objective function value shown in Figure 5.26 relates the LFOPC phases, actuator leg responsible for the maximum magnitude actuator force, and violated inequality constraints as indicated in Table 5.10.

Labels	Iteration No.	LFOPC-Phase	Act. leg	Violated Inequality Constraints			
$\mathbf{X}^0$	0	0	ℓ_2	C_7 C_8 C_9			
	35	0	ℓ_2	C_7	C_{14} C_{15}	C_{16}	C_{18}
	36	0	ℓ_2	C_7	C_{14}	C_{16}	C_{18}
	37	0	ℓ_3	C_7	C_{14} C_{15}	C_{16}	C_{18}
	38	0	ℓ_2	C_7	C_{14} C_{15}	C_{16}	C_{18}
①	39	0	ℓ_3	C_7	C_{14} C_{15}	C_{16}	C_{18}
	40	0	ℓ_3	C_7 C_{14} C_{16} C_{18} maximum violated constraint value $C_{18}(\mathbf{X}^{40}) = 0.02568$			
	41	0	ℓ_3	C_7	C_{14}	C_{16}	C_{18}

	84	0	ℓ_3	C_7	C_{16}
LFOPC phase-changes	85	0	ℓ_3	C_7 C_{16} maximum violated constraint value $C_{16}(\mathbf{X}^{85}) = 0.00220$
	85	1	ℓ_3	C_7	C_{16}
	86	1	ℓ_3	C_7	C_{16}
	86	2	ℓ_3	C_7	C_{16}
	87	2	ℓ_3	C_7	C_{16}
$\mathbf{X}^*$	127	2	ℓ_3	C_7	C_{16} (active)

Table 5.10: Comparative table for the treble clef tool path objective function vs. iteration number curve (see Figure 5.26).

Note that a switch from ℓ_2 to ℓ_3 as the actuator leg responsible for the maximum magnitude actuator force occurs in the vicinity of label ①.

The convergence histories of the respective design variables $\mathbf{X}_i$, $i = 1,2,...,5$ are shown in Figure 5.27. Here the convergence of the design variables is significantly more sluggish, requiring about 100 iterations to converge, compared to the relatively fast and sharp convergence of the objective function value within 40 iterations. Even though, after 40 iterations the objective function value ($F(\mathbf{X}^{40}) = 20.747\,\text{N}$) is close to the optimum objective function value ($F(\mathbf{X}^*) = 20.715\,\text{N}$), the maximum violated constraint function value, $C_{18}(\mathbf{X}^{40}) = 0.02568\,\text{m}$, shows that this is still an infeasible design due to the occurrence of mechanical interference (see expression (D.19)). The corresponding values of the design variables are $\mathbf{X}^{40} = [0.41543, 0.39816, -0.08308, -0.33817, 0.21923]^\text{T}$. Significant further changes occur in the values of design variables $\mathbf{X}_2$, $\mathbf{X}_4$ and $\mathbf{X}_5$ between iterations 40 and 100 ($\mathbf{X}^{100} = [0.42319, 0.34551, -0.08406, -0.30402, 0.25886]^\text{T}$). However, after phase 0 of the LFOPC-algorithm has terminated (iteration number 85), the maximum violated constraint function value is only $2.20\,\text{mm}$ ($C_{16}(\mathbf{X}^{85}) = 0.00220\,\text{m}$), which is negligible for all practical purposes and $\mathbf{X}^{85}$ may be taken as an effective optimum design.

	84	0	ℓ_3	C_7	C_{16}	
LFOPC phase-changes	85	0	ℓ_3	C_7	C_{16} maximum violated constraint value $C_{16}(\mathbf{X}^{85}) = 0.00220$	
	85	1	ℓ_3	C_7	C_{16}	
	86	1	ℓ_3	C_7	C_{16}	
	86	2	ℓ_3	C_7	C_{16}	
	87	2	ℓ_3	C_7	C_{16}	
$\mathbf{X}^*$	127	2	ℓ_3	C_7	C_{16}	(active)

Table 5.10: Comparative table for the treble clef tool path objective function vs. iteration number curve (see Figure 5.26).

Note that a switch from ℓ_2 to ℓ_3 as the actuator leg responsible for the maximum magnitude actuator force occurs in the vicinity of label ①.

The convergence histories of the respective design variables X_i, $i = 1,2,...,5$ are shown in Figure 5.27. Here the convergence of the design variables is significantly more sluggish, requiring about 100 iterations to converge, compared to the relatively fast and sharp convergence of the objective function value within 40 iterations. Even though, after 40 iterations the objective function value ($F(\mathbf{X}^{40}) = 20.747\,\text{N}$) is close to the optimum objective function value ($F(\mathbf{X}^*) = 20.715\,\text{N}$), the maximum violated constraint function value, $C_{18}(\mathbf{X}^{40}) = 0.02568\,\text{m}$, shows that this is still an infeasible design due to the occurrence of mechanical interference (see expression (D.19)). The corresponding values of the design variables are $\mathbf{X}^{40} = [0.41543, 0.39816, -0.08308, -0.33817, 0.21923]^\text{T}$. Significant further changes occur in the values of design variables X_2, X_4 and X_5 between iterations 40 and 100 ($\mathbf{X}^{100} = [0.42319, 0.34551, -0.08406, -0.30402, 0.25886]^\text{T}$). However, after phase 0 of the LFOPC-algorithm has terminated (iteration number 85), the maximum violated constraint function value is only $2.20\,\text{mm}$ ($C_{16}(\mathbf{X}^{85}) = 0.00220\,\text{m}$), which is negligible for all practical purposes and $\mathbf{X}^{85}$ may be taken as an effective optimum design.

Figure 5.27: Convergence histories of design variables X_i, $i = 1,2,...,5$ **for the treble clef tool path.**

5.6.4 Execution of the treble clef tool path.

The four photographs grouped in Figure 5.28 were taken at different time instants along the actually traced treble clef tool path. Note that the moving platform remains horizontal ($\phi_1 \equiv 0$) during the execution of the path.
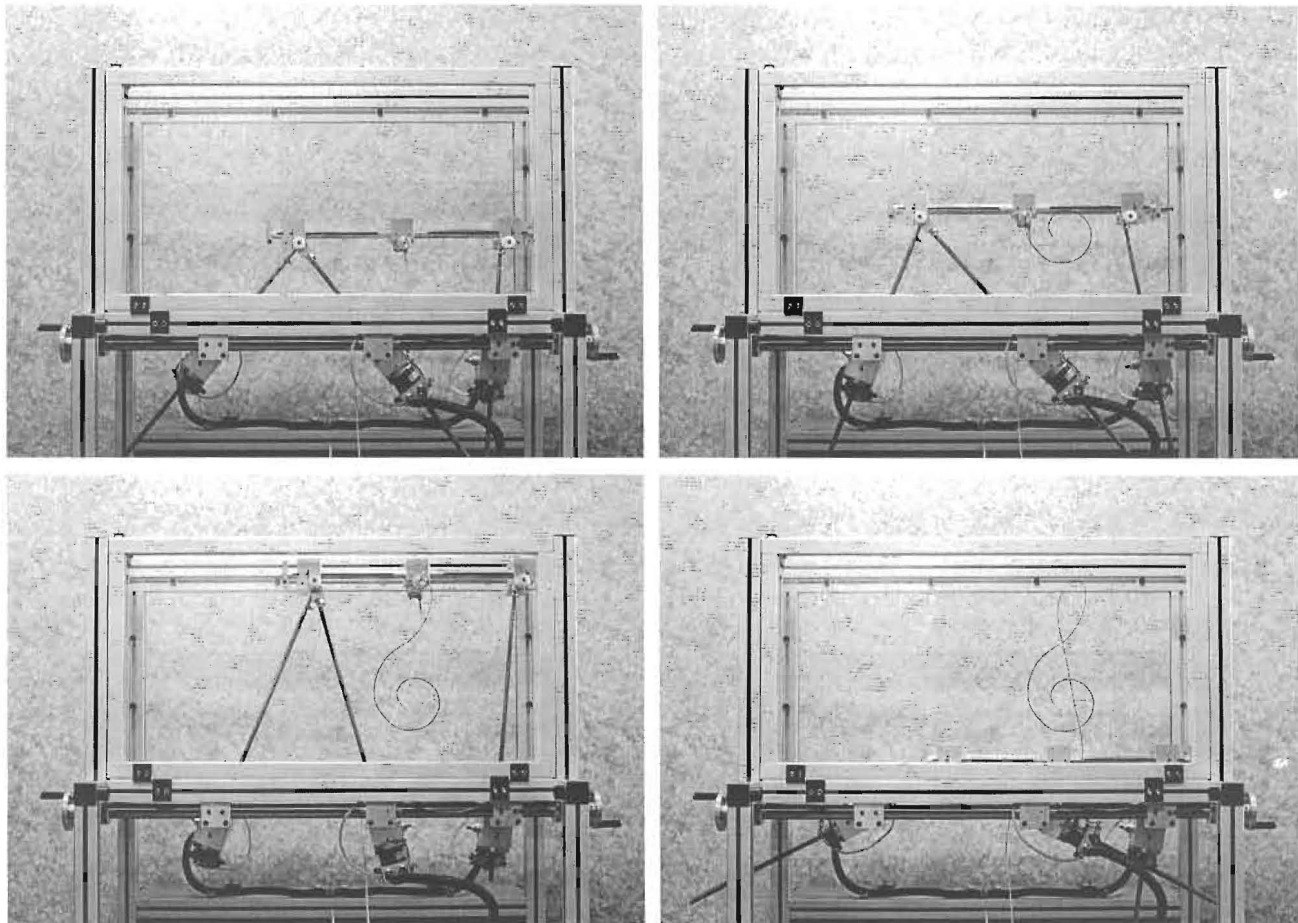
Figure 5.28: Execution of the treble clef tool path.

A close-up view of the executed treble clef tool path is shown in Figure 5.29, for comparison with the prescribed nodal points shown in Figure 5.25. Clearly the path is accurately traced with no practically significant differences in size and proportion between the executed and prescribed tool paths.
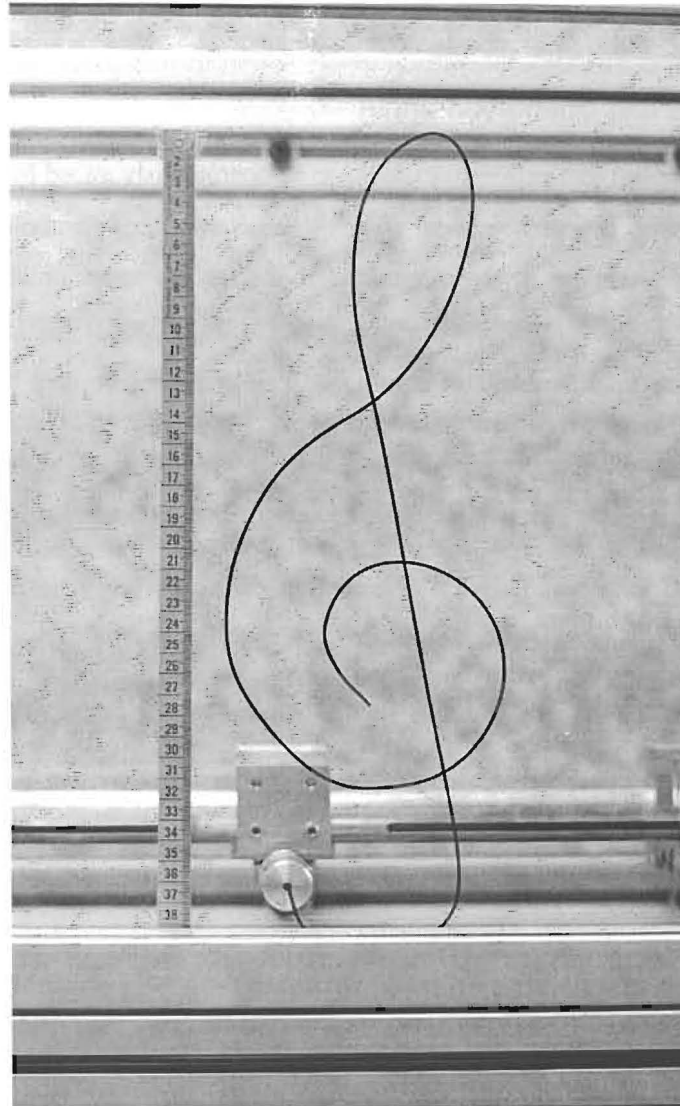
Figure 5.29: Close-up view of the executed treble clef tool path.

5.7   Bigger parabolic tool path

All of the above tool paths are scaled down versions of those represented by the original test functions discussed in Section 3.5. In each instance, the proposed optimization approach determined a feasible design of the adjustable planar machine, with which the (scaled) prescribed tool path could be *continuously* traced. In general, however, a feasible design may not exist for a particular prescribed path, and thus it cannot be continuously traced. In this event, *user intervention* is required to divide the
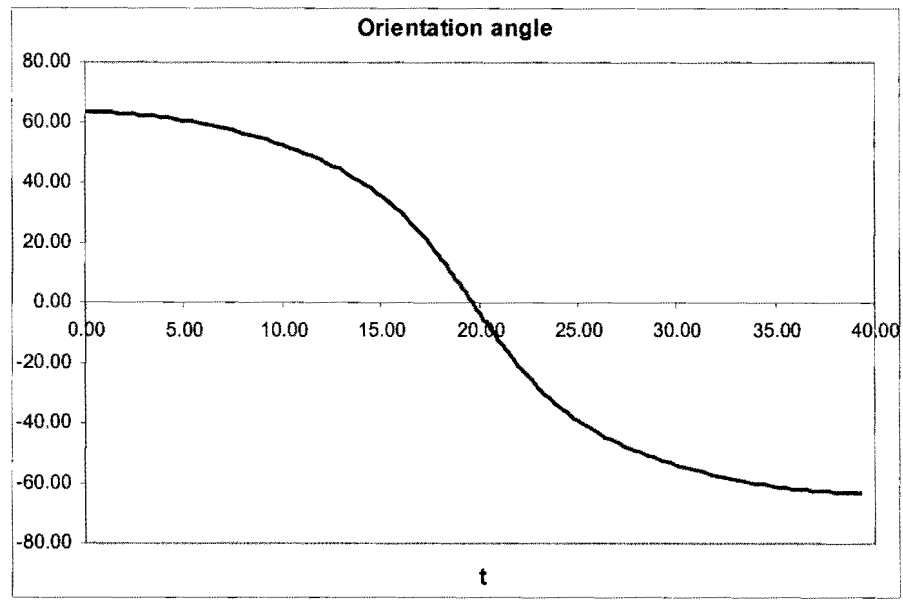
Figure 5.31: Variation in the orientation angle for the bigger parabolic tool path.

5.7.1.2 Optimization results

Whenever the LFOPC-algorithm cannot find an optimum design that is feasible, it computes a "best" *compromised* design corresponding to that with least possible constraint violation, and presents it as the optimum solution. A comparison between the initial test-model design and the compromised optimum test-model design for the bigger parabolic prescribed tool path is given in Table 5.11, with figure insets 6(a) – 6(d).

Initial design		Optimum compromised design	
$\mathbf{X}^0 = [0.4, 0.4, -0.4, -0.4, 0.2]^T$		$\mathbf{X}^* = [0.09643, 0.11018, -0.51561, -0.10841, 0.11015]^T$	
Inequality constraint values (see Section D.3):			
$C_1(\mathbf{X}^0) = -0.05$	$C_2(\mathbf{X}^0) = -0.3$	$C_1(\mathbf{X}^*) = -0.35357$	$\rightarrow C_2(\mathbf{X}^*) = 0.00357$
$C_3(\mathbf{X}^0) = -0.065$	$C_4(\mathbf{X}^0) = -0.287$	$C_3(\mathbf{X}^*) = -0.35482$	$\rightarrow C_4(\mathbf{X}^*) = 0.00282$
$C_5(\mathbf{X}^0) = -0.07$	$C_6(\mathbf{X}^0) = -0.087$	$C_5(\mathbf{X}^*) = -0.15985$	$\rightarrow C_6(\mathbf{X}^*) = 0.00285$
$\rightarrow C_7(\mathbf{X}^0) = 0.11077$	$C_8(\mathbf{X}^0) = -0.02581$	$\rightarrow C_7(\mathbf{X}^*) = 0.01264$	$\rightarrow C_8(\mathbf{X}^*) = 0.591 \times 10^{-3}$
$C_9(\mathbf{X}^0) = -0.00648$	$\rightarrow C_{10}(\mathbf{X}^0) = 0.12769$	$\rightarrow C_9(\mathbf{X}^*) = 0.01347$	$\rightarrow C_{10}(\mathbf{X}^*) = 0.01208$
$\rightarrow C_{11}(\mathbf{X}^0) = 0.12769$	$C_{12}(\mathbf{X}^0) = -0.29548$	$\rightarrow C_{11}(\mathbf{X}^*) = 0.01208$	$C_{12}(\mathbf{X}^*) = -0.36166$
$C_{13}(\mathbf{X}^0) = -0.09548$	$\rightarrow C_{14}(\mathbf{X}^0) = 0.02800$	$C_{13}(\mathbf{X}^*) = -0.16520$	$C_{14}(\mathbf{X}^*) = -0.05061$
$\rightarrow C_{15}(\mathbf{X}^0) = 0.03046$	$\rightarrow C_{16}(\mathbf{X}^0) = 0.04159$	$C_{15}(\mathbf{X}^*) = -0.29681$	$C_{16}(\mathbf{X}^*) = -0.04946$
$\rightarrow C_{17}(\mathbf{X}^0) = 0.05454$	$\rightarrow C_{18}(\mathbf{X}^0) = 0.08839$	$C_{17}(\mathbf{X}^*) = -0.00670$	$C_{18}(\mathbf{X}^*) = -0.04160$
$C_{19}(\mathbf{X}^0) = -0.03549$	$C_{20}(\mathbf{X}^0) = -0.02495$	$C_{19}(\mathbf{X}^*) = -0.05005$	$C_{20}(\mathbf{X}^*) = -0.13960$
$\rightarrow C_{21}(\mathbf{X}^0) = 0.06468$	$\rightarrow C_{22}(\mathbf{X}^0) = 0.04873$	$C_{21}(\mathbf{X}^*) = -0.04202$	$C_{22}(\mathbf{X}^*) = -0.17053$
$\rightarrow$ constraint violation		$\rightarrow$ constraint violation	

Variation of actuator leg lengths along the bigger parabolic tool path:	

6(a)

6(b)

Variation of actuator forces along the bigger parabolic tool path:	

6(c)

6(d)

$F(\mathbf{X}^0) = 23.121\,\mathrm{N}$	$F(\mathbf{X}^*) = 57.681\,\mathrm{N}$
Actuator leg 2	Actuator leg 1
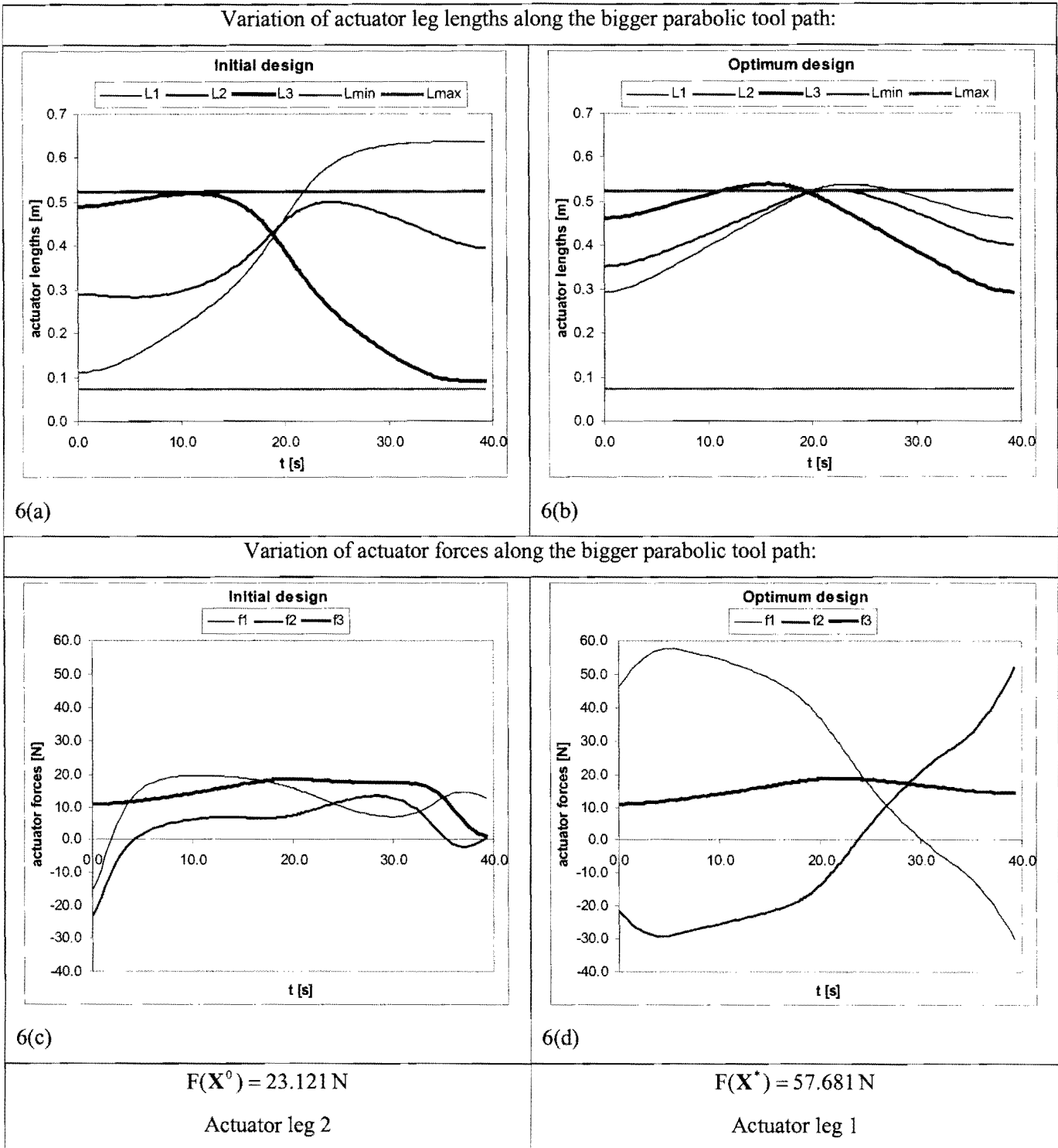
Table 5.11: Comparison between the initial and optimum designs for the bigger parabolic tool path.

The infeasibility of the initial design $\mathbf{X}^0$ is evident from figure inset 6(a), as well as from the violated inequality constraints corresponding to C_7, C_{10}, C_{11}, C_{14}, C_{15}, C_{16}, C_{17}, C_{18}, C_{21} and C_{22}. Figure inset 6(c) shows the variation in actuator forces for this initial design with an objective function value of $F(\mathbf{X}^0) = 23.121\,\mathrm{N}$, with actuator leg 2 responsible for the maximum magnitude actuator force.

Considering the compromised optimum design $\mathbf{X}^*$, the constraints corresponding to C_2, C_4, C_6, C_7, C_8, C_9, C_{10} and C_{11} are violated by the LFOPC-algorithm in its search for a best compromised solution. The variation of the actuator legs for this compromised optimum solution is shown in figure inset 6(b), where the violation of the maximum allowable actuator leg length by actuator legs ℓ_1 and ℓ_3 is clearly visible. In correspondence with Section 5.4.2, the magnitude of constraint function value $C_8(\mathbf{X}^*) = 0.591 \times 10^{-3}$ m (0.591 mm) is indeed negligibly small, and from a practical point of view, the inequality constraint associated with C_8 can be considered *active* rather than *violated* (see expression (D.11)).

The violated inequality constraints associated with C_2, C_4 and C_6 (expression (D.10)) imply that the linearly adjustable revolute joints are positioned outside their allowable ranges. In particular, C_2 has the largest constraint function magnitude of the three with $C_2(\mathbf{X}^*) = 0.00357$ m $= 3.57$ mm. Although substantial, these violations are not critical, since they lie within the minimum safety margin of 5 mm that was used during the formulation of the inequality constraints (see **Appendix D**).

Apart from the critically violated actuator leg length inequality constraints C_7 and C_9 (expression (D.11)), violated constraints C_{10} and C_{11} resulting from the tangential orientation of the moving platform, cannot be ignored. More specifically, of these four inequality constraint functions, the smallest magnitude is $C_{10}(\mathbf{X}^*) = C_{11}(\mathbf{X}^*) = 0.0121$ m (12.1 mm) and the largest magnitude is $C_9(\mathbf{X}^*) = 0.0135$ m (13.5 mm).

The above analysis of the violated inequality constraints is used in the next subsection where the prescribed parabolic tool path is rationally divided into different segments. For the sake of completeness, however, the convergence histories of the objective function (Figure 5.32) and design variables (Figure 5.33) in arriving at the compromised solution, are also included here.
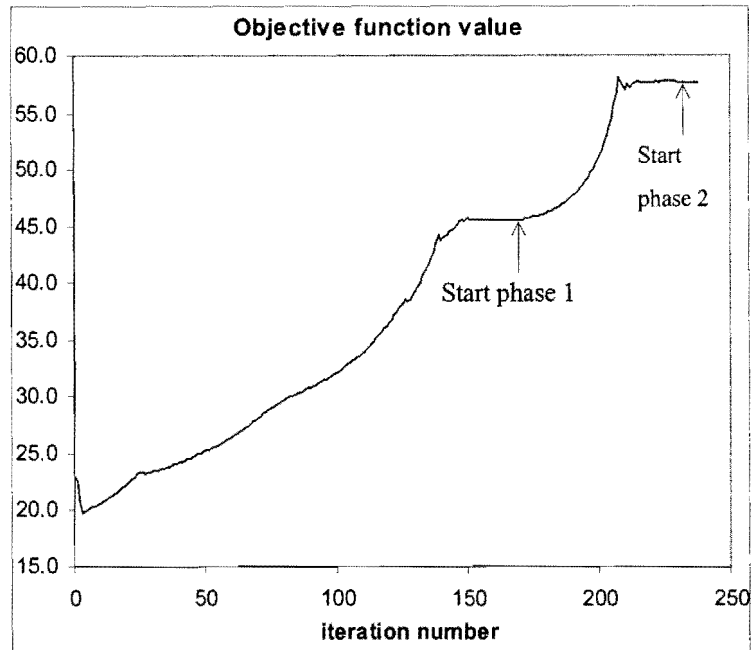
Figure 5.32: **Convergence history of the objective function for the bigger parabolic tool path.**
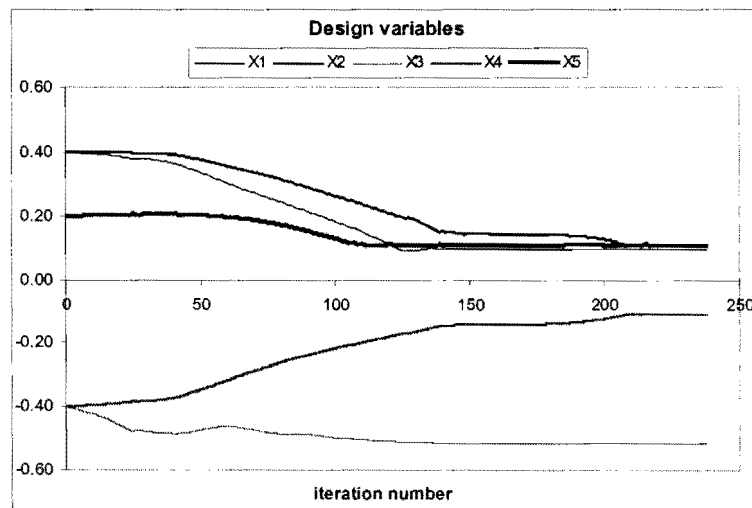
Figure 5.33: **Convergence histories of design variables** X_i, $i = 1,2,...,5$ **for the bigger parabolic tool path.**

Note that the compromised optimum solution $\mathbf{X}^*$ is found in 238 optimization iterations requiring 7 minutes and 29 seconds computational time on a Pentium IV 1.5 GHz computer with 640 MB DDRAM. The LFOPC-algorithm here also terminated on criterion 2 ($\varepsilon_x \leq 10^{-5}$) listed in Section 4.4.

5.7.2 Dividing the prescribed path into segments

5.7.2.1 Nodal points and orientation angle

In the case of a compromised solution the user may intervene in a rational manner in order to execute the path. This is done by firstly analyzing the constraints violated by the compromised design. Note that for the example under consideration, the critically violated inequality constraints are the maximum allowable actuator leg lengths ℓ_1 and ℓ_3 (C_7 and C_9 given by expression (D.11)) and the lower frame boundary constraints C_{10} and C_{11} as explained in Section D.3.3.2. This implies that the "vertical motion" of the moving platform that is required for the complete continuous tracing of the prescribed parabolic tool path shown in Figure 5.30, cannot be accommodated.

(a)

(b)

(c)
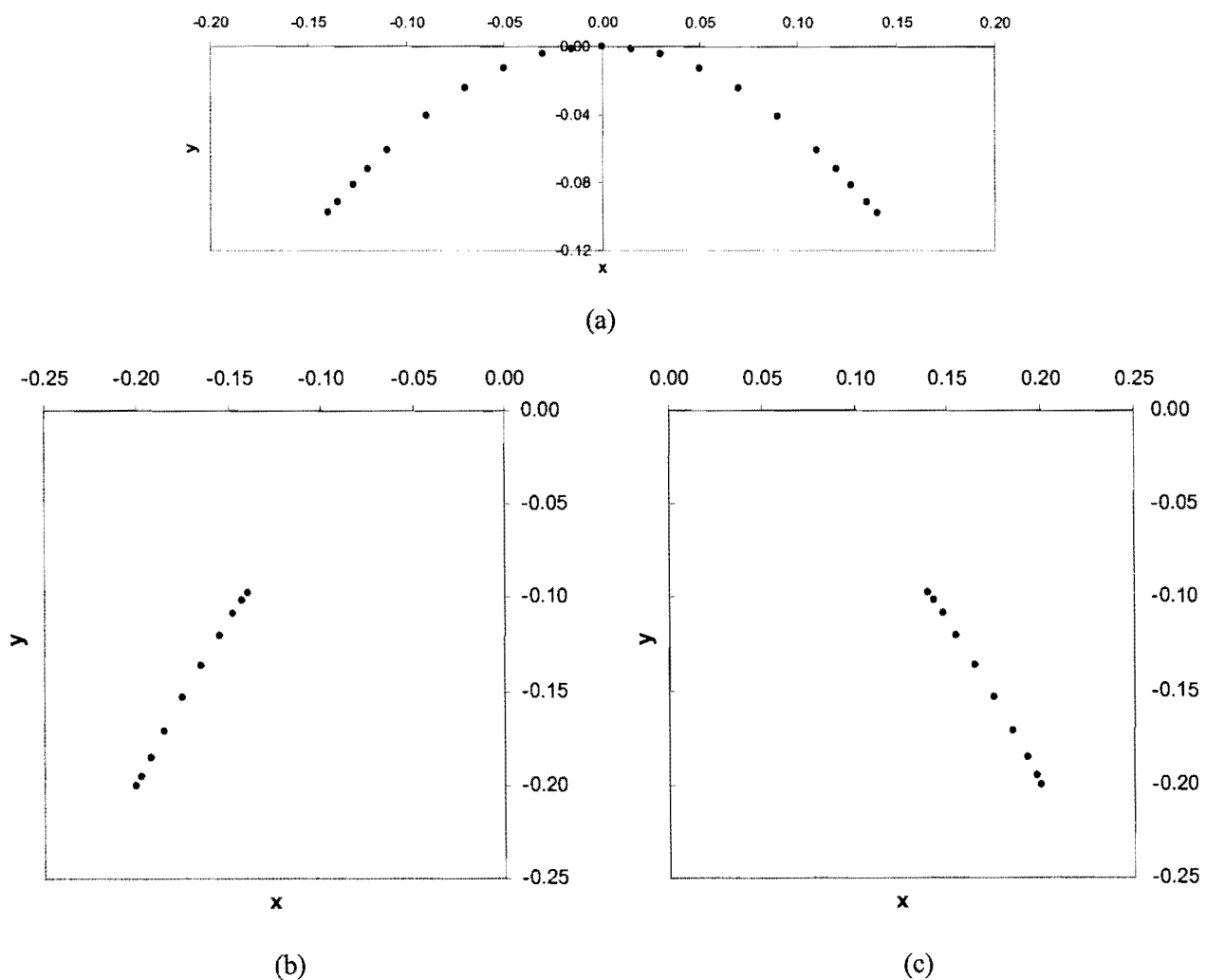
Figure 5.34: Three sets of nodal points used to approximate the bigger parabolic tool path: (a) upper middle segment, (b) bottom left segment and (c) bottom right segment.

The prescribed parabolic tool path is symmetric about the y-axis, hence the "bounds of vertical motion", associated with the execution of the left-hand side of the tool path correspond exactly to the "bounds of vertical motion" associated with the execution of the right-hand side of the tool path. This implies that

dividing the prescribed parabolic tool path into two symmetric segments, will not remedy the problem. An alternative strategy is to divide the prescribed tool path into three seperate segments as shown in Figure 5.34 (a) – (c).

The sequential execution of firstly segment (b), then segment (a) and finally segment (c), is one possible strategy that can be followed to execute the prescribed bigger parabolic tool path. The assumption is made here that the workpiece can be repositioned after each segment is executed. This assumption is justified not only because repositioning is common practice in the machining of larger workpieces, but also because the two "repositioning parameters" correspond to chosen design variables of the constrained optimization problem. In particular, design variables X_3 and X_4 determine the position of the workpiece relative to the base of the planar Gough-Stewart machining platform (see Figure 5.5).

For demonstration purposes it is further assumed that the planar "workpiece" on which the prescribed tool path is to be traced, can be rotated through $180°$ about the vertical y-axis of the prescribed parabola. This assumption implies that a second possible strategy for the execution of the prescribed bigger parabolic tool path, is to sequentially trace segments (b) and (a) of Figure 5.34, then rotate the workpiece through $180°$ about its vertical symmetry axis, and finally trace segment (b) of Figure 5.34 once more.

The advantage of the latter strategy is that for the optimization based operating system of the planar Gough-Stewart platform as proposed in this study, only two of the three segments shown in Figure 5.34 have to be optimized for. In practice segments (b) and (a) are treated as two separate tool paths, each requiring its own optimization run. The subsequent optimization results of the respective prescribed tool paths are presented in sub-sections 5.7.2.2 and 5.7.2.3.

For both prescribed tool paths, the OCAS trajectory-planning methodology (**Chapter 3**) is applied with the maximum allowable acceleration limited to 0.01 meter per second square ($\ddot{s}_{allow} = 0.01\,\mathrm{m/s^2}$), and a specified cutting speed of $1.0\,\mathrm{m/min}$ ($v^* = 1.0\,\mathrm{m/min}$). With these specifications, the *simulated* prescribed motion along segment (b) in Figure 5.34 is completed in $10.07\,\mathrm{s}$, and the *simulated* prescribed motion along segment (a) in Figure 5.34 is completed in $24.16\,\mathrm{s}$.

The original specification that the moving platform of the test-model be tangentially orientated with respect to the prescribed curve, is also incorporated here. In particular, the moving platform orientation angle now varies from $63.4°$ at the starting point $(-0.2, -0.2)$ of segment (b) to $54.5°$ at the end point $(-0.14, -0.098)$ of segment (b) as shown in Figure 5.35.
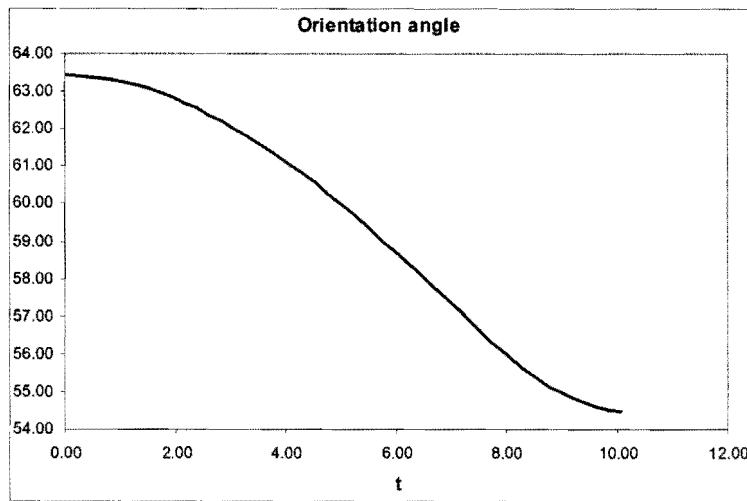
Figure 5.35: Variation in the orientation angle for segment (b) of the bigger parabolic tool path (see Figure 5.34).

For segment (a) in Figure 5.34, the moving platform orientation angle varies from $54.5°$ at the start point $(-0.14, -0.098)$, to $-54.5°$ at the end point $(0.14, -0.098)$ (see Figure 5.36).
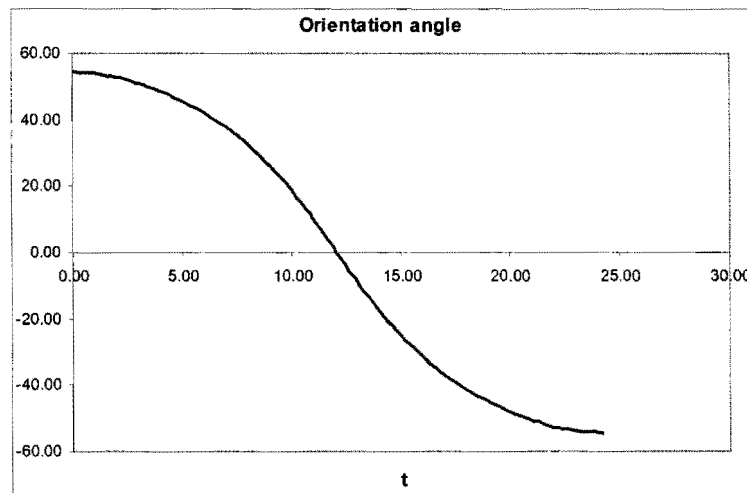
Figure 5.36: Variation in the orientation angle for segment (a) of the bigger parabolic tool path (see Figure 5.34).

5.7.2.2 Optimization results for segment (b) of Figure 5.34.

A comparison between the initial test-model design and the optimum test-model design for segment (b) of the bigger parabolic tool path (see Figure 5.34) is given in Table 5.12 with figure insets 7(a) – 7(d).

Initial design	Optimum compromised design
$\mathbf{X}^0 = [0.4, 0.4, -0.4, -0.4, 0.2]^T$	$\mathbf{X}^* = [0.21606, 0.23581, -0.52924, -0.38758, 0.11917]^T$
Inequality constraint values (see Section D.3):	

$C_1(\mathbf{X}^0) = -0.05$	$C_2(\mathbf{X}^0) = -0.3$	$C_1(\mathbf{X}^*) = -0.23394$	$C_2(\mathbf{X}^*) = -0.11606$
$C_3(\mathbf{X}^0) = -0.065$	$C_4(\mathbf{X}^0) = -0.287$	$C_3(\mathbf{X}^*) = -0.22919$	$C_4(\mathbf{X}^*) = -0.12281$
$C_5(\mathbf{X}^0) = -0.07$	$C_6(\mathbf{X}^0) = -0.087$	$C_5(\mathbf{X}^*) = -0.15083$	$C_6(\mathbf{X}^*) = -0.00617$
$C_7(\mathbf{X}^0) = -0.32486$	$C_8(\mathbf{X}^0) = -0.23336$	$C_7(\mathbf{X}^*) = -0.13510$	$C_8(\mathbf{X}^*) = -0.17790$
$C_9(\mathbf{X}^0) = -0.00911$	$\rightarrow C_{10}(\mathbf{X}^0) = 0.12770$	$C_9(\mathbf{X}^*) = -0.00394$	$C_{10}(\mathbf{X}^*) = -0.00154$
$C_{11}(\mathbf{X}^0) = -0.38212$	$C_{12}(\mathbf{X}^0) = -0.29556$	$C_{11}(\mathbf{X}^*) = -0.51136$	$C_{12}(\mathbf{X}^*) = -0.48845$
$C_{13}(\mathbf{X}^0) = -0.40876$	$\rightarrow C_{14}(\mathbf{X}^0) = 0.02801$	$C_{13}(\mathbf{X}^*) = -0.31045$	$C_{14}(\mathbf{X}^*) = -0.06274$
$\rightarrow C_{15}(\mathbf{X}^0) = 0.03048$	$\rightarrow C_{16}(\mathbf{X}^0) = 0.04160$	$C_{15}(\mathbf{X}^*) = -0.22601$	$C_{16}(\mathbf{X}^*) = -0.07416$
$\rightarrow C_{17}(\mathbf{X}^0) = 0.05455$	$\rightarrow C_{18}(\mathbf{X}^0) = 0.08839$	$C_{17}(\mathbf{X}^*) = -0.03509$	$C_{18}(\mathbf{X}^*) = -0.05569$
$C_{19}(\mathbf{X}^0) = -0.04946$	$C_{20}(\mathbf{X}^0) = -0.06903$	$C_{19}(\mathbf{X}^*) = -0.08209$	$C_{20}(\mathbf{X}^*) = -0.18538$
$C_{21}(\mathbf{X}^0) = -0.05174$	$C_{22}(\mathbf{X}^0) = 0.04874$	$C_{21}(\mathbf{X}^*) = -0.06039$	$C_{22}(\mathbf{X}^*) = -0.01225$

$\rightarrow$ constraint violation

Variation of actuator leg lengths along segment (b) of the bigger parabolic tool path (see Figure 5.34):

7(a)

7(b)

Variation of actuator forces along segment (b) of the bigger parabolic tool path (see Figure 5.34):	
 7(c)	 7(d)
$F(\mathbf{X}^0) = 23.078\,\text{N}$ Actuator leg 2	$F(\mathbf{X}^*) = 17.238\,\text{N}$ Actuator leg 3
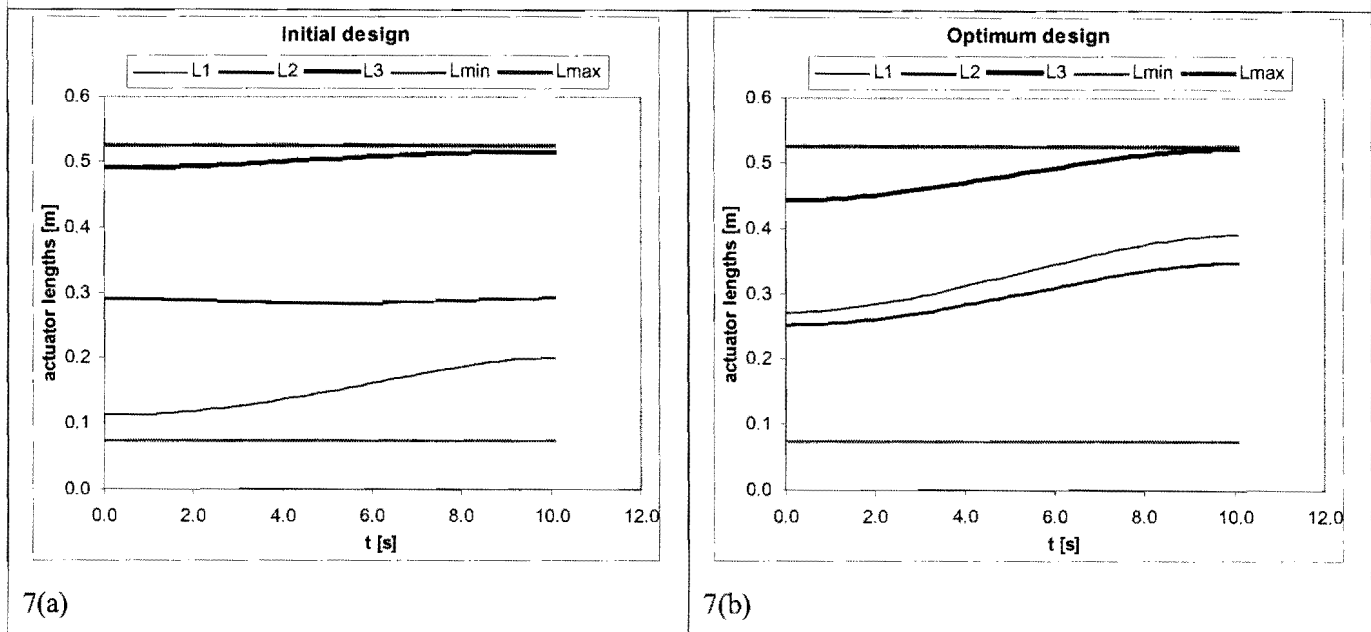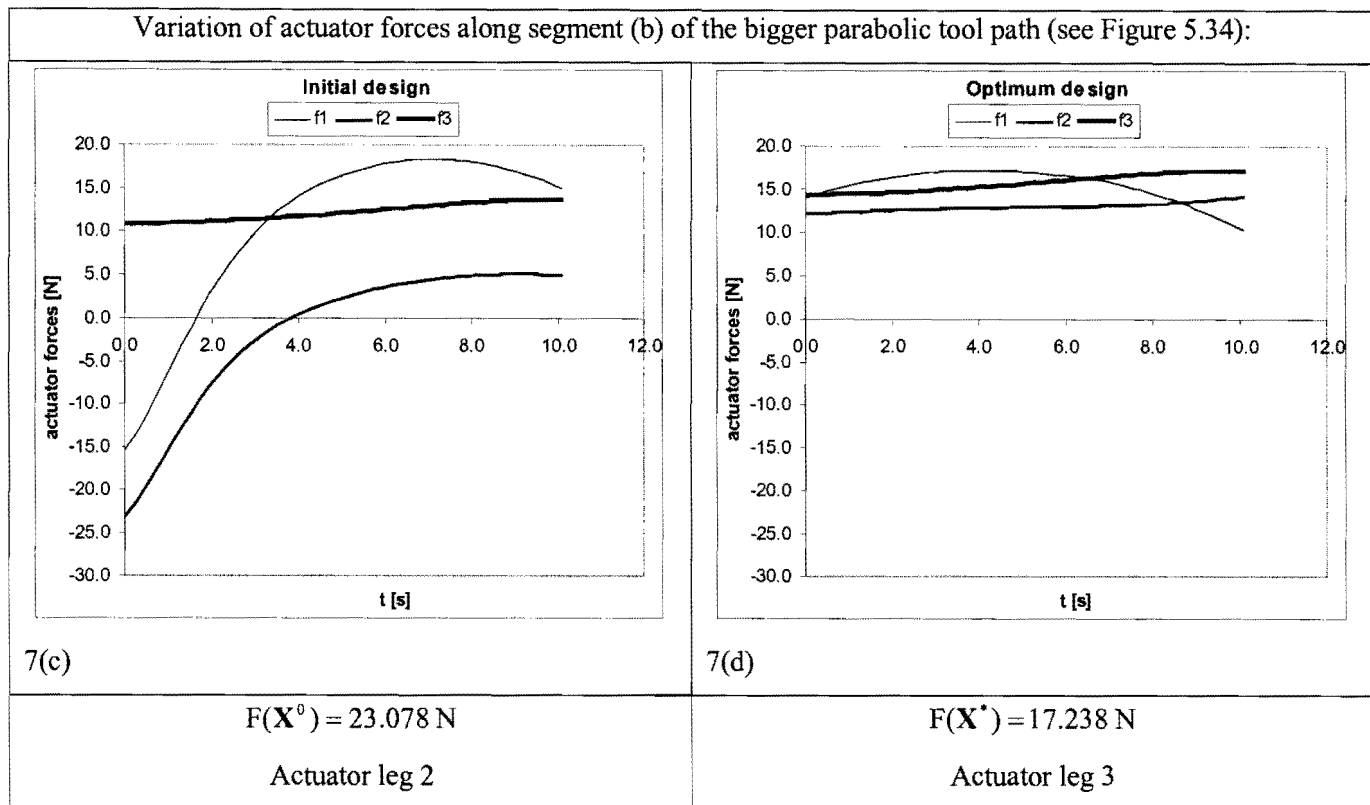
Table 5.12: Comparison between the initial and optimum designs for segment (b) of the bigger parabolic tool path (see Figure 5.34).

The initial design $\mathbf{X}^0$ is infeasible as can be seen from the positive inequality constraint function values $C_{10}(\mathbf{X}^0)$, $C_{14}(\mathbf{X}^0)$, $C_{15}(\mathbf{X}^0)$, $C_{16}(\mathbf{X}^0)$, $C_{17}(\mathbf{X}^0)$ and $C_{18}(\mathbf{X}^0)$ in Table 5.12. The (allowable) initial variation of the actuator leg lengths along segment (b) of the bigger parabolic tool path (see Figure 5.34) is shown in figure inset 7(a).

The LFOPC-optimization algorithm finds the feasible optimum design $\mathbf{X}^*$ in 122 optimization iterations requiring 1 minute and 32 seconds computational time on a Pentium IV 1.5 GHz computer with 640 MB DDRAM.

The optimum design $\mathbf{X}^*$ found is an *unconstrained* optimum as can be seen from the *negative* inequality constraint function values $C_i(\mathbf{X}^*)$, $i = 1,2,3,...,22$ listed in Table 5.12, and the optimum variation of the actuator leg lengths shown in figure inset 7(b). The optimum variation of the actuator forces along segment (b) of the bigger parabolic tool path shown in figure inset 7(d) is significantly different when compared to the initial variation shown in figure inset 7(c). In particular, the initial objective function value is $F(\mathbf{X}^0) = 23.078\,\text{N}$ in actuator leg ℓ_2, while the optimum objective function value is $F(\mathbf{X}^*) = 17.238\,\text{N}$ in actuator leg ℓ_3.

The convergence histories of the objective function (Figure 5.37) and design variables (Figure 5.38) are shown below. Note that since no active constraints were identified as the LFOPC-algorithm progressed along phase 0 (see **Appendix C**), the iterative search terminated on criterion 2 ($\varepsilon_x \leq 10^{-5}$) listed in Section 4.4 before the end of phase 0.
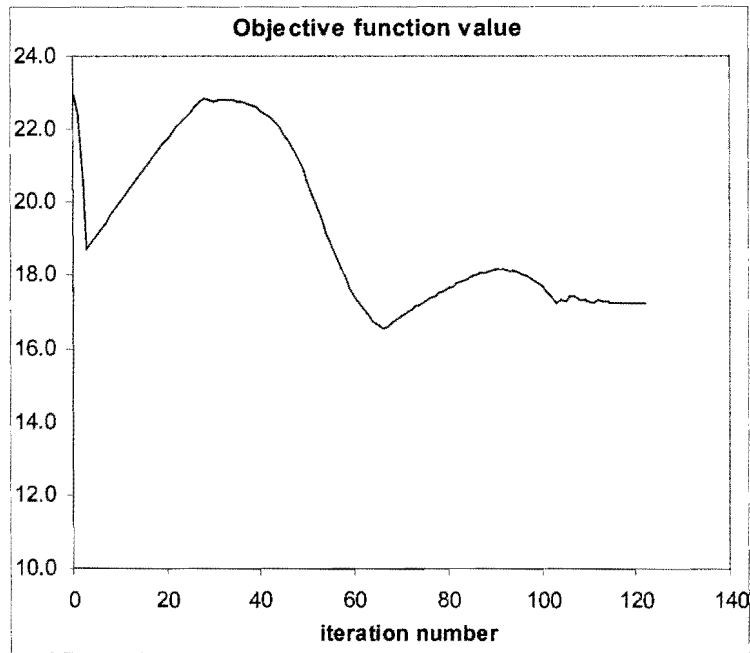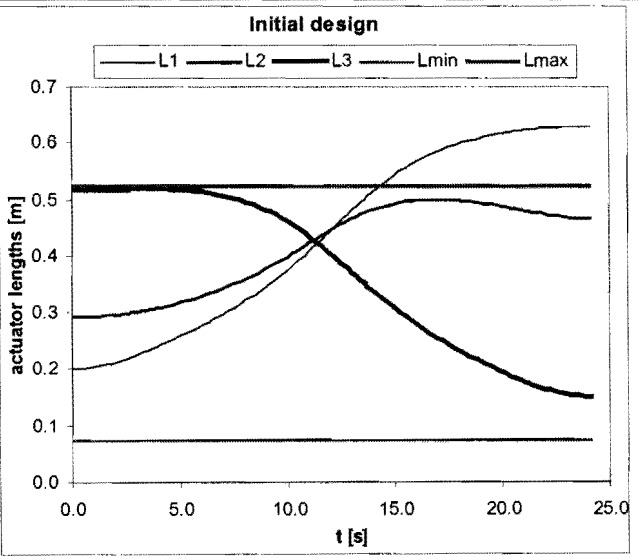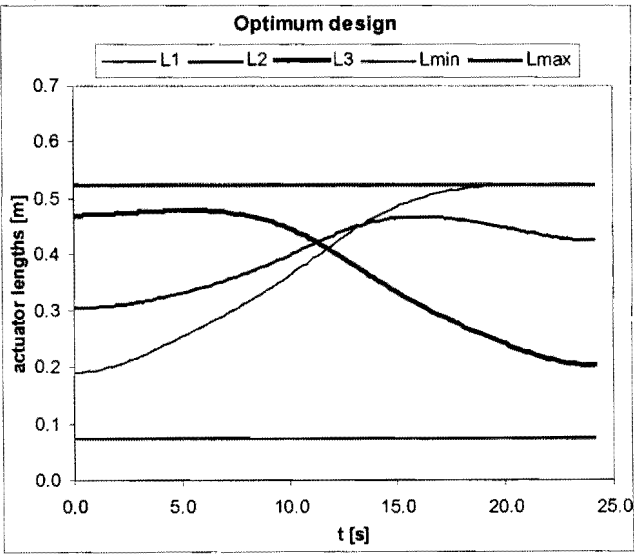
Figure 5.37: Convergence history of the objective function for segment (b) of the bigger parabolic tool path (see Figure 5.34).
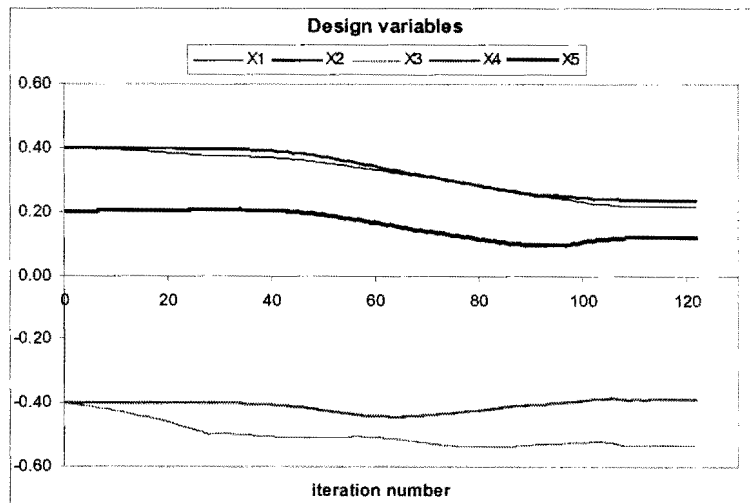
Figure 5.38: Convergence histories of design variables X_i, $i = 1,2,...,5$ for segment (b) of the bigger parabolic tool path (see Figure 5.34).

5.7.2.3 Optimization results for segment (a) of Figure 5.34.

A comparison between the initial test-model design and the optimum test-model design for segment (a) of the bigger parabolic tool path (see Figure 5.34) is given in Table 5.13 with figure insets 8(a) – 8(d).

Initial design	Optimum compromised design
$\mathbf{X}^0 = [0.4, 0.4, -0.4, -0.4, 0.2]^T$	$\mathbf{X}^* = [0.28698, 0.27183, -0.40319, -0.25524, 0.13241]^T$

Inequality constraint values (see Section D.3):	
$C_1(\mathbf{X}^0) = -0.05$　　$C_2(\mathbf{X}^0) = -0.3$ $C_3(\mathbf{X}^0) = -0.065$　　$C_4(\mathbf{X}^0) = -0.287$ $C_5(\mathbf{X}^0) = -0.07$　　$C_6(\mathbf{X}^0) = -0.087$ $\rightarrow C_7(\mathbf{X}^0) = 0.10390$　　$C_8(\mathbf{X}^0) = -0.02582$ $C_9(\mathbf{X}^0) = -0.00651$　　$\rightarrow C_{10}(\mathbf{X}^0) = 0.00321$ $\rightarrow C_{11}(\mathbf{X}^0) = 0.00321$　　$C_{12}(\mathbf{X}^0) = -0.32872$ $C_{13}(\mathbf{X}^0) = -0.12872$　　$C_{14}(\mathbf{X}^0) = -0.03807$ $C_{15}(\mathbf{X}^0) = -0.05491$　　$C_{16}(\mathbf{X}^0) = -0.00827$ $C_{17}(\mathbf{X}^0) = -0.01806$　　$C_{18}(\mathbf{X}^0) = -0.00218$ $C_{19}(\mathbf{X}^0) = -0.07006$　　$C_{20}(\mathbf{X}^0) = -0.09382$ $C_{21}(\mathbf{X}^0) = -0.08689$　　$C_{22}(\mathbf{X}^0) = -0.01093$	$C_1(\mathbf{X}^*) = -0.16302$　　$C_2(\mathbf{X}^*) = -0.18698$ $C_3(\mathbf{X}^*) = -0.19317$　　$C_4(\mathbf{X}^*) = -0.15883$ $C_5(\mathbf{X}^*) = -0.13759$　　$C_6(\mathbf{X}^*) = -0.01941$ $\Rightarrow C_7(\mathbf{X}^*) = 0.375 \times 10^{-4}$　　$C_8(\mathbf{X}^*) = -0.05909$ $C_9(\mathbf{X}^*) = -0.04699$　　$\Rightarrow C_{10}(\mathbf{X}^*) = 0.158 \times 10^{-4}$ $\Rightarrow C_{11}(\mathbf{X}^*) = 0.158 \times 10^{-4}$　　$C_{12}(\mathbf{X}^*) = -0.34499$ $C_{13}(\mathbf{X}^*) = -0.17817$　　$C_{14}(\mathbf{X}^*) = -0.05417$ $C_{15}(\mathbf{X}^*) = -0.17787$　　$C_{16}(\mathbf{X}^*) = -0.02705$ $C_{17}(\mathbf{X}^*) = -0.00307$　　$\Rightarrow C_{18}(\mathbf{X}^*) = 0.108 \times 10^{-3}$ $C_{19}(\mathbf{X}^*) = -0.06970$　　$C_{20}(\mathbf{X}^*) = -0.15416$ $C_{21}(\mathbf{X}^*) = -0.03715$　　$C_{22}(\mathbf{X}^*) = -0.07894$
$\rightarrow$ constraint violation	$\Rightarrow$ constraint active

Variation of actuator leg lengths along segment (a) of the bigger parabolic tool path (see Figure 5.34):	
8(a)	8(b)

Variation of actuator forces along segment (a) of the bigger parabolic tool path (see Figure 5.34):

8(c)

8(d)

| $F(\mathbf{X}^0) = 19.554\,\text{N}$	$F(\mathbf{X}^*) = 24.347\,\text{N}$
Actuator leg 1	Actuator leg 1

Table 5.13: Comparison between the initial and optimum designs for segment (a) of the bigger parabolic tool path (see Figure 5.34).

To start off with, the initial design $\mathbf{X}^0$ is again infeasible as can be seen from the positive inequality constraint function values $C_7(\mathbf{X}^0)$, $C_{10}(\mathbf{X}^0)$ and $C_{11}(\mathbf{X}^0)$ in Table 5.13. Figure inset 8(a) also shows that actuator leg ℓ_1 violates the maximum allowable actuator leg length (inequality constraint C_7) as segment (a) of the bigger parabolic tool path (see Figure 5.34) is traced with the initial design. The lower frame boundary inequality constraints C_{10} and C_{11} (expression (D.12)) are also slightly violated by the initial design.

For the feasible optimum design $\mathbf{X}^*$, the active inequality constraints corresponding to C_7, C_{10}, C_{11} and C_{18} (see Table 5.13) exhibit a behavior similar to that detected for the circular tool path of Section 5.4, and explained in detail with reference to Table 5.6. The LFOPC-optimization terminated on criterion 2 ($\varepsilon_x \leq 10^{-5}$) listed in Section 4.4 after 144 optimization iterations requiring 3 minutes and 40 seconds computational time on a Pentium IV 1.5 GHz computer with 640 MB DDRAM.

The optimum variation of the actuator forces along segment (a) of the bigger parabolic tool path shown in figure inset 8(d) is fairly similar to the initial variation shown in figure inset 8(c). In particular, the

initial objective function value is $F(X^0) = 19.554\,N$ in actuator leg ℓ_1, while the optimum objective function value is $F(X^*) = 24.347\,N$, also in actuator leg ℓ_1.

The convergence histories of the objective function (Figure 5.39) and design variables (Figure 5.40) are shown below. Note that both these graphs indicate that in this case, effective convergence is only reached after only 120 iterations.
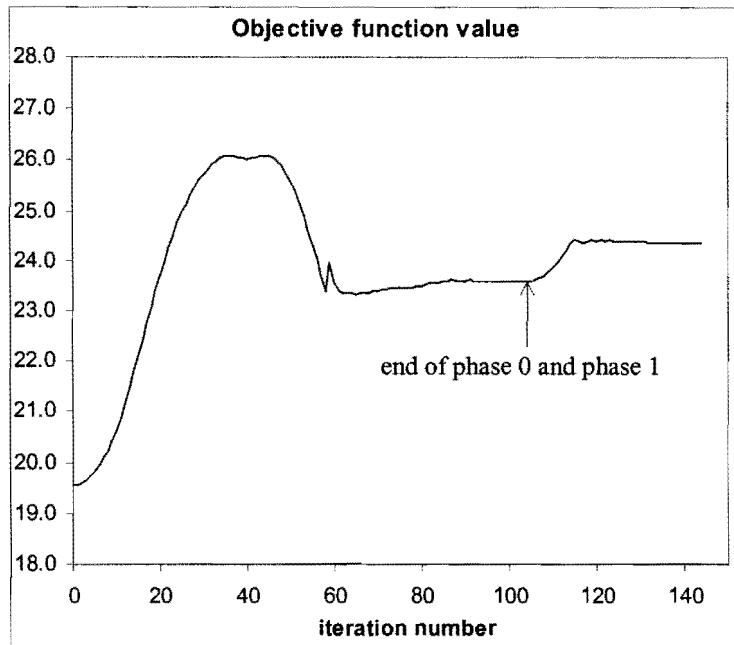
Figure 5.39: Convergence history of the objective function for segment (a) of the bigger parabolic tool path (see Figure 5.34).
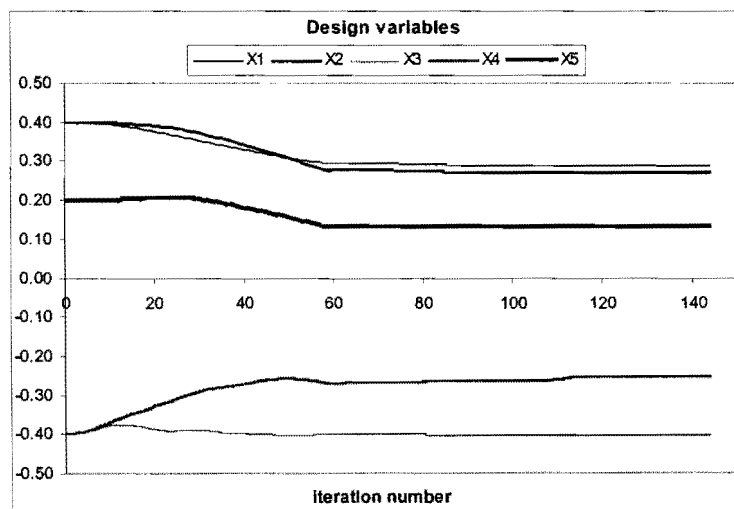
Figure 5.40: Convergence histories of design variables X_i, $i = 1,2,...,5$ for segment (a) of the bigger parabolic tool path (see Figure 5.34).

5.7.3 Execution of the prescribed bigger parabolic tool path

5.7.3.1 First execution of segment (b) (see Figure 5.34)

The series of photographs grouped in Figure 5.41 shows the initial and final time instants during the *first* ("upward") execution of segment (b) of the prescribed bigger parabolic curve (see Figure 5.34). The tangential orientation of the moving platform is clearly visible from these photographs.
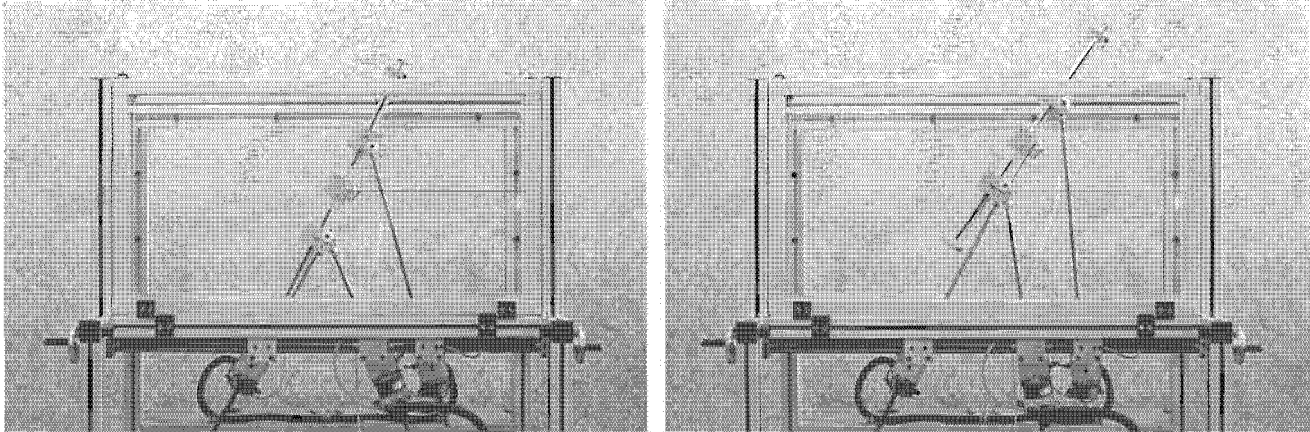
Figure 5.41: First execution of segment (b) of the bigger parabolic tool path (see Figure 5.34).

A close-up view of the executed segment (including a horizontal reference base-line) is shown in Figure 5.42.
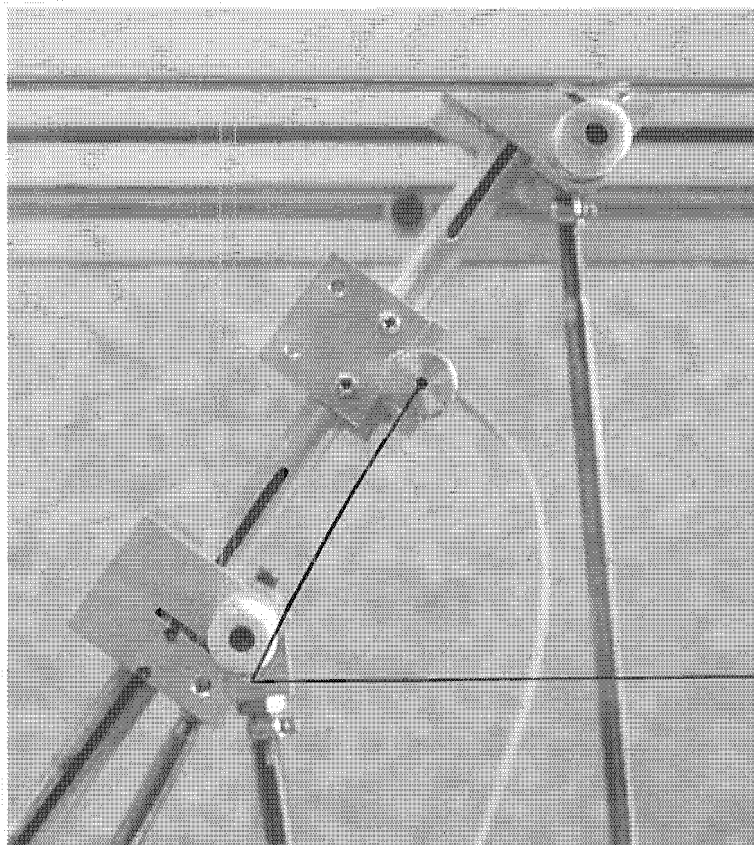
Figure 5.42: Close-up view of the executed segment (b) of the bigger parabolic tool path (see Figure 5.34).

5.7.3.2 Execution of segment (a) (see Figure 5.34)

Once segment (b) has been traced, the "workpiece" is repositioned as explained in Section 5.7.2.1. The series of photographs grouped in Figure 5.43 shows the positioning of the platform at different time instants during the execution of segment (a) of the prescribed bigger parabolic curve (see Figure 5.34). These photographs clearly show that the tangential orientation of the moving platform is maintained as segment (a) is traced.
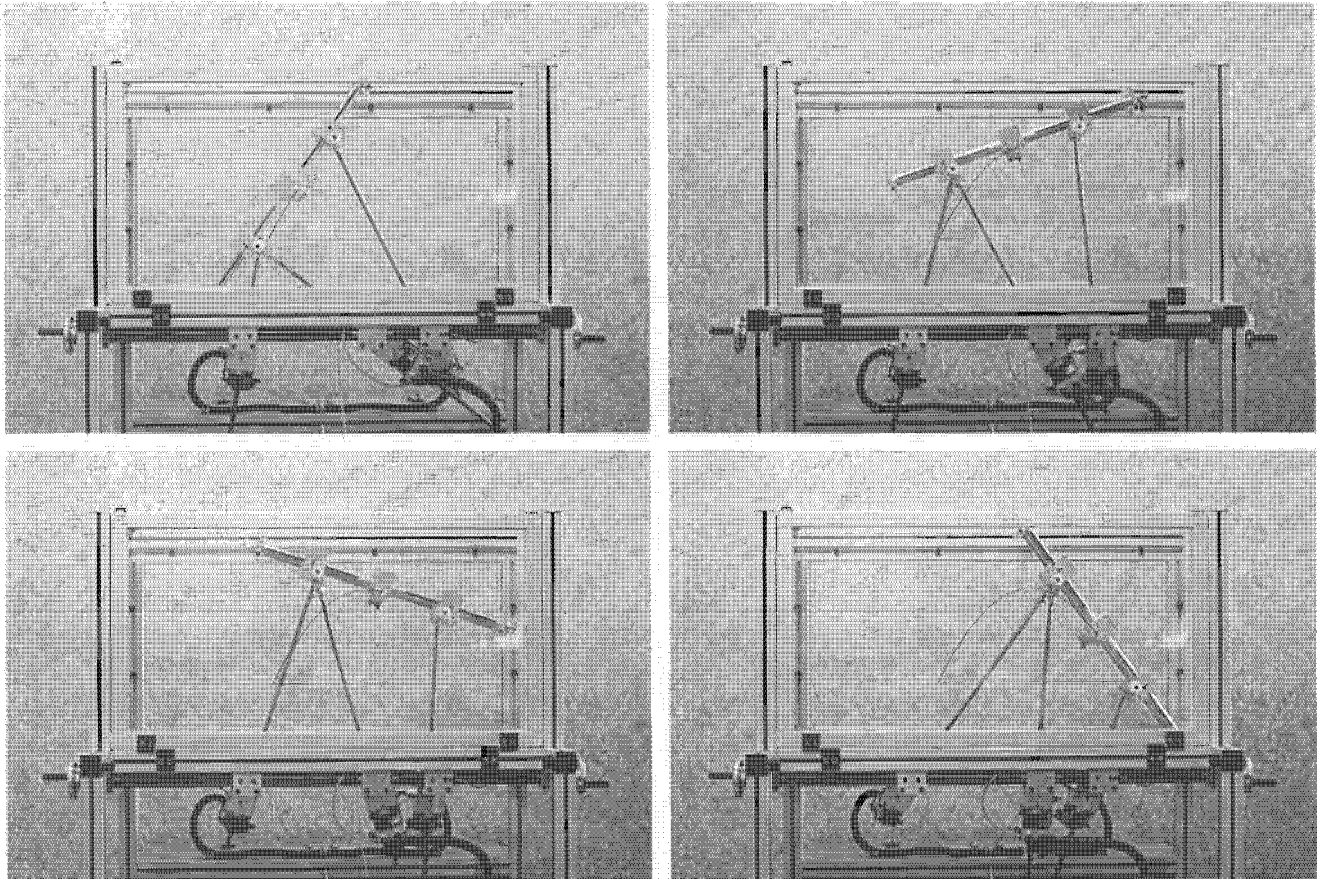
Figure 5.43: Execution of segment (a) of the bigger parabolic tool path (see Figure 5.34).

The close-up view of the executed segments (b) and (a) shown in Figure 5.44, emphasizes the smooth transition between consecutive segments.
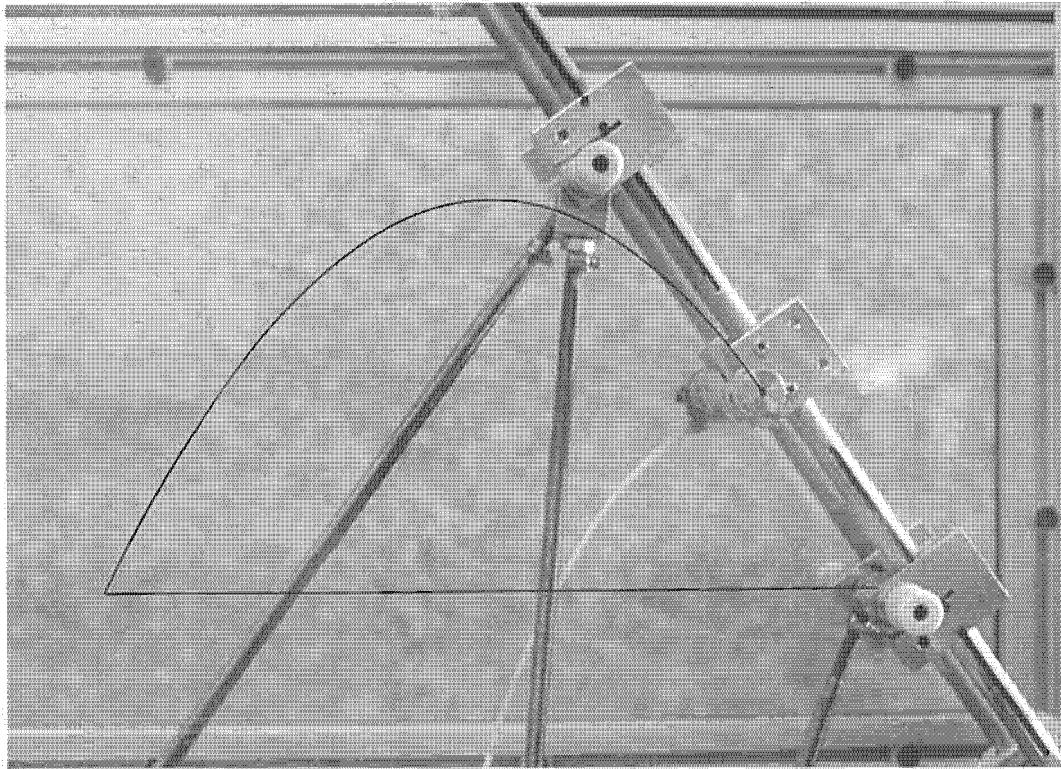
Figure 5.44: Close-up view of the executed segments (b) and (a) of the bigger parabolic tool path (see Figure 5.34).

5.7.3.3 Second execution of segment (b) (see Figure 5.34)

Corresponding to the second possible strategy for the piece-wise execution of the prescribed bigger parabolic tool path (see Section 5.7.2.1), the planar "workpiece" is now rotated through 180° about its vertical symmetry-axis, and repositioned so that segment (b) of Figure 5.34 can be traced for the second time, also "upwards".

The series of photographs grouped in Figure 5.45 shows the initial and final time instants, as well as an intermediate time instant during the *second* execution of segment (b) (see Figure 5.34). The tangential orientation of the moving platform is again clearly visible from these photographs.
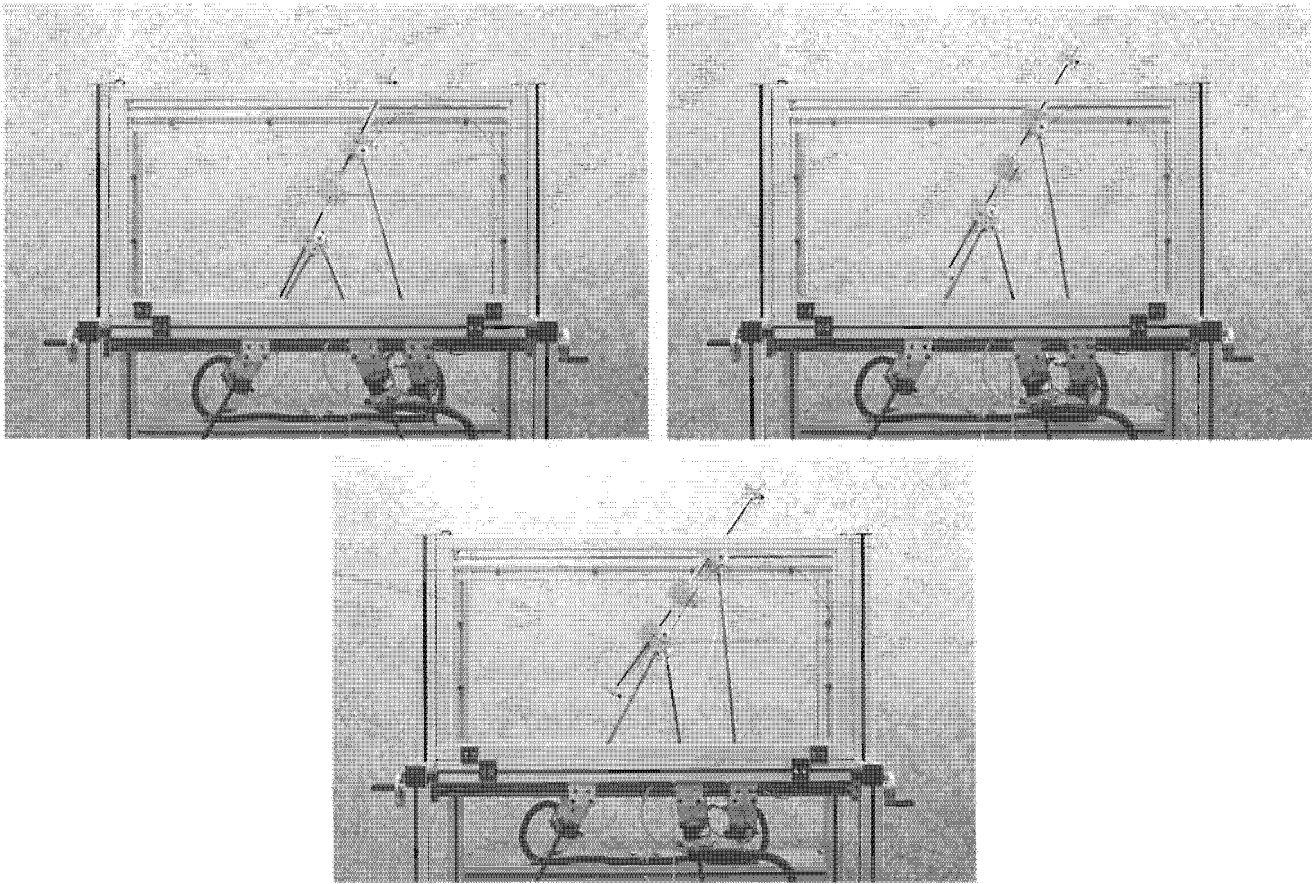
Figure 5.45: Second execution of segment (b) of the bigger parabolic tool path (see Figure 5.34).

A close-up view of the completely executed bigger parabolic tool path is shown in Figure 5.42. In spite of the piece-wise execution of this tool path, it is proportionally shaped and smooth, in agreement with the continuous prescribed tool path specified by Figure 5.30.
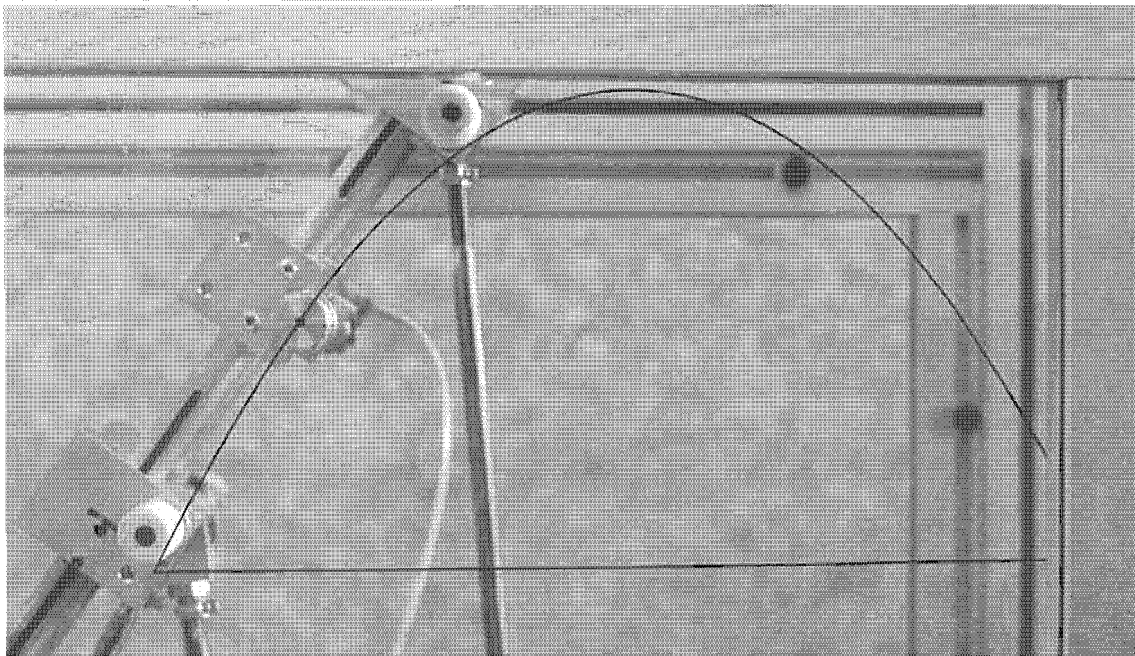
Figure 5.46: Close-up view of the completely executed bigger parabolic tool path (see Figure 5.30).

6   CONCLUSION

In the optimization procedure developed in this study for the optimum operation of a re-configurable machining platform, the evaluation of the objective and constraint functions was done through the computer simulation of the dynamics of the device. For the actual optimization the simulation was coupled to a relatively novel and particularly robust optimization method (LFOPC). The resulting methodology was successful in yielding operational geometries for the re-configurable platform which are not only feasible in accommodating various specified trajectories, but also optimal with respect to the actuator forces required to produce the associated prescribed kinematics.

The validity of the operational designs obtained via theoretical modeling, computer simulation and numerical optimization, was also physically verified through the execution of the non-trivial paths using an actual physically re-configurable device, designed and constructed for the purposes of the current study. The successful execution of the paths demonstrates the practical potential of the device since the paths represent complicated, and free-form planar machining tasks.

In the light of the above, it is clear that the main objective of this study, namely the verification of the feasibility, both from a theoretical and practical point of view, of a novel proposed concept of a re-configurable planar Gough-Stewart machining platform, has been achieved. The remainder of this chapter takes on the form of a detailed review and assessment of the accomplishments of this study.

6.1   Computer simulation

A special purpose computer program was developed in **Chapter 2**, that models the kinematics and the associated dynamical behavior of a planar Gough-Stewart platform. Coupled to this program, the trajectory-planning algorithm developed in **Chapter 3**, allows for the realistic simulation of the continuous motion of the platform.

6.1.1 Kinematic and kinetic modeling

The above mentioned special purpose program, with which the kinematic and kinetic modeling of a planar Gough-Stewart platform may be done, was developed using the Newton-Euler approach as presented by Haug [66] and Nikravesh [65].

This dedicated program yields closed-form solutions for the inverse kinematics (positions, velocities and accelerations) of the seven moving bodies comprising the mechanism. With the positions, velocities and accelerations known, the special purpose program also provides closed-form solutions for the inverse dynamics of the mechanism. Here, the weight and inertia of each moving body, as well as the single external force acting on the mechanism, are taken into consideration to determine in the required input actuator forces.

The single external force referred to is the cutting force resulting from the contact between the cutting tool and the workpiece during material removal. Here the program was successfully adapted to simulate either of two possible machining scenarios, i.e. either with the workpiece or the cutting tool externally fixed.

6.1.2 OCAS trajectory-planning algorithm

Although the OCAS trajectory-planning algorithm was specifically developed for implementation in conjunction with the above mentioned simulation program, its application is not limited to the planar Gough-Stewart platform under consideration. In fact, since all three planar DOF are catered for, the motion of the end-effector of any other planar mechanism can similarly be described.

The results presented in Section 3.5 show that planar motion along test paths described by analytical non-linear functions may realistically be simulated, without compromising on the positional or orientational accuracy. Note that slight positional and orientational inaccuracies are inevitable since the approximating cubic splines are fitted in the time domain, while the nodal points, representing the prescribed path, are specified in the two-dimensional Cartesian domain. For all practical purposes, these discrepancies are negligible.

Apart from specifying the kinematics along test paths described by analytical non-linear functions, the OCAS-algorithm was also successfully used for trajectory-planning along a non-analytical test curve. The treble clef test curve was generated using a Non-Uniform Rational B-Spline (NURBS) with commercial Computer Aided Design (CAD) software. Here it was shown that an adequately refined set of nodal points along this curve is required to ensure sufficient accuracy for the kinematics. For the example, while the NURBS test curve was generated with 42 nodal points, the OCAS-algorithm requires

49 nodal points on this curve for a representation accurate enough to generate the associated kinematic description.

For all test curves considered, continuous position, velocity and acceleration curves as well as the continuous orientation angle, orientation angular velocity and orientation angular acceleration curves are generated using the OCAS trajectory-planning algorithm. These continuous curves representing the kinematics, are essential input data to the simulation program modeling the kinematics of the planar Gough-Stewart platform. As a result of the continuous acceleration curves, the determined input actuator forces required for manipulating the moving platform along a prescribed path, are also continuous.

Although the application of the OCAS trajectory-planning algorithm was limited here to computer *simulation* of planar motion, the increased research interest in bridging the gap between free-form design and *actual machining*, requires further investigation of its applicability to actual physical control. Since a planar Gough-Stewart machining platform is ideally suited to execute non-linear paths, it can theoretically be applied as a machining device for free-form trajectories. The real-time control of such an actual planar Gough-Stewart machining platform could be done by the OCAS-algorithm implemented as part of an open architecture controller.

It should be added that, in principle, the OCAS trajectory-planning algorithm can also be extended to general three-dimensional motion-planning.

6.2   Formulation of the constrained design optimization problem

This study shows that an optimum relative *positioning* for a prescribed trajectory, as well as the associated planar Gough-Stewart platform *geometry* may be determined by the careful *formulation* and *solution* of an appropriate constrained optimization problem.

In particular, the single criterion *cost-function* introduced here is the minimization of the overall maximum magnitude actuator force, as the prescribed trajectory is traced. It is evident from the results presented in **Chapter 5** that the use of this objective function successfully prevents the mechanism from encountering singular or near singular configurations with associated infinitely large actuator forces. The success of this approach is borne out by the moderate optimum objective function values, $F(\mathbf{X}^*)$, obtained for all the prescribed trajectories.

In conjunction with the formulated objective function, non-trivial *inequality constraint functions* allow for the incorporation of additional design requirements. Hence, apart from the limitations imposed on the values of the design variables, inequality constraint functions are successfully used to limit the actuator leg lengths to within their allowable ranges. Furthermore, the complicated issue of prohibiting mechanical interference of the physical machine while in motion, is also achieved by means of inequality constraint functions. The effective formulation of the latter inequality constraints was made possible by the availability of closed-form solutions for the instantaneous positions of the individual bodies comprising the machining platform (see Section 6.1.1).

A sound foundation having been laid for the trajectory-based constrained optimization problem considered in this study, and a logical next step, to be pursued in the near future, is to optimize the adjustable geometry and placement of a planar Gough-Stewart platform for different prescribed *workspace requirements*.

6.3   The LFOPC-algorithm

The study also served to reinforce confidence in the LFOPC optimization algorithm as a method to solve optimization problems of practical engineering importance.

The optimization results have confirmed the LFOPC-algorithm's reputation as a robust method, capable of yielding accurate and reliable results despite the presence of numerical noise, the use of finite difference approximations, and discontinuities in the objective and constraint functions. In particular the discontinuities in the slope of the objective function, that occurred in this study due to switching of the maximum actuator force between the legs, presented no problem and reliable results were obtained with reasonable computational economy. The respective prescribed trajectories investigated in this study required an average of approximately 6 minutes computational time on a Pentium IV 1.5 GHz computer with 640 MB DDRAM before the LFOPC-algorithm converged to the respective optimum operational geometries. In each case, the optimum solution corresponded to the specification of very accurate convergence tolerances. The algorithm was successful in each application, handling the five variables and up to 22 physical constraints with ease, even when starting from a severely infeasible initial design.

Since a standard initial design $\mathbf{X}^0$ was used for all the prescribed tool paths investigated, it cannot be stated with certainty that the determined *local* optimum design is indeed the *global optimum* for all cases. Although the determination of the *global* optimum may be important from a theoretical point of view, the *fact that the proposed methodology provides local optimum solutions that are indeed feasibly*

executable, and correspond to acceptably low objective function values, is considered the most important contribution of this study.

The "analysis of convergence to the optimum" performed for the first five prescribed tasks was important, because it shed light on the functioning of the algorithm when applied to the class of design optimization problems considered in this study. Of particular importance was the finding that sufficiently accurate "engineering solutions" may be obtained by only applying phase 0 of the LFOPC algorithm. Considering the prescribed tasks investigated here, the percentage computational time that can be saved by using only phase 0, varies between 0 % and 62 % with an average of 30 %. Indeed, termination of the LFOPC-algorithm after phase 0, will produce a practically feasible and near optimum design.

The robustness and effectiveness with which the LFOPC-optimization algorithm handles the formulated constrained optimization problem is best illustrated by the case of the "bigger parabolic tool path", investigated in Section 5.7. Here the prescribed tool path cannot be continuously traced because of the physical limitations of the planar test-model. As a result, the LFOPC-algorithm yields a best compromised design. The compromised design, although infeasible, is invaluable in pointing out which inequality constraints are violated, and to what extent. It was shown for the "bigger parabolic tool path" that by analyzing the relevant information provided by the compromised solution, a rational piece-wise execution strategy can be determined for the successful and optimal execution of the complete path.

Consideration of the above mentioned factors, as well as previous successful experience in the LFOPC-algorithm [64], motivated its usage in solving the currently formulated constrained optimization problems. No other optimization algorithms were tested or applied in this study.

6.4 The adjustable geometry planar Gough-Stewart platform test-model

The adjustable capability required for the proposed concept was successfully implemented in the design of the test-model. The test-model's demonstration capability is however limited to tracing different prescribed tool paths on an externally fixed workpiece. This machining option is considered more likely to be used in practice, since the alternative option of mounting the workpiece to the moving platform is limited by the size and weight of the workpiece that can realistically be mounted on the moving platform.

The prescribed trajectories were successfully traced simply by controlling the required variation of the actuator leg lengths. These lengths are found by solving the three closed-form inverse kinematic equations relating the position and orientation of the moving platform to the actuator leg lengths. The position and orientation of the moving platform follows directly from the prescribed trajectory, and hence the required actuator leg lengths may easily be determined.

To further extend the practical application of the proposed planar Gough-Stewart machining platform, its (open architecture) control software will have to be adapted to enable the direct manipulation of the three DOF of the moving platform. Such a capability would however require knowledge of the maximum possible workspace. This raises the possibility of incorporating the *ranges of configurability* as design variables in an extended optimization methodology. Hence, the foreseen extended optimization system, in which the *geometry of the workspace may be prescribed*, should eventually also include the maximum ranges of re-configurability capabilities of the mechanism as possible additional design variables.

Even though the test-model was not calibrated, visual inspection shows that the actual executed paths closely resemble the prescribed trajectories. The positional error of the moving platform is evidently very small compared to the overall size of the respective paths. This shows that a practical adjustable machine tool, corresponding to the design proposed and demonstrated in this study, may confidently be applied to the execution of machining trajectories intended for the rough material removal in the manufacturing of moulds.

In order to eventually fully exploit the inherent accuracy characteristics of the Gough-Stewart platform type machine tool, a calibration strategy remains to be developed, especially if the manipulator is frequently to be re-configured in order to accommodate differently specified trajectories.

A p p e n d i x   A

A DERIVATION OF THE PLANAR EQUATIONS OF

MOTION

A.1 Newton's second law

Kinetics is the study of motion and its relationship with the forces that produce the motion (see [65]). The simplest body arising in the study of motion is a particle, or point mass, defined by Nikravesh [65] as a mass concentrated at a point. According to Newton's second law, a particle will accelerate when it is subjected to unbalanced forces. More specifically, Newton's second law as applied to a particle is

$$\vec{f} = m^{(p)}\vec{a} \qquad\qquad (A.1)$$

where $\vec{f}$, $m^{(p)}$ and $\vec{a}$ respectively represents the total force acting on the particle, the mass of the particle and the acceleration of the particle (see Figure A.1).
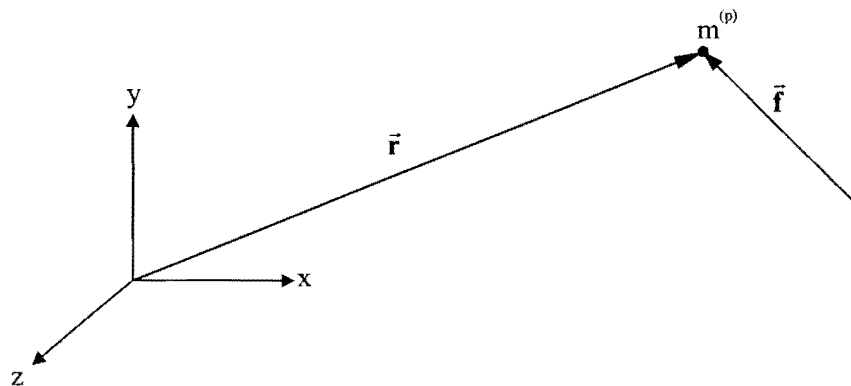
Figure A.1: A particle moving in a global coordinate system (after [65]).

Since $\vec{f}$ and $\vec{a}$ are three-dimensional physical vectors, they may be represented as three-vectors in the global fixed coordinate system, i.e. $\vec{f} : f = [f_{(x)}, f_{(y)}, f_{(z)}]^T$ and $\vec{a} : a = [a_{(x)}, a_{(y)}, a_{(y)}]^T$. The position vector $\vec{r}$ shown in Figure A.1 locates the particle in the global coordinate system and is represented in the global reference frame by $r = [x, y, z]^T$. The acceleration a of the particle is the second time

---

derivative of the position vector, i.e. $\mathbf{a} = \ddot{\mathbf{r}} = [\ddot{x}, \ddot{y}, \ddot{z}]^T$, and the global representation of expression (A.1) therefore is

$$\mathbf{f} = m^{(p)}\ddot{\mathbf{r}} \qquad (A.2)$$

For a system of p particles, the application of expression (A.2) may be extended to describe the motion of each particle i, $i = 1,2,...,p$ in the system, i.e.

$$m_i^{(p)}\ddot{\mathbf{r}}_i = \mathbf{f}_i + \sum_{j=1}^{p}\mathbf{f}_{ij} , \quad i = 1,2,...,p \qquad (A.3)$$

where $\mathbf{f}_i$ is the global representation of the total externally applied force $\vec{\mathbf{f}}_i$ acting on particle i, and $\mathbf{f}_{ij}$ is the global representation of the internal force $\vec{\mathbf{f}}_{ij}$ extended by particle j on particle i. Note that $\vec{\mathbf{f}}_{ii} = \vec{\mathbf{0}}$.

Summing expression (A.3) over all p particles in the system results in

$$\sum_{i=1}^{p} m_i^{(p)}\ddot{\mathbf{r}}_i = \sum_{i=1}^{p}\mathbf{f}_i + \sum_{i=1}^{p}\sum_{j=1}^{p}\mathbf{f}_{ij} \qquad (A.4)$$

and since $\vec{\mathbf{f}}_{ij} = -\vec{\mathbf{f}}_{ji}$ (Newton's third law), it follows that $\sum_{i=1}^{p}\sum_{j=1}^{p}\mathbf{f}_{ij} = 0$, and consequently expression (A.4) reduces to

$$\sum_{i=1}^{p} m_i^{(p)}\ddot{\mathbf{r}}_i = \sum_{i=1}^{p}\mathbf{f}_i \qquad (A.5)$$

or simply

$$m\ddot{\mathbf{r}} = \mathbf{f} \qquad (A.6)$$

where $\quad m = \sum_{i=1}^{p} m_i^{(p)}$ is the total mass of the system of particles,

$\mathbf{r} = \dfrac{1}{m}\sum_{i=1}^{p} m_i^{(p)}\mathbf{r}_i$ is the center of mass of the system of particles, and

$\mathbf{f} = \sum_{i=1}^{p}\mathbf{f}_i$ is the total external force acting on the system of particles.

The translational equation of motion of a system of particles (A.6), also holds for a general continuous rigid body or continuum, the center of mass of which is given by

$$\mathbf{r} = \dfrac{1}{m}\int_{vol}\mathbf{r}^p dm \qquad (A.7)$$

where $\mathbf{r}^p$ locates an infinitesimally small mass element dm as shown in Figure A.2.
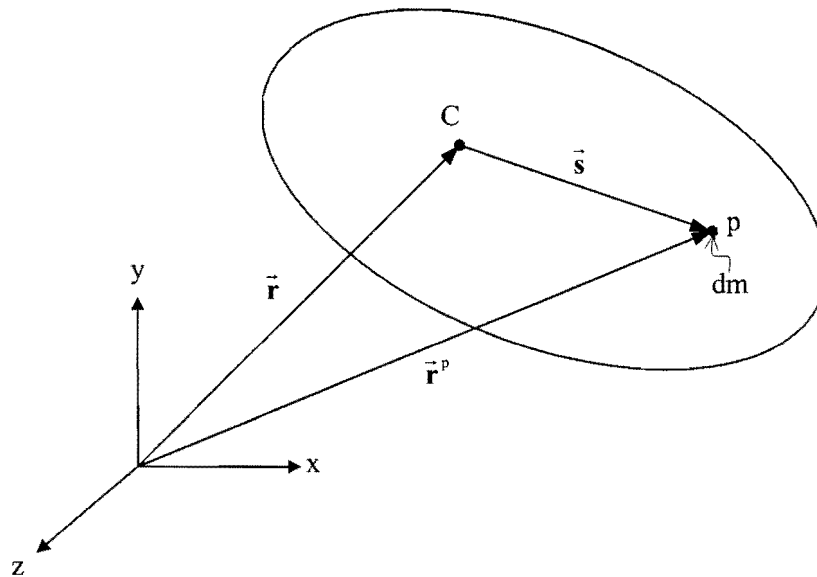
Figure A.2: A body as a collection of infinitesimally small masses (after [65]).

Since vector $\mathbf{r}^\mathrm{p}$ is the sum of two vectors $\mathbf{r}^\mathrm{p} = \mathbf{r} + \mathbf{s}$, it follows that

$$\mathbf{r} = \frac{1}{m} \int_{vol} \mathbf{r}^\mathrm{p}\, dm$$
$$= \frac{1}{m} \int_{vol} (\mathbf{r} + \mathbf{s})\, dm$$
$$= \mathbf{r} + \frac{1}{m} \int_{vol} \mathbf{s}\, dm$$

which implies that

$$\int_{vol} \mathbf{s}\, dm = 0 \tag{A.8}$$

and taking first and second order time derivatives gives

$$\int_{vol} \dot{\mathbf{s}}\, dm = 0 \tag{A.9}$$

and

$$\int_{vol} \ddot{\mathbf{s}}\, dm = 0 \tag{A.10}$$

A.2 Planar equations of motion

For the purposes of analyzing a planar machining center it is required to derive the planar equations of motion. Consider Figure A.3 showing an external force $\vec{\mathbf{f}}_i$ acting on the i-th particle of a system. For planar motion, the center of mass C of the system remains in the Gxy-plane, and coincides with the origin 0 of the body-fixed $\xi\eta\zeta$-coordinate system. The centroidal body-fixed $\xi\eta\zeta$-coordinate system is chosen in such a way that the ζ-axis is parallel to the z-axis. Note that the origin of the global xyz-reference frame is denoted by G.
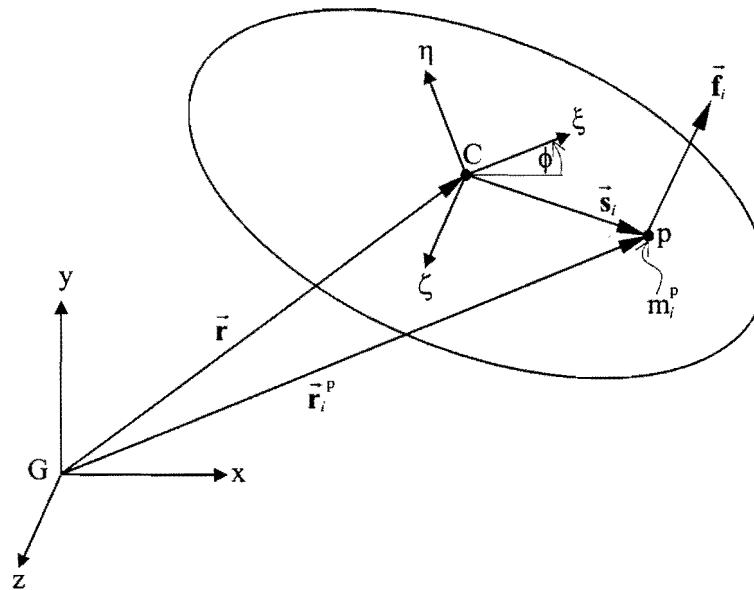
Figure A.3: Rigid body experiencing planar motion.

A.2.1 Planar translational equations of motion

The *first necessary condition* for the system in Figure A.3 to experience *planar motion* in the Gxy-plane, is that the external force $\vec{f}_i$ must be parallel to the xy-plane of motion, which is only possible if the z-component $f_{i(z)}$ of the force $\vec{f}_i$ is zero (see [65]).

More specifically, expression (A.6) gives the two *planar translational equations of motion*, for the system shown in Figure A.3:

$$m\ddot{x} = f_{(x)} \qquad (A.11)$$

and

$$m\ddot{y} = f_{(y)} \qquad (A.12)$$

with of course $f_{(z)} \equiv 0$.

Expressions (A.11) and (A.12) may also be combined in matrix form:

$$\begin{bmatrix} m & 0 \\ 0 & m \end{bmatrix} \begin{bmatrix} \ddot{x} \\ \ddot{y} \end{bmatrix} = \begin{bmatrix} f_{(x)} \\ f_{(y)} \end{bmatrix} \qquad (A.13)$$

with   m representing the total mass of the system,

$\ddot{x}$ and $\ddot{y}$ respectively representing the x- and y-accelerations of the center of mass C, and

$f_{(x)}$ and $f_{(y)}$ respectively representing the x- and y-components of the total external force acting on the mass system.

A.2.2 Planar rotational equations of motion

The *second necessary condition* for the system in Figure A.3 to experience *planar motion*, is that it is only to rotate about the ζ-axis (see [65]). This rotation is due to the *resultant moment* about C of the external forces acting on the system. Since the ζ-axis is parallel to the z-axis, the global representation of the resultant moment of the forces about C must, for planar motion, only have a z-component.

Consider the moment about G as a result of the external forces $\vec{f}_i$ and $\sum_{j=1}^{p}\vec{f}_{ij}$ acting on particle i (see Figure A.3):

$$\vec{n}_i^{\,G} = \vec{r}_i^{\,p} \times (\vec{f}_i + \sum_{j=1}^{p}\vec{f}_{ij}) \qquad (A.14)$$

With particle i located in the global reference frame by

$$\vec{r}_i^{\,p} = \vec{r} + \vec{s}_i \qquad (A.15)$$

the global representation of expression (A.15) is

$$r_i^{\,p} = r + s_i \qquad (A.16)$$

Hence, expression (A.14) may be represented in the global reference frame by

$$n_i^{\,G} = \widetilde{r}_i^{\,p}(f_i + \sum_{j=1}^{p}f_{ij}) \qquad (A.17)$$

with $\widetilde{r}_i^{\,p}$ representing the expansion of $r_i^{\,p}$ into a skew symmetric matrix, i.e.:

$$\widetilde{r}_i^{\,p} = \begin{bmatrix} 0 & -z^p & y^p \\ z^p & 0 & -x^p \\ -y^p & x^p & 0 \end{bmatrix} \qquad (A.18)$$

Substituting expression (A.3) into (A.17) yields

$$n_i^{\,G} = \widetilde{r}_i^{\,p}(f_i + \sum_{j=1}^{p}f_{ij}) = \widetilde{r}_i^{\,p}(m_i^p\ddot{r}_i^{\,p}) \qquad (A.19)$$

Summing expression (A.19) over all $i = 1,2,...,p$, gives the sum of the moments with respect to G as

$$n^{\,G} = \sum_{i=1}^{p}\widetilde{r}_i^{\,p}f_i + \sum_{i=1}^{p}\sum_{j=1}^{p}\widetilde{r}_i^{\,p}f_{ij} = \sum_{i=1}^{p}\widetilde{r}_i^{\,p}(m_i^p\ddot{r}_i^{\,p}) \qquad (A.20)$$

However, since $\widetilde{r}_i^{\,p}f_{ij} = -\widetilde{r}_i^{\,p}f_{ji}$ (see expressions (A.4) and (A.5)), it follows that $\sum_{i=1}^{p}\sum_{j=1}^{p}\widetilde{r}_i^{\,p}f_{ij} = 0$.

Furthermore, expression (A.16) implies that

$$\widetilde{r}_i^{\,p} = \widetilde{r} + \widetilde{s}_i \qquad (A.21)$$

Expression (A.20) may therefore be written as

$$\mathbf{n}^G = \widetilde{\mathbf{r}}\mathbf{f} + \sum_{i=1}^{P}\widetilde{\mathbf{s}}_i\mathbf{f}_i = \sum_{i=1}^{P}m_i^P\widetilde{\mathbf{r}}_i^P\ddot{\mathbf{r}}_i^P \tag{A.22}$$

where $\sum_{i=1}^{P}\widetilde{\mathbf{s}}_i\mathbf{f}_i = \mathbf{n}$ the sum of the moments of the external forces about C.

For a continuous body, m_i^P represents an infinitesimally small mass element dm, i.e. $m_i^P \equiv dm$, and therefore expression (A.22) becomes

$$\mathbf{n}^G = \widetilde{\mathbf{r}}\mathbf{f} + \mathbf{n} = \int_{vol}\widetilde{\mathbf{r}}^P\ddot{\mathbf{r}}^P dm \tag{A.23}$$

with the position of the center of mass of the continuum $\mathbf{r}$ given by expression (A.7).

Since the center of mass of the body under consideration is to remain in the Gxy-plane, the z-component of $\mathbf{r}$ is identically equal to zero, i.e. $\mathbf{r} = [x, y, 0]^T$. The expansion of $\mathbf{r}$ into a skew-symmetric matrix is therefore

$$\widetilde{\mathbf{r}} = \begin{bmatrix} 0 & 0 & y^P \\ 0 & 0 & -x^P \\ -y^P & x^P & 0 \end{bmatrix} \tag{A.24}$$

The force, $\mathbf{f}$ in expression (A.23) is the global representation of the resultant external force acting on the body, and $\mathbf{n}^G$ and $\mathbf{n}$ respectively represent the resultant moment of the external forces acting on the body about the origin of the global reference frame G, and the center of mass of the body C.

In satisfying the second necessary condition for planar motion, the expansion of expression (A.23) may only yield a single non-zero scalar equation corresponding to the z-component of the resultant moment acting on the body with respect to G:

$$n_{(z)}^G = xf_{(y)} - yf_{(x)} + n_{(z)} = \left[\int_{vol}\widetilde{\mathbf{r}}^P\ddot{\mathbf{r}}^P dm\right]_{(z)} \tag{A.25}$$

From expression (A.16) it follows that for a continuous body

$$\mathbf{r}^P = \mathbf{r} + \mathbf{s} = \begin{bmatrix} x \\ y \\ z \end{bmatrix} + \begin{bmatrix} s_{(x)} \\ s_{(y)} \\ s_{(z)} \end{bmatrix} \tag{A.26}$$

with first and second time derivatives given by $\dot{\mathbf{r}}^P = \dot{\mathbf{r}} + \dot{\mathbf{s}} = [\dot{x}, \dot{y}, \dot{z}]^T + [\dot{s}_{(x)}, \dot{s}_{(y)}, \dot{s}_{(z)}]^T$ and $\ddot{\mathbf{r}}^P = \ddot{\mathbf{r}} + \ddot{\mathbf{s}} = [\ddot{x}, \ddot{y}, \ddot{z}]^T + [\ddot{s}_{(x)}, \ddot{s}_{(y)}, \ddot{s}_{(z)}]^T$ respectively.

Substituting expression (A.26) into the right hand side of expression (A.25) results in

$$n_{(z)}^{G} = xf_{(y)} - yf_{(x)} + n_{(z)} = \left[\int_{vol} (\tilde{\mathbf{r}} + \tilde{\mathbf{s}})(\ddot{\mathbf{r}} + \ddot{\mathbf{s}}) dm \right]_{(z)} \tag{A.27}$$

From expressions (A.8) and (A.10) it follows that $\int_{vol} \tilde{\mathbf{s}} \ddot{\mathbf{r}} \, dm = \mathbf{0}$ and $\int_{vol} \tilde{\mathbf{r}} \ddot{\mathbf{s}} \, dm = \mathbf{0}$, and therefore expression (A.27) reduces to

$$n_{(z)}^{G} = xf_{(y)} - yf_{(x)} + n_{(z)} = x(m\ddot{y}) - y(m\ddot{x}) + \int_{vol} s_{(x)} \ddot{s}_{(y)} - s_{(y)} \ddot{s}_{(x)} \, dm \tag{A.28}$$

From expressions (A.11) and (A.12) it also follows that $xf_{(y)} - yf_{(x)} = x(m\ddot{y}) - y(m\ddot{x})$, and therefore (A.28) becomes

$$n_{(z)} = \int_{vol} [s_{(x)} \ddot{s}_{(y)} - s_{(y)} \ddot{s}_{(x)}] \, dm \tag{A.29}$$

For general three-dimensional motion, the above argument would give

$$\mathbf{n} = \int_{vol} \tilde{\mathbf{s}} \ddot{\mathbf{s}} \, dm \tag{A.30}$$

where $\tilde{\mathbf{s}}$ represents a skew-symmetric matrix of the form

$$\tilde{\mathbf{s}} = \begin{bmatrix} 0 & -s_{(z)} & s_{(y)} \\ s_{(z)} & 0 & -s_{(x)} \\ -s_{(y)} & s_{(x)} & 0 \end{bmatrix} \tag{A.31}$$

Nikravesh [65] shows that

$$\tilde{\mathbf{s}} \ddot{\mathbf{s}} = -\tilde{\mathbf{s}} \tilde{\mathbf{s}} \dot{\omega} - \tilde{\omega} \tilde{\mathbf{s}} \tilde{\mathbf{s}} \omega \tag{A.32}$$

with $\omega = [\omega_{(x)}, \omega_{(y)}, \omega_{(z)}]^{T}$ the global representation of the angular velocity vector.

In agreement with the second necessary condition for planar motion, the body shown in Figure A.3 that rotates only about the ζ-axis, has an angular velocity vector of which only the z-component may be non-zero, i.e.:

$$\omega = [0, 0, \omega_{(z)}]^{T} \tag{A.33}$$

with $\omega_{(z)} = \dot{\phi}$ (see Figure A.3).

Consequently, the skew-symmetric matrix $\tilde{\omega}$ in (A.32) is given by:

$$\tilde{\omega} = \begin{bmatrix} 0 & -\dot{\phi} & 0 \\ \dot{\phi} & 0 & 0 \\ 0 & 0 & 0 \end{bmatrix} \tag{A.34}$$

The time derivative of expression (A.33) is

$$\dot{\omega} = [0, 0, \dot{\omega}_{(z)}]^{T} \tag{A.35}$$

with $\dot{\omega}_{(z)} = \ddot{\phi}$.

Hence, by substituting expressions (A.33) - (A.35) into the right hand side of expression (A.32), and isolating the third component of the resultant vector, gives for planar motion:

$$s_{(x)}\ddot{s}_{(y)} - s_{(y)}\ddot{s}_{(x)} = \ddot{\phi}(s_{(x)}^2 + s_{(y)}^2)$$

(A.36)

Since for planar motion, the ζ-axis is parallel to the z-axis (see Figure A.3), it follows that:

$$s_{(x)}\ddot{s}_{(y)} - s_{(y)}\ddot{s}_{(x)} = \ddot{\phi}(s_{(x)}^2 + s_{(y)}^2) = \ddot{\phi}(s_{(\xi)}^2 + s_{(\eta)}^2)$$

(A.37)

Substituting expression (A.37) into expression (A.29) finally gives

$$n_{(z)} = \ddot{\phi} \int_{vol} (s_{(\xi)}^2 + s_{(\eta)}^2)\, dm$$

(A.38)

The integral in expression (A.38):

$$j_{\zeta\zeta} = \int_{vol} (s_{(\xi)}^2 + s_{(\eta)}^2)\, dm$$

(A.39)

is called the mass moment of inertia of the body about the ζ-axis through C.

Finally substituting expression (A.39) into expression (A.38) gives the *planar rotational equation of motion*:

$$n_{(z)} = \ddot{\phi}\, j_{\zeta\zeta}$$

(A.40)

Note that the global representation of the angular velocity vector $\omega = [0,0,\dot{\phi}]^T$ is equal to the local representation of the angular velocity vector $\omega' = [0,0,\dot{\phi}]^T$.

Appendix B

B FLOWCHART OF THE OCAS TRAJECTORY-

PLANNING METHODOLOGY

Figure B.1: OCAS flowchart.

---

* See detailed flowchart in Figure B.2

Determine the dependence of the curve length on parameter t (see Sections 3.1.1.3 & 3.3)

Isolate nodal point N_{MID} (see Section 3.3.2)

Determine time instant T_{MID} and the 4 unknown coefficients of the cubic polynomial function in time $s_I(t)$ specifying $\dot{s}_I(T_{MID}) = v^*$ (see Section 3.1.1.3)

Determine initial acceleration $\ddot{s}_I(0)$ (expression (3.25))

Is central speed v^* attained at nodal point N_{MID} such that $\ddot{s}_I(0) \leq \ddot{s}_{ALLOW}$

No — Determine time instant T_{MID} and the 4 unknown coefficients of the cubic polynomial function in time $s_I(t)$ specifying $\ddot{s}_I(0) = \ddot{s}_{ALLOW}$ (see Section 3.3.2.2)

Determine v_{MID} (expression (3.34))

Determine time instant T_{III} and the 4 unknown coefficients of the cubic polynomial function in time $s_{III}(t)$ specifying $\dot{s}_{III}(T_{MID}) = v_{MID}$ (see Section 3.3.2.2)

Yes — Set $i = 1$

Shift node N_I to coincide with node N_{MID-i}

Determine time instant T_I and the 4 unknown coefficients of the cubic polynomial function in time $s_I(t)$ specifying $\dot{s}_I(T_I) = v^*$ (see Section 3.1.1.3)

Determine initial acceleration $\ddot{s}_I(0)$ (expression (3.25))

Is central speed v^* attained at nodal point N_I such that $\ddot{s}_I(0) \leq \ddot{s}_{ALLOW}$

Yes — Set $i = i + 1$

No — Shift node N_I to coincide with node $N_{MID-i+1}$

Determine time instant T_I and the 4 unknown coefficients of the cubic polynomial function in time $s_I(t)$ specifying $\dot{s}_I(T_I) = v^*$ (see Section 3.1.1.3)

Set $j = 1$

Shift node N_{II} to coincide with node N_{MID+j}

Determine time instant T_{II} (see Section 3.3.1)

Determine time instant T_{III} and the 4 unknown coefficients of the cubic polynomial function in time $s_{III}(t)$ specifying $\dot{s}_{III}(T_{II}) = v^*$ (see Section 3.3.1)

Determine final acceleration $|\ddot{s}_{III}(T_{III})|$ (expression (3.41))

Is deceleration from v^* at nodal point N_{II} to zero at nodal point N_{III} such that $|\ddot{s}_{III}(T_{III})| \leq \ddot{s}_{ALLOW}$ possible?

Yes — Set $j = j + 1$

No — Shift node N_{II} to coincide with node $N_{MID+j-1}$

Determine time instant T_I and the 4 unknown coefficients of the cubic polynomial function in time $s_I(t)$ specifying $\dot{s}_I(T_I) = v^*$ (see Section 3.1.1.3)
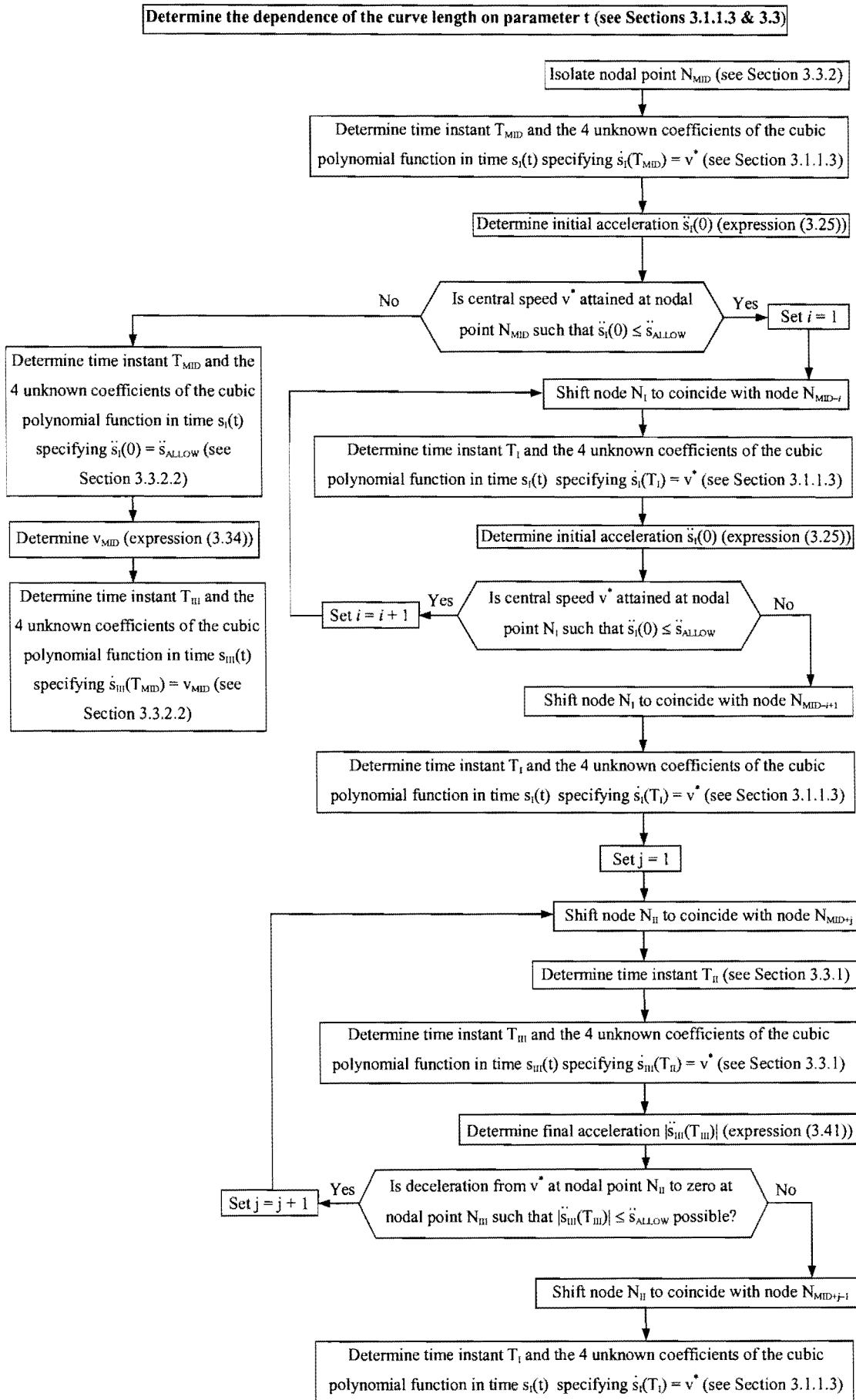
Figure B.2: Detail flowchart of determining the dependence of the curve length on t.

C THE LFOPC MATHEMATICAL OPTIMIZATION

ALGORITHM

C.1 Background

The dynamic trajectory method (also called the "leap-frog" method) for the unconstrained minimization of a scalar function $F(X)$ of n real variables represented by the vector $X = [X_1, X_2, ..., X_n]^T$ was originally proposed by Snyman [64, 74]. The original algorithm has recently been modified to handle constraints by means of a penalty function formulation. (Snyman et al [75, 76]). The method possesses the following characteristics:

- It uses only function *gradient* information $\nabla F(X)$.

- *No* explicit *line searches* are performed.

- It is extremely *robust* and handles steep valleys and discontinuities in functions and gradients with ease.

- The algorithm seeks *low local minimum* and can therefore be used as a basic component in a methodology for global optimization.

- The method is not as efficient as classical methods on smooth and near-quadratic functions.

C.2 Basic dynamic model

The algorithm is modeled on the motion of a particle of unit mass in a n-dimensional conservative force field with potential energy at X given by $F(X)$. At X, the force on the particle is given by

$$a = \ddot{X} = -\nabla F(X)$$

(C.1)

from which it follows that for the time interval $[0, t]$:

$$\frac{1}{2}\|\dot{X}(t)\|^2 - \frac{1}{2}\|X(0)\|^2 = F(X(0)) - F(X(t))$$

$$T(t) - T(0) = F(0) - F(t)$$

(C.2)

---

or

$$F(t) + T(t) = constant \text{ \{conservation of energy\}}$$

Note that since $\Delta F = -\Delta T$ as long as T increases F decreases. This forms the basis of the dynamic algorithm.

C.3 LFOP: Basic algorithm for unconstrained problems

Given $F(\mathbf{X})$ and a starting point $\mathbf{X}(0) = \mathbf{X}^0$

- Compute the dynamic trajectory by solving the initial value problem (IVP)

$$\ddot{\mathbf{X}}(t) = -\nabla F(\mathbf{X}(t))$$
$$\dot{\mathbf{X}}(0) = \mathbf{0}, \quad \mathbf{X}(0) = \mathbf{X}^0 \qquad (C.3)$$

- Monitor $\dot{\mathbf{X}}(t) = \mathbf{v}(t)$. Clearly as long as $T = \frac{1}{2}\|\mathbf{v}(t)\|^2$ increases $F(\mathbf{X}(t))$ decreases and descent follows as required

- When $\|\mathbf{v}(t)\|$ decreases apply some interfering strategy to extract energy and thereby increasing the likelihood of descent.

- In practice a numerical integration "leap-frog" scheme is used to integrate the IVP (C.3). Compute for $k = 0,1,2,...$ and time step Δt

$$\mathbf{X}^{k+1} = \mathbf{X}^k + \mathbf{v}^k \Delta t$$
$$\mathbf{v}^{k+1} = \mathbf{v}^k + \mathbf{a}^{k+1} \Delta t \qquad (C.4)$$

where $\mathbf{a}^k = -\nabla F(\mathbf{X}^k), \quad \mathbf{v}^0 = \frac{1}{2}\mathbf{a}^0 \Delta t$

- A typical interfering strategy is:

If $\|\mathbf{v}^{k+1}\| \geq \|\mathbf{v}^k\|$ continue

else

$$set \ \mathbf{v}^k = \frac{\mathbf{v}^{k+1} + \mathbf{v}^k}{4}, \quad \mathbf{x}^k = \frac{\mathbf{x}^{k+1} + \mathbf{x}^k}{2} \qquad (C.5)$$

compute new $\mathbf{v}^{k+1}$ and continue.

- Further heuristics are used to determine an initial Δt, to allow for magnification and reduction of Δt, and to control the step size.

C.4   LFOPC: Modification for constrained problems

Constrained optimization problems are solved by the application, in three phases, of LFOP to a penalty function formulation of the problem [64, 76]. Given a function $F(X)$, $X \in \Re^n$ with equality constraints $H_i(X) = 0$ ($i = 1,2,...,p < n$) and inequality constraints $C_j(X) \leq 0$ ($j = 1,2,...,m$) and penalty parameter $\mu \gg 0$, the penalty function problem is to minimize

$$P(x,\mu) = F(X) + \sum_{i=1}^{p} \mu H_i^2(X) + \sum_{j=1}^{m} \beta_j C_j^2(X) \qquad (C.6)$$

$$\text{where } \beta_j = \begin{cases} 0 & \text{if } G_j(X) \leq 0 \\ \mu & \text{if } G_j(X) > 0 \end{cases}$$

Phase 0: Given some X^0, then with the overall penalty parameter $\mu = \mu_0 (= 10^2)$ apply LFOP to $P(X,\mu_0)$ to give $X^*(\mu_0)$

Phase 1: With $X^0 = X^*(\mu_0)$, $\mu = \mu_1 (= 10^4)$ apply LFOP to $P(X,\mu_1)$ to give $X^*(\mu_1)$ and identify active constraints $i_a = 1,2,...,n_a$; $g_{i_a}(X^*(\mu_1)) > 0$

Phase 2: With $X^0 = X^*(\mu_1)$, use LFOP to minimize

$$P_a(X,\mu_1) = \sum_{i=1}^{p} \mu_1 H_i^2(X) + \sum_{i_a=1}^{n_a} \mu_1 g_{i_a}^2(X) \qquad (C.7)$$

to give X^*.

.

D PHYSICAL SPECIFICATION FOR SIMULATION AND OPERATIONAL CONSTRAINTS OF THE TEST-MODEL

D.1 Introduction

This Appendix describes the physical specifications required for simulation of the motion of the test-model. In addition it deals in detail with the incorporation of further physical constraints to prevent mechanical interference during the operation of the test-model.

D.2 Physical specifications for simulation of the test-model

A photograph of the test-model is shown in Figure D.1. Figure D.2 is a scaled two-dimensional view of the test-model where the eight bodies comprising the mechanical system are numbered in accordance with Figure 2.5.
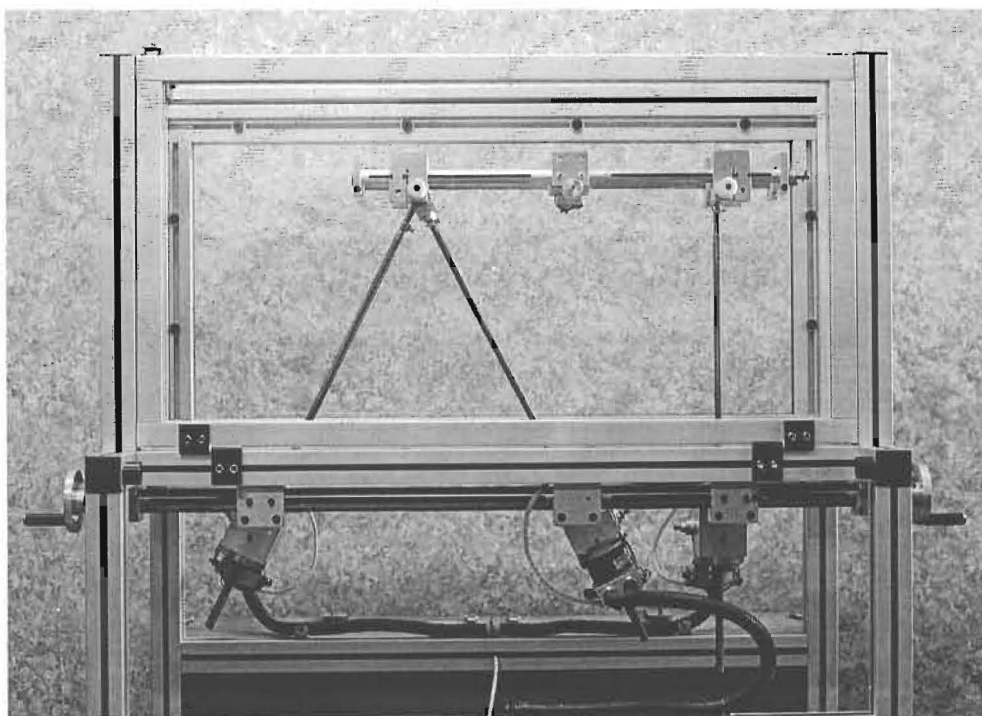
Figure D.1: Photograph of the test-model

Figure D.2: Geometrical representation of the test-model as a mechanical system of eight bodies.

D.2.1 Operational geometry

Note that the same five design variables $\mathbf{X} = [X_1, X_2, X_3, X_4, X_5]^T$, introduced in Section 4.2.1, are used here to describe the adjustable operational geometry of the physical test-model.

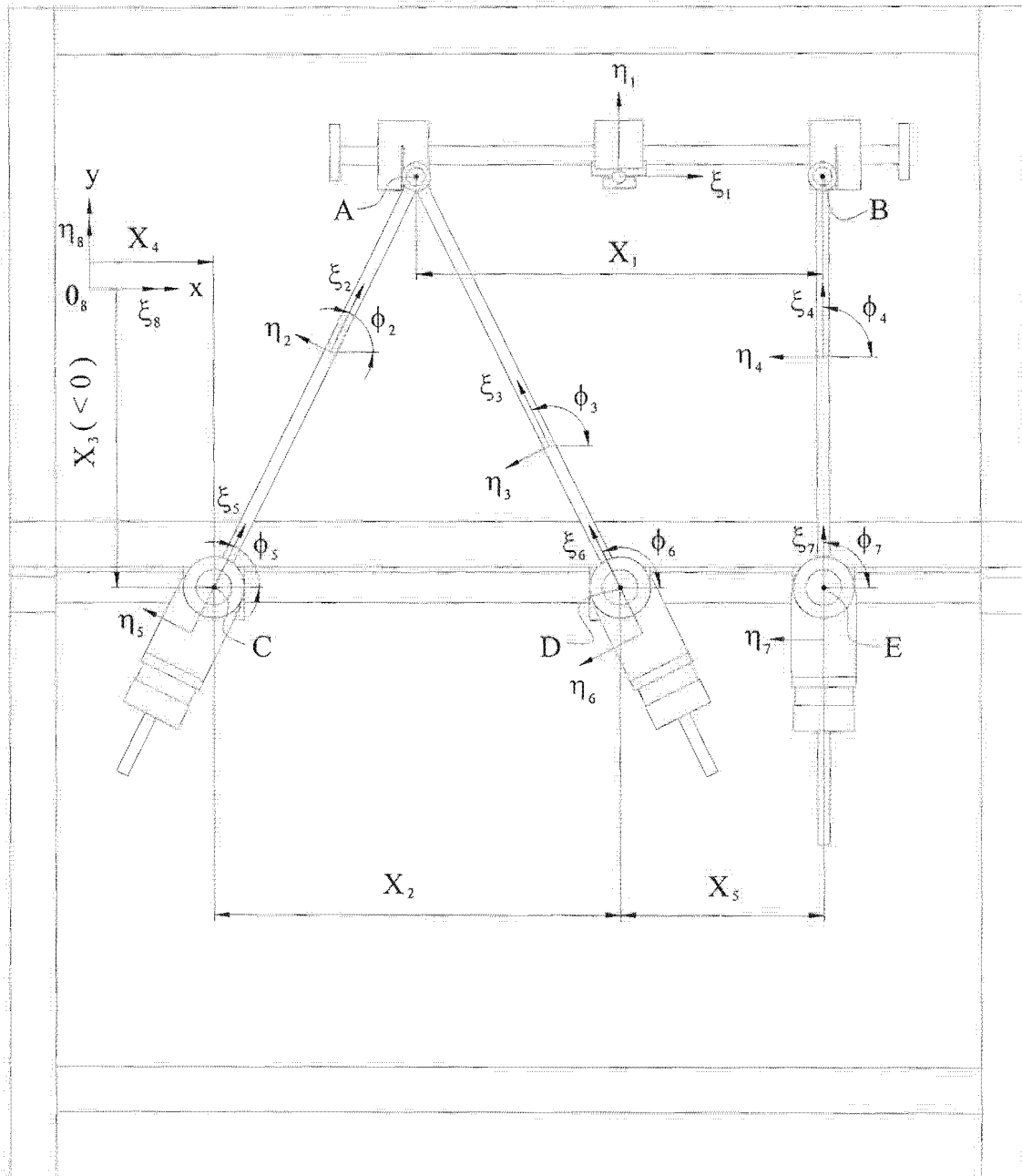Design variable X_1 indicates the distance between revolute joints A and B on the moving platform. The center of mass of the moving platform is taken as midway between revolute joints A and B, hence

$$\xi_1^A = -\frac{X_1}{2} \text{ and } \xi_1^B = \frac{X_1}{2}.$$

Note that the absolute position of revolute joint D on the base twin tubular rails is fixed. Design variables X_2, X_3 and X_4 therefore determine the relative position of the global $0xy$-coordinate system, relative to the positionally fixed revolute joint D. More specifically, $x = 0$ is at $-|X_2| - X_4$ relative to revolute joint D, and $y = 0$ is at $-X_3$ relative to revolute joint D.

For the fixed workpiece case of Section 2.4.1 and 2.6.4.2.1, the prescribed tool path is specified in terms of the global $0xy$- coordinate system. Hence, a change in design variables X_2, X_3 and X_4 will shift the position of the prescribed tool path relative to revolute joint D.

The use of the test-model is currently limited to the execution of prescribed paths specified in the fixed workpiece. With an extension of the test-model capabilities, it would also be possible to demonstrate the machining operation for the fixed tool scenario as explained in Sections 2.4.2 and 2.6.4.2.2.

For the fixed tool case, the fixed tool tip traces the prescribed tool path specified in terms of local $0_1\xi_1\eta_1$ -coordinate system, and a change in design variables X_2, X_3 and X_4 will vary the position of the fixed tool tip relative to revolute joint D.

Finally design variable X_5 indicates the relative distance between revolute joints D and E, so that for simulation purposes, the global positions of revolute joints C, D and E are given by expression (4.3):

$(x,y)_C = (X_4, X_3)$, $(x,y)_D = ((X_4 + X_2),(X_3))$ and $(x,y)_E = ((X_4 + X_2 + X_5),(X_3))$.

D.2.2 Local coordinates

Given a prescribed tool path, as well as an operational geometry $\mathbf{X} = [X_1, X_2, X_3, X_4, X_5]^T$, the physical motion of the test-model platform may be simulated to find the overall maximum magnitudes along the path of the individual actuator forces f_k, $k = 1,2,3$. This objective function (expression (4.4)) is formally defined in Section 4.2.2.

In evaluating the objective function (see Section 4.3.1), the inverse kinematic analysis of the test-model requires that the global coordinates of revolute joints C, D and E, as well as the local coordinates ξ_1^A,

---

ξ_1^B, ξ_2^A, ξ_3^A, ξ_4^B, ξ_5^C, ξ_6^D and ξ_7^E be known. The global coordinates of revolute joints C, D and E are given by substituting the specific values of the relevant design variables into expression (4.3) (see also the last paragraph of Section D.2.1). The value of design variable X_1 fixes the values of local coordinates ξ_1^A and ξ_1^B as explained in the second paragraph of Section D.2.1.

Corresponding to Section 2.3, the origin of each local $0_i \xi_i \eta_i$-coordinate system, $i = 1,2,...,7$ is chosen to coincide with the center of mass of respective bodies $1,2,...,7$. Using the known dimensions and densities of the components that make up each individual body of the test-model, the positions of each body's center of mass may be calculated. With reference to Figure D.2, the following local coordinates of the test-model are fixed:

$$\xi_2^A = 0.1904\,\text{m} \qquad \xi_3^A = 0.2921\,\text{m} \qquad \xi_4^B = 0.1751\,\text{m}$$
$$\xi_5^C = 0.050\,\text{m} \qquad \xi_6^D = 0.050\,\text{m} \qquad \xi_7^E = 0.050\,\text{m} \tag{D.1}$$

The evaluation of the objective function, furthermore involves solving the inverse dynamic equations of motion (expression (2.124)) for the unknown LaGrange multipliers and actuator forces **ff** (see Section 4.3.1).

D.2.3 Gravitational and frictional external forces

The specific entries of the constant diagonal mass matrix **M** in expression (2.124) consist of the specific masses and moments of inertia of the individual bodies of the test-model (see **Chapter 5**), and may also be determined using the known dimensions and densities of the parts constituting each body. With reference to the eight numbered bodies of Figure D.2, the entries of the mass matrix **M** are

$$\mathbf{M} = \text{diag}[\mathbf{M}_1^T, \mathbf{M}_2^T, ..., \mathbf{M}_8^T] \tag{D.2}$$

with

$$\mathbf{M}_1 = [2.1246, 2.1246, 0.0829]^T$$
$$\mathbf{M}_2 = [0.7671, 0.7671, 0.0355]^T$$
$$\mathbf{M}_3 = [0.5696, 0.5696, 0.0263]^T$$
$$\mathbf{M}_4 = [0.8341, 0.8341, 0.0377]^T$$
$$\mathbf{M}_5 = \mathbf{M}_6 = \mathbf{M}_7 = [3.0725, 3.0725, 6.17\times10^{-3}]^T$$
$$\mathbf{M}_8 = [0, 0, 0]^T$$

and specified in SI units.

The vector of known external forces $\mathbf{g}^{(k)}$ in expression (2.124) consists of the cutting force $\mathbf{g}_1^{(\text{cutting f})}$ acting on the moving platform (body 1) and the weights of individual bodies comprising the planar Gough-Stewart platform $\mathbf{g}_i^{(\text{gravity})}$, $i = 1,2,...,7$ (see expression (2.124)).

With the masses of the individual bodies of the platform test-model known (see **Chapter 5**), their respective weights follow from expression (2.104), i.e.:

$$\mathbf{g}_1^{(\text{gravity})} = [0, -20.842 \text{ N}, 0]^T$$

$$\mathbf{g}_2^{(\text{gravity})} = [0, -7.526 \text{ N}, 0]^T$$

$$\mathbf{g}_3^{(\text{gravity})} = [0, -5.588 \text{ N}, 0]^T$$

$$\mathbf{g}_4^{(\text{gravity})} = [0, -8.182 \text{ N}, 0]^T$$

$$\mathbf{g}_5^{(\text{gravity})} = \mathbf{g}_6^{(\text{gravity})} = \mathbf{g}_7^{(\text{gravity})} = [0, -30.141 \text{ N}, 0]^T$$

The platform test-model represents a special case of the fixed work-piece scenario, with a zero tool length $\eta_1^P = 0$ (see Section 2.4.1). This is because the pen, used for demonstration purposes, is mounted on the moving platform (body 1) at local coordinates $(\xi, \eta)_1 = (0,0)$.

The cutting force $\mathbf{g}_1^{(\text{cutting f})}$ of the fixed workpiece case is described in Section 2.6.4.2.1. Note that the cutting force is modeled as a friction force, the magnitude of which is linearly dependent on the magnitude of the cutting velocity (see expression (2.107)). The moving platform of the test-model experiences frictional forces, not only as a result of the pen tracing the prescribed tool path on the Perspex side panel, but also because of the spring loaded lateral stiffeners (see **Chapter 5**) sliding against the Perspex side panels during the motion of the moving platform.

The magnitude of the resultant frictional force may be measured by means of a simple experiment using a spring balance. In particular, the moving platform is disconnected from the three actuator legs, and hung unto a string. The experiment is executed by connecting the moving platform to the spring balance, and pulling the moving platform in a horizontal direction while the pen and spring loaded lateral stiffeners slide against the Perspex side panels. While moving at a constant speed along a known distance, the "constant speed motion" time and spring balance reading are measured.

Since the string supporting the moving platform is very long (1.38 m) compared to the horizontal motion (80 mm) of the moving platform, the vertical displacement of the moving platform may be neglected, hence the reading on the spring balance approximately equals the resultant frictional force.
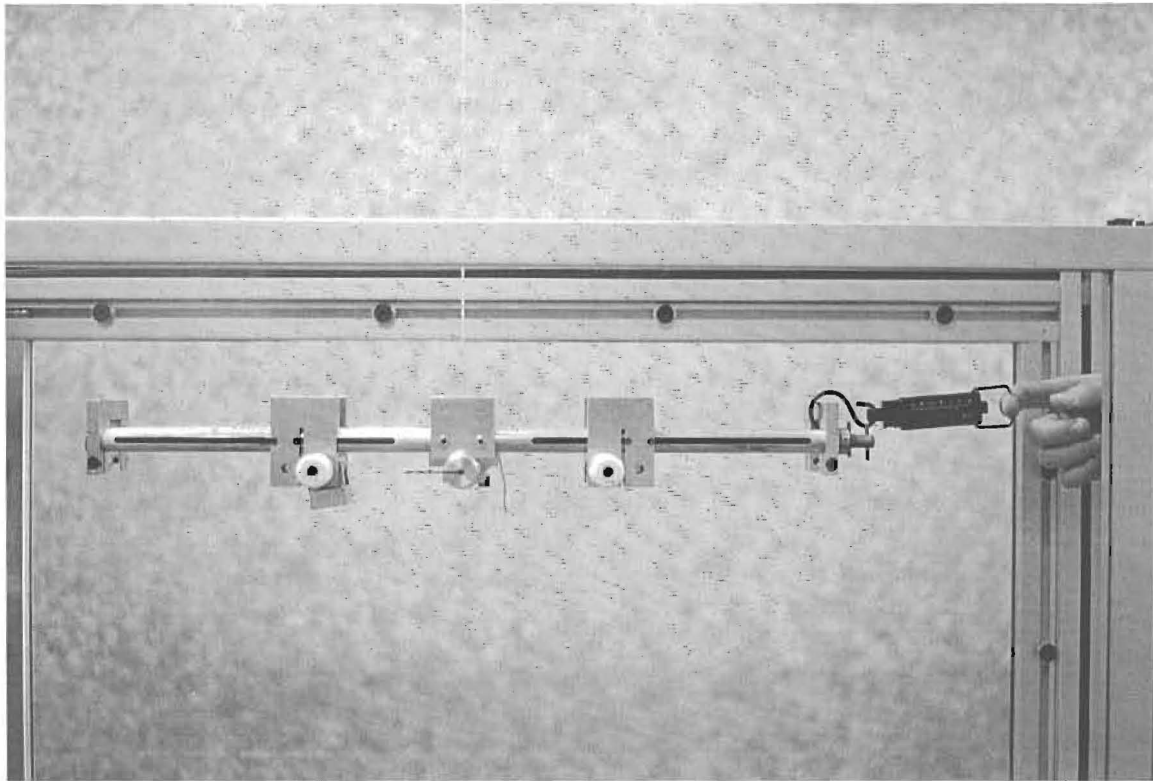
Figure D.3: The experimental setup for measuring the frictional force using a spring balance.

Figure D.3 shows a photograph of the experimental setup used to measure the resultant frictional force on the moving platform using the spring balance. Table D.1 lists the readings that were obtained, as well as the calculation of the average cutting force constant, C_{cut}. The reasonable assumption is made here that the friction forces acting on the moving platform may be merged and simulated as a single cutting force (see Section 2.6.4.2.1). In order to determine the average cutting force constant, C_{cut} used in expression (2.107), the experimental constant speed translations listed in Table D.1 were also measured and timed to yield the magnitudes of the constant speeds.

Spring balance reading No.	Resultant friction force [N]	Distance [mm]	Time [s]	Constant speed [m/s]	C_{cut} [Ns/m]
1	7.85	80 mm	3.74	0.02139	366.894
2	9.81	80 mm	1.54	0.05195	188.843
3	11.28	80 mm	1.13	0.07080	159.351
4	8.34	80 mm	3.57	0.02241	372.106
5	9.81	80 mm	1.23	0.06504	150.829
6	10.3	80 mm	1.39	0.05755	178.971
7	11.77	80 mm	0.77	0.10390	113.306
8	8.34	80 mm	3.17	0.02524	330.413

9	9.81	80 mm	1.42	0.056338	174.128
10	11.28	80 mm	1.39	0.05755	196.016
11	10.79	80 mm	1.17	0.06838	157.818
12	7.85	80 mm	3.43	0.02332	336.483
13	8.83	80 mm	4.16	0.01923	459.108
14	19.81	80 mm	1.58	0.05063	193.748
15	8.34	80 mm	4.89	0.01636	509.691
16	9.81	80 mm	1.71	0.04678	209.689
17	11.28	80 mm	1.01	0.07921	142.429
				Average	249.4

Table D.1: Experimental readings in determining the average "cutting force constant".

The average value for C_{cut} as determined from the experimental measurements is 249.4 . The specific value used in all for the simulations of the motion of the platform test-model, is 250.

D.3 Specification of the physical operational constraints of the test-model

In illustrating the optimization methodology, the configurational constraints (expressions (4.5) and (4.6)), relating to dimensional limitations of the individual components of the manipulator, were the only inequality constraints specified to ensure a feasible design for the *hypothetical* planar machining center. For the *real* test-model some of the physical limitations of the planar mechanism may also be incorporated in these configurational constraints, while others, specifically those relating to the prevention of *mechanical interference*, must be dealt with separately.

In this section, the latter constraints are first explained in general terms below, followed by a categorization of the test-model physical limitations, and an explanation of the necessary inequality constraints with which a feasible test-model design may be obtained.

D.3.1 Inequality constraint specification for the prevention of mechanical interference

In general the instantaneous perpendicular distance between a line in body j and a point in body *i* may easily be determined for the special case where the line is parallel to the ξ-axis of body j.

Consider for example Figure D.4 showing the schematic representation of bodies *i* and j experiencing planar motion.
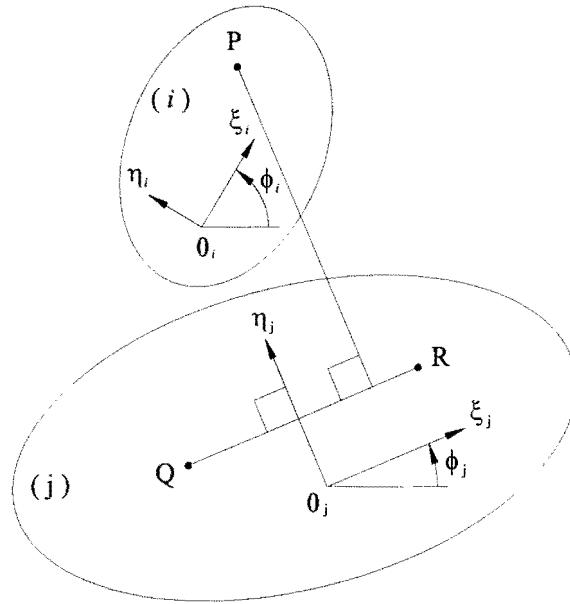
Figure D.4: Schematic representation of bodies i and j experiencing planar motion.

It is assumed here that the following are known:

1. the *instantaneous* positions and orientations of respective bodies i, $\mathbf{q}_i = [\mathbf{r}^T, \phi]_i^T = [x, y, \phi]_i^T$, and

   j, $\mathbf{q}_j = [\mathbf{r}^T, \phi]_j^T = [x, y, \phi]_j^T$, as defined by expression (2.2).

2. the *fixed* local coordinates of point P in body i, $\left(\xi^P, \eta^P\right)_i$, and

3. the *fixed* local η-coordinate of line QR in body j, η_j^{QR}

Using the transformation given by expression (2.1), the *instantaneous* global x- and y coordinates of point P may be determined, i.e.,

$$x^P = x_i + \xi_i^P \cos\phi_i - \eta_i^P \sin\phi_i$$

$$y^P = y_i + \xi_i^P \sin\phi_i + \eta_i^P \cos\phi_i \tag{D.3}$$

The *instantaneous* η-coordinate of point P relative to the local coordinate system of body j, η_j^P, may also be determined using the *inverse* of the transformation given by expression (2.1), i.e.,

$$\mathbf{s}_j'^P = \mathbf{A}_j^{-1}\mathbf{s}_j^P \tag{D.4}$$

with $\mathbf{A}_j^{-1} = \begin{bmatrix} \cos\phi_j & \sin\phi_j \\ -\sin\phi_j & \cos\phi_j \end{bmatrix}$.

Substituting $\mathbf{s}_j^P = \mathbf{r}_j^P - \mathbf{r}_j$ (see expression (2.1)) into expression (D.4), yields

$$\begin{bmatrix} \xi^P \\ \eta^P \end{bmatrix}_j = \begin{bmatrix} \cos\phi_j & \sin\phi_j \\ -\sin\phi_j & \cos\phi_j \end{bmatrix} \begin{bmatrix} x^P - x_j \\ y^P - y_j \end{bmatrix}$$

and therefore

$$\eta_j^P = (y^P - y_j)\cos\phi_j - (x^P - x_j)\sin\phi_j \qquad (D.5)$$

Hence, the instantaneous perpendicular distance between line QR and point P is given by

$$\delta_{P-QR} = \eta_j^P - \eta_j^{QR} \qquad (D.6)$$

Note that for the relative positioning of bodies i and j shown in Figure D.4, δ_{P-QR} will become *smaller* as the two bodies move closer to each other. Hence, if the two bodies shown in Figure D.4 move relative to each other over a time interval $[0,T] = [0, T_{Mtime}]$, the instantaneous perpendicular distance δ_{P-QR} (expression (D.6)) may be monitored at discrete time instants t_j to find the *overall minimum* perpendicular distance, i.e. $\delta_{P-QR}^{min} = \min_j [\delta_{P-QR}(t_j)]$ for $t_j = j\Delta t$; $j = 0,1,2,...,M_{time}$; where $M_{time} = \dfrac{T}{\Delta t}$ and Δt is a suitably small chosen *monitoring* time interval.

The alternative relative positioning of bodies i and j is shown in Figure D.5. Here the instantaneous perpendicular distance δ_{P-QR} (expression (D.6)) becomes *larger* as the two bodies move closer to each other. Hence, if the two bodies shown in Figure D.5 move relative to each other over a time interval $[0,T] = [0, T_{Mtime}]$, the instantaneous perpendicular distance δ_{P-QR} (expression (D.6)) may be monitored at discrete time instants t_j to find the *overall maximum* perpendicular distance, i.e. $\delta_{P-QR}^{max} = \max_j [\delta_{P-QR}(t_j)]$ for t_j as defined above.
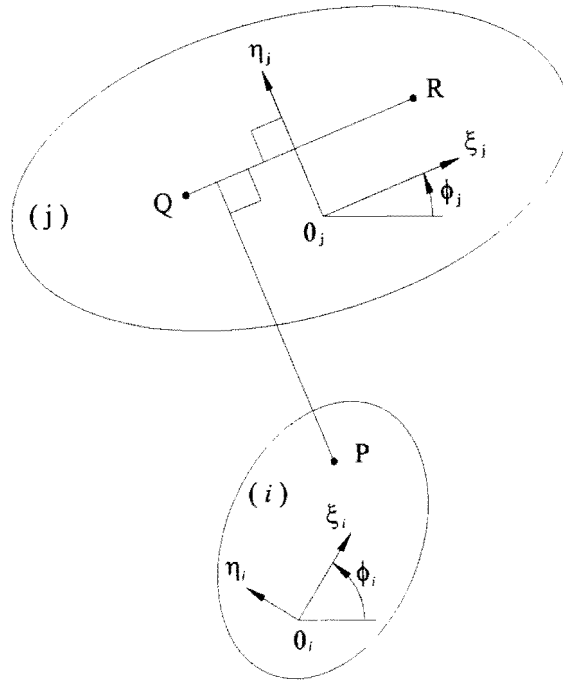
Figure D.5: Schematic representation of bodies *i* and j experiencing planar motion (alternative relative positioning of the two bodies).

With the judicious selection of point P on body *i*, and points Q and R on body j, mechanical interference between bodies *i* and j may be prohibited for both situations as depicted in Figure D.4 and Figure D.5 respectively: Firstly, an *allowable* perpendicular distance $\left|\delta_{P-QR}^{allow}\right|$ is chosen. Secondly, one of the following two inequality constraints is specified:

$$\left|\delta_{P-QR}^{allow}\right| \leq \delta_{P-QR}^{min} \tag{D.7}$$

or

$$\delta_{P-QR}^{max} \leq -\left|\delta_{P-QR}^{allow}\right| \tag{D.8}$$

Inequality constraint (D.7) is used for the relative positioning of bodies *i* and j as shown in Figure D.4, while inequality constraint (D.8) is used for the relative positioning of bodies *i* and j as shown in Figure D.5.

D.3.2 Linearly adjustable revolute joints

The configurational constraints limiting the allowable relative distances between the linearly adjustable revolute joints of the fixed base (X_2 and X_5) and the moving platform (X_1) (see expression (4.5)) are directly applicable on the physical test-model. With reverence to Figure D.6 showing the adjustable capability of the test-model, the specific bounds (given in meters) on design variables X_1, X_2 and X_5 are

$$0.1 \le X_1 \le 0.45$$

$$0.113 \le X_2 \le 0.465 \tag{D.9}$$

$$0.113 \le X_5 \le 0.27$$
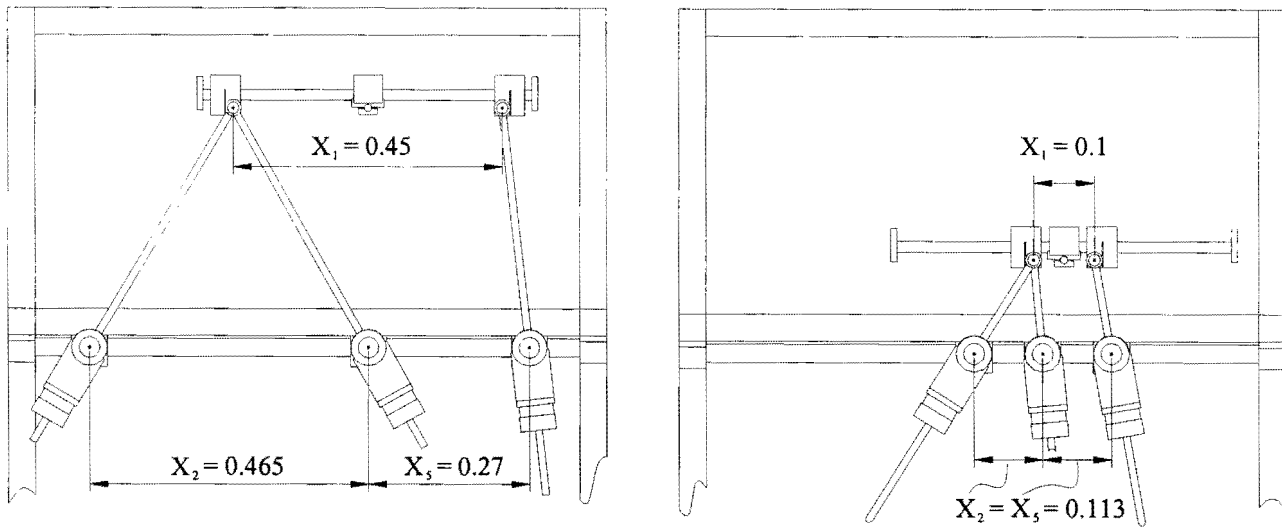
Figure D.6: Adjustable capability of the test-model.

The lower and upper bounds specified in expression (D.9) correspond exactly to the lower and upper bounds that were specified for the optimization test run of the hypothetical planar machining center (see expression (4.14)). Hence, in agreement with the inequality constraints given by expression (4.7), the first six inequality constraints used to ensure a feasible test-model design, are

$$C_1(\mathbf{X}) \equiv X_1 - 0.45 \le 0$$

$$C_2(\mathbf{X}) \equiv 0.1 - X_1 \le 0$$

$$C_3(\mathbf{X}) \equiv X_2 - 0.465 \le 0$$

$$C_4(\mathbf{X}) \equiv 0.113 - X_2 \le 0 \tag{D.10}$$

$$C_5(\mathbf{X}) \equiv X_5 - 0.27 \le 0$$

$$C_6(\mathbf{X}) \equiv 0.113 - X_5 \le 0$$

D.3.3 Extreme motion constraints

The extreme motion of the hypothetical moving platform is bounded by the *allowable* minimum and maximum actuator leg lengths (see expressions (4.6) and (4.8)). On the other hand, the motion of the physical moving platform is to be confined within the four frame boundaries represented by the four sides of rectangle FGHI as annotated in Figure D.7.
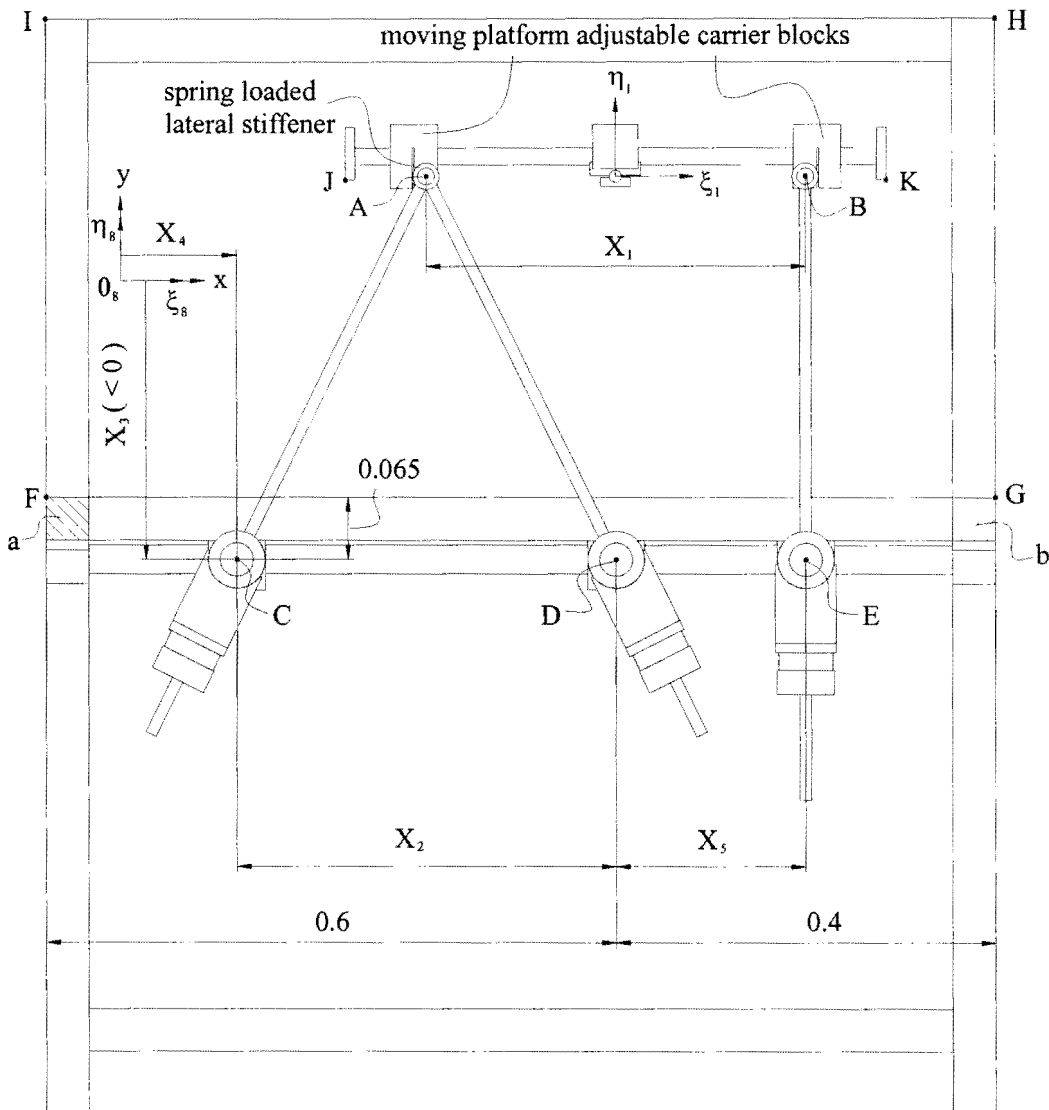
Figure D.7: Frame boundaries FGHI.

D.3.3.1 Upper frame boundary

The *upper frame boundary* (line HI) cannot be exceeded by the lateral stiffeners on the moving platform with specification that the *allowable* maximum actuator leg length $\bar{\ell}_k$ for all three actuator legs $k = 1,2,3$ is 0.525 m. Figure D.8 serves to illustrate this fact.
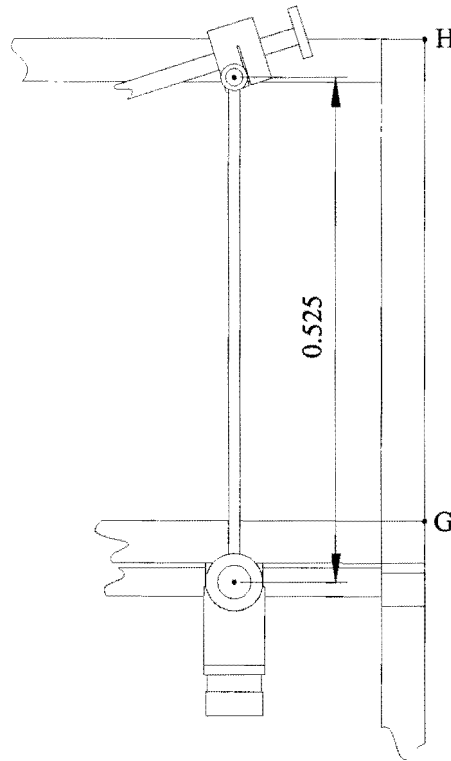
Figure D.8: Scaled two-dimensional view of an actuator leg extended to its maximum allowable leg length.

Test-model inequality constraints 7-9 are given by

$$C_7(\mathbf{X}) \equiv \ell_1^{\max}(\mathbf{X}) - 0.525 \leq 0$$

$$C_8(\mathbf{X}) \equiv \ell_2^{\max}(\mathbf{X}) - 0.525 \leq 0 \qquad\qquad (D.11)$$

$$C_9(\mathbf{X}) \equiv \ell_3^{\max}(\mathbf{X}) - 0.525 \leq 0$$

where the overall maximum leg lengths for any prescribed path are given by $\ell_k^{\max}(\mathbf{X})$, $k = 1,2,3$ as explained in Section 4.3.2. These constraints (expression (4.8)) correspond exactly to the constraints $C_{k+6}(\mathbf{X}) \equiv \ell_k^{\max}(\mathbf{X}) - 0.525 \leq 0$, $k = 1,2,3$ specified for the optimization of the hypothetical platform see expression (4.8).

D.3.3.2 Lower frame boundary

The *lower frame boundary* of the test-model is represented by line FG in Figure D.7. Here it is important to prevent mechanical interference between the moving platform and the bottom frame cross members indicated by shaded regions a and b in Figure D.7. Line FG coincides with the top plane of the two bottom frame cross members.

With the moving platform in a horizontal orientation, the bottom ends of the adjustable brackets of revolute joints A and B are the lowest points on the moving platform (see Figure D.7). Due to the fact that the relative positions of the revolute joints may be adjusted, it is highly unlikely that the adjustable

brackets of revolute joints A and B will collide with the bottom frame cross members (shaded regions a and b), even with the moving platform in a horizontal orientation ($\phi_1 = 0$). Furthermore, for a large enough CCW rotation of the moving platform, point J indicated in Figure D.7 is the lowest point on the moving platform. Similarly, for a large enough CW rotation of the moving platform, point K (see Figure D.7) is the lowest point on the moving platform.

The lower frame boundary is therefore treated here by monitoring the perpendicular distances between line FG on the frame, and respective points J and K on the moving platform following the methodology explained in Section D.3.1. In particular, assumptions 1 - 3 listed in Section D.3.1 are valid here, since the instantaneous position (x_1, y_1) and orientation ϕ_1 of the moving platform (body 1 in Figure D.2) are known as the prescribed path is traced (see expressions (2.27) – (2.29)). Furthermore, the global position (x_8, y_8) and orientation ϕ_8 of the frame (body 8 in Figure D.2) are fixed: $[x_8, y_8, \phi_8]^T = [0,0,0]^T$. The fixed local coordinates (in meters) of points J and K are $(\xi^J, \eta^J)_1 = (-0.285, -0.004)$ and $(\xi^K, \eta^K)_1 = (0.285, -0.004)$, and the fixed local η-coordinate of line FG is $\eta_8^{FG} = X_3 + 0.065$. Note that X_3 is the design variable representing the y-coordinate of the three base revolute joints C, D and E (see Figure D.2). Hence, the respective instantaneous perpendicular distances $\delta_{J-FG}(X, t_{i,j})$ and $\delta_{K-FG}(X, t_{i,j})$ may be determined at any time instant $t_{i,j}$, $i = 0,1,2,...,N-1$, $j = 0,1,2,...,n_{time}$ (see Section 4.2.2) in accordance with expressions (D.3) - (D.6). The default value for $n_{time} = 10$ (see **Appendix B**).

Since the relative positioning of the moving platform with respect to the lower frame boundary conforms to the relative positioning of the bodies i and j as depicted in Figure D.4, the *lower frame boundary inequality constraints* formulated here correspond to the inequality (D.7):

$$C_{10}(X) \equiv 0.006 - \delta_{J-FG}^{min}(X) \leq 0$$
$$C_{11}(X) \equiv 0.006 - \delta_{K-FG}^{min}(X) \leq 0$$

(D.12)

where $\delta_{J-FG}^{min}(X) = \min_{i,j}[\delta_{J-FG}(X, t_i + t_j)]$, and $\delta_{K-FG}^{min}(X) = \min_{i,j}[\delta_{K-FG}(X, t_i + t_j)]$, and with t_i and t_j as defined above.

The same value of $0.006\,m$ is used for both allowable perpendicular distances $\left|\delta_{J-FG}^{allow}\right|$ and $\left|\delta_{K-FG}^{allow}\right|$ in expression (D.12). This value was chosen, so that the shortest attainable actuator leg length, without violating inequality constraints C_{10} and C_{11} (expression (D.12)), is $0.075\,m$ as shown in Figure D.9. This length is also the *allowable* minimum actuator leg length specified for the hypothetical platform in expression (4.15).
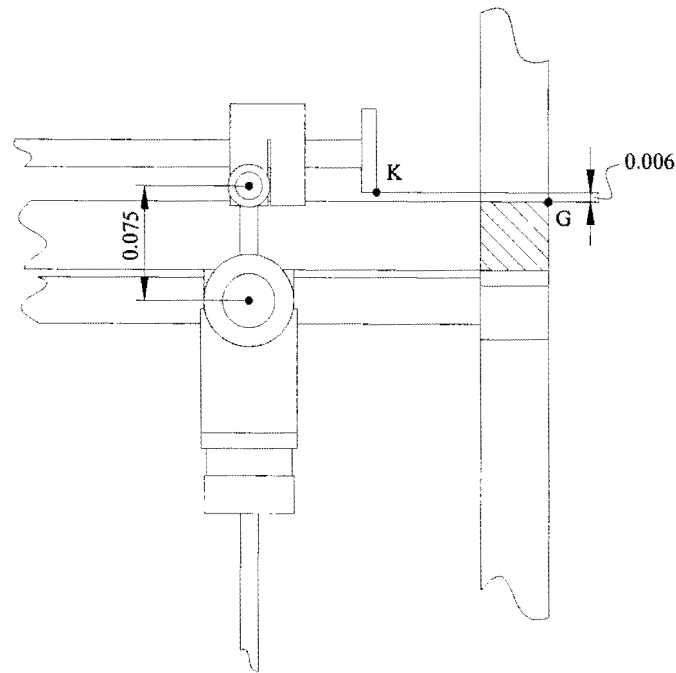
Figure D.9: Shortest attainable actuator leg length.

Since the shortest attainable actuator leg length corresponds exactly to the allowable minimum actuator leg length, inequality constraints $C_{k+9}(\mathbf{X}) \equiv \underline{\ell}_k - \ell_k^{min}(\mathbf{X}) \leq 0$, $k = 1,2,3$ (expression (4.8)) specified for the hypothetical platform are redundant in the optimization of the platform test-model.

D.3.3.3 Left hand frame boundary

The *left-* and *right hand frame boundaries* limit the horizontal movement of the physical moving platform. With the use of the spring loaded lateral stiffeners (see **Chapter 5**), point A is restricted to the right hand side of line FI, and point B is restricted to the left hand side of line GH (see Figure D.7).

Consider for the moment the left hand frame boundary. Point A is on the moving platform (body 1 in Figure D.2) at local coordinates $(\xi^A, \eta^A)_1 = \left(-\dfrac{X_1}{2}, 0\right)$, and the global position and orientation of body 1 $[x_1, y_1, \phi_1]^T$ are known at each time instant as the prescribed path is traced. The global position of point A may therefore be determined in accordance with expression (D.3).

Line FI on the frame (body 8 in Figure D.2) is dealt with in a special manner. According to the definitions given in Section 2.3, the fixed body 8 is considered as the *ground* of the planar Gough-Stewart platform mechanism. Figure D.2 shows that the origin of body 8 is chosen to coincide with the origin of the global $0xy$-reference frame, $(x_8, y_8) = (0,0)$, and that the local $0_8 \xi_8 \eta_8$-coordinate system and the global $0xy$-reference frame are identically orientated, i.e. $\phi_8 = 0$. This implies that the fixed

vertical line FI is parallel to the η-axis of body 8. However, the proposed collision prevention methodology explained in Section D.3.1 is based on the assumption that the line in body j is parallel to the ξ-axis of body j (see Figure D.4). The special treatment of line FI consists of the specification that body 8 is angled at $90°$, i.e. $\phi_8 = \frac{\pi}{2}\,\text{rad}$, and is allowable, since each inequality constraint is treated separately and independent of the kinematic and kinetic analysis (**Chapter 2**).

The global x-coordinate of line FI is $x^{FI} = X_4 + X_2 - 0.6$ (see Figure D.7), with X_4 and X_2 two of the five design variables describing the adjustable geometry of the planar Gough-Stewart platform machining center (see Figure 4.1). With the specification that $[x_8, y_8, \phi_8]^T = \left[0, 0, \frac{\pi}{2}\right]^T$, the local η-coordinate of line FI may be determined using the transformation given by expression (D.4):

$\eta_8^{FI} = -(X_4 + X_2 - 0.6)$.

The instantaneous perpendicular distance between point A on the moving platform and line FI on the frame δ_{A-FI} may therefore be determined in accordance with expression (D.6). The relative positioning of the moving platform with respect to the left hand frame boundary agrees with the relative positioning of bodies *i* and j as depicted in Figure D.5. As a result of this, the instantaneous perpendicular distance δ_{A-FI} becomes *larger* as the moving platform moves closer to the left hand frame boundary. The *left hand frame boundary inequality constraint* is therefore given by

$$C_{12}(\mathbf{X}) \equiv \delta_{A-FI}^{max}(\mathbf{X}) + 0.015 \leq 0 \tag{D.13}$$

with $\delta_{A-FI}^{max}(\mathbf{X}) = \max_{i,j}[\delta_{A-FI}(\mathbf{X}, t_i + t_j)]$ and $t_i + t_j$ as defined in Section D.3.3.2. Since the radius of the spring loaded lateral stiffener is $15\,\text{mm}$, a value of $0.015\,\text{m}$ is assigned to the allowable perpendicular distance $\left|\delta_{A-FI}^{allow}\right|$ in the above expression. Note also that expression (D.13) corresponds to inequality (D.8) derived for the general situation depicted in Figure D.5.

D.3.3.4 Right hand frame boundary

The *right hand frame boundary* restricts point B on the moving platform to the left hand side of line GH in Figure D.7. Point B on the moving platform (body 1 in Figure D.2) is at local coordinates $(\xi^B, \eta^B)_1 = \left(\frac{X_1}{2}, 0\right)$ (see Section D.2.1). Line GH on the frame (body 8 in Figure 2.5) is treated here in a similar manner to line FI of the left hand frame boundary (see Section D.3.3.3) with the specification

---

that $[x_8, y_8, \phi_8]^T = \left[0, 0, \dfrac{\pi}{2}\right]^T$. The global x-coordinate of line GH is $x^{GH} = X_4 + X_5 + 0.4$, from which

the local η-coordinate, $\eta_8^{GH} = -(X_4 + X_5 + 0.4)$, may be determined (see expression (D.4)).

Note that since the perpendicular distance between line GH and point B becomes *smaller* as the platform moves closer to the right hand frame boundary, the *right hand frame boundary inequality constraint* is given by

$$C_{13}(\mathbf{X}) \equiv 0.015 - \delta_{B-GH}^{min}(\mathbf{X}) \leq 0 \qquad\qquad (D.14)$$

with $\delta_{B-GH}^{min}(\mathbf{X}) = \min_{i,j}[\delta_{B-GH}(\mathbf{X}, t_i + t_j)]$, and $\delta_{B-GH}(\mathbf{X}, t_i + t_j)$ solved for in accordance with expression

(D.6) at each time instant $t_i + t_j$. Once again, an allowable perpendicular distance $\left|\delta_{B-GH}^{allow}\right| = 0.015\,\text{m}$ is

specified to compensate for the 15 mm radius of the spring loaded lateral stiffener (see **Chapter 5**).

D.3.4 Revolute joint mechanical interference constraints

There are no explicit constraints specified for the relative rotations about the revolute joints of the hypothetical platform. In practice however, the allowable rotations about the revolute joints of the physical test-model are limited as a result of mechanical interferences.

The design and assembly of the test-model is explained in detail in **Chapter 5**. Figure D.10 shows an annotated two-dimensional view of the planar Gough-Stewart platform test-model, where the different components involved in the revolute joint mechanical interferences are annotated.
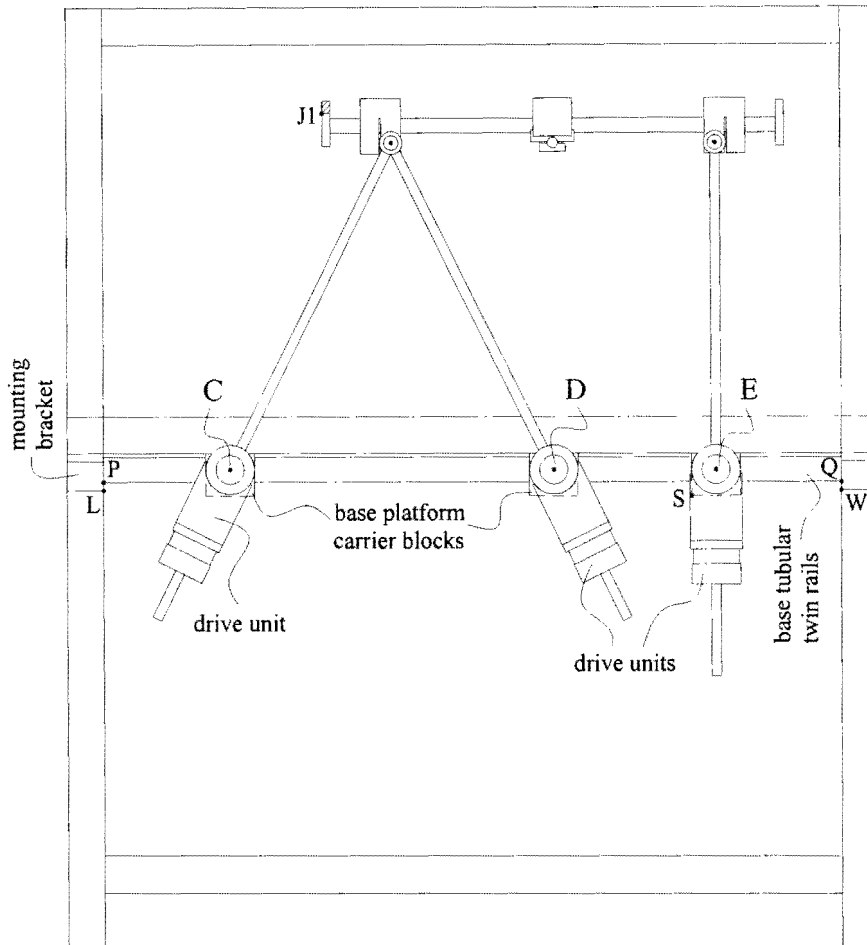
Figure D.10: Annotated drawing of the planar Gough Stewart platform test-model.

Consider for the moment the fixed base platform assembly. In essence, and with reference to Figure D.10 each of the three revolute joints C, D and E is connected to a pair of *carrier blocks*, which are linearly adjustable along the *base tubular twin rails*. These base tubular twin rails are connected to the frame by means of *mounting brackets*. The base revolute joints C, D and E carry the actuator leg *drive units*, each consisting of a motor and gearbox assembly.

Varying the actuator leg lengths, not only causes the moving platform to change its position and orientation, but also causes the relative orientations of the actuator legs to vary. The relative orientations of the actuator legs and drive units correspond exactly, hence the potential danger exists of mechanical interference between the drive units and the different components of the fixed base frame.

## D.3.4.1 Revolute joint C mechanical interference constraints

The relative position of revolute joint C on the base tubular twin rails is determined by design variable X_2 (see Section D.2.1). Depending on the magnitude of X_2, an excessively large CW rotation of

actuator leg 1 will cause the drive unit carried by revolute joint C to collide with either the left hand mounting brackets, or with the base tubular twin rails.

The proposed inequality constraint methodology for the prevention of mechanical interference (Section D.3.1) may however be applied here to formulate two separate inequality constraints with which both potential collisions may be avoided:

$$C_{14}(\mathbf{X}) \equiv \delta_{M1-PQ}^{max}(\mathbf{X}) + 0.005 \leq 0 \qquad (D.15)$$

$$C_{15}(\mathbf{X}) \equiv 0.005 - \delta_{L-M1M2}^{min}(\mathbf{X}) \leq 0 \qquad (D.16)$$
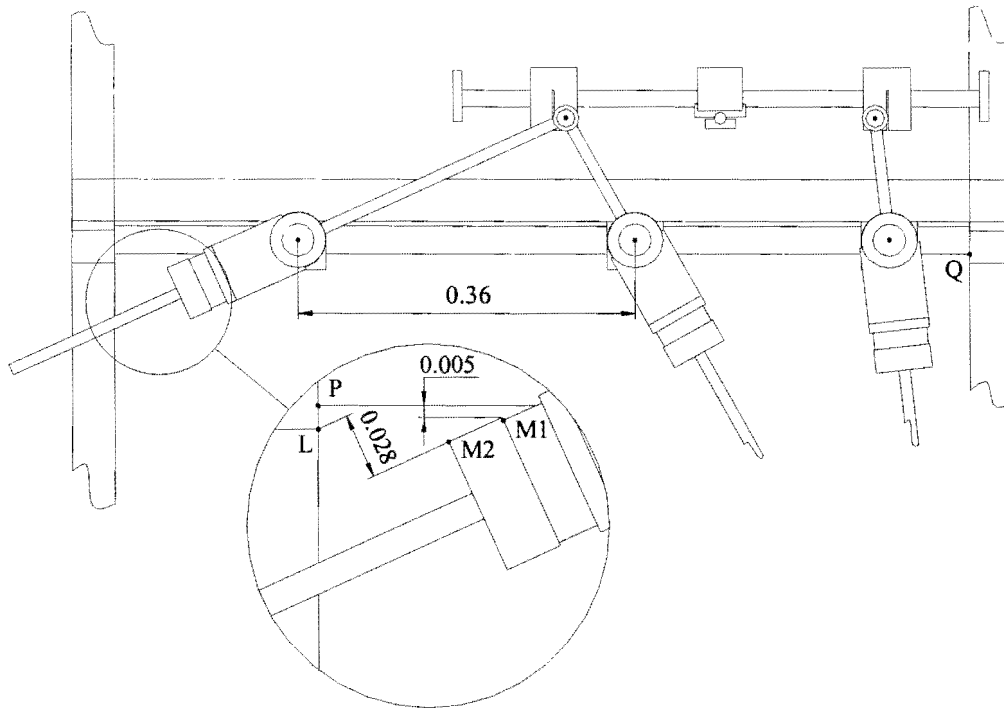
Figure D.11: Inequality constraint C_{14} (expression (D.15)) active.

Figure D.11 shows a scaled two-dimensional view of the test-model with $X_2 = 0.360\,\text{m}$, where drive unit C is about to collide with the base twin tubular rails, but *not* with the mounting brackets. Note that the perpendicular distance between line PQ and point M1 is $\delta_{M1-PQ} = 0.005\,\text{m}$, rendering inequality constraint C_{14} (expression (D.15)) active. In spite of this, the perpendicular distance between line M1M2 and point L is $\delta_{L-M1M2} = 0.028\,\text{m}$, so that inequality constraint C_{15} (expression (D.16)) is not active.

The evaluation of inequality constraints C_{14} is summarized in Table D.2 below:

General case analogy	Inequality constraint C_{14}
$\delta_{P-QR}^{max} \leq -\left\lvert\delta_{P-QR}^{allow}\right\rvert$ (expression (D.8))	$C_{14}(\mathbf{X}) \equiv \delta_{M1-PQ}^{max}(\mathbf{X}) + 0.005 \leq 0$ (expression (D.15))
Figure D.5	Figure D.11
Assumption 1: (see Section D.3.1)	
$[x,y,\phi]_i^T$ must be known	$[x,y,\phi]_5^T$ known from the inverse kinematic analysis (see Section 2.5)
$[x,y,\phi]_j^T$ must be known	$[x,y,\phi]_8^T = [0,0,0]^T$ fixed frame position and orientation (see Figure D.2)
Assumption 2: (see Section D.3.1)	
$(\xi^P,\eta^P)_i$ must be known	$(\xi^{M1},\eta^{M1})_5 = (-0.06439, 0.03)$ (see Figure D.13)
Assumption 3: (see Section D.3.1)	
η_j^{QR} must be known	$\eta_8^{PQ} = X_3 - 0.015$

Table D.2: Evaluation of constraint C_{14} (expression (D.15)).
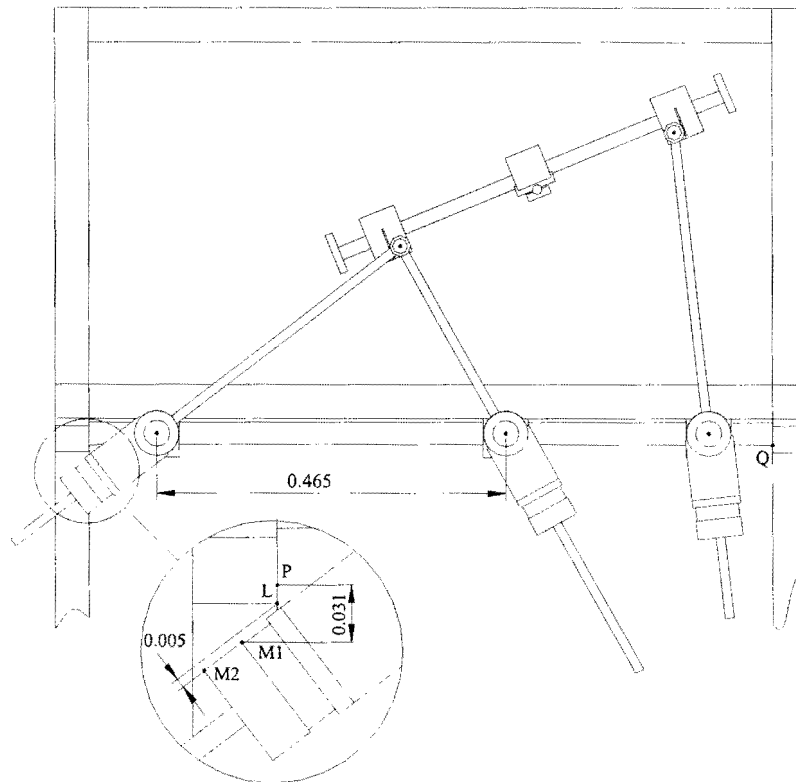

Figure D.12: Inequality constraint C_{15} (expression (D.16)) active.

On the other hand, Figure D.12 shows a scaled two-dimensional view of the test-model with $X_2 = 0.465\,\text{m}$, where drive unit C is about to collide with the left hand mounting bracket, and *not* with the base twin tubular rails. As expected, the perpendicular distance between line PQ and point M1, is greater than $0.005\,\text{m}$ ($\delta_{M1-PQ} = 0.031\,\text{m}$) so that inequality C_{14} (expression (D.15)) is *not* active, while $\delta_{L-M1M2} = 0.005\,\text{m}$, so that inequality C_{15} (expression (D.16)) becomes active.

The evaluation of inequality constraint C_{15} are summarized in Table D.3 below:

General case analogy	Inequality constraint C_{15}
$\left|\delta_{P-QR}^{allow}\right| \le \delta_{P-QR}^{min}$ (expression (D.7))	$C_{15}(\mathbf{X}) \equiv 0.005 - \delta_{L-M1M2}^{min}(\mathbf{X}) \le 0$ (expression (D.16))
Figure D.4	Figure D.12
Assumption 1: (see Section D.3.1)	
$[x,y,\phi]_i^T$ must be known	$[x,y,\phi]_8^T = [0,0,0]^T$ fixed frame position and orientation (see Figure D.2)
$[x,y,\phi]_j^T$ must be known	$[x,y,\phi]_5^T$ known from the inverse kinematic analysis (see Section 2.5)
Assumption 2: (see Section D.3.1)	
$(\xi^P,\eta^P)_i$ must be known	$(\xi^L,\eta^L)_8 = \big((X_4 + X_2 - 0.555),(X_3 - 0.025)\big)$
Assumption 3: (see Section D.3.1)	
η_j^{QR} must be known	$\eta_5^{M1M2} = 0.03$ (see Figure D.13)

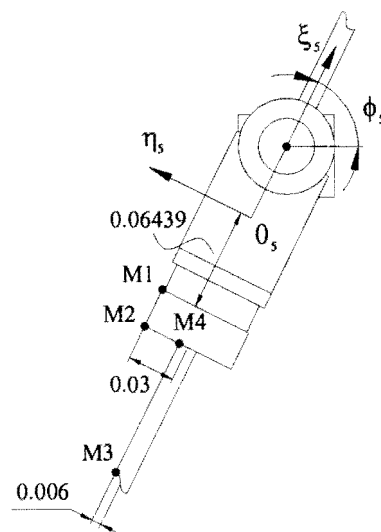**Table D.3: Evaluation of constraint C_{15} (expression (D.16)).**

Figure D.13: Local coordinates on drive unit C.

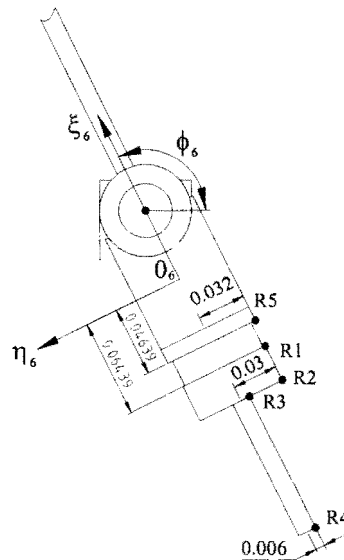## D.3.4.2 Revolute joint D mechanical interference constraints

The relative position of revolute joint D on the base twin tubular rails is fixed (see Section D.2.1). However, the adjustable relative position of revolute joint E, given by the magnitude of design variable X_5, influences whether drive unit D will collide with the base twin tubular rails, or with the carrier blocks of revolute joint E. These potential collisions will of course only occur for excessively large CCW rotations of actuator leg 2. A third possible collision may occur between actuator leg 2 and drive unit E, depending on the value of X_5, as well as the relative orientations of actuator legs 2 and 3.

In order to prevent all three potential collisions from happening, three inequality constraints are formulated (refer to the annotations in Figure D.10 and Figure D.14 respectively):

$$C_{16}(\mathbf{X}) \equiv \delta_{R1-PQ}^{max}(\mathbf{X}) + 0.005 \leq 0 \tag{D.17}$$

$$C_{17}(\mathbf{X}) \equiv \delta_{S-R1R2}^{max}(\mathbf{X}) + 0.005 \leq 0 \tag{D.18}$$

$$C_{18}(\mathbf{X}) \equiv \delta_{T5-R3R4}^{max}(\mathbf{X}) + 0.005 \leq 0 \tag{D.19}$$

Figure D.14: Local coordinates on drive unit D.

D.3.4.3 Revolute joint E mechanical interference constraints

As previously stated in Sections D.2.1 and D.3.4.2, the magnitude of design variable X_5 determines the relative position of revolute joint E on the base twin tubular rails. For an extreme CCW orientation of actuator leg 3, and depending on the magnitude of design variable X_5, drive unit E will collide either with the base twin tubular rails, or with the right hand mounting bracket. There also exists the possibility of mechanical interference between actuator leg 3 and drive unit D, depending on the magnitude of design variable X_5, and the relative orientations of actuator legs 2 and 3.

Following the same recipe as before, three inequality constraint equations are formulated to prevent the above mentioned potential collisions from happening (refer to the annotations in Figure D.10 and Figure D.15 respectively):

$$C_{19}(\mathbf{X}) \equiv \delta^{max}_{V1-PQ}(\mathbf{X}) + 0.005 \leq 0 \qquad (D.20)$$

$$C_{20}(\mathbf{X}) \equiv \delta^{max}_{W-V1V2}(\mathbf{X}) + 0.005 \leq 0 \qquad (D.21)$$

$$C_{21}(\mathbf{X}) \equiv 0.005 - \delta^{min}_{R5-T3T4}(\mathbf{X}) \leq 0 \qquad (D.22)$$
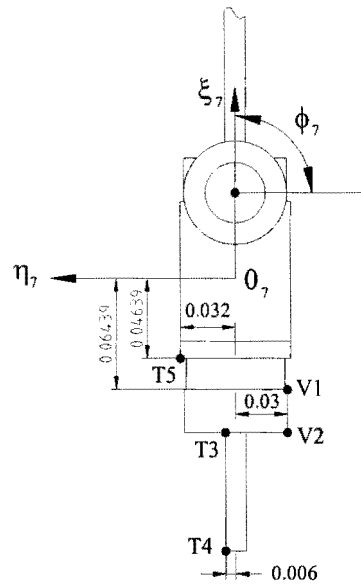
Figure D.15: Local coordinates on drive unit E.

D.3.4.4 Revolute joint A mechanical interference

Depending on the relative orientation of the moving platform (body 1 in Figure D.2) and actuator leg 1 (body 2 in Figure D.2), point J1 on the moving platform left hand bracket may collide with actuator leg 1. In order to avoid such a collision from happening, the following inequality constraint is formulated (see Figure D.16):

$$C_{22}(\mathbf{X}) \equiv 0.005 - \delta^{min}_{J1-M3M4}(\mathbf{X}) \leq 0 \qquad (D.23)$$
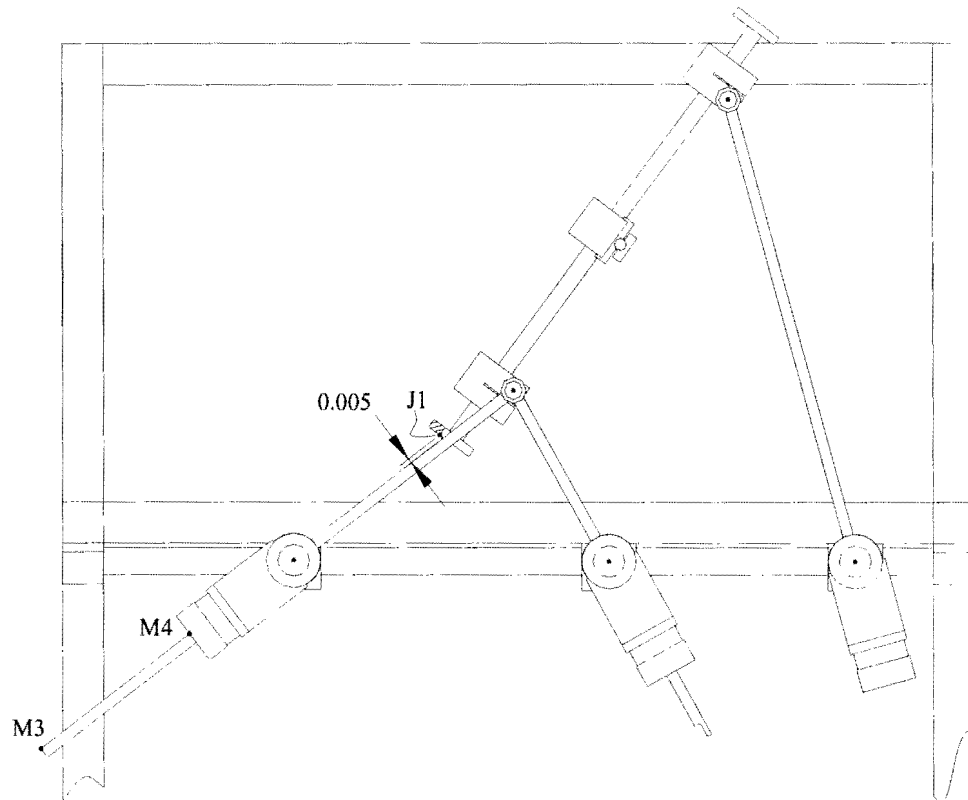
Figure D.16: Inequality constraint C_{22} **(expression (D.23)) active.**

REFERENCES

[1] Merlet, J-P. *Parallel Robots*. Dordrecht: Kluwer Academic Publishers, 2000.

[2] Dasgupta, B. and Mruthyunjaya, T.S. The Stewart Platform Manipulator: a Review. *Mechanism and Machine Theory*, Vol. 35, pp. 15-40, 2000.

[3] Lin, W., Griffis, M. and Duffy, J. Forward Displacement Analyses of the 4-4 Stewart Platforms. *Transactions of the ASME Journal of Mechanical Design*, Vol. 114, pp.444-450, 1992.

[4] Gough, V.E. and Whitehall, S.G. Universal Tyre Test Machine. In *Proceedings 9th International Technical Congress F.I.S.I.T.A.*, Vol. 117, pp. 117-137, 1962.

[5] Stewart, D. A Platform with Six Degrees of Freedom. In *Proceedings of the Institute of Mechanical Engineers Part 1*, Vol. 180, No. 15, pp. 371-386, 1965/66.

[6] Di Gregorio, R. and Parenti-Castelli, V. Benefits of Twisting the Legs in the 3-UPU Tsai Mechanism. In Proceedings *Year 2000 Parallel Kinematics Machines International Conference, September 13-15, 2000, Ann Arbor, Mi. USA,* [Orlandea, N. et al. (eds.)], pp.201 - 211.

[7] Hunt, K.H. *Kinematic Geometry of Mechanisms*. Oxford: Clarendon Press, 1978.

[8] Lewis, G. It's Here – Six Ways at Once. *Engineering News*, No. 234, pp. 1, 1966.

[9] Pritschow, G. Research and Development in the Field of Parallel Kinematic Systems in Europe. In Boër, C.R., Molinari-Tosatti, L. and Smith, K.S. (eds.) *Parallel Kinematic Machines: Theoretical Aspects and Industrial Requirements*. London: Springer-Verlag, pp.3-15, 1999.

[10] Boër, C.R., Molinari-Tosatti, L. and Smith, K.S. (eds.) *Parallel Kinematic Machines: Theoretical Aspects and Industrial Requirements*. London: Springer-Verlag, 1999.

[11] Powell, N.P., Whittingham, B.D. and Gindy, N.N.Z. Parallel Link Mechanism Machine Tools: Acceptance Testing and Performance Analysis. In Boër, C.R., Molinari-Tosatti, L. and Smith, K.S. (eds.) *Parallel Kinematic Machines: Theoretical Aspects and Industrial Requirements*. London: Springer-Verlag, pp.327-344, 1999.

[12] Wavering, A.J. Parallel Kinematic Machine Research at NIST: Past, Present, and Future. In Boër, C.R., Molinari-Tosatti, L. and Smith, K.S. (eds.) *Parallel Kinematic Machines: Theoretical Aspects and Industrial Requirements*. London: Springer-Verlag, pp.17-31, 1999.

[13] Gindy et al. The Variax Machining Centre, its Design and Application to a Rapid Response Integrated Manufacturing System. *Technical Report, Department of Mechanical Engineering and Operations Management, University of Nottingham, U.K.*, 1997.

[14] Ziegert, J.C., Jokiel, B. and Huang, C-C. Calibration and Self-Calibration of Hexapod Machine tools. In Boër, C.R., Molinari-Tosatti, L. and Smith, K.S. (eds.) *Parallel Kinematic Machines: Theoretical Aspects and Industrial Requirements.* London: Springer-Verlag, pp.205-225, 1999.

[15] Neugebauer, R. et al. Experiences with a Hexapod-Based Machine Tool. In Boër, C.R., Molinari-Tosatti, L. and Smith, K.S. (eds.) *Parallel Kinematic Machines: Theoretical Aspects and Industrial Requirements.* London: Springer-Verlag, pp.313-326, 1999.

[16] Tönshoff, H.K. and Grendel, H. A Systematic Comparison of Parallel Kinematics. In Boër, C.R., Molinari-Tosatti, L. and Smith, K.S. (eds.) *Parallel Kinematic Machines: Theoretical Aspects and Industrial Requirements.* London: Springer-Verlag, pp.295-312, 1999.

[17] Orlandea, N. et al. (eds.) Proceedings *Year 2000 Parallel Kinematics Machines International Conference, September 13-15, 2000, Ann Arbor, Mi. USA.*

[18] Koepfer, C. A New Twist on Five-Axis Machining [Online]. MMS Online, 2001. Available from http://www.mmsonline.com/articles/1000rt1.html [Accessed 18 October 2001].

[19] Gopalakrishnan, V., et al. Parallel Structures and Their Applications in Re-configurable Machining Systems. In Proceedings *Year 2000 Parallel Kinematics Machines International Conference, September 13-15, 2000, Ann Arbor, Mi. USA,* [Orlandea, N. et al. (eds.)], pp.87 - 97.

[20] Duffy, J. *Statics and Kinematics with Applications to Robotics.* Cambridge University Press, 1996.

[21] Shirkhodaie, A.H. and Soni, A.H. Forward and Inverse Synthesis for a Robot with Three Degrees of Freedom. In *Proceedings of the Summer Computer Simulation Conference.* Montréal, pp. 851-856, 1987.

[22] Pennock, G.R. and Kassner, D.J. Kinematic Analysis of a Planar Eight-Bar Linkage: Application to a Platform-Type Robot. *Transactions of the ASME Journal of Mechanical Design,* Vol. 114, pp. 87-95, 1992.

[23] Peysah, E.E. Determination of the Position of the Member of Three-Joint and Two-Joint Four Member Assur Groups with Rotational Pairs. (in Russian) *Maschinowedenie,* No. 5, pp. 55-61, 1985.

[24] Wohlhart, K. Direct Kinematic Problem of the Planar Stewart Platform. In *Proceedings of the International Conference on Computer Integrated Manufacturing,* Zakopane, pp. 403-411, 1992.

[25] Gosselin, C., Sefroui, J. and Richard, M. "Solutions polynomiales au problème de la cinématique directe des manipulateurs parallèles plans à trois degrés de liberté." *Mechanism and Machine Theory,* Vol. 27, pp. 107-119, 1992.

[26] Gosselin, C. Parallel Computational Algorithms for the Kinematics and Dynamics of Planar and Spatial Parallel Manipulators. *Transactions of the ASME Journal of Dynamic Systems, Measurement and Control*, Vol. 118, pp. 22-28, 1996.

[27] Sefroui, J. and Gosselin, C. Singularity Analysis and Representation of Planar Parallel Manipulators. *Journal of Robotics and Autonomous Systems*, Vol. 10, pp. 209-224, 1993.

[28] Gosselin, C. and Angeles, J. The Optimum Kinematic Design of a Planar Three-Degree-of-Freedom Parallel Manipulator. *Transactions of the ASME Journal of Mechanisms, Transmissions and Automation in Design*, Vol. 110, pp. 35-41, 1988.

[29] Williams, R.L. (II) and Reinholtz, C.F. Closed-form Workspace Determination and Optimization for Parallel Robotic Mechanisms. In *Proceedings of the ASME Mechanisms Conference*, Kissimmee, Vol. 15-3, pp.341-351, 1988.

[30] Laliberté, T., Gosselin, C. and Jean, M. Static Balancing of 3-DOF Planar Parallel Mechanisms. *IEEE/ASME Transactions on Mechatronics*, Vol. 4, pp. 363-377.

[31] Satya, S.M., Ferreira, P.M. and Spong, M.W. Hybrid Control of a Planar 3-DOF Parallel Manipulator for Machining Operations. *Technical Report, Department of Mechanical and Industrial Engineering, University of Urbana-Champaign, Illinois USA*, 1995.

[32] El-Khasawneh, B., Satya, S. and Brunner, R. SMARTCUTS (Simultaneous Machining through Real Time Control of Universal Tooling Systems) [Online]. Available from http://marshall.me.uiuc.edu/PROJECTS/SCUTS/SMARTCUTS.html [Accessed 30 January 1998]

[33] El-Khasawneh, B.S. and Ferreira, P.M. The Tetrahedral Tripod. In Boër, C.R., Molinari-Tosatti, L. and Smith, K.S. (eds.) *Parallel Kinematic Machines: Theoretical Aspects and Industrial Requirements*. London: Springer-Verlag, 1999, pp.419-430.

[34] El-Khasawneh, B.S. and Ferreira, P.M. On Using Parallel Link Manipulators as Machine Tools. *NAMRC XXV – North American Manufacturing Research Conference; 25th. Transactions of the North American Manufacturing Research Institution of SME, 1997; Conf. 25*, pp. 305-310, 1997.

[35] El-Khasawneh, B.S. and Ferreira, P.M. Computation of Stiffness and Stiffness Bounds for Parallel Link Manipulators. *International Journal of Machine Tools & Manufacture*, Vol. 39, pp. 321-342, 1999.

[36] Weck, M. and Giesler, M. Dyna-M Development of Machine-Tools with Parallel Kinematic. *WZL RWTH AACHEN Lehrstuhl für Werkzeugmashinen.* Available via e-mail from: M.Giesler@wzl.rwth-aachen.de (22 November 2000).

---

[37] Moriwaki, T. Survey of R&D Activities Related to Parallel Mechanisms in Japan. In Boër, C.R., Molinari-Tosatti, L. and Smith, K.S. (eds.) *Parallel Kinematic Machines: Theoretical Aspects and Industrial Requirements.* London: Springer-Verlag, 1999, pp.431-440.

[38] Chrisp, A.G. and Gindy, N.N.Z. Parallel Link Machine Tools: Simulation, Workspace Analysis and Component Positioning. In Boër, C.R., Molinari-Tosatti, L. and Smith, K.S. (eds.) *Parallel Kinematic Machines: Theoretical Aspects and Industrial Requirements.* London: Springer-Verlag, pp. 245-256, 1999.

[39] Whittingham, B.D. et al. Capabilities of Parallel Link Machine Tools: Preliminary Investigations of the Variax Hexacenter. *Technical Report, Department of Mechanical Engineering and Operations Management, University of Nottingham, U.K.,* 1998.

[40] Du Plessis, L.J. and Snyman, J.A. A Numerical Method for the Determination of Dextrous Workspaces of Gough-Stewart platforms. *International Journal for Numerical Methods in Engineering,* Vol. 52, pp 345–369, 2001.

[41] Yan, H-S. and Chen, F-C. Configuration Synthesis of Machining Centers without Tool Change Arms. *Mechanism and Machine Theory,* Vol. 33, pp. 197-212, 1998.

[42] Koren, Y. Foreword to the *CIRP 1st International Conference on Agile, Re-configurable Manufacturing, May 21-22, 2001, University of Michigan, Ann Arbor, Michigan, USA.*

[43] Ji, Z. and Leu, M.C. Design, Re-configuration, and Control of Parallel Kinematic Machines. In Boër, C.R., Molinari-Tosatti, L. and Smith, K.S. (eds.) *Parallel Kinematic Machines: Theoretical Aspects and Industrial Requirements.* London: Springer-Verlag, pp.111-129, 1999.

[44] Ji, Z. and Song, P. Design of a Re-configurable Platform Manipulator. *Journal of Robotic Systems,* Vol. 15, pp. 341-346, 1998.

[45] Ji, Z. Analysis of Design Parameters in Platform Manipulators. *Transactions of the ASME Journal of Mechanical Design,* Vol. 118, pp. 526-531, 1996.

[46] Fitzgerald, J.M. and Lewis, F.L. Evaluating the Stewart Platform for Manufacturing. *Robotics Today,* Vol. 6, pp. 1-3, 1993.

[47] Chedmail, P. Optimization of Multi-DOF Mechanisms. In Angeles, J. and Zakhariev, E. (eds.) *Computational Methods in Mechanical Systems – Mechanism Analysis, Synthesis, and Optimization.* Berlin: Springer-Verlag, pp.97-129, 1998.

[48] Kodiyalam, S. and Saxena, M. (eds.) *Geometry and Optimization Techniques for Structural Design.* Billerica: Computational Mechanics Inc. and Essex: Elsevier Science Publishers Ltd., 1994

[49] Zhang, D and Gosselin, C.M. Kinetostatic Analysis and Optimization of the Tricept Machine Tool Family. In Proceedings *Year 2000 Parallel Kinematics Machines International Conference, September 13-15, 2000, Ann Arbor, Mi. USA,* [Orlandea, N. et al. (eds.)], pp.174 - 188.

[50] Wang, Z., et al. A Study on Workspace, Boundary Workspace Analysis and Workpiece Positioning for Parallel Machine Tools. *Mechanism and Machine Theory,* Vol. 36, pp. 605-622, 2001.

[51] Kirchner, J. and Neugebauer, R. How to Optimize Parallel Link Mechanisms – Proposal of a New Strategy. In Proceedings *Year 2000 Parallel Kinematics Machines International Conference, September 13-15, 2000, Ann Arbor, Mi. USA,* [Orlandea, N. et al. (eds.)], pp.307-315.

[52] Hernández, S. Multiobjective Structural Optimization. In Kodiyalam, S. and Saxena, M., (eds.) *Geometry and Optimization Techniques for Structural Design.* Ashurst: Computational Mechanics Publications / Barking: Elsevier Science Publishers Ltd., pp. 341-362, 1994.

[53] Merlet, J-P. DEMOCRAT: A Design Methodology for the Conception of Robots with Parallel Architecture. *Robotica,* Vol. 15, pp. 367-373, 1997.

[54] Merlet, J-P. Designing a Parallel Manipulator for a Specific Workspace. *International Journal of Robotics Research,* Vol. 16, pp. 545–556, 1997.

[55] Burden, R.L. and Faires, J.D. *Numerical Analysis,* 6th ed. Pacific Grove: Brooks/Cole Publishing Company, 1997.

[56] Shamblin, S.A. and Wiens, G.J. Characterization of Dynamics in PKMs. In Proceedings *Year 2000 Parallel Kinematics Machines International Conference, September 13-15, 2000, Ann Arbor, Mi. USA,* [Orlandea, N. et al. (eds.)], pp. 24-33.

[57] Gosselin, C.M. and Hadj-Messaoud, A. Automatic Planning of Smooth Trajectories for Pick-and-Place Operations. *Transactions of the ASME Journal of Mechanical Design,* Vol. 115, pp. 450-456, 1993.

[58] Dasgupta, B. and Mruthyunjaya, T.S. Singularity-Free Path-planning for the Stewart Platform Manipulator. *Mechanisms and Machine Theory,* Vol. 33, pp. 711-725, 1998.

[59] Merlet, J-P. An Efficient Trajectory Verifier for Motion Planning of Parallel Machine [sic]. In Proceedings *Year 2000 Parallel Kinematics Machines International Conference, September 13-15, 2000, Ann Arbor, Mi. USA,* [Orlandea, N. et al. (eds.)], pp.126-134.

[60] Wolovich, W.A. *Robotics: Basic Analysis and Design.* New York: CBS College Publishing, 1987.

[61] Zhang, Q.G. and Greenway, R.B. Development and Implementation of a NURBS Curve Motion Interpolator. *Robotics and Computer-Integrated Manufacturing,* Vol. 14, pp. 27-36, 1998.

[62] Bahr, B., Xiao, X. and Krishnan, K. A Real-Time Scheme of Cubic Parametric Curve Interpolations for CNC Systems. *Computers in Industry*, Vol. 45, pp. 309-317, 2001.

[63] Kim, J-H. Ryuh, B-S. and Pennock, G.R. Development of a Trajectory Method for a Five-axis NC Machine. *Mechanism and Machine Theory*, Vol. 36, pp. 983 – 996, 2001.

[64] Snyman, J.A. The LFOPC Leap-Frog Algorithm for Constrained Optimization. *Computers and Mathematics with Applications*, Vol. 40, pp. 1085-1096, 2000.

[65] Nikravesh, P.E., *Computer-Aided Analysis of Mechanical Systems*, Englewood Cliffs: Prentice-Hall, Inc., 1988.

[66] Haug, E.J. *Computer-Aided Kinematics and Dynamics of Mechanical Systems, Volume 1: Basic Methods*, Massachusetts: Allyn and Bacon, 1989.

[67] Haug, E.J., Wang, J.Y. and Wu, J.K. Dextrous Workspace of Manipulators. I. Analytical Criteria., *Mechanical Structures and Machines*, Vol. 30, pp. 321-361, 1992.

[68] Buchanan, J.L. and Turner, P.R. *Numerical Methods and Analysis*, New York: McGraw-Hill, Inc., 1992.

[69] Granville, W.A., Smith, P.F. and Longley, W.R. *Elements of Differential and Integral Calculus, New Revised Edition*, Massachusetts: Blaisdell Publishing Company, 1962.

[70] Du Plessis, L.J., Snyman, J.A. and Smit, W.J. Optimization of the Adjustable Geometry of a Planar Stewart Platform Machining Center with respect to Placement of Workpiece relative to Tool Path. In Proceedings *Year 2000 Parallel Kinematics Machines International Conference, September 13-15, 2000, Ann Arbor, Mi. USA*, [Orlandea, N. et al. (eds.)], pp. 316-329.

[71] Snyman J.A. and Smit, W.J. The Optimal Design of a Planar Stewart Platform for Prescribed Machining Tasks. to appear in *Multibody System Dynamics*, 2001.

[72] Dynamic Analysis Design System, DADS, Computer Aided Design Software Inc., Copyright 1998.

[73] Haug, E.J., et al., Numerical Algorithms for Mapping Boundaries of Manipulator Workspaces. Proceedings *IUTAM Summer School, Aalborg, Denmark, 1994* 1 – 13, 1994 .

[74] Snyman, J.A. An Improved Version of the Original Leap-Frog Method for Unconstrained Minimization. *Applied Mathematical* Modelling, Vol. 7, pp. 216-218, 1983.

[75] Snyman, J.A. The LFOPC Leap-Frog Algorithm for Constrained Optimization. *Computers and Mathematics with Applications*, Vol. 40, pp.1085-1096, 2000.

[76] Snyman, J.A., Roux, W.J. and Stander, N. A Dynamic Penalty Function Method for the Solution of Structural Optimization Problems, *Applied Mathematical* Modelling, Vol. 180, pp. 371-386, 1994.